Non-Deterministic Design and Analysis of Parameterized Optical Structures during Conceptual Design

by

Scott Alan Uebelhart

S.B., Massachusetts Institute of Technology (1998)
S.M., Massachusetts Institute of Technology (2001)

Submitted to the Department of Aeronautics and Astronautics
in partial fulfillment of the requirements for the degree of

Doctor of Philosophy

at the

MASSACHUSETTS INSTITUTE OF TECHNOLOGY

June 2006

Author .....
Department of Aeronautics and Astronautics
May 26, 2006

Certified by .....
David W. Miller, Associate Professor of Aeronautics and Astronautics
Thesis Supervisor

Certified by .....
Daniel Frey, Assistant Professor of Mechanical Engineering
Thesis Committee Member

Certified by .....
Carl Blaurock, President, Nightsky Systems, Inc.
Thesis Committee Member

Accepted by .....
Jaime Peraire, Professor of Aeronautics and Astronautics
Chair, Committee on Graduate Students

Non-Deterministic Design and Analysis of Parameterized Optical Structures during Conceptual Design

by

Scott Alan Uebelhart

Submitted to the Department of Aeronautics and Astronautics
on May 26, 2006, in partial fulfillment of the
requirements for the degree of
Doctor of Philosophy

Abstract

The next generation of space observatories will use larger mirrors while meeting tighter optical performance requirements than current space telescopes. The spacecraft designs must satisfy the drive for low-mass, low-cost systems, and be robust to uncertainty since design validation will be based on analysis instead of pre-launch tests. Analytical techniques will be required to identify which technologies or structural architectures are most appropriate to meet conflicting system requirements, but traditionally, model-based dynamic analysis would only take place after a single point design is chosen. The challenges facing future space telescopes require a new approach to conceptual design, and motivate the creation of design tools to identify superior, robust designs earlier in the design lifecycle using model-based analysis methods.

A conceptual design methodology is proposed, in which both nominal performance as well as robustness to uncertainty are evaluated across multiple design realizations. A modeling environment is created so that for any set of design variables, such as mirror architecture or dimensions of the spacecraft, a finite element model is automatically generate and analyzed. A frequency-based dynamic analysis is performed for each design realization using integrated disturbance-to-performance models that include control systems and vibration isolators. Next, the uncertainty in early stages of design is considered and Design of Experiments tools such as the analysis of variance are used to identify critical uncertainty parameters. Lastly, parametric uncertainties are propagated through the model to bound the outputs.

Aspects of this methodology are applied to several telescopes in order to demonstrate the practicality of this approach in real-life design studies. Critical uncertainty parameter identification and uncertainty analysis tools are applied to the Terrestrial Planet Finder interferometer. A parameterized model is prepared and a trade-space analysis performed for the ground-based Thirty Meter Telescope. Finally, the methodology as a whole is applied to a new space telescope design employing lightweight mirrors and a segmented aperture. An exploration of the design space is followed by uncertainty evaluation of the optimal designs. Over 1200 unique design realizations are evaluated, and the architecture families that provide the best performance and robustness to uncertainty are identified.

Thesis Supervisor: David W. Miller
Title: Associate Professor of Aeronautics and Astronautics

Acknowledgments

This work was supported in parts by: NASA Langley Research Center, contract #NAG1-01025, with Sean Kenny as technical monitor and Sharon Leah Brown as MIT fiscal officer. The Jet Propulsion Laboratory under contract #1255406 with John Treichler as contract monitor, and Chia-Yeng Peng and Marie Levine as technical monitors. The Association of Universities for Research in Astronomy (AURA), under contract #C10413A, "Development of Methods and Software Tools for Analyzing Integrated Computer Models of Extremely Large Ground Based Telescopes," with George Angeli as the Technical Monitor and Angela Olsen as MIT financial officer.

Many people have helped and supported me these last four years of my PhD program, and throughout the twelve years since I arrived at MIT. I thank all of the members of the Space Systems Lab. These include our indispensable staff, Sharon Leah Brown, Paul Bauer and Angela Olsen my old office neighbor. I give a very warm thanks to Marilyn Good, who always did her very best to get me on Dave's schedule even when it seemed impossible, and who was always there with a smile.

This thesis certainly would not have been possible without the assistance and hard work of the members of the DOCS team. These include the TMT modeling team of Deborah Howell, Soon-Jo Chung and Julien Lamamy. With the lessons learned from TMT, Deborah Howell and Ryan Lim helped build the initial MOST model that would go on to become the final capstone application of my thesis. The MOST team soon grew to include Lucy Cohan, Elizabeth Jordan and Andrzej "Longhorn" Stewart, new graduate students who all promptly exceeded our expectations. It has been a pleasure working with them, and I was lucky to have the chance at supporting them at the beginning of their graduate careers. Lucy and Liz were also generous with their computers when I needed to run nightly batch jobs for a month.

In the Aero/Astro Department I would like to thank Oli de Weck for his support throughout my graduate program, and Annalisa Weigel for her career advice and for reading my thesis. A huge thanks to Marie Stuppard; she is the heart of our department, the first person I met in Aero/Astro during my freshman year hunt for a UROP, and my constant supporter through it all. Thank you Marie for always being here for the students.

My committee members Dan Frey and Carl Blaurock provided guidance and lots of help

with DOCS over the years.

Many friends have had to listen to me complain about grad school, but more often have reminded me to have fun in life. Adriane Faust cracked composites with me, enjoyed Thursday nights at the Thirsty, and was there with the sake when I needed it. The year I escaped from MIT I spent many wonderful nights out on the town with Karl Butler and Joanne Foster, who didn't want to see me leave Munich but luckily keep flying over to visit with me. Stephanie Schur was the first person I met after returning to MIT, introduced me to my fiancée, and together with Rob Keep have become close friends over dinners, brunches, ball games and Settlers. Simon and Xue'en have been wonderful neighbors, and it's been a special treat to watch them raising beautiful Claire. In the lab, Ray Sedwick, Edmund Kong, Tom McGuire, Jess Marquez, Deb Howell, Dan Kwon, Seung Chung and Mark Hilstad were there for post-defense parties, authentic Mexican restaurants and BBQs at the sailing pavilion. Thanks to my office mate back in the cluster, Soon-Jo Chung, for his warmth and humor. Becky Masterson read my thesis, and has provided very much appreciated advice, encouragement and motivation - often over a burger at Wendy's - throughout my PhD.

Alvar Saenz Otero has been a great friend and office mate these last few years. We started out together in Unified long ago, and have made it all the way through MIT. Despite how busy he remains, he always has time to run to LaVerdes when I need a break.

Dave Miller brought me aboard the SSL eight years ago and has always supported me. He has provided PhD guidance and given me insights into the larger world of engineering. I thank him in particular for all of his efforts on my behalf.

I am lucky to be joining a wonderful, caring family that has not seemed to mind that their daughter's boyfriend was a perpetual grad student: Chris and Pat Bever, along with Katie and Ted. And I'm even luckier to be part of a family that has supported me and given me the strength to grow and prosper through Powers, MIT undergrad and these years of grad school. Thank you so very much, Mom and Dad, Lori and Granny.

Lastly, I have been fortunate to have a partner who has stayed at my side through the good and bad of this experience. I met my fiancée Erica Bever nearly the very week I started my PhD, and she has been a constant presence through this entire process. Thank you Erica, I could not have done this without you.

This thesis is dedicated to Erica Bever.

Contents

List of Figures

List of Tables

Nomenclature

Abbreviations

ACS	attitude control system
AO	adaptive optics
ANOVA	analysis of variance
CDF	cumulative distribution function
CG	center of gravity
CST	controlled structures technology
DOE	Design of Experiments
DOF	degrees of freedom
FE	finite element
FEA	finite element analysis
FEM	finite element model
FSM	fast steering mirror
GSTM	Giant Segmented Mirror Telescope
IR	infrared
IM	integrated model
LCP	linear covariance propagation
LFT	linear fractional transformation
LOS	line-of-sight
JPL	Jet Propulsion Laboratory
JWST	James Webb Space Telescope
mas	milli-arcseconds
MIT SSL	MIT Space Systems Laboratory
MS	mean square
MOST	Modular Optical Space Telescope
NOAO	National Optical Astronomy Observatory
nm	nanometer
OPD	optical pathlength difference
OTA	optical telescope assembly
PDF	probability density function
PM	primary mirror
PSD	power spectral density
RMS	root mean square

RWA	reaction wheel assembly
SM	secondary mirror
SST	secondary support tower
TPF	Terrestrial Planet Finder
TPF-FFI	TPF Free Flying Interferometer
TPF-SCI	TPF Structurally Connected Interferometer
TMT	Thirty Mirror Telescope

Chapter 1

Introduction

The future of space-based astronomy is to use large mirrors and advanced technologies to increase the resolution of orbiting telescopes. Missions that aim to look back in time to nearly the Big Bang, or whose goal is to detect an Earth-sized planet orbiting a star millions of times brighter, are as technologically challenging as they are scientifically exciting. In order to meet the packaging requirements for launching apertures three or more meters in diameter, deployable optics, segmented arrays of mirrors and interferometric visible telescopes are all proposed. These instruments will fly aboard spacecraft that are increasingly lightweight and flexible, in order to meet mission mass and cost requirements. No spacecraft of this type, with optical requirements on the order of nanometers and milli-arcseconds, has yet been flown, and there are significant challenges in meeting the technology requirements. There are challenges also in how to go about designing such missions to meet a complex set of both performance and systems-level requirements, while also ensuring validation of the mission concept when integrated pre-launch systems tests may not be possible.

The last decade has seen several new trends in the design of complex systems. These include optimization routines that search across large design spaces in order to identify optimal designs amongst many possible combinations of design variables. Greater attention is being paid to non-deterministic analysis routines, or uncertainty analysis, in order to place bounds or probabilities of success about nominal analysis predictions. Dramatic increases in computer speeds have prompted simulation-based analysis; large models can be repeatedly run in a timely manner and used to investigate the effect of changes in the model. All of these advances are occurring at the same time that there is increased focus on modeling

and analyzing the dynamic behavior of flexible spacecraft subjected to onboard disturbance excitations. These analyses require integrated spacecraft models that combine individual disciplines of structures, controls, optics and disturbance modeling, in order to predict the entire disturbance-input to performance-output behavior of the spacecraft.

This thesis focuses on early stages of the design lifecycle and proposes a conceptual design methodology that relies on model-based dynamic analysis of competing designs to identify superior architectures in terms of both performance as well as robustness to uncertainty. Parameterized structural and integrated models are created that allow the designer to change design variables and evaluate alternative architectures. Uncertainty techniques are considered specifically for early-stage integrated models with limited or no access to testbeds or data. Finally, to show the practicality of the approach, the developed design tools are applied to a series of ground- and space-based telescopes. Although the focus is on flexible opto-mechanical systems, the design methods could easily be applied to any high-performance, technologically challenging mission.

1.1 Space telescope design and validation

1.1.1 Optical telescope science missions

NASA is planning a fleet of large science observatories to build upon the success of the Hubble Space Telescope and Chandra X-Ray Observatory. The James Webb Space Telescope (JWST, formerly the Next Generation Space Telescope) is the direct successor of Hubble, and will use a large 6.5-meter segmented mirror to observe some of the most distant objects in the universe at infrared wavelengths [1]. SIM Planetquest (formerly the Space Interferometry Mission) will use optical interferometry to determine the position of stars, and by detecting the slight motion of stars find Jupiter-sized extra-solar planets [2]. The Terrestrial Planet Finder (TPF) missions, which include both a visible/near-infrared coronagraph telescope and a mid-infrared interferometer, have the goal to visually detect Earth-sized terrestrial planets orbiting other stars, and to determine from a spectroscopic analysis of the light whether molecules suitable for life ("bio-markers") exist on those planets [3].

TPF is in the earliest phases of development and requires extensive research and analysis to meet its technical goals. Its challenge is in detecting the light of a planet closely orbiting a much brighter star. The contrast ratio between the planet's brightness and the star's

is 10^{-6} in the mid-infrared (IR), and 10^{-10} at visual wavelengths of light. The planets of interest are also very close to the star, approximately 0.7-1.5 AU (astronomical unit, approximately equal to the Earth-Sun distance of 150 million kilometers), and within the "habitable zone" where liquid water can exist [4]. For the stars likely to be surveyed, the angular separation between the star and planet to be detected, as seen from Earth, may be no more than 0.1 to 1.0 arcseconds.

Two separate missions are being planned to achieve the mission goals. A coronagraph telescope is planned for visible and near-IR wavelengths (500-1100 nm). It uses pupil masks to attenuate the diffracted light from the brighter star [5]. A nulling interferometer is planned for the mid-IR (670-1700 nm). The interferometer combines light collected from two telescopes, and adds a shift of π to the wavelength of one side. The on-axis light from the star falls into the null that results from the destructive interference of the waves; the trough of one wave interferes with the peak of another, resulting in both signals cancelling each other out. Beyond the central null, corresponding to the interference of off-axis light, there are fringes within which the faint light of a planet could be seen. The fringes are at angles of $\sim\lambda/\mathrm{B}$, where λ is the wavelength of light being observed, and B is the baseline distance between the collecting telescopes [5]. The baseline should be large enough to detect planets close to the star, meaning that the collecting telescopes must be set distant from each other, but not so distant as to resolve the parent star and permit its light to 'leak' around the central null.

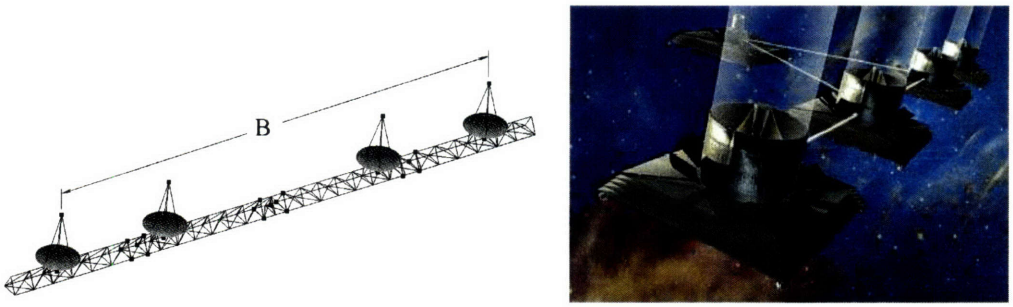

(a) Finite element model of the Structurally Connected Interferometer

(b) Artist's rendition of the Free Flying Interferometer [6]

Figure 1-1: Terrestrial Planet Finder concepts

Two interferometric spacecraft were investigated by the NASA Jet Propulsion Laboratory (JPL). The first was a structurally connected interferometer (TPF-SCI, shown in

Figure 1-1(a)), in which four collecting telescopes are placed along a truss, with the longest baseline around 36 meters. The second was a free-flying interferometer concept (TPF-FFI, shown in Figure 1-1(b)), in which the individual collector telescopes are on separate spacecraft which fly in formation with each other and with a fifth spacecraft that combines the light. The baseline for the TPF-FFI design may be between 55 to 70 meters between the outermost collectors. Each of the architectures has unique challenges. For the SCI mission, a challenge is launching such a large truss structure which must be deployed on-orbit. For the FFI mission, a challenge is controlling this array of spacecraft so that the light meets at the combiner with only nanometers of optical pathlength difference (OPD). For the dynamics problem investigated in this work, requirements on wave front error of the mirror are around one nanometer, with line-of-sight jitter on the order of 10 milli-arcseconds (mas) [7]. These are ambitious goals and can only be met through detailed analysis of the spacecraft designs.

Other telescopes of interest remain here on Earth. The Thirty Meter Telescope (TMT) has been proposed as a large optical observatory that uses adaptive optics (AO) to compensate for image distortions due to the atmosphere [8]. Based on another proposed large telescope, the Giant Segmented Mirror Telescope (GMST, shown in Figure 1-2), TMT proposes to use over 700 1.2-meter diameter mirror segments to fill up the entire 30 meter diameter mirror surface [9].

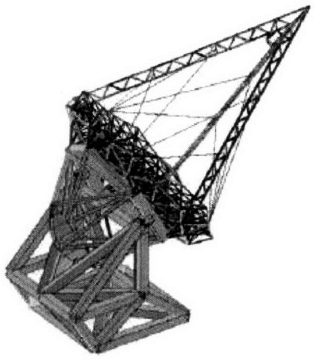

Figure 1-2: Artist rendition of the Giant Segmented Mirror Telescope [10]

A great concern for this telescope is the effect of gravity across the mirror surface, especially as the mirror slews to new targets and the gravity vector changes in relation to the segments. Similar to spaceborne telescopes, TMT will also experience dynamic disturbances caused by wind blowing within the observatory enclosure and past the mirror [10]. These

disturbances must be modeled and attenuated using some manner of control or isolation. The analysis required to characterize the system and predict final performance involves frequency-based disturbance models and integrated models of the structures, optics and control systems. The size and environment of the telescope is different than TPF, but the same approaches to analysis can be used. Given the size of the telescope, mass and flexibility is still an issue, and the optical requirements of TMT are similar to TPF; wind vibrations should contribute no more than 40 mas to the line-of-sight jitter, and before adaptive optics are even used the diffraction-limited root mean square (RMS) wave front error across the 700 segments must be less than 50 nm [11].

1.1.2 Design lifecycle

Since the methods and tools used to analyze spacecraft will change based on the maturity of the mission and the point it has reached in the design lifecycle, a brief definition of the design stages is given. The design lifecycle, from concept to flight operations, is illustrated in Figure 1-3. Initially it starts with a set of scientific requirements, produced by the scientific community to study or search for astronomical bodies or phenomena, or for Earth observation. For instance, for TPF to meet its science goals requires that it can pick out the reflected light of a terrestrial-sized planet less than one arcsecond offset from a bright star. Once the basic mission requirements are established, the engineering aspects of meeting those scientific requirements are addressed.

Alternative mission architectures are developed and evaluated against each in the conceptual design stage. For the TPF mission, there were at least four different mission concepts being considered at one point: a coronagraph, a large structurally connected interferometer, a smaller structurally connected interferometer and the free-flying interferometer. Even with the interferometers, there are multiple concepts for how the different telescopes are arrayed. Each of these architectural concepts must be evaluated to determine first whether they would meet the scientific requirements, and second whether they have acceptable associated costs, risks and scientific productivity. The single, or at most several missions that are judged to best fulfill the mission requirements are selected to continue into the preliminary design stage.

In the preliminary design stage, the first detailed mechanical models of the spacecraft are built. These may include finite element models (FEM) of the structure, or ray-traces of the

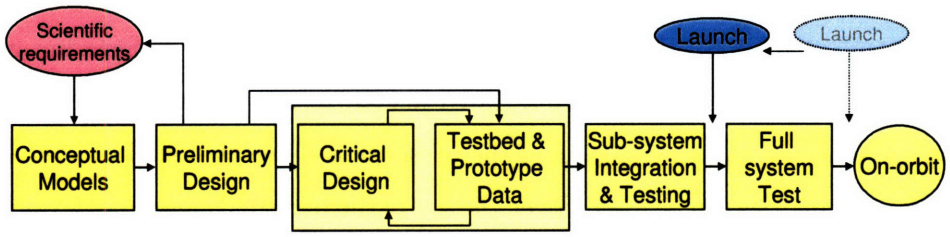

Figure 1-3: Space system design lifecycle

optical sub-systems. The level of fidelity for many of these models may be low; the structure may be represented by simplified finite element "stick" models of several thousand degrees of freedom. These are appropriate for dynamic analysis (up to several tens of hertz) but not for stress or thermal analyses, which typically require FE models with many thousands or millions of degrees of freedom. These initial models are meant to focus attention on the chosen mechanical design, and to identify areas of concern early in the program. The preliminary design stage often involves the first model-based analysis of the chosen designs.

The critical design stage is combined with the acquisition of testbed or prototype data to represent the detailed design and analysis of the chosen spacecraft architecture. At this stage, the final architecture has been chosen and detailed spacecraft studies are performed to guarantee that the mission can meet its technical requirements. High-fidelity integrated models may be updated with data from testbeds, and technical challenges may be solved using laboratory prototypes. Examples are the hurdles that SIM Planetquest has successfully overcome in suppressing nanometer-level vibrations, or detecting the angular position of a laboratory "pseudostar" to within a millionth of an arcsecond [2].

Once the detailed design work is complete and actual flight hardware is available, the stage of sub-system integration and testing includes tests performed on the hardware and updates to the models once component-level validation can be performed. Integration of the hardware continues until the final structure is assembled. If it is possible to perform a full systems test on the ground, validation of the design can occur. Test will confirm the spacecraft meets all of its technical requirements. Once this full systems test is complete, the telescope is launched for on-orbit operations. The situation where a full systems test cannot be performed on the ground will be addressed in the next section.

Although this is a highly simplified description of these design stages, this framework is still useful for determining what types of tools and analysis procedures are appropriate

at different stages. For example, in early stages of preliminary design the linear state-space models used in this thesis are appropriate to describe the general behavior of the entire structure. As higher fidelity models becomes available, it may be necessary to use time-domain simulations in which non-linear effects and the complex interaction of control systems, isolators and disturbance inputs can be more accurately modeled. The work in this thesis is based on the simplified integrated models of the preliminary design stage. A goal of the thesis is to perform that level of modeling earlier in the design lifecycle, during the conceptual design stage when many architectures are still being evaluated.

1.1.3 Design validation

One of the key concerns with the next generation of space telescopes is that validation of the designs may no longer be possible through ground-based testing. A complete systems test may require the spacecraft to be in its operational environment, on-orbit, thus shifting the time of 'Launch' in Figure 1-3 to before the full systems test.

Validation and verification are often mentioned with these missions, without clear definitions of the words. Guidance on the meaning of the words comes from the American Institute of Aeronautics and Astronautics' (AIAA) guide to validation and verification [12], which gives the following definitions:

Verification The process of determining that a model implementation accurately represents the developers conceptual description of the model and the solution to the model.

Validation The process of determining the degree to which a model is an accurate representation of the real world from the perspective of the intended uses of the model.

A similar definition is used by the Institute of Electrical and Electronics Engineers (IEEE) [13]:

Verification Confirmation by examination and provisions of objective evidence that specified requirements have been fulfilled.

Validation Confirmation by examination and provisions of objective evidence that the particular requirements for a specific intended use are fulfilled.

For both sets of definitions, a key component of *validating* a mission is that the system under study is in its operational environment, and being examined with respect to its intended use. So a model whose outputs are mathematically correct and agree with the expected outcome of the designer is verified. A model of a system that agrees with the real world is validated.

The issue with these large space structures then, is that the operational environment can never be fully simulated on Earth, so validation of the intended use of the telescopes is not possible through a full systems test prior to launch. Reasons for this have been described by engineers at NASA centers and in industry[1]. The effect of gravity is obviously a concern on the ground, especially with lightweight, flexible structures that will behave differently on the ground than in orbit. Suspension systems and gravity off-loading harnesses come with dynamics of their own and can not fully relieve gravity loading across membranes, joints and low-frequency isolators. The size of proposed telescopes will be a limiting factor for environmental testing chambers. JWST's sunshade is itself nearly the size of a tennis court. Validation of the fully deployed sunshade is expected to be a huge challenge, and is critical to the mission for both the dynamic environment, due to its very low vibration modes, and the thermal state of the optical instruments which must be kept at cryogenic temperatures. Testing the "intended use" of interferometers such as SIM (to say nothing of free-flying interferometers such as TPF-FFI) requires optical test setups that match or exceed the already rigorous optical requirements of the instrument. This is challenging from both a technical and cost standpoint.

Given these issues, there is increased acceptance that validation of the designs must come from analysis supported by data from testbeds, rather than from a direct test of the flight hardware in a simulated environment [14]. The role of testing becomes one of validating as many aspects of the integrated model as practical, and thereby reducing the uncertainty in the model's ability to accurately predict operational performance. This new paradigm means that by the time the telescope is fully test-validated on-orbit, it will be too late to make any hardware changes to the system (although tuning techniques such as changing the reaction wheel speeds have been proposed as alternative means of affecting the dynamics on-orbit [15]). Accepting validation by analysis requires a much greater level

[1]Informal discussions with NASA engineers working on SIM Planetquest, JWST and TPF, along with industry representatives studying these issues at the Aerospace Corporation indicate that these validation issues are of great concern for many future missions.

of confidence in the analysis predictions than has traditionally been the case. This, in turn, motivates the need for robust designs and a characterization of the uncertainties in the system. The entire design lifecycle from Figure 1-3 must not only be focused on improving the nominal performance prediction, but also on reducing the uncertainties in the system to the point that by launch, any remaining performance uncertainty does not jeopardize the mission.

The tools used to predict system uncertainty depend on the stage in the design lifecycle and the desired goals of the analysis. The ultimate goal prior to launch is an accurate prediction of the on-orbit performance and the probability that the mission will meet its requirements. In earlier stages of design however, the analysis should be focused on identifying sources of uncertainty. Resources can be directed to reduce the identified uncertainties, thereby contributing to the eventual system validation. In early conceptual design it may not be necessary to run time-consuming probabilistic uncertainty analyses across many competing designs. Rather, a relative comparison of worst-case bounds indicating which architectures are more robust to uncertainty would suffice. Coarse uncertainty methods that bound the performance may be adequate to motivate research efforts or drive the creation of testbeds to reduce the uncertainties of particular critical subsystems.

At more mature stages of the design, data from testbeds or prototypes may be available to create uncertainty models of input parameters or of component behaviors. Since robustness requirements are often broken down into percentages (e.g. component X must achieve a 99.99999% success rate), probabilistic methods will eventually be called upon to generate probabilities of success. Once the structure is assembled, ground-based empirical uncertainty models can be mapped to on-orbit computer models to provide final validation of a design [16]. Until the final pre-flight validation routine is run, a key objective of an uncertainty analysis must be to motivate further studies that will feed into the *next* uncertainty analysis. The uncertainty tools in this thesis will concentrate on the early stages of the design process, in which the first integrated models of the selected architecture have been created, but no testbed data are yet available. One goal of this stage should be to identify those parameters which most contribute to the overall uncertainty, so as to motivate research into reducing these critical uncertainties.

1.2 Problem statement

Design validation through analysis will be necessary for large high-performance, high-risk missions such as JWST, SIM and TPF. For these spacecraft, these analyses must be able to accurately predict the performance of the selected architectures in their operational environment and also characterize the uncertainty of those predictions to build confidence in the results. Beyond these missions however, there is a greater need for large, flexible telescopes to satisfy both the scientific and programmatic needs. Future missions must not only meet tight requirements for optical precision, but must be robust to uncertainties, cost-effective, and lightweight. These challenges can be met using advanced technologies such as rib-stiffened, deformable mirrors [17, 18, 19], actively controlled optics [20], and advanced aperture designs [21]. Since this class of telescopes has not been demonstrated and the technologies are new, there are no existing architectures to guide their designs. The need to identify new spacecraft architectures utilizing these technologies provides an opportunity to explore new methods of design in which steps necessary to analytically validate the design can begin from the conceptual stage of the lifecycle.

New methods of design can be based upon research in the fields of non-deterministic analysis and computer simulations using complex models. The combination of these analysis tools combined with dramatic increases in computational speed have opened up new possibilities for design, in which simulations and model-based analysis across large opto-mechanical design trade spaces can take place.

1.2.1 Spacecraft conceptual design

There has been increased emphasis on computer simulations in the conceptual design stage to examine the design space and identify optimal designs. Many of the key design decisions that will drive the performance, mass and ultimately the cost of the mission are decided at the start of the project. The difficulty with this is a common one in engineering: that the most important design decisions must be made when the least amount of information is available. By emphasizing methods that provide better information about competing architectures at this early stage, there is the possibility of a great long-term benefit to the entire project. Conversely, the dangers of too little information in this stage are that the missions may ultimately suffer cost overruns from the need to modify a poorly chosen

design. In his doctoral thesis, Jilla describes this issue [22]:

> By not properly exploring the system trade space and converging on an optimal or even efficient solution during the conceptual design phase, the lifecycle cost of the system can greatly increase as modifications are required to properly integrate and operate the system during the latter stages of the design process, when changes become much more expensive to implement.

Jilla shows examples of how optimization routines can quickly search the conceptual trade space of distributed satellite systems for optimal designs. He uses algebraic models to represent high-level mission metrics such as reliability or cost per image, based on parametric inputs such as the number of satellites in a distributed cluster or orbital altitudes. By employing a parameterized model of the high-level system metrics, a broad examination of the design space is possible. Many combinations of design variables can be automatically evaluated and judged. This approach to conceptual design, of searching across the design space using parameterized models, has typically only been attempted for smaller models that run fast enough to allow thousands of evaluations in a reasonable period of time.

In order to evaluate the mechanical architectures of design concepts, individual finite element models must be created and evaluated. This is a much more difficult proposition, since not only must the model process exist to automatically generate the models, but the computational speed must be fast enough to allow a search of the trade space in a reasonable period of time. For one of Jilla's examples, an evaluation is performed every 22 seconds using a 600 MHz Pentium II processor. In [23], it takes Uebelhart tens of minutes to run a single dynamic analysis with the normal modes already solved for, using a similar computer (circa 2000). Running a large trade space of designs would have taken prohibitively long at that time. In just six years, however, computer speed has increased to the point that a similar study across the mechanical design space is practical.

This thesis proposes a design methodology for the opto-mechanical design of a satellite, and has as its goal the development and implementation of such a methodology. Instead of examining high-level mission parameters such as constellation size or orbital altitude, which treat the satellite as only a point in space, parameters that define the structure and integrated dynamical system are opened up for trades. While it is relatively easy to edit a single finite element input file to change parameters such as Young's Modulus or plate

thicknesses, this thesis demonstrates the practical use of models where the basic form and dimensions of the structural model can be changed. These parameterized models are used to identify optimal designs that are robust to parametric uncertainties, thereby increasing confidence that the chosen design meets its optical requirements and can be validated using analytical means.

1.2.2 Research approach

The aim of this work is to show how the practical combination of design variable-parameterized models along with uncertainty identification and analysis methods provides a design tool for choosing robust architectures of high performance space telescopes using FEM-based analysis techniques in the early stages of conceptual design. An overview of the analytic approach is illustrated by the block diagram in Figure 1-4. A simulation procedure will be developed that begins with all of the parameters of the system, and ends with simulation results bounded due to uncertainties in the inputs. By the end of the thesis a completely parametric conceptual model is created that identifies superior, robust architectures and determines which design variables are most useful knobs for choosing between conflicting requirements.

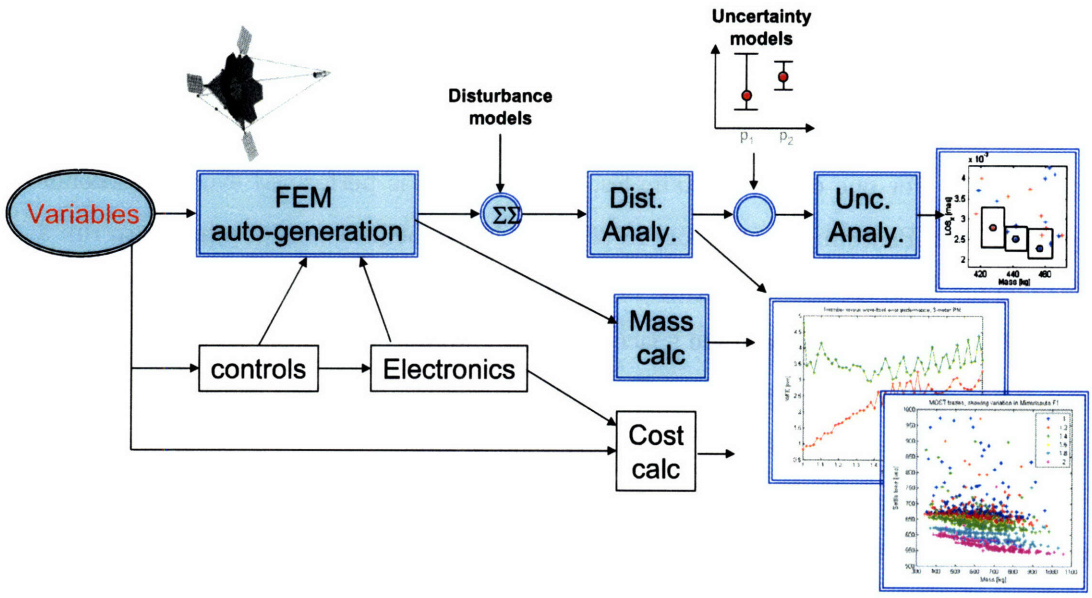

Figure 1-4: Flow diagram of parameterized integrated analysis. Shaded blocks will be described in this thesis.

The simulations depend on access to all of the parameters in the integrated models.

While only a single spacecraft is modeled at this point (performance across a constellation of formation flown telescopes is not considered), that spacecraft could have any shape or size. All of the parameters that influence the design will be available to the designer; examples include the type, size and shape of the mirrors, or the use of isolators versus optical controllers.

For every set of design variables, a finite element model can be constructed. For most spacecraft, including JWST, SIM or TPF, only the finalized mechanical configuration is modeled in this way; these point designs can be optimized, but are of no help in conceptual design. The ability to generate new models automatically, even if they are not individually optimized, is a powerful tool that can be used to examine the effect of design choices on the mechanical system. While any analysis routine could be run with these models, their level of fidelity is best suited for dynamic analysis. Uebelhart [23] and deWeck [24] both provide overviews of the type of dynamic integrated modeling and analysis that is also used here. Vibration disturbances are modeled and used to excite the system. The resulting degradation to optical performance metrics are computed through a frequency-based power-spectral density disturbance analysis.

In order to evaluate the design realizations for robustness to uncertainty, several methods of uncertainty analysis are investigated. A key factor in this research is to identify the appropriate methods of modeling and propagating uncertainties in the system. While there are approaches for placing bounds on the outputs based on historical data [25] or expert opinion, these provide little insight into the differences between unique conceptual designs. Since a goal of the conceptual design methodology is to compare the designs in terms of robustness, uncertainty analysis techniques based on the available information of the design at this early design stage are proposed. Simulations are run to first identify critical uncertainty parameters, and then to propagate the parametric uncertainty. In order to reduce the necessary number of simulations, lessons from the field of Design of Experiments (DOE) are incorporated into this analysis methodology.

The analysis methods proposed can be extendable to include other aspects of the mechanical system. In Figure 1-4 for example, alternative control systems, models of the spacecraft electronics, and financial cost models for large mirrored telescopes are natural extensions of this work, and could easily be integrated into the developed analysis routines.

The entire modeling procedure also makes significant use of the DOCS® (Disturbance,

Optics, Controls and Structures) integrated modeling toolbox. Originally developed in the MIT SSL by Gutierrez [26], DOCS is now a commercially available software suite expanded and distributed by Nightsky Systems, Inc. [27]. The DOCS tools have been used extensively throughout this entire work in order to interface MATLAB® with Nastran®, to create and manipulate integrated models, to run the dynamic analysis routines described in this work, and to demonstrate design tools such as sensitivity analysis and parametric dependency of state-space systems.

1.2.3 Spacecraft case studies

The individual segments of the conceptual design modeling methodology have been created to support telescope systems that are actively in development. The missions, listed in Table 1.1, include several variants of the Terrestrial Planet Finder spacecraft (Figures 1-1(a) and 1-1(b)), along with the ground-based Thirty Meter Telescope (Figure 1-2).

This association with real missions has yielded several important benefits, beyond the help that has come from directly communicating with government and industry engineers. The first benefit is that the research has been directly influenced by the real-world needs of engineers planning these missions. Validation of spacecraft such as JWST or SIM is an immediate concern for NASA engineers, along with how to begin to place uncertainty bounds on models of TPF. The second benefit is that the methodology developed here must be practical for actual system evaluation. The tools are demonstrated on models either provided directly from government sources, or are developed to closely mirror the size and complexity of those early conceptual point design models. No aspect of this work is so simplified that it only applies to single degree of freedom mass-spring models, nor are the routines so complex or time-consuming that they require computational resources beyond what is likely to be available in a modern engineering computer facility. Lastly, great benefit has come from having access to optimized point-design models created by industry. In order to build confidence in the results from a conceptual design trade space, it is critical that the individual design realizations successfully capture the key feature of actual telescopes. By setting the design variables of the parameterized models to the design values of a point design model, the parameterized model is validated at a unique point in the design space. Ideally several such validation points would be evaluated in order to ensure that the parameterized model captures design trends accurately.

Table 1.1: Case studies used in this thesis

Mission	Sponsoring Organization	Status	Thesis contribution
TPF- Structurally Connected Interferometer	NASA JPL	design not selected	Integrated modeling procedure and parameter trades
TPF- Free Flying Interferometer	NASA JPL	tentative launch date 2019, but funding on hold	Identified need for simulation-based uncertainty analysis; performed critical parameter identification using DOE and worst-case bounds uncertainty analysis
TMT (formerly GSMT)	National Optical Astronomy Observatory (NOAO)	TMT organization created, first light in 2014	Parameterized finite element models with variable dimensions; computed static and dynamic performance outputs. Identified need for robust, modular software environment and better trade space simulation and visualization tools
Modular Optical Space Telescope (MOST)	MIT	Laboratory testbed planned in 2007	Parameterized design variables; auto-generated FEM and analysis in fully modular software environment; ran trade space analysis using uncertainty. Shows complete example of conceptual design methodology

This case study approach to the thesis means that in each chapter, a separate telescope model will be used to motivate the work and to provide an example of the routines described or developed. Lessons learned from each mission are incorporated into the next study. All aspects of the conceptual design methodology are finally brought together at the end of the thesis to develop an entirely new optical space telescope.

1.3 Literature review

1.3.1 Parametric modeling in conceptual design

An overview of literature shows several methods of parameterizing a finite element model. A routine in MSC/Nastran [28] (SOL 200) allows for model optimization by changing either model properties (e.g. bar area or plate thickness) or by moving identified grid points along defined shape basis vectors. This manner of optimization is useful once a nearly complete geometry is already chosen. If that geometry has not been chosen, there are examples in both the automotive and aircraft industries for design exploration across structural shapes and forms. For automotive design, Botkin [29] uses a parameterized computer-aided design (CAD) model to create different realizations of the front structure of an automobile, which is then meshed for FEA with plates with thickness optimized using the aforementioned Nastran routine. Fenyes [30] describes how to develop larger parametric models by producing the models in a hierarchic fashion, where high level parameters flow down through the model to control lower level parameters associated with sub-component geometries. In aircraft design there are examples of structures being automatically generated for computational fluid dynamics (CFD) analyses. Baker and Hoffman [31] describe how to auto-generate FEMs from CAD models by using a coding language in the FE pre-processor Patran. They also discuss the importance of a parametric design in the conceptual design stage. Alexandrov, et al. [32] create a parametric wing design for CFD analysis, and suggest how optimization can proceed quickly with low-fidelity models which are periodically validated and updated using high-fidelity models. Smith et al. [33] automatically generate an entire aircraft body using parameters such as wing camber, fuselage length and grid spacing passed to modules that create aircraft components such as the fuselage, wing and tail sections.

Parametric design for structural analysis is described by Sensmeier and Samareh [34] and Sensmeier, Stewart and Samareh [35] in order to predict the structural weight of aircraft wings in conceptual analysis. An optimization loop in the conceptual design is paired with an automatic finite element generator to result in an optimum structure and improved weight estimate before entering the preliminary design stage. Similarly, Cerulli et al. [36] describe a model generator in conceptual design that can produce different aircraft models to examine loading cases and for aerodynamic analysis. Their structural model is created using wing and fuselage structural primitives to build an entire aircraft body; separate

modules are used specifically to connect components together. There are fewer examples of such an automatically generated finite element model for space applications. Szewczyk and Schaeffert [37] describe an object-oriented method using component models to produce an entire structural model, but they consider the component responses individually and map responses across boundary nodes rather than produce a single finite element model. Jilla [22] also describes a parameterized model for the TPF spacecraft, but it models only gross features such as layout and location of the apertures, and does not include a realistic structure with optical surfaces. Lobosco [38] develops a TPF-SCI model with variable height along the baseline, so that the truss tapers out to the furthest collector telescopes. This model is used to determine the effect of tapering the truss on the first mode of the system.

1.3.2 Uncertainty analysis in conceptual design

Many uncertainty analysis techniques are proposed and described in the literature, however the majority concern either the propagation of known parameters through a single model, or bounding the performance of a model or testbed using measured data. There are not as many examples of how to apply uncertainty specifically to low-fidelity models in the earliest stages of design. Walton [39] gives an argument for the need to include uncertainty analysis in conceptual design, and shows the results of an uncertainty analysis on a network-based model of a space system such as the one created by Jilla [22].

One tool that is available for the analysis of mechanical systems (defined by frequency-based transfer functions) is Hasselman's [25] database of aerospace structures, in which uncertainty results from a compilation of legacy flexible testbeds and satellites can be mapped to new, similar structures. Bourgault [40] used this method to map uncertainties onto an early model of the Space Interferometry Mission. Another attempt at mapping expert opinion onto new models is to use model uncertainty factors (MUFs). Similar to the safety factors in structural design, these are little more than multiplicative factors applied to the models' outputs. Although used by some organizations[2], there are no literature references on the subject of MUFs for conceptual design (although Blair, Sills and Semple [41] describe how to compute MUFs from data).

Other sources in the literature described model uncertainty in conceptual design through analysis of the model properties, and not just by mapping bounds onto the model outputs.

[2]MUFs were described by engineers at the Jet Propulsion Laboratory.

Masterson [15] shows an analysis of a TPF-structurally connected interferometer model in which bounded models of uncertain parameters are propagated through the system using the vertex search method, in which simulations are run at each combination of parameter bounds. The same approach to uncertainty will be taken in this thesis across a wide range of architectural concepts.

Du and Chen [42] propose a methodology for managing uncertainty in multidisciplinary models using simulations. For a situation in which a series of models are connected to each other to yield the system performance parameters, the uncertainty of the design variables x and linking variables y can be evaluated one after the other to obtain bounds on the outputs z. The uncertainties in this case can be evaluated either in a vertex-style search or using Monte Carlo simulations. They show an example with a five bar truss, where the truss is broken into two sections to represent multiple components of a multidisciplinary model.

Babuška et al. [43], motivated by the inability to validate spacecraft before launch, propose uncertainty propagation across substructures using linear fraction transformations (LFTs). Substructure synthesis based on the Craig-Bampton method [44] is combined with the variation of linear parameters using the LFT. This propagation method treats parameter variations as gains of a feedback controller, where "closing the loop" evaluates the system at a new parameter value. A mass-spring example is shown. A distribution of uncertainty values is propagated through the integrated substructures using Monte Carlo sampling. The best and worst-case parameter combinations are identified. The LFT will be described in this thesis in Section 4.2, although for a single structure.

Sandgren and Cameron [45] describe an approach to robust design coupled with optimization of the topography of a truss structure using genetic algorithms. They show an example of how the bars for a simple truss can be added or removed, and their geometry properties chosen using optimization routines. Following this, uncertainty parameter distributions are propagated through the system via Monte Carlo simulations. Either minimum mass or robust designs can be identified in this manner. They recognize that this approach is computationally intensive, especially with the Monte Carlo simulations necessary to determine robustness. The largest trusses they examine contain 110 beam elements.

Baghdasaryan et al. [46] recommend using response surface models for applying sample-based uncertainty techniques such as Monte Carlo to computationally and time intensive simulations. Response surface models, also referred to as metamodels, map the input-

output relationship of complex systems from a small number of simulations using polynomial regression techniques, or Kriging methods [47]. Liaw, DeVries and Cronin [48] also propose using response surface models for the robust design of automotive parts, and show which design variables are most effective at meeting performance targets.

Many of the examples in these works are of mass-spring systems or smaller structures with tens hundreds of degrees of freedom. Only Bourgault [40] and Masterson [15] provide examples of uncertainty analysis for large structures of the size seen in conceptual and preliminary models. A contribution of this work will be to apply uncertainty analysis tools on realistically-sized integrated models with thousands of degrees of freedom, across the larger design variable trade space.

1.3.3 Simulation-based analysis and Design of Experiments

Variations in the model, of both design variables and uncertainty parameters, are evaluated in this thesis by re-running the simulation at new parameter values. Because of the computational expense this entails, a review of literature sources on methods of simulation or experimentation was performed. The statistical field of Design of Experiments (DOE) was examined. Jebb and Wynn [49] provide a foundation for the need of robust design using statistical methods. Based on the work of Genichi Taguchi, they promote an approach to design that reduces variations in a process and leads to more robust products. This method relies on statistical evaluation of the design parameters that the engineer controls, versus noise parameters in the system. As originally developed, this approach is geared toward physical experimentation and is used to guide the number of physical experiments that must be run to identify the effect of changing variables.

As computer simulations of physical phenomena have become the dominant method of testing complex processes and structures, DOE now has applicability to deterministic computational simulations as well. Sacks et al. [47] describe how methods of experimental DOE can be applied to computer simulations which by their very nature contain no experimental error; re-running the simulation should give identical results. Simpson et al. [50] provide a good overview of response surface methods for computer experiments, and Giunta, Wojtkiewicz and Eldred [51] provide an overview of the many different sampling techniques available for computer simulations.

Many sampling techniques have been promoted as alternatives to Monte Carlo sampling

for propagating distributions of input variables and determining statistical properties of the output distributions. Pseudo-Monte Carlo sampling techniques are described by Guinta et al. [51], and include stratified Monte Carlo sampling, where the input distributions are divided into bins with equal probabilities. Latin hypercube sampling described by McKay, Beckman and Conover [52] was an early alternative to Monte Carlo methods, followed by Hammersley sampling by Kalagnanam and Diwekar [53], and quadrature-based techniques described by Frey, Reber and Lin [54]. The individual techniques are appropriate to different problems based on the number of variables, interactions between the variables and allowable number of runs.

Since ultimately the uncertainty analysis in this thesis relies on bounded descriptions of the uncertainty, and not propagation of probabilistic distributions, it becomes more important to identify which parameters contribute the most to the outputs. Experimental design techniques that identify the contributions of input parameters includes "one factor at a time" experimentation [55, 56], Taguchi's orthogonal arrays [57] and fractional factorial designs which are described by Lorenzen and Anderson [58] and by Montgomery in his text, *Design and Analysis of Experiments* [59]. Analysis of variance (ANOVA) techniques to determine the effect of parameters on the outputs of an experiment are also described by Montgomery in [59]. Application of these techniques to computer experiments is highlighted by Santer, Williams and Notz [60], and used by Jilla [22] to determine the percentage of total output variation due to each input variable in conceptual design models.

In this thesis, fractional factorial design matrices will be generated in order to reduce the number of spacecraft dynamic simulations run in a critical parameter identification process. The parameters that most influence the system outputs are identified using ANOVA.

1.3.4 Open issues for telescope design and analysis

From a review of the literature and through discussions with industry representatives, the following comments on the state-of-the-art or current practices in the field of conceptual design of complex systems, with a focus on optical space telescopes, can be made.

1. Methods of conceptual design for new spacecraft are based largely on expert opinions. Given the scientific requirements for a new mission, architecture selection often begins with concurrent engineering and design teams consisting of experts across dis-

ciplines (for example, Team X at the Jet Propulsion Laboratory, or the Integrated Mission Design Center at NASA Goddard). These teams can produce a basic system architecture in a week.

2. Spacecraft finite element models that describe the structure and can be used for analysis (dynamic, thermal, etc.) are only produced after the spacecraft concept is selected. These preliminary models may be anywhere from several thousand to several tens of thousands of node points.

3. Uncertainty analysis on these early models is limited to the application of model uncertainty factors on the outputs, or on mapping heritage uncertainty bounds to the dynamic transfer functions.

4. Parameterized structural modeling for conceptual design of vehicles or parts is being used in limited cases in the automotive industry, and for some aircraft fluid dynamic and stress analysis. Methods have been described that build an entire aircraft body using sub-component modules based on an input design vector.

5. Parameterized models used to sample the telescope design trade space for ground- or space-based observatories are limited to parametrization of sub-models that integrate with a fixed structural model, or to higher-level systems analysis that does not model the mechanical spacecraft behavior.

6. The field of Design of Experiments is actively being applied to computer models, including chemical reaction processes, automotive part design, even the effect of public policy decisions on global warming. New DOE sampling procedures are still being developed and compared to existing methods such as Monte Carlo or Latin Hypercube sampling.

7. Active programs exist to build testbeds and prototypes for adaptive optics, rib-stiffened mirrors, and wave front sensing and control; many of these technologies are proposed for the next generation of space telescopes.

There remain open issues with the methods used for design of optical space telescopes.

- The ability of most finite element models to accurately predict modal frequencies is

still limited to the tens of hertz. Increasing the prediction to higher frequencies will require models with much finer meshes than are currently used.

- The ability to validate new space telescope designs is a major concern of government and industry. Particular issues include the dynamics of JWST's sunshade, SIM's optics, and the thermal environment of TPF's collectors. New approaches to validation are needed.
- Uncertainty analysis techniques are underdeveloped for early design stages. Techniques are needed to evaluate thermal uncertainties for early spacecraft designs. If MUFs are used, it is not clear what values should be used.
- There is no formalized approach for how to use uncertainties through the entire design lifecycle to drive the design to a successful validation.
- Parameterized modeling and trade space analyses are not used for the spacecraft structure and dynamic environment. The first model-based analysis does not occur until the architecture concept has been selected and a single finite element model constructed.
- Uncertainty analysis does not occur in conceptual design because of the lack of models. Design robustness cannot be evaluated using analysis techniques.
- Design of Experiments tools are not used for opto-mechanical integrated modeling analyses for either critical parameter selection or trade space analysis.
- Tools and techniques that are applicable for non-linear and thermal analysis are needed, over the traditional linear models and reaction wheel assembly dynamic disturbance analysis.

This thesis aims to address some of these issues. Table 1.2 specifically indicates the contributions of this thesis in the intersection of analysis tools and application to opto-mechanical design.

1.4 Thesis roadmap

This thesis develops a conceptual design methodology for opto-mechanical space structures under dynamic disturbance. The methodology is based on using parametric structural and

Table 1.2: Thesis contributions. References to works in the literature given in brackets.

	"Complex systems"	Automobile: mass	Aircraft: CFD	Spacecraft: systems analysis	Spacecraft: dynamic analysis
Use of DOE in computer simulations	[51], [47]			[22]	**Thesis contribution**
Uncertainty analysis in early design stages	[61], [62], [42], [45]	[48]			[25], [15], [40], "MUFs"
Automated structural models (FEM)		[29], [30]	[32],[33],[31]		[38], **Thesis contribution**
Trade space analysis tools			[34],[36]	[22]	**Thesis contribution**
Automated mechanical analysis with uncertainty					**Thesis contribution**

dynamic models to explore the design trade space, and includes uncertainty evaluation to compare competing designs. This methodology is motivated by the need to design space telescopes to meet increasingly tight performance, mass and cost requirements. Further, the designs must be robust to uncertainty given that design validation must be performed without a full systems test. Figure 1-5 shows an overview of this approach, with the relevant chapters and case study examples highlighted.

Chapter 2, not listed in the figure, goes into greater detail on the unique contributions that a parameterized modeling approach provides in conceptual design. Attention is focused on the improvements in computer speed that make simulation-based design possible, when even six years ago it would have been computationally prohibitive.

Chapter 3 provides background on the components of the dynamic integrated model, and describes the frequency-based analysis routines used to compute the RMS performance outputs of a state-space system, given a disturbance model. Components of the integrated

model include the optical performance models, reaction wheel disturbance models, isolation systems and control loops. The TPF-Structurally Connected Interferometer and Free-Flying Interferometer models are used to illustrate the process, and a nominal disturbance analysis is run on the system.

In Chapter 4, methods of parameter variation are explored in greater detail. Linear fractional transformation, the approach used in DOCS to add parametric variation to state-space systems, is described. Parameters in the TPF-SCI integrated model are varied to determine the effect on the response across reaction wheel speed. For even greater latitude in changing the design, an automatic finite element generation routine is developed that allows the designer to vary the shape and dimensions of a structure. Rules to follow in building a modular software environment for parameterized structural and integrated models are listed. An example is shown with the Thirty Meter Telescope, in which design variables such as the type of telescope, curvature of the primary mirror and location of the elevation axis are changed.

Chapter 5 focuses on non-deterministic analysis of conceptual design models. Identification of critical uncertainty parameters out of a large set of possible uncertain parameters is explored first. Tools from Design of Experiments are applied to the issue of spacecraft uncertainty, and are used to examine the uncertainty space of the TPF-Free Flying Interferometer spacecraft. The results are compared to the outputs of an analytic sensitivity routine. Finally, the type of uncertainty analysis is chosen based on the maturity of the design, and example bounds for TPF-FFI are computed.

In Chapter 6, all of the individual tools developed in the previous chapters are brought together to create a new space telescope design. A modular, parameterized model is created that allows the designer access to material, geometry and integrated model component variables, to the shape and dimensions of the apertures, and even to the very form of the spacecraft. Two unique mirror apertures are examined, along with structural changes to the tower supporting the secondary mirror. Nearly 1300 trade space simulations are run, and methods of visualization are developed to help analyze the results. Finally, critical uncertainty parameters are identified, and bounded uncertainty analyses are run on the optimal design points across the trade space. Superior architecture families are identified that both meet the performance requirements and are robust to parametric uncertainty. Finally, conclusions and thesis contributions are described in Chapter 7.

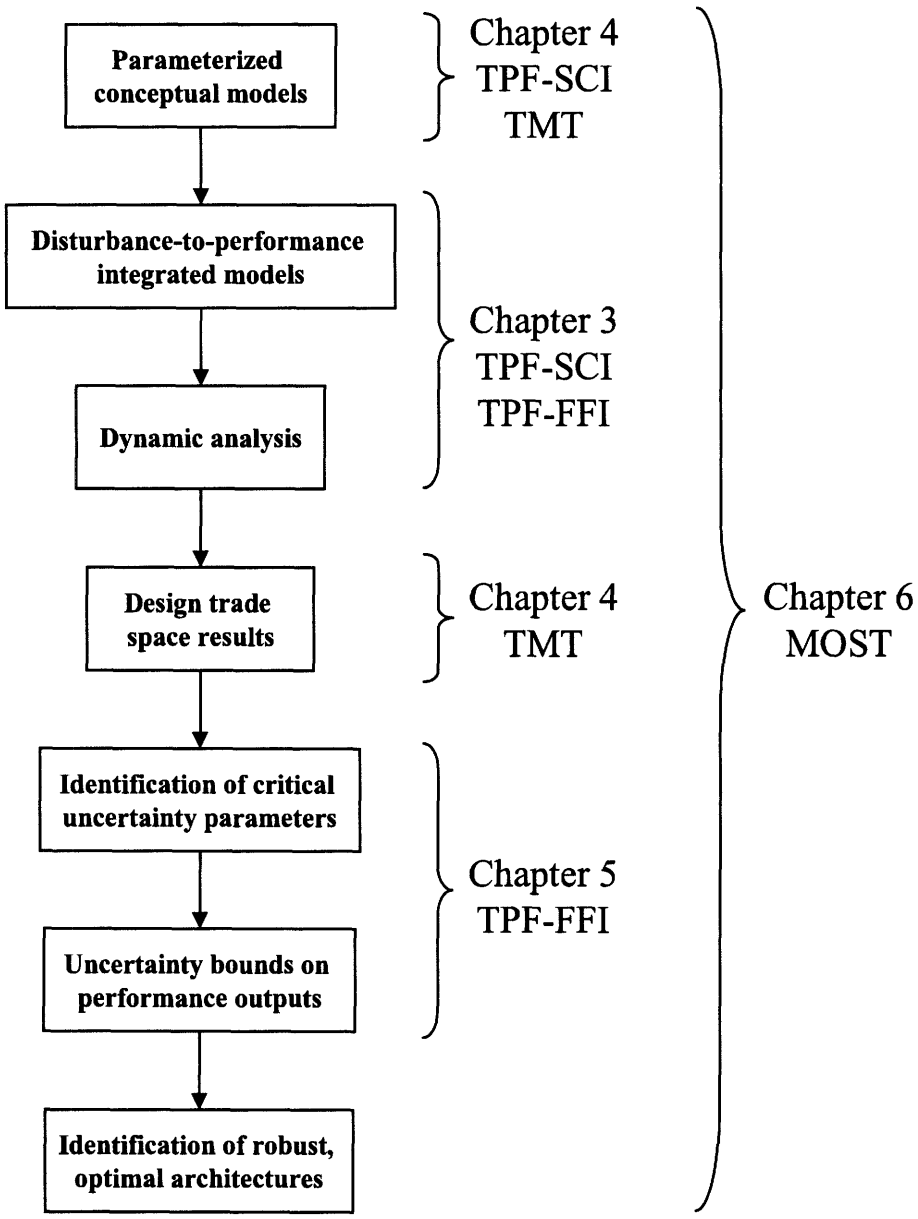

Figure 1-5: Thesis roadmap

Chapter 2

Approaches to Spacecraft Conceptual Design

The proposed conceptual design methodology for spacecraft structures uses parameterized models combined with uncertainty analysis at the start of conceptual design. This approach to design is compared to the traditional spacecraft design approach, where only a single point-design model is built after the conceptual stage is complete. The benefits and drawbacks of this simulation-based approach are reviewed. Since a simulation-based approach across a large trade space is made possible through the increases in computer speed, a comparison of computer speeds from 2000 to 2006 is included, based on a typical dynamic analysis simulation.

2.1 Selection of a point design

The design lifecycle outlined in Figure 1-3 starts with the conceptual and preliminary design stages, when the mission architecture is selected and the mechanical system is defined and modeled. Conceptual design begins with scientific requirements, and relies on design teams to consider many different spacecraft architectures to satisfy those requirements. The systems-level architecture design space may include different types of optical systems (e.g. coronograph versus interferometer), possible orbits, allowable costs and different levels of technology. The opto-mechanical architecture may include different control strategies, structural forms, fabrication materials or overall dimensions. The chosen architecture must not only meet the scientific requirements, but also satisfy mission requirements including

mass, cost, risk, science throughput, mission life and that the structure survive launch loads.

Methods of exploring that design space for the "best" architectures have traditionally been driven by engineering experience, or skill in making a design work. A single "point design" is selected from the greater architecture space and propagated to the preliminary design stage where the chosen design is modeled and analyzed. This approach to design is illustrated in Figure 2-1.

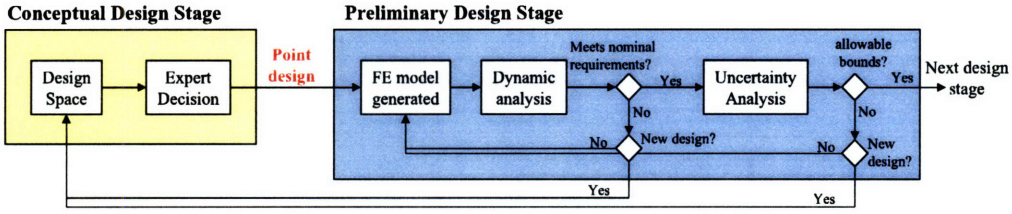

Figure 2-1: Conceptual and preliminary design stages based on a single point design

Mosher [63] describes three approaches commonly taken in the conceptual stage to select amongst the possible architectures. The 'experience' factor relies on experts who come together and select an architecture based on their cumulative years of experience in the field. The 'bottoms up' design approach starts with the mission requirements, and develops the most important subsystems to meet the need. Development of higher subsystems is followed iteratively by the development of lower-level subsystems until the design is complete. Finally, the 'modification' method relies on modifying an existing design so that the new requirements are met. With these approaches, systems level requirements are met either based on knowledge of past missions, or by identifying and modifying the systems level outputs after a design is chosen. The end result, says Mosher [64], is that

> "... the conceptual spacecraft design process is very unstructured ... designers often pursue a single design concept, patching and repairing their original idea rather than generating new alternatives."

Further, the result on the system level requirements is that:

> "... there is no guarantee that a system level focus will be taken. Without this system focus, the resulting spacecraft design is usually a collection of subsystems that are themselves high-performance implementations. This usually does not result in a highly efficient system implementation once the subsystems

are integrated. Compromise is normally made at the systems level to get the subsystems to work together. " -Mosher [63]

The single chosen point design[1] becomes the only point in the entire design space that is evaluated in greater detail through structural modeling and analysis in the preliminary stage of the design lifecycle. In the preliminary design stage, low-fidelity finite element models may be built based on the chosen architecture. Analysis of the point design provides the first model-based results on the ability of the design to meet requirements such as optical performance or mass. An example is the dynamics analysis given for the point-design of a TPF-FFI collector spacecraft in Chapter 3. An uncertainty analysis should also be performed at this stage to establish the performance bounds and robustness of the design to uncertainties. If the design looks to meet the requirements with sufficient margin for uncertainties, the design process can continue with higher fidelity models and construction of appropriate prototypes and testbeds, as shown in Figure 1-3. If these criterion are not met, further optimization of the existing design may be possible by modifying the structure or sub-components. An approach developed by Masterson [15] is to design the system to be sensitive to tuning parameters which can be varied if the performance requirements are not met once hardware is built. If these methods are not successful at improving the design to where it could meet requirements, it may be necessary to reconsider the chosen architecture. In this case, the cycle must begin anew in the conceptual design stage.

The point-design approach to conceptual and preliminary design was appropriate when computer speeds were slow. The extensive vibration analysis required to characterize a system was computationally and time restrictive for rapid design studies. Also, this design approach has been very successful. The accolades bestowed upon the Hubble and Spitzer Space Telescopes, the Chandra X-ray Observatory, the Galileo mission to Jupiter and Cassini mission to Saturn, not to mention the host of recent successes on and orbiting Mars, all show how the traditional design methods have met the requirements of those missions. A challenge to this approach however is in meeting more ambitious performance requirements using spacecraft that can not be test-validated before launch. Designs must be developed with a systems level focus in which performance requirements are met while also satisfying requirements on mission costs, schedule and operations.

[1] Or at most two to four points designs. Several versions of SIM were modeled, and at one point four separate TPF configurations were being considered.

Given the expensive consequences of choosing the wrong design at this stage, new methods of design must be considered. While expert opinion alone is sufficient for derivatives of existing architectures, concepts considered for most space science applications are much more advanced than any existing telescopes. No spacecraft currently exist from which to judge the effectiveness of new concepts, and there are many possible concepts that could be considered. Instead of relying solely upon experience to pick a single design, revolutionary new designs will benefit from model-based evaluations of alternative concepts. Baker and Hoffman [31] summarize the issue when these evaluations are not performed in conceptual design:

> "In the development of conventional configurations for which a large body of experience is available... it is rare for real show stoppers to appear that make a configuration infeasible. This is due to the fact that configuration designers have been working with these configurations for many years... However, when unconventional configurations are being designed... there is a much smaller heuristic experience base upon which to draw, and it is very possible that an unforeseen structural issue will prove to make the configuration impossible. Since this process has historically taken six months to a year, many man-years of effort could easily be wasted on configurations that have show stopping structural issues."

The difficulty with the point design approach is that of all possible concepts in the design space, only the point design is modeled and evaluated, leaving all other concepts untested. The proposed missions include advanced technologies such as lightweight optics and control-structures technologies that have not been flight validated. Without access to the design variables that define the architecture, and without an early evaluation of the inherent uncertainties and complexities in the system, the risks grow that a sub-optimal design will be chosen in conceptual design. If this sub-optimality is only identified after time and resources are spent in subsequent modeling stages, the budget and schedule of the mission will suffer as either a new design is chosen or the existing design is modified. If the sub-optimality is not identified before launch, the lack of full systems validation test may jeopardize the entire mission.

2.2 Exploration of the robust design trade space

The alternative approach is to perform a much larger exploration and evaluation of the trade space in the conceptual design stage, and to include robustness as a key metric that drives the design.

Trade studies performed on multiple designs would provide information on which particular architectures or families of architectures are superior in terms of scientific return, cost, mass and dynamic performance. Jilla provides examples of how parameterized space systems models can be used with optimization routines to identify superior designs [22]. In his work, the architecture and key system metrics such as availability of the services over time and cost per image are made a function of high-level design variables by modeling the subsystems as part of an information network. For an example TPF system, the design vector includes variables such as orbital radius, collector geometry, number of apertures and aperture diameter. This work, along with other multidisciplinary design approaches by Riddle [65] and Mosher [64], have shown how trade space evaluations can identify optimal architectures superior to the original point designs.

If an issue is revealed with these optimal designs, for instance if the absence of a model component seems to negatively impact the results, this issue can be integrated into the trade space model and it can be re-explored. In this way, the trade model provides a foundation upon which detailed analyses are built and to which the design process can return in the event of an unexpected problem. The role of experience in design becomes one of defining the design space in which to model alternative concepts, and in analyzing the results, rather than in choosing the single design to carry forward.

The design variables of previous spacecraft conceptual design studies were very high-level, in which the numbers of spacecraft, orbital altitudes, or key dimensions such as optical collection area are traded using algebraic relationships between the parameters and cost functions. Once these trades are run to determine factors such as the type of satellites and operational environment of the spacecraft, there is still the need in conceptual design to address the design of the spacecraft structure and subsystems. Engineers in industry agree that key design decisions such as the type of interface between spacecraft elements can have a very large effect on the predictability of opto-mechanical models. So a similar trade space approach for choosing the mechanical and dynamic system design variables is

warranted.

A key concept in the trade space analysis is the parametrization of the models, which requires an understanding of the key design variables that define the system. Figure 2-2 illustrates the levels of parametrization that must occur. In the high-level trade studies where the spacecraft is little more than a dot in space, parameters such as orbits, collector area, scientific throughput and subsystem reliability estimates are the design variables that ultimately lead to a baseline class of architectures (e.g. interferometer versus coronagraph) and a description of their environment (low earth orbits, geostationary orbits, Lagrange points, etc.). Once that trade study is done, or even simultaneous with it, design variables that describe the mechanical system and the actual physical hardware must be defined. These parameters may include the type and size of the primary mirror, the shape of the supporting structure, the types of interfaces between sub-assemblies such as the payload and bus, and the control architectures that will be used to mitigate vibrational disturbances or thermal effects. From these inputs, nominal performance predictions can be computed, along with mass of the spacecraft. Finally, evaluation of the robustness of the designs will likely be based around parametric uncertainty analyses. The largest sources of parameter uncertainty must be identified. Since the design variable parameters are set by the designer, and are assumed to be fixed, the uncertainty parameters are likely to be material properties, geometric tolerances and values used to approximate modal damping or spring stiffnesses.

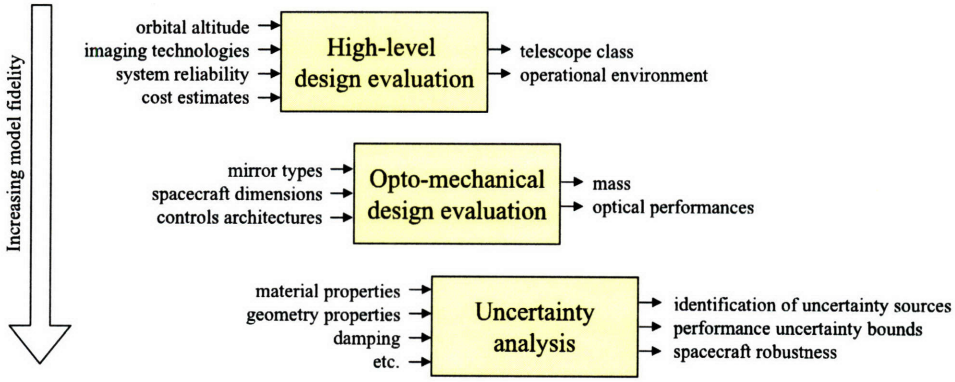

Figure 2-2: Types of parameters varied as a model progresses through conceptual design

Since this type of parametrization of the physical structure and subsystems is lacking in the point design method of conceptual design, the new method of parameterized dynamic analysis coupled with an evaluation of robustness is proposed. This method, which closely

follows high-level trade space analyses such as Jilla's, is illustrated in Figure 2-3. The first model-based analysis has been moved from the preliminary stage to the conceptual stage. Given a selection of design variables, the models are parameterized so that finite element models and integrated models are automatically generated for any combination of design variable inputs. For each design realization, a suite of analysis tools including frequency-based dynamic analysis is used. After a large trade space is explored, those designs that nominally meet performance requirements can then be analyzed to determine the uncertainties of the outputs. The final result of the conceptual design process is a family of architectures that should meet the science requirements while also performing well across systems-level metrics such as mass, cost, and robustness to uncertainty.

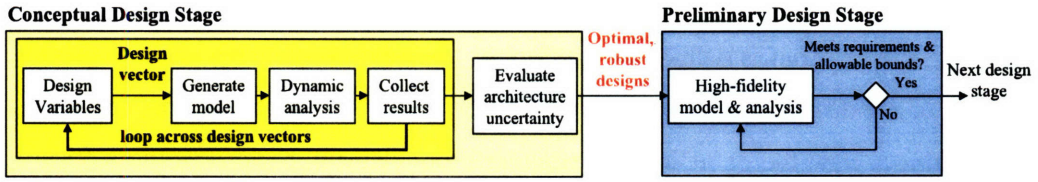

Figure 2-3: Design approach using parameterized models in the conceptual design stage

Note that it is not expected that the individual models created in this stage will be themselves fully optimized. The goal of the modeling process should be to provide comparisons between competing architectures, rather than absolute predictions on the final performance. It is for this reason that the output of this design stage may include families of architectures, rather than a single design. The trade space analysis can highlight which characteristics of an architecture are required to meet either performance or robustness bounds, but also may indicate to the designers which design variables are available as knobs, moving the design along optimal fronts where competing outputs may be traded against each other. A higher fidelity design is necessary in the preliminary design stage for more accurate absolute prediction results. The higher fidelity model allows for a more detailed analysis of the chosen architecture and optimization of lower-level design variables. Although more effort is needed upfront in the conceptual stage, this approach should reduce the need for modifying the design in subsequent stages, and more importantly eliminate the possibility of a "show-stopper" requiring a costly mission reassessment.

2.3 Benefits and shortcomings of conceptual design methodology

The proposed conceptual design methodology for complex space systems relies on parameterized models coupled with uncertainty evaluation to explore the design trade space. This methodology is a practical option for system design only if there is a clear benefit to this approach. There are drawbacks to the approach, mainly in terms of the computational power required to run large trade spaces. Given the strength of the benefits however, and with the increase in speed of available computers, a model-based examination of the design space is practical and useful.

The first advantage from parameterized structural and subsystem models is the access to key design variables. With a single finite element model it is not easy to make changes to the fundamental geometry that is defined by grid points and element connectivities. Changing the diameter or curvature of a mirror, or modifying the type of secondary support tower, requires creating a new file or at least re-running finite element pre-processing software. These steps would require knowledge of the software or finite element tools which the spacecraft designer might not possess. A parameterized model bridges this gap. By creating a model with dimensional and shape inputs, the model components themselves can be built by the specialized structural engineer, but the individual design realizations can be specified by the design engineer. With this capability in hand, it is possible to directly explore the effect that changing a variable has on all of the system outputs. If there are any variables of particular interest this method provides a model-based quantitative analysis tool to investigate their effect on the entire spacecraft.

While the method has been used for examining single-axis effects, the real benefit at this stage comes from identifying optimal designs based on interactions of multiple variables. As Mosher remarked in the quote on page 46, design of each subsystem to be high-performance does not necessarily result in the most efficient complete system. An example would be the tradeoff between passive vibration attenuation versus active control of optical surfaces. Advances in control-structures technologies have come to the point where sensor and actuator suites supported by advanced controllers may be used for wave front sensing and control. Depending on the situation, the use of control may be the only method of achieving the requisite optical stability. However, there are associated costs as well, in terms of added

weight, computation and power requirements and procurement costs. By studying the system across the larger trade space, it may be determined that improving the passive isolation or thermal systems is a superior approach in terms of systems costs to building a highly optimized feedback controller. An interaction example shown in this thesis will compare the corner frequencies of a pair of isolators (Chapter 6). Frequency bands are identified in which two isolators provide much better vibration attenuation than a single isolator, and in which two isolators are actually worst than a single isolator. These interaction effects may be difficult to recognize without a multidisciplinary approach to the model, especially for complex systems. In order to identify which effects provide the best overall system results, the multidisciplinary model must be able to explore across ranges of design variables.

Another benefit of the proposed conceptual design methodology is that uncertainty evaluation begins at the very start of design. The need to analytically validate designs before launch increases the importance of the uncertainty analysis. While mission risk and reliability studies are commonly described in higher-level systems studies, understanding the reliability of a system is not the same as understanding the uncertainty. The predicted performance may be very uncertain, but as long as the variation in system performance remains under set thresholds, the actual risk to the mission is low. Uncertainty analysis concerns the characterization of those variations in performance, and ensures that the variations do not exceed given bounds.

Including an uncertainty analysis at the very start of conceptual design serves two purposes. First, it provides guidance as to the likely sources of uncertainty. Resources can be allocated from the beginning to reducing the uncertainties of those sources. The benefit to the mission is that once higher fidelity models are created, a database of uncertainty models is available for rigorous analysis. Second and more important, running an uncertainty analysis so early means that the design will be evaluated not only on its expected nominal performance outputs, but also against its robustness to uncertainty. Design choices that may be more sensitive to uncertainties, even though they may have superior nominal performance attributes, can be removed from consideration early in the process.

A final benefit of the conceptual design methodology is that of cost savings. While it may be costlier in the short-term to build highly parameterized models, the end result should be spacecraft designs that are more robust to uncertainty, require less modification to meet requirements, and that are optimized from the very beginning to make the most

efficient use of limited schedule and resources. Jilla [22] mentions how the decisions made in the early design stages determine the majority of the final missions costs, and he references an INCOSE report in saying that,

> "...70-90% of development cost of a large system is predetermined by the time only 5-10% of the development time has been completed"

Riddle describes a similar sentiment [65].

> "System level trades are rarely completed until after a baseline design is already achieved because of the perceived time and effort required for credible analyses. This severely hampers the potential for cost-effective designs because a large percent of total system cost is committed at the beginning of the design process, as initial decisions are made."

A shortcoming of the method is that it does take longer than the traditional approaches to conceptual design. More time and resources are needed to build a highly parameterized finite element and integrated model, than are needed to build a single design realization. Also, in an effort to model structural components with generic interfaces (allowing a connection to many types of subcomponents), the actual spacecraft model and interfaces will likely not be optimized in terms of lower-level variables (plate thicknesses, cross-sectional areas of bars, placement of connecting bars, etc.). For designs of evolutionary vehicles, which are based on validated, well-understood precursors, this method may not be necessary. In that case, expert decisions leading to new point designs may be more appropriate.

The parameterized, non-deterministic method is more appropriate and even desirable for designs in which there are no similar precursors, and when the best mission architecture out of many choices is not obvious. Also, exploration of the system trade space is useful when new untested technologies are brought together for the first time without understanding how they will interact in the complete system.

The other shortcoming of this method is that it is computationally intensive. This is foremost a simulation-based approach, where each simulation requires assembly of a finite element model, the running of a normal modes analysis, and multiple model analysis routines including a frequency-based disturbance-to-performance analysis. Since optimization

algorithms are not used in this work (see Jilla [22] or Masterson [15] for ways of incorporating optimization into spacecraft design), a lengthy full factorial approach is taken in exploring the design space. In the example of Chapter 6, this requires nearly 1300 simulations for a coarse exploration of six variables. Even more are required afterward to determine critical uncertainty parameters and to run an uncertainty analysis. This computational expense, which is far greater than the multidisciplinary optimization examples in other referenced works, has traditionally been the greatest impediment toward a broader search of the mechanical design space.

However, this shortcoming is being rapidly overcome through the speed of modern computers. Those 1300 simulations were run over the weekend on two desktop computers purchased in 2006. Given the anticipated benefits of this approach, it is entirely reasonable to wait a weekend for the results of a large analysis. A larger cluster of computers could reduce this time even further. Individual analysis runs take on the order of minutes, and multiple single-axis trades with a much finer step size across the design variable range can be run overnight. Where even five years ago this method of simulation-based structural analysis could have taken weeks, today the same routines take only days or even hours. The next section provides an example of the increases in computer speed for dynamic analysis.

Lastly, the benefit of learning more about a system under review, especially one with inherent uncertainty, is promoted by Jebb and Wynn [49]:

> "The designer... needs to have enough and as many different kinds of information at his disposal so that he may immerse himself in the life history of the project and be able to identify the sources of variability... He needs to surround himself with the necessary equipment for doing this. Nowadays this will invariably be computer based."

2.4 Computational speeds for dynamic analysis

An example of the increases in computational speed for dynamic analyses is shown by contrasting the computers used in this thesis and the results from Uebelhart [23] in 2000.

One approach that can be used to solve for the output of a dynamic system begins with

a state-space representation of the dynamics.

$$\begin{aligned} \dot{q}(t) &= A_{zw}\, q(t) + B_w\, w(t) \\ z(t) &= C_z\, q(t) \end{aligned} \tag{2.1}$$

The matrix B_w maps the force inputs $w(t)$ to the states $q(t)$, and C_z and D_{zw} map the states and inputs to the outputs $z(t)$. If the force inputs $w(t)$ can be described in the form of a while noise state-space shaping filter, Equation 2.1 can be re-written with white-noise inputs $d(t)$.

$$\begin{aligned} \dot{q}(t) &= A_{zd}\, q(t) + B_d\, d(t) \\ z(t) &= C_{zd}\, q(t) \end{aligned} \tag{2.2}$$

In this case, the mean square values for the outputs $z(t)$ can be found by first computing the system covariance matrix Σ_q, which requires solving the steady-state Lyapunov equation[2].

$$A_{zd}\Sigma_q + \Sigma_q A_{zd}^T + B_d B_d^T = 0 \tag{2.3}$$

The mean square values are along the diagonal of the performance covariance matrix, found with a simple matrix multiplication.

$$\begin{aligned} \Sigma_z &= \mathcal{E}\left[zz^T\right] \\ &= \mathcal{E}\left[C_{zd}\, qq^T C_{zd}^T\right] \\ &= C_{zd}\, \mathcal{E}\left[qq^T\right] C_{zd}^T \\ &= C_{zd}\Sigma_q C_{zd}^T \end{aligned} \tag{2.4}$$

where $\mathcal{E}[\cdot]$ is the expectation operator.

The computational roadblock in this analysis is solving the steady-state Lyapunov equation, Equation 2.3, especially for large dynamic systems where the number of states n (length of the vector $q(t)$) grows into the hundreds or thousands. In [23], Uebelhart developed a method of improving the speed of this operation in the situation where the dynamics matrix

[2]Note that an alternative approach using power spectral densities is taken in the rest of this thesis to solve for the mean square values.

Table 2.1: Increase in computational speed for solving a $n \times n$ Lyapunov equation

n states	850 MHz (2000)	2.53 GHz (2002)	3.6 GHz (2006)
	time (sec)	time (sec)	time (sec)
600	210	3.92	2.11
1000	966	13.41	9.56
1500	3222	63.6	33.1
2000	8730	183.5	82.2

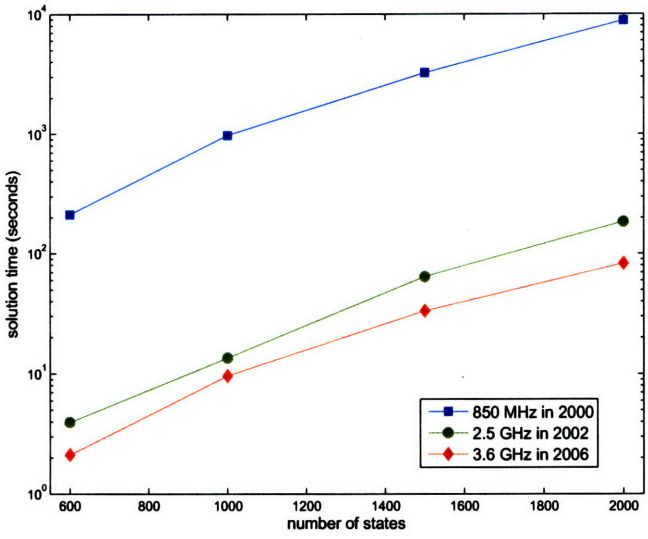

Figure 2-4: Computational speed to solve $n \times n$ Lyapunov equations

A_{zd} is block-diagonal. To compare computation times of systems with increasing numbers of states, example systems are generated with n = 600, 1000, 1500, and 2000 states. A modal system is created using $n/2$ logarithmically even-spaced frequencies between 10^{-3} and 10^{3}. Damping of 0.1% is used, and an input B matrix is chosen randomly.

The results from 2000 were obtained on a 850 MHz Pentium III computer with approximately 1 GB of RAM running Windows NT. These are compared to the results run on two newer computers. The first is a 2.53GHz Dell Precision 340 computer with a Pentium 4 processor, 1GB RAM, running Windows XP, purchased in 2002. The newest computer - one of the two that analyzed 1300 design realizations over a weekend - is a 3.6 GHz Dell Optiplex GX620 desktop with 3.5GB RAM also running Windows XP, purchased in 2006.

The time it takes to solve the entire $n \times n$ Lyapunov problem is given in Table 2.1 and plotted in Figure 2-4 for the three computers, for four different values of n. For a large, 2000-state system, the solution took nearly 2.5 hours back in 2000. The same sized problem

took less than a minute and a half with the fastest computer in 2006. This is a speed increase of over two orders of magnitude. The same speed increase is seen for all values of n, and the 2002 computer is only slightly slower than the 2006 computer. This dramatic result shows that while only six years ago running several dynamic analysis cases would be computationally and time prohibitive, today those same problems can be run in a matter of minutes.

These results support the idea that increases in computer speed have opened up new methods of analyzing broad trade spaces for dynamic systems.

2.5 Conclusion

Instead of applying model-based analysis techniques to only a single point design, the proposed conceptual design methodology relies on automatically generating and analyzing multiple designs across the trade space. The benefits of this approach for the next generation of telescopes is many unique designs can be evaluated using model-based analysis methods. This provides more information to the designer in determining the appropriate combinations of design variables or technologies to meet mission performance and system needs. By identifying superior designs earlier in the design lifecycle, confidence is raised that the designs will ultimately meet their requirements without requiring costly re-design.

The following sections will describe the types of analyses used, the methods by which the models are parameterized, and the approach taken to describe uncertainty of the dynamic response.

Chapter 3

Integrated Modeling and Analysis

An important contribution of the proposed conceptual design methodology is the ability to evaluate competing designs using model-based dynamic (time-varying) analysis techniques. This chapter describes both the type of models that are created as well as the analysis routines used to predict performance under vibration excitation. For each design a structural model is produced. Comparison of competing designs is based on metrics such as optical performance. Since the optics are affected by the manner of vibration disturbances as well as systems used to attenuate those disturbances, models of sub-systems that influence the optics are needed. Evaluating a structure for optical performance thus requires an inter-disciplinary approach. The final model, termed an *integrated model* (IM), combines the sub-system models produced by separate disciplines into a single representation of the dynamic disturbance-input to performance-output system.

In this thesis, the integrated model will refer to a state-space system that is assembled from the sub-systems defining the path between the vibration inputs to the optical performance outputs. The structure is represented by a finite element model, based on the design architecture and geometry. Optical outputs are defined based on optical design variables such as mirror curvature, and are related to the structural model through the motion of the structural mirror elements. Disturbances from reaction wheel assemblies are described by empirically-derived models. Additional sub-models, such as for disturbance isolators or feedback control, are incorporated into the IM by relating their inputs and outputs to those of existing sub-models.

Figure 3-1 provides an overview of the integrated modeling process for a single point

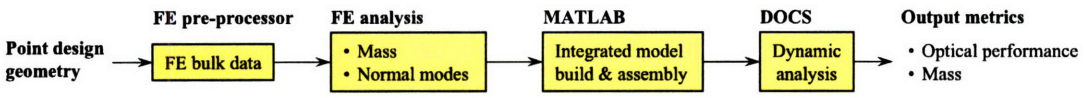

Figure 3-1: Schematic overviewing the integrated modeling process for a point design

design. The structural model is constructed first, often using a finite element (FE) pre-processing program (e.g. FEMAP®). A finite element processor (e.g. Nastran) is used to compute the structural mass and normal modes for a dynamic analysis. State-space models describing the system sub-models are built and then assembled into the integrated model. Frequency-based analysis routines are finally used to predict the root mean square values of the performance outputs under steady-state vibration excitation. Additionally, analysis of the system under transient excitation, such as during a slew maneuver, could be performed using time-history simulations.

This chapter will provide an overview of the integrated model components used in this thesis. The structural finite element is described first, followed by overviews of the discipline models such as optics and disturbances. Example finite element models and optics models are shown for two versions of the Terrestrial Planet Finder (TPF) spacecraft. Next, the assembly of the individual state-space models into the complete integrated model is described. Finally, a complete dynamic analysis of the TPF Free Flying Interferometer is performed.

3.1 Structural finite element modeling

The structural models for all of the examples in this thesis are constructed using the finite element technique, in which the continuous nature of the structure is approximated using a discrete number of elements. Since the use of finite elements is so pervasive in structural modeling and there are many texts available (e.g. [44]), only a very brief description of the technique as applied to structural dynamics follows.

The finite element method models the behavior of a structure only at a discrete number of nodes. An unconstrained node (or grid point) is allowed motion in six degrees of freedom (DOF): three translations and three rotations. The relationships between adjacent nodes are determined by equations which represent different element types (bar, rod or plate, for example) that connect the nodes. The element types are based on the material and

geometric properties of the structure at that point. For a dynamics problem, summing the forces for an undamped element yields Equation 3.1.

$$M\ddot{\bar{u}}(t) + K\bar{u}(t) = \bar{F}(t) \tag{3.1}$$

Internal forces are included in the stiffness matrix, K, that multiples the nodal displacement vector $\bar{u}(t)$. Inertial forces in the dynamic system are included in the mass matrix M multiplying nodal accelerations $\ddot{\bar{u}}(t)$. External time-varying forces are represented by the vector $\bar{F}(t)$. The form of the M and K matrices is determined based on the element type. An example element taken from Craig [44] is a Bernoulli-Euler beam in bending, where the two nodes at either end of the beam have one upward displacement and one rotation (Figure 3-2). The displacement vector $\bar{u}(t)$ contains four elements.

$$\bar{u}(t) = \begin{Bmatrix} u_1(t) \\ \theta_1(t) \\ u_2(t) \\ \theta_2(t) \end{Bmatrix}$$

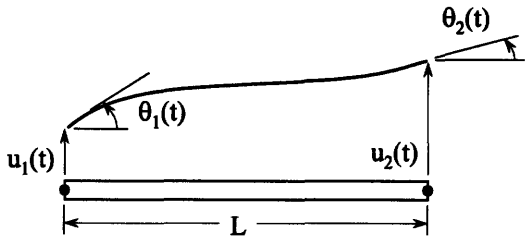

Figure 3-2: Example beam finite element with one displacement and rotation at each node

The beam is made of a material with density ρ and modulus of elasticity E. The beam has length L, cross-sectional area A and area moment of inertia I. Given this information, the mass and stiffness matrices in Equation 3.1 are given by

$$K = \left(\frac{EI}{L^3}\right)\begin{bmatrix} 12 & 6L & -12 & 6L \\ & 4L^2 & -6L & 2L^2 \\ & & 12 & -6L \\ symm. & & & 4L^2 \end{bmatrix} \tag{3.2}$$

$$M = \left(\frac{\rho AL}{420}\right)\begin{bmatrix} 156 & 22L & 54 & -13L \\ & 4L^2 & 13L & -3L^2 \\ & & 156 & -22L \\ symm. & & & 4L^2 \end{bmatrix}. \tag{3.3}$$

Similar mass and stiffness matrices are constructed for adjacent elements that share several degrees of freedom. By mapping the shared degrees of freedom across the entire structure, global mass and stiffness matrices for an entire structure can be assembled. The final equations of motion for the global system are identical to Equation 3.1, with global mass and stiffness matrices substituting for the individual element M and K, and the displacement vector $\bar{u}(t)$ representing all of the degrees of freedom for the system.

Once the global system mass and stiffness matrices are constructed, the next step for the dynamics problem is to assume a solution to Equation 3.1,

$$\bar{u}(t) = \bar{\phi}e^{j\omega t} \tag{3.4}$$

where $\bar{\phi}$ is the modeshape describing the displacements at a frequency ω. For the homogenous, unforced problem, substituting Equation 3.4 into 3.1 yields

$$\left(-\omega^2 M + K\right)\bar{\phi} = 0 \tag{3.5}$$

which is an eigenproblem with eigenvalue ω^2 and eigenvector $\bar{\phi}$. More generally, the $n \times n$ matrices M and K produce n eigenvalues ω_i^2, $i = 1 \rightarrow n$, and n associated eigenvectors $\bar{\phi}_i$. These can be collected into matrices as follows:

$$\Phi \equiv \begin{bmatrix} \bar{\phi}_1 & \dots & \bar{\phi}_n \end{bmatrix} \qquad \Omega^2 \equiv \begin{bmatrix} \omega_1^2 & & 0 \\ & \ddots & \\ 0 & & \omega_n^2 \end{bmatrix}$$

and solved in the generalized eigenproblem.

$$\Omega^2 M\Phi = K\Phi \tag{3.6}$$

The ω_i represent the modal frequencies of the system, and the $\bar{\phi}_i$ represent the modeshapes. These will be used in subsequent sections to produce the state-space representation of the structure.

In practice, all of the finite element modeling in this work will be performed using commercial finite element software. The structures are built using a set of pre-defined elements such as rods, beams or plates. Equation 3.6 is solved using the normal modes analysis for the modal frequencies and modeshapes.

Two example finite element models that will be evaluated in this thesis are described next. They are both designs of NASA's Terrestrial Planet Finder (TPF) telescope. A structurally connected interferometer (SCI) is described first. This is followed by the model for a single collector spacecraft of the free flying interferometer (FFI) constellation.

3.1.1 TPF Structurally Connected Interferometer model

The structural model for TPF-SCI is provided by the Jet Propulsion Laboratory (JPL). This model is illustrated in Figure 3-3. It consists of 2039 grid points, 1478 CBAR elements, and 172 CQUAD4 plates in each of the four telescopes. Concentrated masses are used to represent the secondary mirrors, collector payload masses, the beam combiner, and hinge points. Critical grid points are listed in Table 3.1. The telescopes are numbered #1 for the telescope furthermost along the -x direction, sequentially along the truss to #4 which is the furthermost in the +x direction.

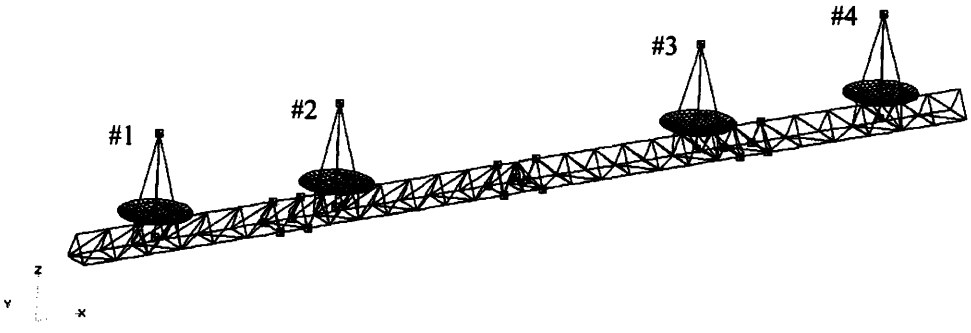

Figure 3-3: TPF-SCI finite element model

Table 3.1: Important grid points in the TPF-SCI finite element model

Grid Point #	Description
9893	Secondary mirror mass, telescope #1
9892	Secondary mirror mass, telescope #2
9890	Secondary mirror mass, telescope #3
9891	Secondary mirror mass, telescope #4
9896	Collector Payload mass, telescope #1
9897	Collector Payload mass, telescope #2
9895	Collector Payload mass, telescope #3
9894	Collector Payload mass, telescope #4
1001	Center of Primary Mirror, telescope #1
1002	Center of Primary Mirror, telescope #2
1003	Center of Primary Mirror, telescope #3
1004	Center of Primary Mirror, telescope #4
9898	Collector and Bus

All of the modes below 1000 Hz (1772 in all) are obtained from Nastran. Six reaction wheel forces and torques are input at the combiner node. There are three optical performance outputs (described in the next section) and three attitude control system rotation sensors at the combiner node. Modal damping of $\zeta = 0.01\%$ is applied to all modes. This damping value is based on JPL studies suggesting that structural damping is low at the cryogenic temperatures that TPF will experience [66, 67]. Finally, a state-space model is built that defines the system transfer functions from the disturbance inputs to the performance outputs.

Because of the large size of this system ($2 * 1772$ modes $= 3544$ states), model reduction is performed. A reduction technique should maintain the dynamic behavior of the model while reducing the size of the state matrices, thereby improving computational speed. A two-stage model reduction process is implemented, in which the contributions of individual modes are computed and ranked. Modes with less contribution to the desired transfer functions are then truncated from the model. The system is thus reduced from 1772 modes (3522 states) to 300 modes (600 states). Example reduced transfer functions are provided in Figure 3-4.

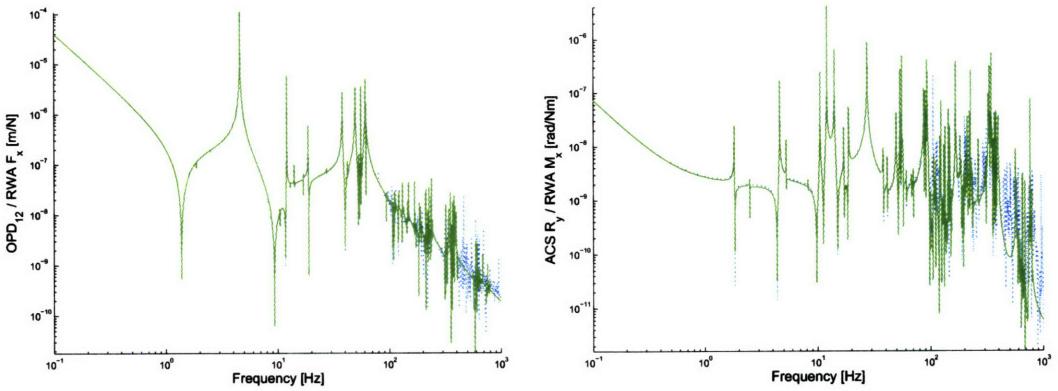

(a) RWA F_x to OPD_{12}

(b) RWA M_x to ACS Sensor F_y

Figure 3-4: Sample TPF-SCI transfer functions of the full system (solid line) and reduced 600-state model (dotted line)

3.1.2 TPF Free Flying Interferometer model

An alternative TPF design is the free-flying interferometer, provided to MIT by JPL [68]. The model is visualized in Figure 3-5. Its 6933 grid points are connected using a combination of CTRIA3 and CQUAD4 plate elements, CBAR and CBEAM elements, CBUSH springs and RBE2 rigid body elements. There are a total of 41 CONM2 concentrated masses. Key spacecraft components include the telescope mirror, stray light trays, sunshade booms and masses representing everything from spacecraft sensors in the bus to the telescope secondary mirror.

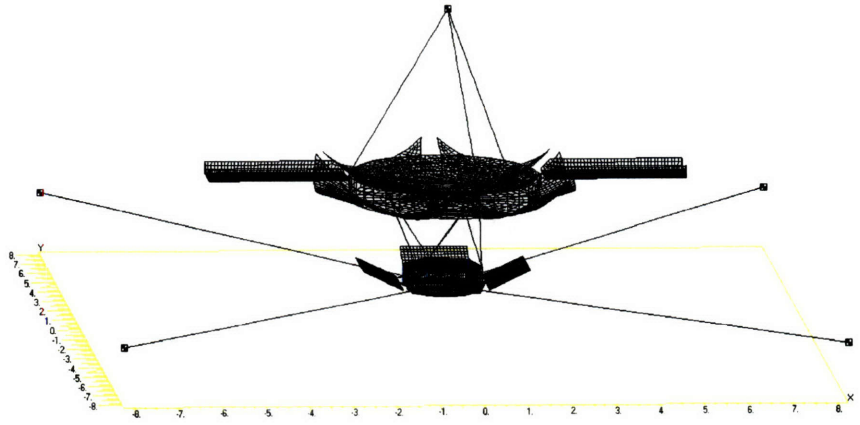

Figure 3-5: TPF-FFI spacecraft finite element model

Concentrated masses are identified both for later use in an uncertainty analysis and also to determine those finite element nodes to be used as inputs and outputs in a dynamics

analysis. A "spacecraft control assembly" mass is treated as the location of the reaction wheel assembly. Two spacecraft control assemblies are described at node numbers 80059 and 80060. For this analysis, wheels are placed at only one of these nodes, node 80059. Node 80063 is the location of the inertia reference unit, which is assumed to be a gyroscope for sensing rotational attitude. The rotations of this node are treated as sensor outputs for the attitude control system.

A normal modes analysis is run with the structural model. For the nominal model, all modes up to 500 Hz were obtained (Figure 3-6), 770 modes in all. These include the six rigid body modes.

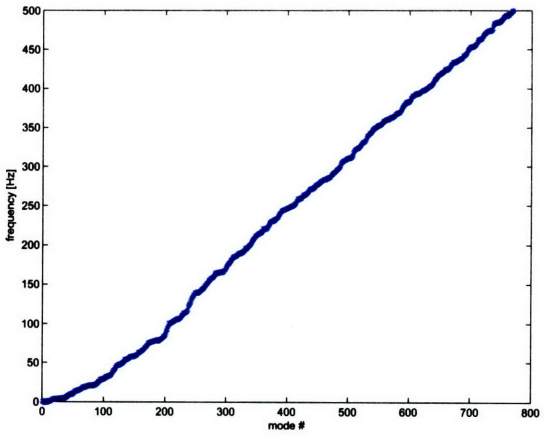

Figure 3-6: Modal frequencies obtained from Nastran, up to 500 Hz

3.2 Integrated model components

Besides the structural model, additional sub-system models that comprise the integrated model include the optics, disturbances, isolators and controls. A brief description is given for each of these system.

3.2.1 Optical models

Since the performance metrics of the telescopes are most often described in terms of optical quality, an optical model representing the degradation of the optics due to deformation of the primary mirror and displacement of optical surfaces is required. A key requirement for interferometers is that the optical pathlength difference (OPD) remain small. The OPD

represents the difference in length that two rays of light, originating from the same source and having been sampled by two separate apertures, travel before interfering at the beam combiner. Other important metrics include line-of-sight (LOS) errors that represent a decentering of the optical image, and wave front error (WFE) that represents aberrations of the mirror surfaces.

LoBosco [38] shows an example of a ray-traced model using the Code V optical design software package for the TPF-SCI model. For the present models, however, simple approximations for OPD, LOS and WFE based on the displacements of key nodes are used in place of a more rigorous optics model. Since structural models are often built before optical models, these simple approximations provide a means of evaluating optical performance for a structure as soon as its finite element model is complete. The optical models for both TPF-SCI and TPF-FFI are described next.

Optical pathlength difference for TPF-SCI

Optical pathlength differences based on geometry are used for TPF-SCI. As illustrated in Figure 3-7, the pathlength of a ray of light is computed based on the positions of key grid points on each of the telescopes. These grid points include the center of the primary mirror, up to the secondary mirror, down to the collector payload (treated as a fold mirror), and over to the combiner for telescopes #1 and #4. For telescopes #2 and #3, there is an additional bounce off of the "fold mirror" of the opposite inside telescope in order to ensure that all rays travel the same length when the system is perfectly aligned.

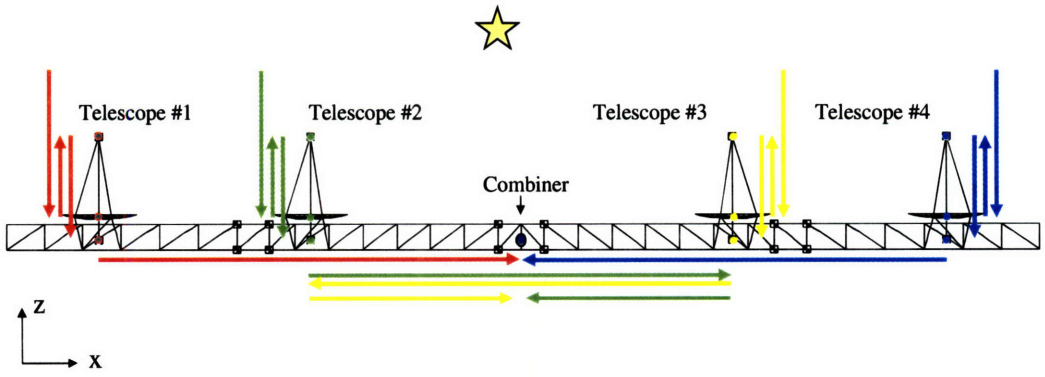

Figure 3-7: Schematic showing the pathlengths for each of the four TPF telescopes

The following equations are used to compute the pathlength of light from the source, through each telescope and to the combiner. The initial distance from the star to the coordinate frame of the spacecraft is given as OP_o. All other terms refer either to z-displacements or x-displacements of the primary mirror center grid point (P), secondary mirror concentrated mass (S), fold mirror concentrated mass (F), or combiner concentrated mass (c), at telescopes 1-4.

$$\begin{aligned} OP_1 &= (OP_o - z_{1P}) + (z_{1S} - z_{1P}) + (z_{1S} - z_{1F}) + (x_c - x_{1F}) \\ OP_2 &= (OP_o - z_{2P}) + (z_{2S} - z_{2P}) + (z_{2S} - z_{2F}) + (x_{3F} - x_{2F}) + (x_{3F} - x_c) \\ OP_3 &= (OP_o - z_{3P}) + (z_{3S} - z_{3P}) + (z_{3S} - z_{3F}) + (x_{3F} - x_{2F}) + (x_c - x_{2F}) \\ OP_4 &= (OP_o - z_{4P}) + (z_{4S} - z_{4P}) + (z_{4S} - z_{4F}) + (x_{4F} - x_c) \end{aligned} \tag{3.7}$$

Once the pathlengths are computed, optical pathlength differences (OPD) are easily obtained by subtracting one from the other. OPD is computed between telescopes 1 and 2, 1 and 3, and 1 and 4. The appropriate degrees of freedom are accessed through the system displacement output matrix, so that three performance metrics are output to the final system. OPD_{12}, OPD_{13} and OPD_{14} can be derived from Equation 3.8.

$$\begin{aligned} OPD_{12} &= OP_1 - OP_2 \\ OPD_{13} &= OP_1 - OP_3 \\ OPD_{14} &= OP_1 - OP_4 \end{aligned} \tag{3.8}$$

Line-of-sight jitter for TPF-FFI

The LOS calculation is based off a memo by Perrygo and Burg [69] that derives simple expressions for LOS jitter of focal telescopes based on the displacements and rotations of primary and secondary mirror nodes. It is assumed that the TPF collector telescopes will be afocal since the light must be reflected across space to the combiner spacecraft. The equations in [69] are modified for afocal telescopes[1]. The approximations for LOS about the x- and y-axes are given in Equation 3.9.

[1]Modifications made by SoonJo Chung of the MIT Space Systems Laboratory

$$\begin{aligned} \theta_x &= -\frac{1}{f_1}\delta_{P_y} + \frac{1}{f_1}\delta_{S_y} + 2\alpha_{P_x} - \frac{2}{MP+1}\alpha_{S_x} \\ \theta_y &= \frac{1}{f_1}\delta_{P_x} - \frac{1}{f_1}\delta_{S_x} + 2\alpha_{P_y} - \frac{2}{MP+1}\alpha_{S_y} \end{aligned} \tag{3.9}$$

where the θ_i represent the LOS errors based on displacements δ and rotations α of the primary (P) and secondary (S) mirror nodes. The focal length of the primary mirror is f_1, and MP is the angular magnification of the afocal telescope found by the ratio of f_1 and the secondary mirror focal length, f_2.

$$MP = -\frac{f_1}{f_2} \tag{3.10}$$

Since no optical information on the mirror has been provided, the focal lengths are computed using several dimensions of the telescope, found by measuring lengths on the finite element model (Figure 3-8). The overall diameter D of the primary mirror is 4.2 meters; the depth of the primary mirror is 0.22 meters, and the total distance d from the bottom of the primary mirror to the secondary mirror is 4.0 meters.

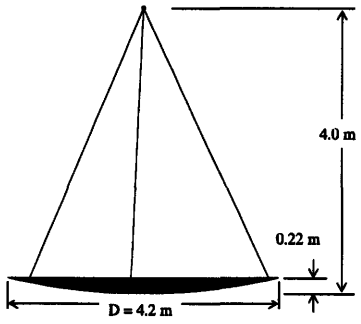

Figure 3-8: Dimensions of the TPF-FFI telescope assembly from the FE model.

The focal length of the primary mirror is computed assuming that the mirror is a parabola. In this case the surface of the mirror is described by the equation [70]

$$y^2 = 4f_1 x \tag{3.11}$$

where x is along the line-of-sight. Solving this for a point on the mirror's edge at $y = D/2$

and $x = 0.22$ meters gives

$$f_1 = 5.0\text{m}$$

and corresponds to an f-number, or focal ratio, of

$$f_{\#} = \frac{f_1}{D} = 1.19$$

The focal length of the secondary mirror is obtained from the relationship for the effective focal length f_{eff} [71].

$$f_{eff} = M \cdot f_1 = \frac{f_1 f_2}{f_1 + f_2 - d} \tag{3.12}$$

where M represents the secondary magnification factor. Since the afocal telescope does not focus the image to a point, the effective focal length is infinite. Equation 3.12 is reduced to

$$M = \frac{f_2}{f_1 + f_2 - d} \rightarrow \infty \tag{3.13}$$

and given that f_2 is a real number, this results in the equation $f_1 + f_2 - d = 0$, which is solved for f_2.

$$f_2 = -1.0\text{m}$$

The negative indicates a convex mirror which, together with the concave primary mirror, is typical of Cassegrain telescopes. Equation 3.10 can then be used to compute the angular magnification MP.

$$MP = 5.0$$

LOS-x and LOS-y outputs are computed using Equation 3.9. Requirements for LOS jitter are found in Noecker, et al. [7], which budget a pointing jitter requirement of 10.48 milli-arcseconds (mas) for a dual bracewell TPF interferometer.

Wave front error for TPF-FFI

Aberrations in the mirror surfaces distort the planar wavefront arriving from an observed target. These aberrations often result from thermal expansion of the mirror or its supports, although for this study the effect from dynamic excitation is considered. The resulting wave front error (WFE) is approximated based on the motion of mirror grid points. A simple approximation of the wave front error involves computing the out-of-plane z-displacements

of grid points along the mirror surface. A sample of points across the mirror are root-sum-squared to produce a metric that indicates the level of wave front error.

For a large number of grid points it may be more computationally efficient to relate the grid point displacements to wave front error using Zernike basis functions. Zernike polynomials describe types of circularly symmetric distortions of a mirror surface using polynomial basis functions [72, 73]. The polynomials are described in polar coordinates of circle radius ρ and angle θ. For a unit circle these basis functions will be orthogonal.

The polynomials for the first 15 Zernikes are given in Table 3.2, and selected examples are plotted in Figure 3-9. Note that the numbering notation is not agreed upon by all organizations; the numbering system shown here is based on the "fringe form" used by an optics group at the University of Arizona [74]. The first term, #0, is simply piston, or uniform motion of the entire mirror along the line-of-sight. Terms #1 and #2 are tip and tilt, an example of which is illustrated in Figure 3-9(a). Term #3 is focus, or power, illustrated in Figure 3-9(b). Higher order terms give rise to even more complex geometries, such as the "trefoil" terms (#'s 9 and 10), illustrated in Figure 3-9(f).

Table 3.2: Zernike polynomial terms (fringe numbering system)

Number	Name	Term	Weight
0	Piston	1	1
1	Tip	$\rho\cos\theta$	4
2	Tilt	$\rho\sin\theta$	4
3	Focus	$2\rho^2-1$	3
4	Astigmatism x	$\rho^2\cos 2\theta$	6
5	Astigmatism y	$\rho^2\sin 2\theta$	6
6	Coma x	$(3\rho^2-2)\rho\cos\theta$	8
7	Coma y	$(3\rho^2-2)\rho\sin\theta$	8
8	Spherical	$6\rho^4-6\rho^2+1$	5
9	Trefoil x	$\rho^3\cos 3\theta$	8
10	Trefoil y	$\rho^3\sin 3\theta$	8
11	Secondary astigmatism x	$(4\rho^2-3)\rho^2\cos 2\theta$	10
12	Secondary astigmatism y	$(4\rho^2-3)\rho^2\sin 2\theta$	10
13	Secondary coma x	$(10\rho^4-12\rho^2+3)\rho\cos\theta$	12
14	Secondary coma y	$(10\rho^4-12\rho^2+3)\rho\sin\theta$	12
15	Secondary spherical	$20\rho^6-30\rho^4+12\rho^2-1$	7

A method of relating the grid point displacements to the Zernike terms is described by Angeli and Gregory [74]. Displacements $\delta\bar{z}$ of N grid points across the mirror surface can

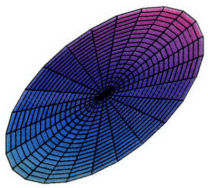

(a) Zernikes #1,2: tip and tilt

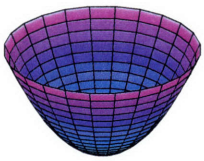

(b) Zernike #3: focus

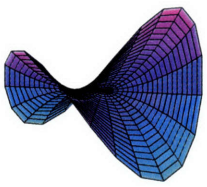

(c) Zernikes #4,5: astigmatism

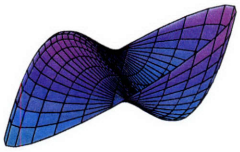

(d) Zernikes #6,7: coma

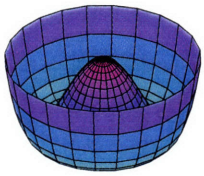

(e) Zernike #8: spherical

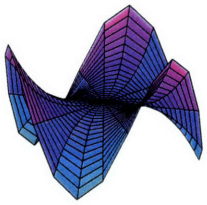

(f) Zernikes #9,10: trefoil

Figure 3-9: Zernike shape functions

be decomposed through:

$$\delta\bar{z} = \begin{Bmatrix} \delta z_1 \\ \delta z_2 \\ \vdots \\ \delta z_N \end{Bmatrix} = \Gamma\bar{a} = \begin{bmatrix} \bar{\gamma}_1 & \bar{\gamma}_2 & \cdots & \bar{\gamma} \end{bmatrix} \begin{Bmatrix} a_1 \\ a_2 \\ \vdots \\ a_m \end{Bmatrix} \tag{3.14}$$

where the column vectors $\bar{\gamma}_i$ represent the sampled Zernike functions at each grid point. This involves transforming the grid point locations in Cartesian x and y coordinates to polar ρ and θ coordinates. The m Zernike coefficients a_i indicate the contribution of each Zernike term to the displacements. A pseudo-inverse of the $N \times m$ matrix Γ relates the Zernike coefficients to the displacement outputs of the finite element model.

$$\bar{a} = \Gamma^{\dagger} \cdot \delta\bar{z} \tag{3.15}$$

This decomposition reduces the model outputs from the N mirror surface grid points, to the m Zernike coefficients, where in most cases $N \gg m$.

From [74], the RMS wave front error is finally calculated by the weighted root-sum-

square of the Zernike coefficients.

$$\sigma_{WFE} \simeq \sqrt{\sum_{i=1}^{N} \frac{a_i^2}{w_i}} \tag{3.16}$$

The weights w_i for each of the first 15 Zernike terms are given in Table 3.2. For the TPF-FFI model, the wave front error is computed only across the primary mirror surface. It is assumed that piston errors are controlled by optical delay lines, so the piston Zernike terms are not included in this evaluation. A more complex optics model could compute the effect of wave front error on the light at the exit pupil of the optical instruments, due to all of the mirrors. A model of this sort will be used for the analysis of the Thirty Meter Telescope in Section 4.5

3.2.2 Disturbance models: reaction wheel assemblies

There are several sources for vibration disturbances that may degrade spacecraft performance [26]. These include disturbances external to the spacecraft such as torques due to gravity gradients or solar pressure. Internal disturbances may include vibrations caused by the firing of thrusters, fuel sloshing, or the mechanical actions of cryo-coolers and tape drives. The dominant source of vibration disturbance is expected to result from reaction wheel assemblies (RWA). RWAs are used to hold the attitude of the telescope by storing angular momentum and to produce reaction torques that slew the telescope. For the spacecraft examined in this work, all of the disturbances are models of the disturbance forces F_x, F_y and F_z, and moments M_x, M_y and M_z caused by RWAs.

Reaction wheels store momentum through the gyroscopic effects of a spinning flywheel. The momentum stored in the wheel with inertia I_w spinning at a rotation rate ω is

$$H_z = I_w \cdot \omega \tag{3.17}$$

For slewing maneuvers, reaction torques on the spacecraft are the negative of the derivative of the wheel momentum, or the inertia multiplied by the angular acceleration of the wheel.

$$\tau_z = -\frac{\partial H_z}{\partial t} = -I_w \cdot \dot{\omega} \tag{3.18}$$

Bialke [75] provides a good overview of the components of an individual wheel. A minimum

of three wheels is required to provide torque about all three spacecraft axes. In practice four to six wheels are often used to provide both redundancy and non-uniqueness in the torque profile so that torque requirements can be shared amongst wheels.

Vibrational disturbances arise from sources such as wheel imbalance, bearing stiction, motor ripple and cogging [75]. The disturbances are harmonic and are dependent on the wheel speed. The fundamental harmonic at the frequency of the wheel speed is usually the largest contributor, resulting from mass imbalance. Higher harmonics resulting from other sources can be described at multiples of the fundamental.

Models of these disturbances are described in [76] where the forces and torques at each harmonic are treated as sinusoidal functions whose amplitude is proportional to the square of the wheel speed. Each generalized force is described by

$$m(t) = \sum_{i=1}^{n} C_i \omega^2 \sin(2\pi h_i \omega t + \alpha_i) \tag{3.19}$$

where $m(t)$ is the sum of the disturbance forces or torques from n harmonics. The i^{th} harmonic with harmonic number h_i has an amplitude coefficient C_i and random phase α_i. The wheel speed ω is in hertz. These models are utilized by Masterson [77, 78] to produce empirical values for the amplitude coefficients C_i and harmonic numbers h_i. Figure 3-10 shows an example for the Ithaco (now Goodrich) E-wheels (TW-50E300). This example is of an off-the-shelf wheel prior to the balancing needed for minimum vibration operation. The harmonics are proportional to the wheel speed, where the fundamental harmonic at 1.0 occurs at the wheel speed. If the wheel z-axis is along the axis of rotation, the radial forces and torques are along (or about) the x- and y-axes. The axial force is along the z-axis. Since the axial moment about the z-axis is coincident with the reaction torque created by the spinning wheel, the disturbance in this direction is assumed to be zero.

Gutierrez [26] describes how the forces and torques of multiple wheels can be broken into components along the spacecraft x-, y- and z-axes using Euler angles, and summed to produce a three-force, three-moment disturbance input for an arbitrary number of wheels and wheel orientations. Instead of analyzing the system at each wheel speed separately, a broadband reaction wheel model is produced that treats wheel speed as a random variable and determines the statistically averaged disturbance forces and torques across wheel speeds [76]. Power spectral density curves for each spacecraft disturbance force and torque

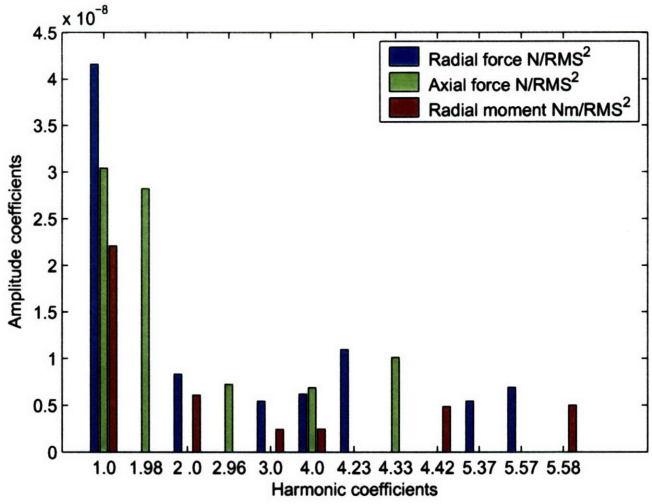

Figure 3-10: E-wheel amplitude coefficients at each harmonic

can be computed, and are included in DOCS. The power spectral density (PSD) describes the spectral contribution of a signal across frequencies, and will be described in greater detail in Section 3.4.

The PSDs of the combined disturbance components across wheel speeds of 0–3000 RPM are shown in Figure 3-11. Note that the highest frequency contribution is at 279 Hz resulting from the highest harmonic (5.58) at the maximum wheel speed (3000 RPM).

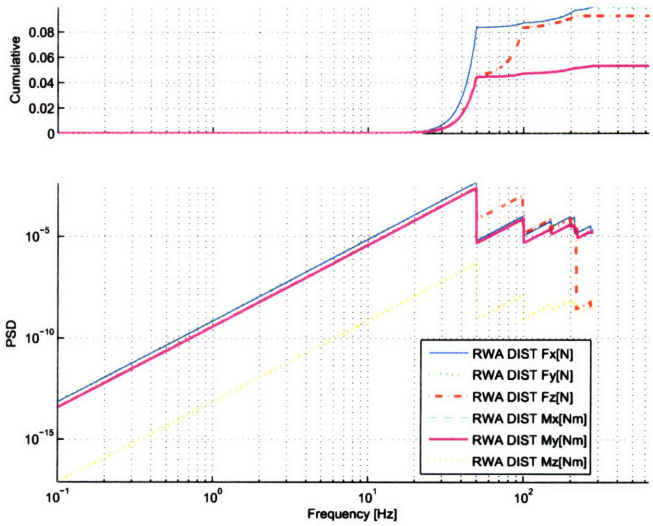

Figure 3-11: Broadband reaction wheel disturbance PSDs

3.2.3 Disturbance isolators

Disturbance isolation is included as a passive means of reducing the disturbance energy. The disturbance to performance path can be affected by isolators placed either between the disturbance source and the structure (between the reaction wheel assembly and its connection to the spacecraft bus, for example), or between the structure and the performance (between the bus and the optical telescope assembly (OTA)). The passive isolator structure acts to block high-frequency vibrations, such as those produced by the higher harmonics of a reaction wheel [2].

The isolators are modeled as second order low-pass filters with corner frequencies represent the limits of passive isolation. The basic form of the filter is

$$H(s) = \frac{K\omega_{iso}^2}{s^2 + 2\zeta_{iso}\,\omega_{iso}\,s + \omega_{iso}^2} \tag{3.20}$$

with gain K, corner frequency ω_{iso} and isolator damping ζ_{iso}. The basic filters used for these integrated models use $K = 1$ for unity gain at low frequencies and 5% damping ($\zeta_{iso} = 0.05$). Figure 3-12 shows an example transfer function that also levels off at higher frequencies to represent the attenuation limits of physical isolators.

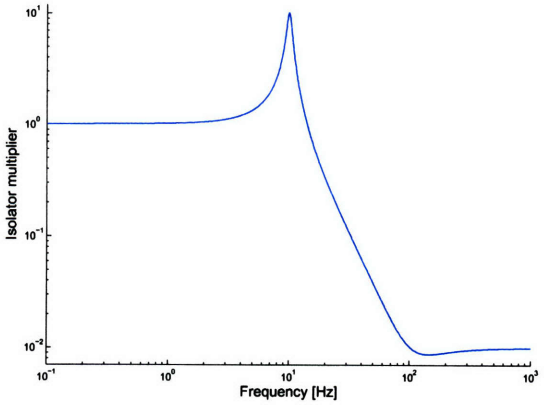

Figure 3-12: A single isolator channel, with corner frequency at 10 Hz

A isolation model described in this manner is incorporated into the integrated model by

[2] Although not investigated here, there is also much interest in active isolation systems, in which feedback control loops are used in conjunction with devices such as piezo-electric actuators to isolate individual frequencies.

converting Equation 3.20 to state-space form using a controller canonical representation [79].

$$\begin{aligned} \dot{x}_{iso} &= \begin{bmatrix} 0 & 1 \\ -\omega_{iso}^2 & -2\,\zeta_{iso}\,\omega_{iso} \end{bmatrix} x_{iso} + \begin{bmatrix} 0 \\ 1 \end{bmatrix} \tilde{w} \\ w &= \begin{bmatrix} K\omega_{iso}^2 & 0 \end{bmatrix} x_{iso} \end{aligned} \tag{3.21}$$

where $\tilde{w}$ represents the disturbance inputs before isolation, and w represents the attenuated inputs that excite the structural system. For the case of reaction wheel forces and torques, this system is repeated six times to filter the three forces and three torques.

3.2.4 Feedback control

Attitude control

The free boundary conditions of the spacecraft finite element models result in six rigid body modes. These modes represent the translational and rotational rigid motion of the spacecraft in orbit. Since they correspond to modal frequencies of $\omega_i = 0$, their presence in the A-matrix of Equation 3.26 makes that matrix singular. This singularity may affect subsequent computations [23], and the rigid body mode distorts the outputs unless stabilized. The observable modes are stabilized using an attitude control system (ACS) using reaction wheel torques to control the rotational rigid body modes. The translational rigid body modes are not observable in the optical outputs being used, and so are truncated from the system directly.

The ACS feedback loop uses the rotations of a node to represent the outputs from an attitude sensor (for instance a rate gyroscope). The rotations of the node are received by a controller, producing reaction wheel torque commands for pointing stability. Since the reaction wheel torques are already input to the system for their disturbance components, the attitude control torques can be combined with the disturbances for the total reaction wheel input to the system.

The ACS controller is provided by DOCS. It is an uncoupled proportional-derivative controller with inertia decoupling. The crossover frequency can be set as a fraction of the first flexible mode in order to keep flexible and ACS modes decoupled (for the TPF spacecraft the frequency is set to 0.01 times the first flexible mode).

Optical Control models

In order to achieve necessary levels of performance, closed-loop control of optical surfaces is necessary. Jacques [80] describes system identification and control methods, and Mallory [81] describes sensor/actuator placement and tuning for different control schemes. For the initial conceptual stage analysis however, such controllers may not be developed yet. In their absence, the effect of optical control is approximated using appropriate filters. Since optical controllers tend to improve performance up to a certain bandwidth, high-pass filters are used to attenuate low-frequency response. Above the filter corner frequency (set at an approximate controller bandwidth) the filter is set to unity gain and has no effect on the output.

The filter is described by the transfer function

$$H(s) = \frac{z_{hpf}}{z} = \frac{Ks}{s + \omega_{opt}} \tag{3.22}$$

where the gain K is set to unity, and ω_{opt} represents the control bandwidth. This transfer function is written in state-space form where $A_{opt} = -\omega_{opt}$, $B_{opt} = 1$, $C_{opt} = -\omega_{opt}$ and $D_{opt} = 1$. In practice a high-frequency roll-off would be included to avoid a non-zero D feed-through term.

3.3 Integrated model construction

The entire disturbance-to-performance system, from reaction wheel force and torque inputs to optical outputs, is described using a modal state-space formulation. The state matrices are formed using the outputs of the normal modes analysis, Equation 3.6. The modeshape matrix Φ obtained by the finite element solver is used to transform the physical coordinates $\bar{u}(t)$ from the equation of motion, Equation 3.1, to modal coordinates $x(t)$.[3]

$$u(t) = \Phi\, x(t) \tag{3.23}$$

The length of u is equal to the number of degrees of freedom, n_{dof}, often in the thousands. The length of x is equal to the number of modes obtained from the eigensolution, n_{modes},

[3]For purposes of clarity, the vector notation ($\bar{\cdot}$) and explicit time dependence will be dropped in subsequent equations.

often much less than n_{dof}. Equation 3.23 is substituted into Equation 3.1, and the resulting equation is pre-multiplied by Φ^T.

$$\Phi^T M \Phi \ddot{x} + \Phi^T K \Phi x = \Phi^T \beta_u u + \Phi^T \beta_w w \tag{3.24}$$

The force vector $F(t)$ is replaced by the actuator inputs f and disturbances w, which are mapped to the proper degrees of freedom by β_f and β_w, respectively. The modeshape vectors in Φ are mass normalized so that $\Phi^T M \Phi = I$, the identity matrix. Then $\Phi^T K \Phi = \Omega^2$ from Equation 3.6. Modal damping is added using a diagonal matrix Z containing damping values for each mode.

$$\ddot{x} + 2Z\Omega\dot{x} + \Omega^2 x = \Phi^T \beta_f f + \Phi^T \beta_w w \tag{3.25}$$

This second order differential equation can be turned into a first order differential equation of the form

$$\begin{Bmatrix} \dot{x} \\ \ddot{x} \end{Bmatrix} = \begin{bmatrix} 0 & I \\ -\Omega^2 & -2Z\Omega \end{bmatrix} \begin{Bmatrix} x \\ \dot{x} \end{Bmatrix} + \begin{bmatrix} 0 \\ \Phi^T \beta_f \end{bmatrix} f + \begin{bmatrix} 0 \\ \Phi^T \beta_w \end{bmatrix} w \tag{3.26}$$

Physical degrees of freedom in u that are desired outputs of the system (on important optical grid points, for example), are identified using pointing vectors. These are collected in $n_{outputs} \times n_{dof}$ matrices C_d or C_v, depending on whether displacement or velocity states are desired. The matrix equation defining these outputs can be transformed from physical coordinates u into modal coordinates x.

$$y = \begin{bmatrix} C_d & C_v \end{bmatrix} \begin{Bmatrix} u \\ \dot{u} \end{Bmatrix} = \begin{bmatrix} C_d \Phi & C_v \Phi \end{bmatrix} \begin{Bmatrix} x \\ \dot{x} \end{Bmatrix} \tag{3.27}$$

Optical performances may be described in terms of linear combinations of mirror node displacements, such as for the TPF models in Equations 3.7 and 3.9. The coefficients that multiply the displacements are collected into a matrix C_{opt}. An example from Equation 3.9 is shown, in which all six degrees of freedom (T_x, T_y, T_z, R_x, R_y and R_z) for the primary mirror and secondary mirror nodes are included.

$$C_{opt} = \begin{bmatrix} 0 & -\frac{1}{f_1} & 0 & 2 & 0 & 0 & 0 & \frac{1}{f_1} & 0 & -\frac{2}{MP+1} & 0 & 0 \\ \frac{1}{f_1} & 0 & 0 & 0 & 2 & 0 & -\frac{1}{f_1} & 0 & 0 & 0 & -\frac{2}{MP+1} & 0 \end{bmatrix} \tag{3.28}$$

The optics model is integrated with the structural model by multiplying the output displacements by C_{opt}. The integrated model performance outputs are described by a modified form of Equation 3.27.

$$z = \begin{bmatrix} C_{opt} C_d \Phi & 0 \end{bmatrix} \begin{Bmatrix} x \\ \dot{x} \end{Bmatrix} \tag{3.29}$$

The complete state-space representation of the model with $q = [\ x \quad \dot{x}\ ]^T$ includes the modal system from Equation 3.26 with the sensor outputs of Equation 3.27 and performance outputs of Equation 3.29. The actuator inputs $\beta_f f$ are renamed $\beta_u u$ to agree with convention, and the force feed-through matrices D_{ij} are included for completeness, but are most often zero for these models, particularly if w is white noise.

$$\begin{aligned} \dot{q} &= A\,q + B_u u + B_w w \\ y &= C_y\,q + D_{yu} u + D_{yw} w \\ z &= C_z\,q + D_{zu} u + D_{zw} w \end{aligned} \tag{3.30}$$

If the state matrices that describe the disturbance isolator in Equation 3.21 are labeled A_{iso}, B_{iso} and C_{iso}, Equation 3.30 is augmented by relating its inputs w to the outputs of Equation 3.21. The new state vector is $x_{int} = [\ q \quad x_{iso}\ ]^T$.

$$\begin{Bmatrix} \dot{q} \\ \dot{x}_{iso} \end{Bmatrix} = \begin{bmatrix} A & B_w C_{iso} \\ 0 & A_{iso} \end{bmatrix} \begin{Bmatrix} q \\ x_{iso} \end{Bmatrix} + \begin{bmatrix} B_u \\ 0 \end{bmatrix} u + \begin{bmatrix} 0 \\ B_{iso} \end{bmatrix} \tilde{w} \tag{3.31}$$

$$y = \begin{bmatrix} C_y & D_{yw} C_{iso} \end{bmatrix} \begin{Bmatrix} q \\ x_{iso} \end{Bmatrix} + D_{yu} u$$

$$z = \begin{bmatrix} C_z & D_{zw} C_{iso} \end{bmatrix} \begin{Bmatrix} q \\ x_{iso} \end{Bmatrix} + D_{zu} u$$

Similarly, the ACS control laws are described in state-space form.

$$\begin{aligned} \dot{x}_{acs} &= A_{acs}\, x_{acs} + B_{acs}\, y \\ u &= C_{acs}\, x_{acs} \end{aligned} \tag{3.32}$$

For ACS sensor outputs y and torque inputs u, the feedback loop is implemented by matching inputs and outputs with Equation 3.31. The new state vector is now $[\ q \quad x_{iso} \quad x_{acs}\ ]^T$.

$$\begin{Bmatrix} \dot{q} \\ \dot{x}_{iso} \\ \dot{x}_{acs} \end{Bmatrix} = \begin{bmatrix} A & B_w C_{iso} & B_u C_{acs} \\ 0 & A_{iso} & 0 \\ B_{acs} C_y & B_{acs} D_{yw} C_{iso} & A_{acs} + B_{acs} D_{yu} C_{acs} \end{bmatrix} \begin{Bmatrix} q \\ x_{iso} \\ x_{acs} \end{Bmatrix} + \begin{bmatrix} 0 \\ B_{iso} \\ 0 \end{bmatrix} \tilde{w}$$

$$z = \begin{bmatrix} C_z & D_{zw} C_{iso} & D_{zu} C_{acs} \end{bmatrix} \begin{Bmatrix} q \\ x_{iso} \\ x_{acs} \end{Bmatrix} \tag{3.33}$$

The high-pass filter used to approximate optical control is integrated with the system in a similar manner to the isolator low-pass filter. The final integrated model used in all subsequent analysis is:

$$\begin{aligned} \dot{x}_{int} &= A_{int}\, x_{int} + B_{w_{int}}\, \tilde{w} \\ z_{hpf} &= C_{int}\, x_{int} \end{aligned} \tag{3.34}$$

which describes the system from the disturbance inputs $\tilde{w}$ to the controlled optical performance outputs z_{hpf}. Figure 3-13 illustrates the components that comprise the integrated model for TPF-FFI. The plant represents the finite element structure. Reaction wheel disturbances including three forces and three torques excite the systems at a single node. The disturbances are attenuated by two levels of isolation: isolation between the wheels and the bus, and between the bus and the optics. An ACS is used to control the rotational rigid body modes by sensing the rotation rates and commanding the reaction wheel torques. Optical outputs include line-of-sight jitter about the x- and y-axes, and wave front error resulting from the root-sum-square of the first 15 zernike coefficients. Optical control filters are used on the LOS output channels to represent a level of optical control. All of the

integrated models investigated in this work are connected in a similar fashion.

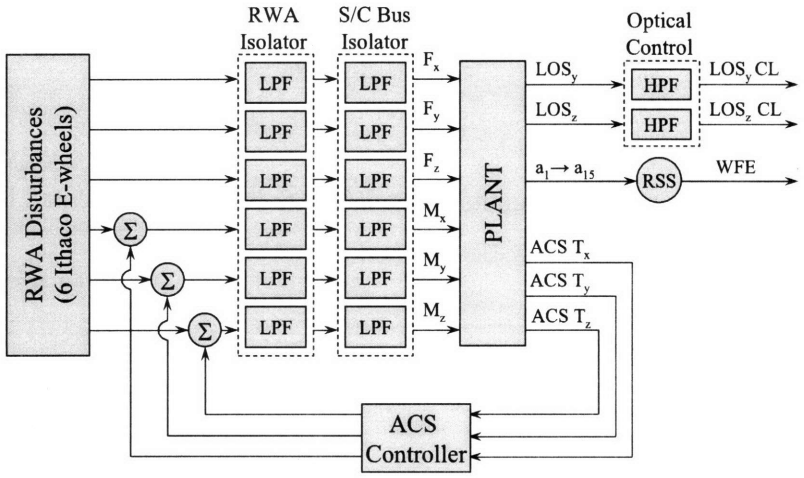

Figure 3-13: Block diagram for the TPF-FFI integrated system

3.4 Disturbance analysis

A brief overview of random processes in dynamic response is provided to give a background to the frequency-based disturbance analysis routines used in this thesis. Any textbook on the subject (for instance Brown and Hwang [82] or Siebert [83]) should be consulted for greater depth. Following this overview, an example disturbance analysis of the TPF-FFI spacecraft is shown.

3.4.1 Dynamic response

The dynamic problems examined in this work assume that the inputs and outputs can be described by stochastic processes, meaning that the signals are random variables. For any stochastic signal, $X(t)$, the expectation of the signal is the mean $E[X(t)]$, which can be found given the probability density function of the signal, $f_X(x(t))$.

$$E[X(t)] = \int_{-\infty}^{\infty} x(t) f_X dx(t) \tag{3.35}$$

The autocorrelation function of a stationary signal is

$$R_X(\tau) = E[X(t)X(t+\tau)] \tag{3.36}$$

which instead of being computed using the (often unknown) probability density function, can be found for a signal using the time average.

$$R_X(\tau) = \lim_{T\to\infty} \frac{1}{T} \int_0^T X(t)X(t+\tau)dt \tag{3.37}$$

When the time difference τ is zero, Equation 3.36 shows that the autocorrelation function gives the mean square value of the process, $E[X(t)X(t)]$. The root mean square (RMS) value is often the final output of the analysis. For a zero-mean process, the RMS value is identical to the standard deviation of the signal, which measures the variation of the process.

The autocorrelation function evaluates signals in the time domain. Given an input $x(t)$ going through a system with the impulse response $g(t)$, a convolution is required to solve for the output $y(t)$.

$$y(t) = x(t) * g(t) = \int_{-\infty}^{\infty} x(\tau)g(t-\tau)d\tau = \int_{-\infty}^{\infty} g(\tau)x(t-\tau)d\tau \tag{3.38}$$

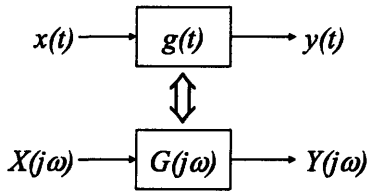

Figure 3-14: Equivalence of the time and frequency domains in dynamic response

For steady state dynamic analysis the frequency domain is often used. The time domain and frequency domain approaches are equivalent (as Figure 3-14 indicates), however in the frequency domain the convolution can be replaced with simple multiplication, once the Fourier transform of each signal is calculated.

$$Y(s) = X(s) \cdot G(s) \tag{3.39}$$

Applying the Fourier transform to the autocorrelation function gives the frequency-based power spectral density (PSD) of a signal, which represents the distribution of signal strength across the frequency spectrum.

$$S_X(j\omega) = \mathscr{F}[R_X(\tau)] = \int_{-\infty}^{\infty} R_X(\tau) e^{-j\omega\tau} d\tau \tag{3.40}$$

The inverse Fourier transform of the PSD gives back the autocorrelation function:

$$R_X(\tau) = \mathscr{F}^{-1}[S_X(j\omega)] = \frac{1}{2\pi} \int_{-\infty}^{\infty} S_X(j\omega) e^{j\omega\tau} d\omega \tag{3.41}$$

which, at $\tau = 0$, gives the mean square value of the signal. The advantage of describing a signal with a PSD then, is that the mean square value can be easily computed with an integration of the PSD curve.

$$R_X(0) = E[X^2(t)] = \frac{1}{2\pi} \int_{-\infty}^{\infty} S_X(j\omega)\, d\omega \tag{3.42}$$

For a dynamic state-space system of the form of Equation 3.30, where the inputs $w(t)$ and outputs $z(t)$ can both be described by stochastic processes, the transfer function $G(j\omega)$ from Figure 3-14 can be computed from the state matrices.

$$G_{zw}(j\omega) = \frac{Z(j\omega)}{W(j\omega)} = C_z \left(j\omega I - A\right)^{-1} B_w + D_{zw} \tag{3.43}$$

Given inputs described by PSDs $S_{ww}(j\omega)$ (such as for the reaction wheel disturbances, whose PSDs were shown in Figure 3-11), the PSDs of the performance outputs can be computed by a simple matrix multiplication.

$$S_{zz}(j\omega) = G_{zw}(j\omega)\, S_{ww}(j\omega)\, G_{zw}^H(j\omega) \tag{3.44}$$

Finally, the mean square values of the outputs are found by applying Equation 3.42 to the performance PSDs:

$$\Sigma_z = \frac{1}{2\pi} \int_{-\infty}^{\infty} S_{zz}(\omega)\, d\omega \tag{3.45}$$

where ω is in rad/sec. Mean square (MS) values for individual outputs $\sigma_{z_i}^2$ can be found using the single-sided integral from zero to infinity.

$$\sigma_{z_i}^2 = \Sigma_{z_{i,i}} = \frac{1}{2\pi}\int_{-\infty}^{+\infty}[S_{zz}(\omega)]_{i,i}\,d\omega = \frac{1}{\pi}\int_{0}^{+\infty}[S_{zz}(\omega)]_{i,i}\,d\omega \tag{3.46}$$

The final RMS values are σ_{z_i}. Example results including performance PSDs and the cumulative mean square results across frequency are given in the next section.

3.4.2 TPF-FFI disturbance analysis results

An example dynamic analysis on an integrated opto-mechanical model is shown for the TPF-FFI spacecraft. Disturbance vibrations are propagated through the system in order to predict their effect on optical performance outputs. This type of analysis is used throughout this thesis; it is based on earlier works including Gutierrez [26] for an early model of the SIM spacecraft, Uebelhart [23] for a later model of SIM, and de Weck [24] for the James Webb Space Telescope.

The schematic of the integrated model is shown in Figure 3-13. Disturbance PSD inputs plotted in Figure 3-11 are used to excite the system. Two stages of vibration isolation (modeled as low-pass filters) are used to attenuate the vibration energy that is transmitted to the optics; the first has a 2 Hz corner frequency, and the second a 10 Hz corner frequency. The DOCS ACS controller is used to stabilize rotational rigid body modes, and translational rigid body modes are not observable in the outputs and so are truncated.

Two optical performances are output from the system: line-of-sight jitter is calculated using the approximation in Equation 3.9, and wave front error is computed by the root-sum-square of the weighted Zernike coefficients (Equation 3.16). The advantage to using Zernikes is that the instead of outputting 525 grid points across the mirror surface, a much smaller number of Zernike coefficients can be evaluated. The first 15 Zernikes are computed (where numbers 1 and 2 are tip and tilt). The line-of-sight outputs are passed through a 10 Hz high-pass filter to approximate the effect of optical control. The wave front error is left open loop, without any optical control. Noecker et al. [7] have described the performance requirements for a TPF interferometer; for a dual Bracewell interferometer, where four telescopes are arranged in a line, the line-of-sight requirement is 10.48 milli-arcseconds and the wave front error due to focus and other effects sums to 12.08 nanometers.

A total of 350 modes are obtained from the finite element solver; this includes frequency content up to 212 Hz. A low value for modal damping, 0.01%, is chosen based on the anticipated effect of cryogenic temperatures on damping [66, 67]. Equation 3.44 is used to propagate the disturbance PSDs through the system transfer functions, to obtain the performance PSDs. These are integrated (Equation 3.46) to compute the mean square values for the outputs, from which the root mean square values are obtained. The RMS line-of-sight results for both open- and closed-loop are given in Table 3.3, as is the final (open-loop) wave front error computed from the Zernike coefficient outputs.

Table 3.3: RMS Performance values for TPF-FFI under reaction wheel disturbances

	Open loop	**Closed loop**	**requirement**[7]
Line-of-sight jitter X (mas)	8.91	3.37	10.48
Line-of-sight jitter Y (mas)	9.51	2.49	10.48
Wave front error (nm)	1300	n/a	12.08

Table 3.3 shows that the LOS requirements are met about both axes for both open loop and closed loop. The use of optical control with a 10 Hz bandwidth could improve the performance and provide additional margin of at least 7 mas. Figure 3-15 gives the open and closed loop performance PSDs about both the x- and y-axes. The bottom plots of both sub-figures are the PSD curves. The upper plots are the cumulative mean square curves, which asymptote to the final MS values (the square of the results in Table 3.3).

The plots are useful in indicating which modes contribute to the final mean square

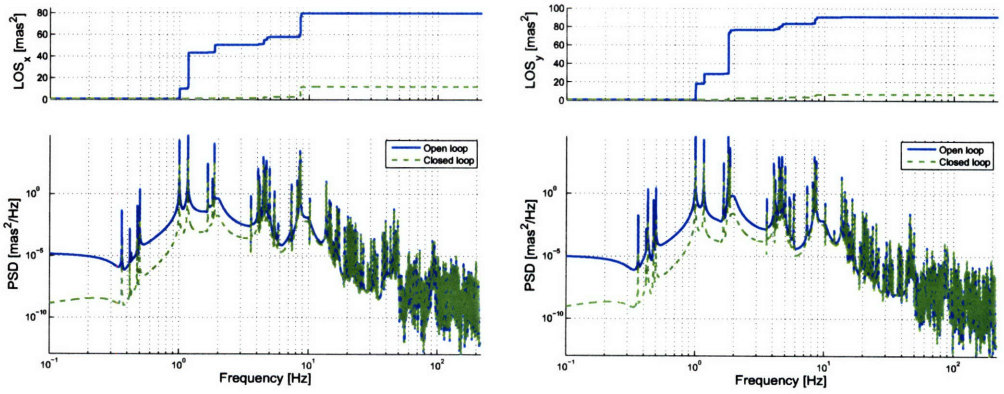

(a) LOS_X (mas) (b) LOS_Y (mas)

Figure 3-15: Power spectral density and cumulative mean square plots for open- and closed-loop line-of-sight performance

output. The largest contributors in open loop include modes at 1.17 Hz and 1.00 Hz, as well as a mode at 8.55 Hz for LOS-x and one at 1.81 Hz for LOS-y. The 1.00 Hz modeshape is illustrated in Figure 3-16(a); together with the 1.17 Hz mode these appear as rigid body modes for the telescope instruments, with deflections of the sunshade booms and stray light trays. The 1.81 Hz mode, illustrated in Figure 3-16(b) is due to the rotations of the stray light trays, with the spacecraft rocking as a result. The effect of these modes could be reduced by moving disturbance energy away from these frequencies. If this is not possible, the modes could be shifted by strengthening connection points between the stray light trays and telescope assembly, or by stiffening the sunshade booms. The 8.55 Hz mode, which also dominates the LOS-x closed-loop response, includes bending of the secondary mirror tower, rotations of the primary mirror, distortions of the optical bench and a "breathing" mode of the stray light trays about the OTA. This modeshape involves the entire spacecraft and it is not clear that making any one change to a particular component would effect the mode. The contribution of the 8.55 Hz mode to the response should be reduced by eliminating or reducing the disturbance energy at that frequency.

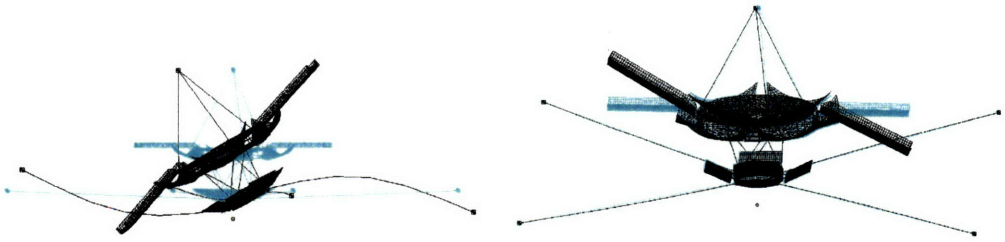

(a) Mode #12: 1.004 Hz

(b) Mode #15: 1.8113 Hz

Figure 3-16: Critical modes for TPF-FFI

Besides identifying critical modes, the cumulative MS curves in Figure 3-15 are also useful in indicating how many modes should be obtained from Nastran. Since nearly all of the contributions to the outputs come from frequencies less than 15 Hz, it is not necessary at this stage to solve for 350 modes up to 212 Hz. For subsequent analyses in Chapter 5, only 140 modes with modal frequencies up to 55 Hz will be used.

While the LOS meets requirements in both open and closed loop, Table 3.3 shows that in open loop WFE fails to meet its requirement by two orders of magnitude. Figure 3-17 shows the RMS weighted Zernike coefficients that contribute to the WFE. The greatest contribution comes from Zernike #2, tilt, with lesser contributions from Zernikes #7 (coma

about the y-axis), and #s 9 and 10 (trefoil x- and y-axes). Two of the PSDs and cumulative MS curves (#s 2 and 7) are plotted in Figure 3-18. The frequency content of these outputs look very similar. Both are dominated by three modes: 1.81 Hz, 1.00 Hz and 1.17 Hz, in decreasing order of importance. All of these modes were identified for the LOS, and they all primarily involve rotations of the primary mirror, rather than distortions of the mirror. Tailoring the allowable reaction wheel speeds to reduce disturbance energy at these frequencies would significantly improve the mirror wave front error.

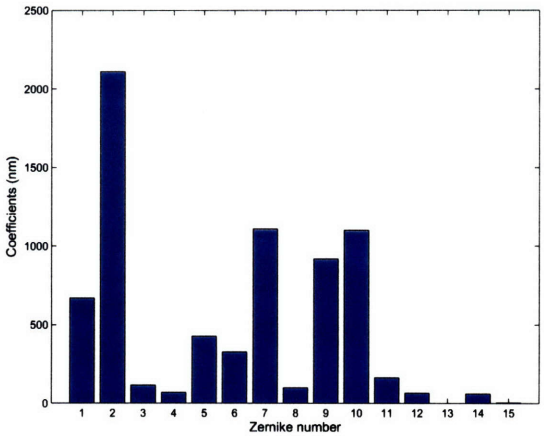

Figure 3-17: Weighted RMS Zernike coefficients

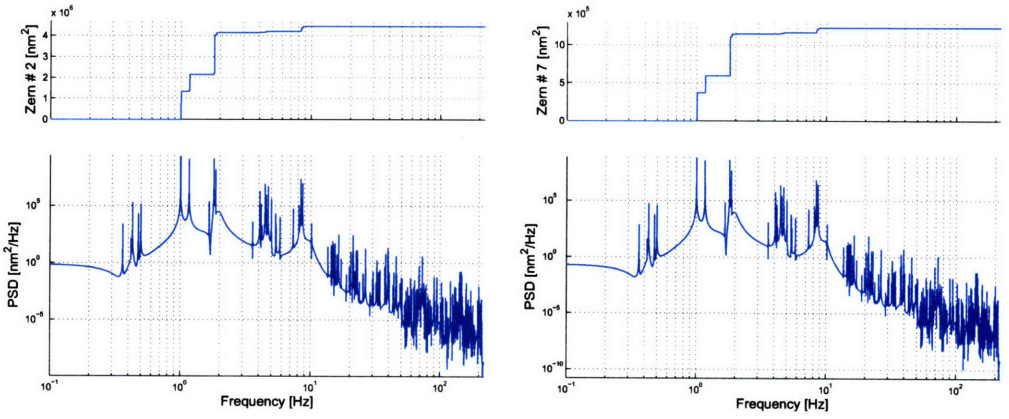

(a) Zernike #2: tilt (nm)

(b) Zernike #7: coma-y (nm)

Figure 3-18: PSD and MS curves for Zernike coefficients #2 and #7

3.5 Conclusions

The modeling and analysis approach that will be used throughout this thesis is outlined. Dynamic integrated models are built using a multidisciplinary approach including structural finite element models, equations describing the optics, feedback control systems and approximations for optical control and vibration isolation. All of the sub-models are assembled together into a single, linear time-invariant (LTI) state-space model. Dynamic response techniques are used to propagate disturbance energy described using power spectral density curves through the state-space systems, to obtain performance PSD curves. These curves, along with the cumulative mean square curves, can be used to predict the final RMS system performances and to identify critical modeshapes that contribute to the outputs.

Example models are shown for two of the TPF spacecraft: the structurally-connected interferometer and the free-flying interferometer. A complete disturbance analysis is run for the TPF-FFI spacecraft. The results using a broadband RWA disturbance model show that the LOS metric meets its requirements even in open loop, and using an optical controller will likely improve the LOS output by at least 7 mas. WFE, on the other hand, fails to meet its requirement by several orders of magnitude. Specific modeshapes that contribute to the performance outputs are identified, and removing disturbance energy at the frequencies of these modeshapes could improve the performance values.

The evaluation of the TPF concepts is limited to the two point designs (SCI and FFI) so far created. The next chapter will introduce methods that will parameterize the finite element and integrated models, allowing new design realizations to be automatically constructed and evaluated by changing key design variables.

Chapter 4

Parameter Dependent Models

The disturbance analysis example in the previous chapter is performed on a single point design model. All of the model parameters are at their nominal values. As is illustrated in Figure 3-1, this analysis indicates whether the nominal system meets its requirement, but no information is available on the uncertainty of those predictions or on whether an alternative design is superior. For conceptual design of structures, it is necessary to be able to evaluate deviations from the single point design. Evaluation of off-nominal parameters due to uncertainty can motivate a redesign so that a system is more robust to uncertainty. For conceptual design studies, examination of additional design points may lead to superior designs in terms of optical performance, cost or mass. Since the proposed conceptual design methodology is based on evaluating alternative designs across the design space, methods of parameterizing the structural and integrated models are required.

In performing this parametrization, two types of parameters are defined. Uncertainty parameters $\bar{p}$ are those parameters that the designer has no control over. These may be physical parameters such as Young's modulus or modal parameters such as damping. The goal of the uncertainty analysis is to determine the bounds on the outputs based on variations of $\bar{p}$. The relationship between the outputs $\bar{y}$ and the uncertain parameters $\bar{p}$ can be described in functional form.

$$\bar{y} = f(\bar{p})$$

The second set of parameters are the design variables, $\bar{x}$, that the designer is allowed to vary. These parameters explicitly define the design, and the range of design variables defines

the possible design space for a system. Design variables may include the type of telescope: coronagraph versus interferometer, the type of aperture: circular monolithic versus hexagonal segmented mirrors, or continuous values such as the diameter of a telescope's primary mirror. Since for every unique design defined by $\bar{x}$ there are still uncertain parameters $\bar{p}$, the functional relationship is now written as

$$\bar{y} = f(\bar{x}, \bar{p})$$

where the model outputs $\bar{y}$ are ultimately a function of both types of parameters. In order to evaluate $\bar{y}$ across design variables and uncertain parameters, a parameterized model is required that allows changes in $\bar{x}$ and $\bar{p}$ to be propagated through the model.

The desired model is illustrated in Figure 4-1. Instead of starting with the geometry of a single point design and constructing a single structural model, the designer inputs a vector of design variables and system parameters. Based on these inputs, the model creates the structural form by placing grid points and assembling the finite elements. An analysis is automatically run using a finite element solver, and an integrated model is assembled. This model can be used for any desired analysis, including the dynamic disturbance analysis described in the last chapter or an uncertainty analysis based on the parameters $\bar{p}$. For every design realization, the model outputs all of the desired metrics.

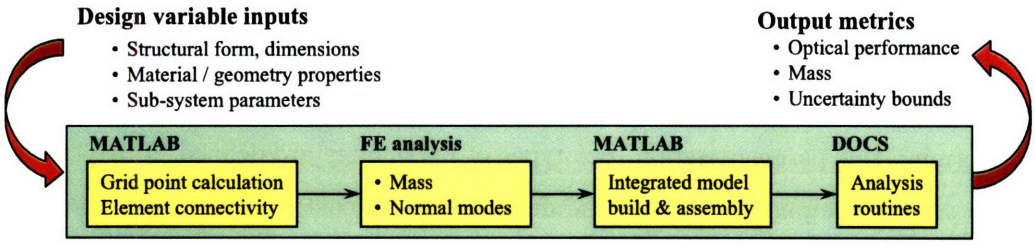

Figure 4-1: Schematic overviewing the parameterized integrated modeling process

This chapter describes methods that can be used to create parameterized structural and integrated models. An overview of alternative methods is described first, with recommendations on which methods are more appropriate for different types of parameters or design variables. Next, the linear fractional transformation is described that allows a variation of linear parameters in state-space models. An example with the Terrestrial Planet Finder, Structurally Connected Interferometer is shown. In order to evaluate a greater range of

design variables, a modeling environment is then proposed to automatically generate structural finite element models and dynamic integrated models. This environment builds and analyses unique telescope design realizations based on high-level design variable inputs. Finally, an example of this modeling environment is shown with a parameterized model of the ground-based Thirty Meter Telescope.

4.1 Methods of structural model parametrization

The methods used to parameterize a model depend highly on the type of variable to be studied. Four options could be used for the integrated models being examined.

1. Manipulate K, M matrices directly
2. Add parameter dependence through ΔK, ΔM matrices
3. Add linear variation to the state-space model
4. Rebuild the model, creating a new bulk data and integrated model

The first two options focus on inputs to the stiffness and mass matrices of the structural model. Given that these matrices have already been generated for a given structure, option 1 is to vary the individual parameters directly in the proper matrix entries (such as in the M and K matrices defined in Equations 3.2 and 3.3). For a normal modes analysis, this requires that the eigenproblem be solved and the state-space model be created for each instance. Option 2 improves upon this by including the parameter variation in the state-space realization using the sensitivity matrices of mass and stiffness for the parameter. Option 3 provides a similar variation to any parameter that appears explicitly in the state-space formulation, and can include parameters of sub-models other than the structure. Finally, option 4 is to completely rebuild the model for every new design vector. While this option is the most time-intensive in terms of running the model, it also allows for a much more diverse design space.

Table 4.1 lists a selection of parameters that have been used in analysis of precision telescopes. The finite element values include all of those parameters that are included in a finite element data deck, for example. These often include material properties, geometry properties representing cross-sectional areas and plate thicknesses, and spring stiffnesses.

The integrated modeling (IM) inputs are more geared toward models of a space telescope, but generally can represent parameters that appear in the disturbance, control and performance models, whatever their form. Finally, the design variables determine the overall architecture. The structure layout for telescopes refers to the arrangement of the aperture, e.g. monolithic mirror versus segmented, or free-flying interferometers versus structurally connected. Shape may describe the curvature of the mirror, while the dimensions of the structure can include mirror diameter, or height of the secondary mirror.

Table 4.1: Modeling parameters and methods of parametrization. x's represent possible methods, check marks represent recommended methods.

		Option 1	**Option 2**	**Option 3**	**Option 4**
FE values	material properties	x	✓		x
	geometry values	x	✓		x
	spring stiffnesses	x	✓		x
	concentrated masses	x	✓		x
	damping			✓	x
	element choice	x			✓
	mesh density				✓
IM inputs	# of reaction wheels				✓
	controller gains			✓	x
	controller bandwidth			✓	x
	filter corner frequencies			✓	x
	optical parameters				✓
Design Variables	structural layout				✓
	structural shape				✓
	structural dimensions				✓

For each of these parameters, the possible options for parametrization are denoted by either x's or check marks, where the check marks emphasize the options that provide either the most flexibility or greatest computational time savings. In conceptual design all of these parameters may be varied, and the designer should utilize the best tools available for evaluating many concepts. Mathematical tools have been developed to analyze parameters such as material properties or controller gains for robust design or uncertainty analysis, but broader tools or frameworks for performing large trade space analyses on unique structures are not as mature. This lack of trade space analyses is due to the computational cost of

running many finite element analyses, but as computer speed has increased it has become possible to run many instances of a parameterized finite element model. The choice of which parametrization tool to use still relies on the type of parameter, and can be guided by Table 4.1.

The next section describes a method for options 2 and 3, that add parameter variation directly to the state-space models. A modeling environment is proposed in Section 4.3 to enable option 4; finite element models are automatically generated based on parameter inputs. Examples of these parametrization methods are shown using two telescope structural and integrated models.

4.2 Linearized parameter variation in state-space models

The linear fractional transformation is described, allowing linearized variations in parameters to be incorporated directly into state-space models. An example is shown with results from the Terrestrial Planet Finder, Structurally Connected Interferometer integrated model.

4.2.1 Linear fractional transformation

Parametrization of linear inputs to a system can be performed with the linear fractional transformation (LFT), originally used for robust control design techniques such as μ-synthesis or design of $\mathcal{H}_2$ controllers [84]. The LFT separates a linear, time-invariant (LTI) state-space representation of a model into nominal and uncertain parts, and creates non-physical inputs and outputs so that a parameter with bounded uncertainty is included in a feedback loop. The resulting system is a linear, parameter varying (LPV) model in which changes in a parameter value can be quickly computed, without having to re-evaluate the model. References [85] and [86] provide good overviews of the technique. Examples of its use in uncertainty analysis can be found in References [87] and [88].

The LFT method allows the state-space matrices to be dependent upon parameters δ.

$$\begin{aligned} \dot{x} &= A(\delta)\,x + B(\delta)\,u \\ y &= C(\delta)\,x + D(\delta)\,u \end{aligned} \tag{4.1}$$

A standard form of the LFT implementation is to treat both lines of Equation 4.1 as a single

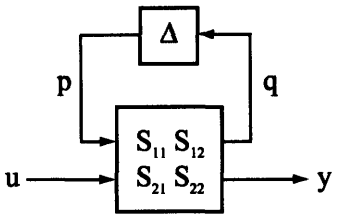

Figure 4-2: System block diagram with LFT inputs and outputs

first order equation. The matrix $S(\delta)$ is formed from the individual state-space matrices,

$$S(\delta) = \begin{bmatrix} A(\delta) & B(\delta) \\ C(\delta) & D(\delta) \end{bmatrix} \tag{4.2}$$

and the full model is described by a single matrix equation with inputs x and u, and outputs $\dot{x}$ and y.

$$\begin{Bmatrix} \dot{x} \\ y \end{Bmatrix} = [S(\delta)] \begin{Bmatrix} x \\ u \end{Bmatrix} \tag{4.3}$$

A requirement of the LFT method is that the parameter dependent (or uncertain) part of $S(\delta)$ can be separated from the nominal part.

$$\begin{Bmatrix} \dot{x} \\ y \end{Bmatrix} = [S_o + S_\Delta(\delta)] \begin{Bmatrix} x \\ u \end{Bmatrix} \tag{4.4}$$

With the nominal and uncertain parts of $S(\delta)$ divided, the form of the LFT is illustrated by Figure 4-2. The physical system inputs u and outputs y are still as given in Equation 4.3, but the system also now includes inputs p and outputs q connecting the system to an uncertainty block Δ. This form, sometimes called a $S-\Delta$ model [1] includes the uncertainty in an additional feedback loop where the new model equation is of the form:

$$\begin{Bmatrix} \dot{x} \\ y \end{Bmatrix} = [S_{22}] \begin{Bmatrix} x \\ u \end{Bmatrix} + S_{12}p \tag{4.5}$$

$$q = [S_{21}] \begin{Bmatrix} x \\ u \end{Bmatrix} + S_{11}p \tag{4.6}$$

[1] or $P-\Delta$ model, since P is often used as the variable name in place of S in Figure 4-2

The loop is closed by treating the parameter values in Δ as feedback gains.

$$p = \Delta q \tag{4.7}$$

Equation 4.7 is then used to simplify the equations 4.5 and 4.6.

$$\left\{ \begin{array}{c} \dot{x} \\ y \end{array} \right\} = \left[S_{22} + S_{21}\Delta(I - S_{11}\Delta)^{-1}S_{12} \right] \left\{ \begin{array}{c} x \\ u \end{array} \right\} \tag{4.8}$$

By comparison to Equation 4.4 it is apparent that $S_o = S_{22}$. The goal of the LFT is then to find the other matrices S_{12}, S_{21} and S_{11} so that a single system with inputs u and p and outputs q and y describe the entire parametric model, with the parameter values included in the form of feedback gains. The model is an augmented state-space system that can be described using either the S_{ij} notation, or using A, B, C and D matrices where the $(\cdot)_o$ references the nominal system matrices and the $(\cdot)_\Delta$ matrices are additions of the LFT formulation.

$$\left\{ \begin{array}{c} \dot{x} \\ y \\ q \end{array} \right\} = \left[\begin{array}{cc} S_{22} & S_{12} \\ S_{21} & S_{11} \end{array} \right] \left\{ \begin{array}{c} x \\ u \\ p \end{array} \right\} = \left[\begin{array}{cc|c} A_o & B_o & B_\Delta \\ C_o & D_{yu} & D_{yp} \\ \hline C_\Delta & D_{qu} & D_{pq} \end{array} \right] \left\{ \begin{array}{c} x \\ u \\ p \end{array} \right\} \tag{4.9}$$

The parameter dependent state matrices from Equation 4.2 are computed at a new value for Δ by closing the feedback loop using Equation 4.7. The state matrices can be written out in LFT form.

$$\begin{aligned} A(\delta) &= A_o + B_\Delta\Delta(I - D_{pq}\Delta)^{-1}C_\Delta \\ B(\delta) &= B_o + B_\Delta\Delta(I - D_{pq}\Delta)^{-1}D_{uq} \\ C(\delta) &= C_o + D_{py}\Delta(I - D_{pq}\Delta)^{-1}C_\Delta \\ D(\delta) &= D_{yu} + D_{py}\Delta(I - D_{pq}\Delta)^{-1}D_{uq} \end{aligned} \tag{4.10}$$

For all of the systems examined, the D_{pq} (which equals S_{11}) matrix is zero. This reduces the Equations 4.10 to

$$
\begin{aligned}
A(\delta) &= A_o + B_\Delta \Delta C_\Delta \\
B(\delta) &= B_o + B_\Delta \Delta D_{uq} \\
C(\delta) &= C_o + D_{py} \Delta C_\Delta \\
D(\delta) &= D_{yu} + D_{py} \Delta D_{uq}
\end{aligned}
\tag{4.11}
$$

and reduces Equation 4.8 to

$$
\left\{ \begin{array}{c} \dot{x} \\ y \end{array} \right\} = [S(\delta)] \left\{ \begin{array}{c} x \\ u \end{array} \right\} = [S_{22} + S_{21} \Delta S_{12}] \left\{ \begin{array}{c} x \\ u \end{array} \right\} \tag{4.12}
$$

The sensitivity of the parameters to Δ is written

$$
\frac{\partial}{\partial \Delta} S(\delta) = \left[\begin{array}{cc} \frac{\partial A(\delta)}{\partial \Delta} & \frac{\partial B(\delta)}{\partial \Delta} \\ \frac{\partial C(\delta)}{\partial \Delta} & \frac{\partial D(\delta)}{\partial \Delta} \end{array} \right] \tag{4.13}
$$

where, from Equation 4.11,

$$
\begin{aligned}
\frac{\partial A(\delta)}{\partial \Delta} &= B_\Delta C_\Delta \\
\frac{\partial B(\delta)}{\partial \Delta} &= B_\Delta D_{uq} \\
\frac{\partial C(\delta)}{\partial \Delta} &= D_{py} C_\Delta \\
\frac{\partial D(\delta)}{\partial \Delta} &= D_{py} D_{uq}.
\end{aligned}
\tag{4.14}
$$

All of the parameters examined in this work are in the A matrix, so the only variations from the matrices in Equations 4.10 are described by

$$
A(\delta) = A_o + B_\Delta \Delta C_\Delta. \tag{4.15}
$$

The matrices B_Δ and C_Δ, and similarly the matrices S_{21} and S_{12} in Equation 4.12, can be obtained by factoring $S_\Delta(\delta)$ from Equation 4.4 or just factoring the parametric part of $A(\delta)$ using a singular value decomposition (SVD). Two examples of this are shown next.

LFT of state matrices with explicit parameters

An example in which the parameter dependence is explicit in the state matrices is shown using a high pass filter with corner frequency ω and gain K.

$$H(s) = \frac{Y(s)}{U(s)} = \frac{Ks}{s+\omega} \tag{4.16}$$

This transfer function is realized as a state-space system using the controller canonical form [79].

$$\begin{aligned} \dot{x} &= -\omega x + u \\ y &= -K\omega x + Ku \end{aligned} \tag{4.17}$$

where $A = -\omega$, $B = 1$, $C = -K\omega$ and $D = K$. For a variation in frequency ω, this system can be represented by a S-matrix of the form

$$S(\omega) = \begin{bmatrix} -\omega & 1 \\ -K\omega & K \end{bmatrix} \tag{4.18}$$

It is assumed that the uncertainty of this system can be represented by expanding each element of $S(\omega)$ in a Taylor series, keeping only the linear dependence on the parameter and ignoring higher order terms.

$$S_{ij}(\omega) = S_{ij_o} + \frac{\partial S_{ij}}{\partial \omega}\,\Delta\omega \tag{4.19}$$

Note that in this case, the Δ symbol in front of the parameter ω represents the change in the parameter. It should be clear in the context of an equation whether the Δ represents change of a parameter or whether it is the collection of closed loop gains in the LFT derivation.

The system can now be divided into nominal S_o and uncertain $S_\Delta(\omega)$ parts

$$\begin{aligned} S(\omega) &= S_o + S_\Delta(\omega) \\ &= S_o + \frac{\partial S}{\partial \omega}\Delta\omega \\ &= \begin{bmatrix} -\omega - \Delta\omega & 0 \\ -K\omega - K\Delta\omega & 0 \end{bmatrix} \end{aligned} \tag{4.20}$$

$$= \begin{bmatrix} -\omega & 1 \\ -K\omega & K \end{bmatrix} + \begin{bmatrix} -1 & 0 \\ -K & 0 \end{bmatrix} \Delta\omega$$

Since the system is now in the form given by Equation 4.12 with the Δ gain matrix replaced by the scalar $\Delta\omega$, the S_{21} and S_{12} matrices are found by performing a singular value decomposition on the $\frac{\partial S}{\partial \omega}$ matrix.

$$\begin{aligned} \frac{\partial S}{\partial \omega} &= U \Sigma V^T \\ &= (U \Sigma^{1/2}) \cdot (\Sigma^{1/2} V^T) \\ &= S_{21} \cdot S_{12} \end{aligned} \tag{4.21}$$

DOCS is capable of creating LFT state-space models by this method [89], where the sensitivity matrix is provided by the user.

LFT with physical parameters

It is also possible to include variations in physical parameters that appear linearly in the model mass and stiffness matrices, but that do not explicitly appear in the final modal state matrices. That procedure begins with the physical equations of motion, assuming that the M and K matrices can be divided into nominal and varying parts.

$$(M_o + M_\Delta)\ddot{x} + (K_o + K_\Delta)x = \beta_u u \tag{4.22}$$

where matrix β_u maps the inputs u to the physical states x. DOCS computes the M_Δ and K_Δ matrices for parameters that enter M and K linearly by identifying those elements in the matrices that contain the parameter and dividing out the nominal parameter value [90]. The analysis continues in DOCS by assuming that the nominal modeshape matrix Φ is valid for the perturbed system. In this case, the undamped modal equation of motion (using the transformation $x = \Phi\eta$), pre-multiplied by Φ^T can be written.

$$\left[\Phi^T M_o \Phi + \Phi^T M_\Delta \Phi\right] \ddot{\eta} + \left[\Phi^T K_o \Phi + \Phi^T K_\Delta \Phi\right] \eta = \Phi^T \beta_u u \tag{4.23}$$

The modeshapes are mass-normalized, so that the equation reduces to

$$\left[I + \Phi^T M_\Delta \Phi\right] \ddot{\eta} + \left[\Omega^2 + \Phi^T K_\Delta \Phi\right] \eta = \Phi^T \beta_u u \tag{4.24}$$

where the modal frequencies are in the diagonal matrix Ω. This equation can be re-written in first order form.

$$\left(I + \begin{bmatrix} 0 & 0 \\ 0 & \Phi^T M_\Delta \Phi \end{bmatrix} \right) \begin{Bmatrix} \dot{\eta} \\ \ddot{\eta} \end{Bmatrix} = \left(\begin{bmatrix} 0 & I \\ -\Omega^2 & 0 \end{bmatrix} + \begin{bmatrix} 0 & 0 \\ -\Phi^T K_\Delta \Phi & 0 \end{bmatrix} \right) \begin{Bmatrix} \eta \\ \dot{\eta} \end{Bmatrix} + \begin{bmatrix} 0 \\ \Phi^T \beta_u \end{bmatrix} u \tag{4.25}$$

In the case where only the K matrix is dependent upon the parameter (M_Δ=0), this system looks like Equation 4.15, and $\Phi^T K_\Delta \Phi$ can be factored using the SVD to obtain the B_Δ and C_Δ matrices, assuming that the parameter values are contained in the diagonal Δ matrix.

$$\Phi^T K_\Delta \Phi = U \Sigma V^T = (U \Sigma^{1/2}) \cdot (\Sigma^{1/2} V^T) = B_\Delta \cdot C_\Delta \tag{4.26}$$

The final system in this case looks like

$$\begin{aligned} \ddot{\eta} &= -\Omega^2 \eta + \Phi^T \beta_u u + B_\Delta p \\ y &= C_d \eta + C_r \dot{\eta} \\ q &= C_\Delta q \end{aligned} \tag{4.27}$$

where C_d and C_r map the displacement and rate states to the system output y, and using LFT inputs p and outputs q, assuming feedback $p = \Delta q$. The entire system can be described using a single matrix equation.

$$\begin{Bmatrix} \dot{\eta} \\ \ddot{\eta} \\ y \\ q \end{Bmatrix} = \begin{bmatrix} 0 & I & 0 & 0 \\ -\Omega^2 & 0 & \Phi^T \beta_u & B_\Delta \\ C_d & C_r & 0 & 0 \\ C_\Delta & 0 & 0 & 0 \end{bmatrix} \begin{Bmatrix} \eta \\ \dot{\eta} \\ u \\ p \end{Bmatrix}$$

A similar approach is taken when the mass matrix is dependent upon the parameters. Equation 4.23 can be rewritten with only the M_Δ term retained (Φ assumed to be mass-normalized).

$$\ddot{\eta} = -\Phi^T K_o \Phi\ \eta + \Phi^T \beta_u u - \Phi^T M_\Delta \Phi\ \ddot{\eta} \tag{4.28}$$

In this case, the SVD is performed on the M_Δ matrix, $M_\Delta = B_\Delta C_\Delta$, which is substituted into Equation 4.28.

$$\ddot{\eta} = -\Phi^T K_o \Phi \eta + \Phi^T \beta_u u - \Phi^T B_\Delta \underbrace{C_\Delta \Phi \ddot{\eta}}_{p} \tag{4.29}$$

Acceleration feedback is required for the closed loop system, where the feedback relationship is still $p = \Delta q$.

$$\begin{aligned} q &= C_\Delta \Phi \ddot{\eta} \\ &= -C_\Delta \Phi \Phi^T K \Phi \eta + C_\Delta \Phi \Phi^T \beta_u u + C_\Delta \Phi \Phi^T B_\Delta p \\ &= -C_\Delta K \Phi \eta + C_\Delta \beta_u u + C_\Delta B_\Delta p \end{aligned}$$

The entire system in this case is described by:

$$\begin{Bmatrix} \dot{\eta} \\ \ddot{\eta} \\ y \\ q \end{Bmatrix} = \begin{bmatrix} 0 & I & 0 & 0 \\ -\Omega^2 & 0 & \Phi^T \beta_u & \Phi^T B_\Delta \\ C_d & C_r & 0 & 0 \\ -C_\Delta K \Phi & 0 & C_\Delta \beta_u & C_\Delta B_\Delta \end{bmatrix} \begin{Bmatrix} \eta \\ \dot{\eta} \\ u \\ p \end{Bmatrix}$$

An example of a parameter dependent system using the LFT is shown next.

4.2.2 LFT example using TPF-SCI

An example of the LFT as implemented in DOCS is shown using the TPF-Structurally Connected Interferometer model, described in Section 3.1.1. The ability of the LFT model to correctly capture the behavior of a parameter at off-nominal values is shown in Figure 4-3. The modulus of elasticity for bars supporting the secondary mirror is varied over 20% of its nominal value. The response from the LFT model is compared to re-evaluating the entire finite element model in Nastran using the new modulus value, and re-building the state-space model. The LFT-parameterized model tracks the off-nominal response, including peaks in the response caused by overlapping modes. An advantage to the LFT method

is the speed in evaluating off-nominal response; in tests, re-evaluating the FEM takes six times as long as evaluating the LFT.[2].

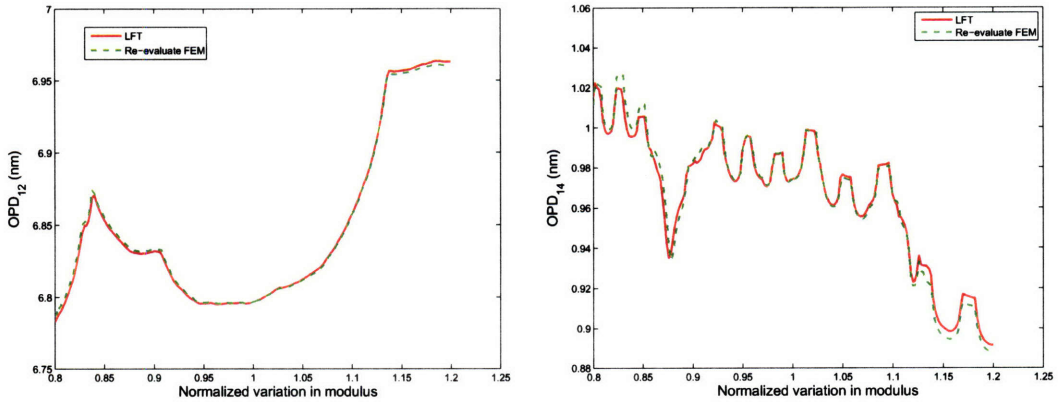

(a) OPD_{12} (b) OPD_{14}

Figure 4-3: Comparison of off-nominal results using the LFT versus re-evaluating the FEM

A trade study analysis for TPF-SCI is performed by varying the parameters listed in Table 4.2. The analyses are performed on a reduced order model of the system that includes attitude control, pseudo-optical control using high pass filters, and up to two stages of isolation on the disturbance inputs. The performance outputs are the optical pathlength difference between telescopes 1 and 2, OPD_{12}, as described in Equation 3.8. Instead of using the broadband reaction wheel model illustrated in Figure 3-11, the response is computed across the disturbance at individual wheel speeds, with wheel speeds given in hertz.

Table 4.2: TPF-SCI parameters varied using LFT

Parameter	**units**	**Values (nominal in bold)**			
RWA isolator corner frequency	Hz	2	6	**10**	
Bus isolator corner frequency	Hz	0.5	**1**	2	5
Optical control bandwidth	Hz	1	**10**	50	100
Modal damping	-	0.005%	**0.01%**	0.1%	1%
Normalized secondary telescope support strut modulus	-	0.8	**1.0**	1.2	

Isolator corner frequencies were examined first. Figure 4-4(a) shows the closed loop system with only the RWA isolator as its corner frequency is varied. Performance improves as the corner frequency decreases. For a isolator frequency of 10 Hz, only at wheel speeds

[2]Using a 2.53 GHz Pentium PC, solving for the RMS outputs using the LFT takes on average 25 seconds, versus 164 seconds for re-evaluating the FEM at new parameter values.

near zero would the performance requirement of 1 nm (drawn on each plot) be met. A 6 Hz corner frequency provides bands of wheel speeds that meet requirements, and those bands grow as the corner frequency drops to 2 Hz. Including a 1 Hz bus isolator along with the RWA isolator, as is shown in Figure 4-4(b), provides an even more dramatic improvement in the response. Except for low wheel speeds below 9.5 Hz the backbone of the response curve remains below the 1 nm line and only the response peaks exceed the requirement. There is an interesting development that at higher wheel speeds the isolator with the 6 Hz corner frequency is actually an improvement over the isolator with the 2 Hz corner frequency. This results from interactions between the two isolators. The response is larger when the peaks in the two isolator curves (seen in Figure 3-12) fall on top of each other. The 2 Hz RWA corner frequency is close to the 1 Hz bus corner frequency, and this excitation is starting to occur. The larger distance between the 1 Hz bus and 6 Hz RWA corner frequencies is shown to be more desirable. An optimum distance between the isolators could be found with this method.

Figure 4-4(c) shows the effect of changing the bus isolator's corner frequency about its nominal 1 Hz value, with the nominal 10 Hz RWA isolator in place. At lower wheel speeds the lowest frequency provides the least response. However, as wheel speed increases, the higher corner frequencies take turns at providing the lowest response. This behavior results from the zero in the isolator system (see the example in Figure 3-12) as it sweeps upward. In particular, at a corner frequency of 5 Hz, the zeros in both isolators combine to provide the very low response levels around 50 Hz wheel speed. This response shows another example of the interactions between the isolators, and suggests that the two stages of isolation should be designed together for maximum disturbance attenuation.

The modulus of the struts supporting the four telescopes is varied in Figure 4-4(d). These support struts should play an important role in transferring energy from the truss to the telescope assemblies, and it is assumed that their stiffness has an impact on the optical performances. At low frequencies the dynamics are dominated by global truss modes and the stiffness does not have as large an effect. At higher wheel speeds modeshape animations show the telescopes flexing on the truss, and at these frequencies there is the most change in response due to changing the stiffness. The results agree with logic, in that the excitation frequencies increase as the supports are stiffened, and decrease as the supports are softened. While not producing any overall decrease in the response, this could be used to shape the

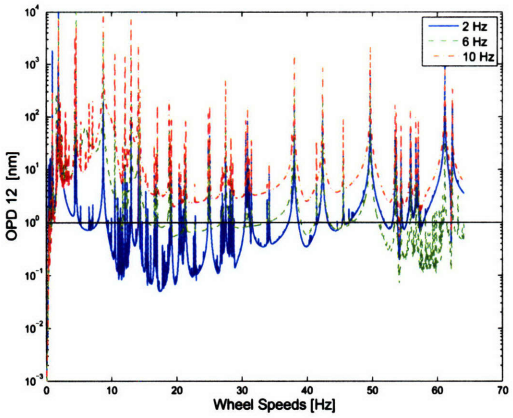

(a) RWA isolator corner frequency (no bus isolation)

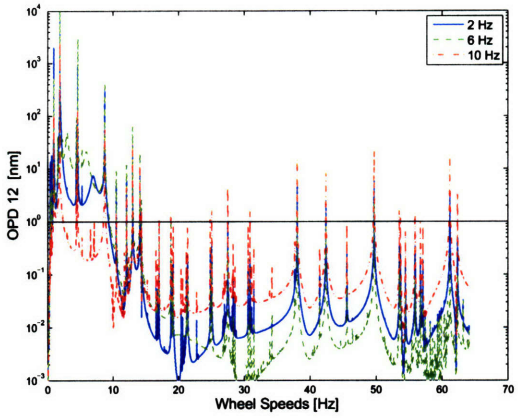

(b) RWA isolator corner frequency (includes bus isolation)

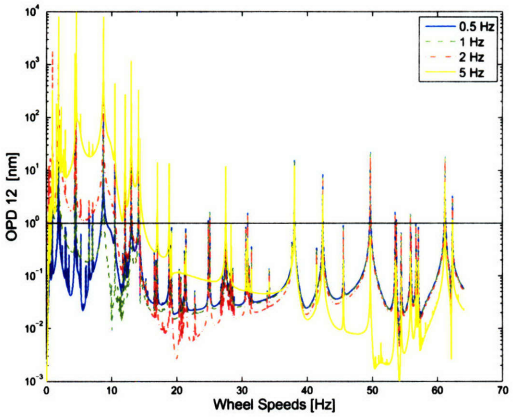

(c) bus isolator corner frequency

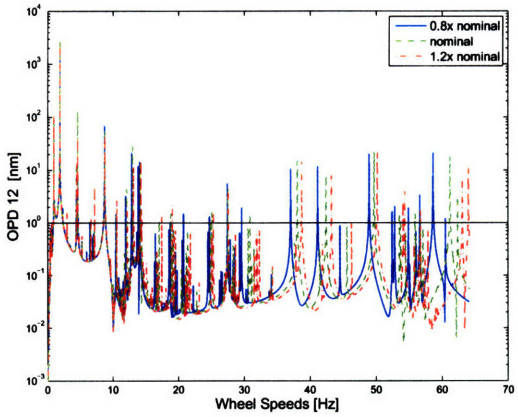

(d) modulus of the telescope support struts

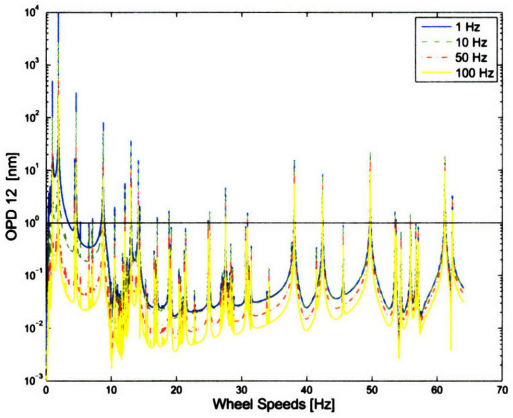

(e) optical control bandwidth

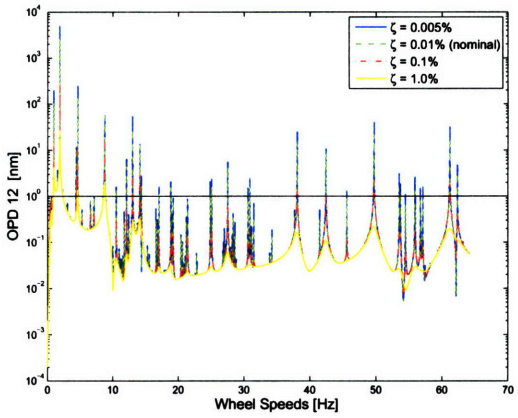

(f) modal damping

Figure 4-4: Variation in parameters for TPF-SCI, for OPD_{12}. Horizontal line on plots represents 1 nm requirement.

response about particular wheel speeds.

The effect of changing the optical control bandwidth is shown in Figure 4-4(e). Since the optical control is approximated using a filter, these results can not indicate any stability issues with a controller, or show any controls-structure interactions, but they do provide a sense of the performance improvement that could be possible as control bandwidth is increased. Since the largest disturbance contributor is the fundamental harmonic operating at the frequency of the wheel speed, once the wheel speed is greater than the control bandwidth the fundamental harmonic is not controlled and the dynamic response is not attenuated. Since wheel speeds may be as fast as 64 Hz (3850 RPM), control bandwidths of 1 Hz or 10 Hz do not affect most of the wheel speed range. A larger portion of the range is influenced by a controller operating at a 50 Hz bandwidth, and the response across all wheel speeds is improved with a 100 Hz controller. In all of these cases, the two stages of isolation have already reduced most of the response to below the requirements line, and the effect of control is to reduce the peaks caused by lightly damped modes.

Figure 4-4(f) shows the effect of different levels of modal damping. As expected, higher damping (0.1%) reduces the modal peaks, bringing many of the peaks below the requirement line. Even if these higher levels of damping are not expected on the spacecraft as a whole, one mitigation strategy would be to target extra damping on specific modes. If a particular mode could be identified as causing a large response, an investigation of the strain energy of that mode could suggest locations for additional damping.

These trade studies indicate that the interaction between the two isolation systems be used to maximize the attenuation by passive means. Targeted damping could help reduce the peaks of excited modes, while changing the stiffness of the telescope support struts could be used to change the frequency of modes at mid-range wheel speeds.

4.3 Design variable parametrization of finite element models

Evaluating alternative designs requires changing key design variables that define the very form and dimensions of a structure. A method of parameterizing the model to include such design variables is necessary in the proposed conceptual design methodology.

This section proposes an automated finite element modeling environment that inputs design variables, either continuous or discrete. The environment builds a complete finite

element model for each design vector, creates an integrated model, and analyzes the model for dynamic performance and system metrics such as mass or cost. Important aspects of the automated model are described, and an example model of the ground-based Thirty Meter Telescope (TMT) is shown.

4.3.1 Parametric modeling environment

The challenge in parameterizing conceptual models is that no aspect of the design is settled upon, and there are limitless options for new configurations. Conceptual spacecraft models vary based on physical geometries, aperture layouts and unique dimensions. Any combination of design variables may be considered during the earliest stages of design to meet the mission's scientific requirements. Parametrization of the model then entails not only the ability to change the values of any particular numerical input, as is done in the previous section, but also to change the basic structure of the spacecraft including locations of grid points and element connectivity.

The challenge is how to develop the software tools to create finite element input files (Nastran `.dat` files, for example) and state-space system realizations given an entire list of parameters that includes all of the design variables. Generation of variable grid points and elements is not difficult; for example, coordinate locations of grid points along a bar of variable length can be solved for knowing the location of the end points and the desired spacing between grids. The challenge is in creating an environment that allows many structural components to be built and then assembled into a complete model. The end-product must be a fully working parameterized model. The model must allow user flexibility so that changes to individual sub-models can be made, additions included, or new analyses performed without having to edit or change other parts of the model.

Simulating such a variable, complex system requires a model environment that clearly defines the relationships between spacecraft components. By separating the components into unique modules, the modeling task is easier since individual modules can be built by specialists and incorporated into the entire system once complete. The environment must also provide for growth by allowing the integration of future modules. The needs for individualized sub-models combined in a common framework suggest a modular, hierarchical model structure as illustrated in Figure 4-5.

Each box in Figure 4-5 represents a module that performs one function in the telescope

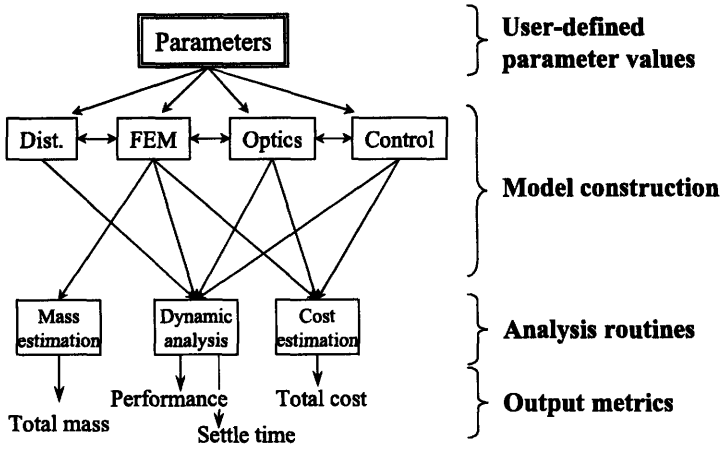

Figure 4-5: Schematic of modules which create and analyze a parameterized model

analysis. The modules may require inputs from each other, but are created independently and should be replaceable without the need to edit neighboring modules. The input/output relationship between the modules must be clearly defined. Table 4.3 provides an overview of the inputs and outputs for the modules illustrated in Figure 4-5.

The high-level modules shown in Figure 4-5 may themselves be comprised of lower-level modules that create individual model components. Figure 4-6 shows additional sub-modules within the finite element module. Each sub-module contributes one piece of the complete structure of a generic space telescope. The individual modules in Figure 4-6 will be described in greater detail in the next section.

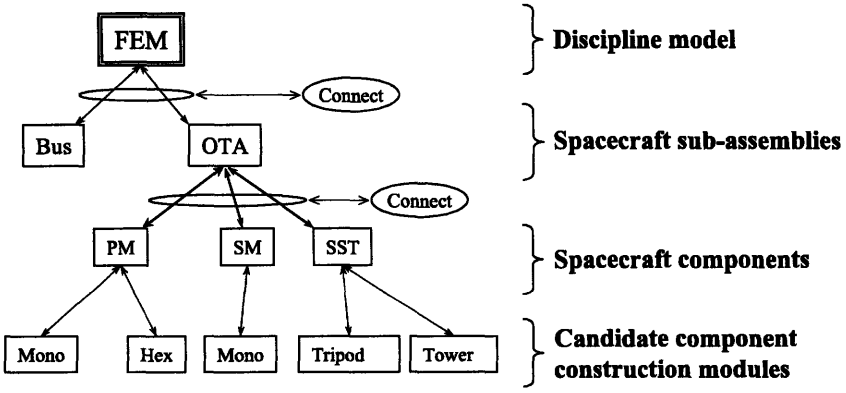

Figure 4-6: Schematic of modules creating the finite element model

Table 4.3: Example module inputs and output for the integrated system

Modules	Inputs	Outputs
Parameters	Values defined by designer	Necessary modules parameters
Model construction modules		
Disturbances	Wind parameters	Mass of RWA
	Reaction wheel parameters	Disturbance PSD curves
Finite element	Telescope form and geometry	Finite element bulk data
	Structural dimensions	I/O degrees of freedom
	Mirror curvatures	FE material and property cards
Optics	Optical parameters	Optical sensitivity matrices
	Mirror grid point locations	Mirror sizes
		# of optical instruments
Control	Control architecture	Controller model
	Gains and bandwidths	# of actuators and sensors
Model analysis modules		
Mass estimation	FE bulk data	FE total mass
Dynamic analysis	FE bulk data	State-space performance outputs
	I/O degrees of freedom	Transient settle time after a slew
	Disturbance PSD curves	Optics and controls models
Cost estimation	FE dimensions	Estimated telescope cost
	Necessary optical elements	
	Necessary control elements	

Maintaining a clear flow of information requires a hierarchy of the modules. All parametric variables are contained at the highest level of the model for easy access by the designer. The parameters are then passed down from the top levels to the lower-level models as required. The level of modularity described by Figure 4-5 must be defined at the start of the modeling process and changes depending on the complexity of the system under investigation. Whatever the size of the model however, the framework follows several basic rules to facilitate the integration and analysis of many unique realizations of the spacecraft. These rules are summarized.

Rule #1: Centralized parameter space

In order to provide the most flexibility for all users of the model, all model variables and constants should be kept in a central, high-level Parameter module as shown at the top of the hierarchy in Figure 4-5. By feeding all parameters and constants from the top of the hierarchy to lower levels, any variable can be accessed quickly without need to dig through layers of functions. This also allows the designer to easily change a constant to a variable, and vice versa.

The parameter space includes design variables, physical geometries, engineering parameters, finite element parameters and integrated modeling values. Examples of design variables include continuous variables such as optical focal ratios and discrete variables such as the type of aperture. Physical dimensions of the spacecraft that are defined directly (as opposed to those that are computed from design variables) may include the size of a spacecraft bus, depth of a mirror supporting truss, or even plate thicknesses and bar areas. Engineering parameters such as material properties or spring stiffnesses are stored. For finite element models, integers specifying grid and element ID numbers are kept as constants and passed to files that build the model. By allowing these ID numbers to be re-defined as the models grow, the framework guards against a lengthy search through layers of sub-models in case of overlapping ID numbers. Any other parameter associated with the integrated models are also included in the Parameters module, including modal damping values, controller bandwidths, and isolator corner frequencies. Ideally the designer would have access to every explicitly defined parameter or value in the entire model. Even if access to all parameters is not required during a conceptual trade space exploration, access to other parameters may be useful for future analysis with the model.

Rule #2: Structural component modules

The spacecraft structure follows the modular nature of the rest of the design so that distinct structural components can be combined to form unique realizations of the spacecraft. For each design, a basic structural architecture is assumed. For example, Figure 4-6 outlines a generic spacecraft that includes a bus for spacecraft operations and a separate optical telescope assembly (OTA) as the payload. The form of those components may be different to represent alternative architectures. Widely different primary mirror apertures such as

monolithic circular versus segmented mirrors may be included as separate modules that are invoked based on the design variable parameter settings.

Besides modeling a specific component, the modules may also represent primitive structures that are copied to create multiple spacecraft components. In Figure 4-6, for example, a function creating a monolithic circular mirror (`Mono`) can be used to create both the primary and secondary mirrors depending on the functional inputs.

Each component module is a stand-alone function that is modified or updated without the need to modify any other function. By isolating the individual components in this way, new component models are easily incorporated. A new mirror model, for example, can be attached onto the spacecraft with no modification of other modules, as long as the new module uses a consistent input-output format. The need for a consistent module I/O is the next rule.

Rule #3: Consistent module input/output

Supporting the modular format requires that an input-output format be specified and applied consistently across the entire model. Higher level functions pass appropriate parameters to lower-level functions using variable names set in the Parameters module. Similarly, each module that builds a structural component passes back information on important nodes or elements used as attachment points or as locations of force inputs and sensor outputs in the state-space model.

Ensuring that all of the necessary data is communicated between modules is the responsibility of the design team. At a minimum, each module must output all of the data needed by the rest of the system to assembly the model. For example, the integrated modeling module needs the mirror grid points from the finite element module to identify the performance output degrees of freedom. If different individuals are responsible for those areas, it is necessary that the interface needs are communicated early in the design. In anticipation of future additions to the model, it is prudent to output additional information that may be of use. For example, the module that creates a hexagonal mirror segment should output grid points along the side of the mirror that could be used to cantilever the segment to the rest of the structure, as well as gridpoints on the mirror's lower surface that would connect to bipods, assuming the mirror was supported from below. While only one option may be used initially, outputting all the data points allows changes in the connections to

be incorporated without going back into the mirror code.

Rule #4: Component connections

Since geometries of structural components are created individually in separate modules, additional modules are used to form all structural connections between components. For example, Figure 4-6 shows individual modules that build the primary mirror (PM), the secondary mirror (SM) and the secondary support tower (SST). All of these are called from a higher module that creates the OTA. The OTA modules calls a new function to perform the task of attaching the components. This connection function creates the attachments between the components, adding additional structural elements if required.

A challenge for the parameterized model is how to attach different components given the changes in structural form across model realizations. Since grid points may change across multiple structural realizations, the grid points at the proper joint locations must be re-computed for each run. Identification of connection grid points is performed in the component modules and the proper grid identification numbers must be passed to the connection function. The connection module inputs these data from the parts to be joined, aligns the points on either side of a joint and creates additional attachment elements as needed. The modeling of the joint is also a critical factor in capturing the proper dynamic behavior of the model. Rigid elements or springs are often used at this stage of design, to approximate the behavior of complex joints. By creating separate modules for these connections, it is easier to update the joints once higher fidelity representations are prepared.

4.3.2 Parametric auto-generated finite element models

Within the modeling environment the finite element models are generated automatically based on any given set of design variable inputs. This allows a large design space to be explored without user interaction, other than initially setting the design variables to examine. Creating a finite element model that can be generated from parameter inputs requires effort on the part of the designers to compute grid point locations and element connectivity based on defined geometries.

An example of automated finite element modeling is shown with the Thirty Meter Telescope (TMT). Four finite element realizations of TMT are shown in Figure 4-7 with details for each architecture given in Table 4.4. The basic architecture is a segmented

mirror with tripod secondary support tower (SST). Spring elements at two elevation axis grid points connect the telescope structure to the ground. Unique structural realizations are created by varying design variables such as focal length of the primary mirror (PM) and height of the elevation axis. Key steps in the creation of the automatic finite element model are described, including definition of the basic geometries of the structural components, setting property and material parameters, and defining non-structural masses. A complete analysis of the TMT design is presented at the end of this chapter.

Table 4.4: Design variables for TMT structures in Figure 4-7

	Example A	**Example B**	**Example C**	**Example D**
Primary mirror focal ratio	1	0.8	0.8	1.5
Final focal ratio	-15	+22	-15	-22
Segment radius [m]	0.5	0.5	0.5	0.665
Elevation axis location [m]	+3.5	-2.2	+3.5	-2.2
Total mass [kg]	817,800	918,490	872,420	1,043,200

All of the modeling in this work is performed in MATLAB, meaning that the relations between design variables and telescope dimensions are defined in MATLAB functions (m-files), along with the code that computes grid point locations and element connectivity. Alternate tools have been described in the literature to parameterize a model, including parametric CAD programs [29] and PATRAN session files that directly interface with the Nastran input decks [31]. Since the goal of the spacecraft analysis in this work is to perform dynamic analysis of integrated models, it is easiest to combine the finite element geometry creation with the MATLAB tools already developed for dynamic analysis. Note however that this approach to automatic finite element generation and analysis is not dependent on any particular software package, and the rules of the modeling environment can be applied across applications.

Finite element model creation

Parameterizing finite element models requires that all grid points, elements, element properties and materials be generated anew with each design iteration. Individual structural modules in Figure 4-6 receive dimensional information that is used to determine the locations for structural grid points. Once the grid points are located the correct element connectivity must be created. Since the dimensional information is dependent upon the

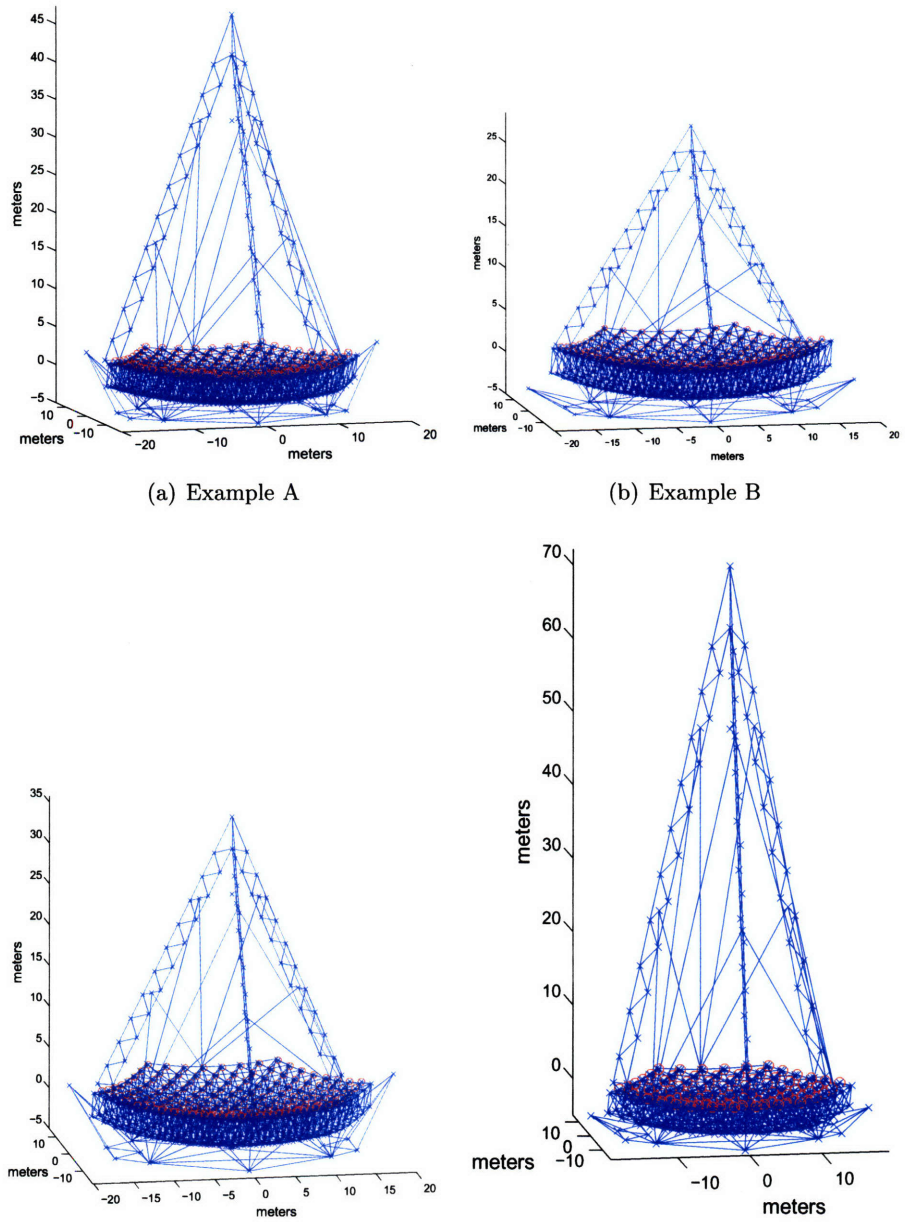

(a) Example A

(b) Example B

(c) Example C

(d) Example D

Figure 4-7: Example structural realizations of the Thirty Meter Telescope

high-level design variables, changing those variables results in new grid point locations and element connections. Following is a description of each module in Figure 4-6. Key inputs and outputs for each module are listed, along with an overview of the processing that occurs.

- **FEM**
  - **Purpose:** High-level finite element creation module that interacts with the rest of the integrated model, as illustrated in Figure 4-5
  - **Inputs:** Design variables defining the type of telescope, dimensions of the telescope, parameters describing the optics (i.e. shape of the mirror surfaces)
  - **Outputs:** The complete finite element bulk data file, along with details on degrees of freedom for the force inputs and sensor outputs.
  - **Process:** Assembles necessary parameters for each sub-module. Calls each sub-module and runs connection code to assemble the entire FEM.
- **OTA**
  - **Purpose:** Build the optical telescope assembly
  - **Inputs:** Telescope type, SST type. Diameter and curvature of primary and secondary mirrors. Height and width of SST. Desired mesh density of all components.
  - **Outputs:** Bulk data defining the OTA and identification numbers of key grid points and degrees of freedom across the OTA.
  - **Process:** Assembles necessary parameters for each sub-module. Calls each sub-module and runs connection code to assemble the OTA components.
- **Bus**
  - **Purpose:** Build the spacecraft bus, which contain all non-optical instruments needed to sustain the mission (computers, attitude sensors, reaction wheels, power systems, etc.)
  - **Inputs:** OTA dimensions.
  - **Outputs:** Bulk data defining the bus elements and identification numbers of key grid points and degrees of freedom across the bus.

- **Process:** The bus is sized to match the dimensions of the OTA. A single basic architecture is used, but based on the size of the OTA the grid point locations and element connectivity for bar or beam elements are re-evaluated. Grid points and elements are numbered sequentially, given an initial grid point and element ID number. Property ID card numbers are associated with the relevant element cards. Critical grid points are identified across the bus that may be used by other modules. These grid points include attachment points to the OTA. Concentrated masses representing spacecraft instruments are placed across the bus structure.

- **PM**

  - **Purpose:** Build the primary mirror by calling the appropriate construction module.
  - **Inputs:** Type of aperture desired, dimensions and mesh densities for the PM
  - **Outputs:** PM bulk data and identification numbers of key grid points and degrees of freedom across the PM.
  - **Process:** Based on which type of primary mirror aperture is desired, calls the necessary construction module. If a segmented system is desired, will call the same construction modules multiple times to build up the necessary number of mirror segments. For example, to build a segmented aperture of hexagonal mirrors, the module will define a unique coordinate system for each mirror segment, determine where the segments are placed, and call the same 'Hex' module multiple times to build the requisite bulk data entries for each segment.

- **SM**

  - **Purpose:** Build the secondary mirror by calling the appropriate construction module.
  - **Inputs:** Dimensions and mesh densities for the SM
  - **Outputs:** SM bulk data and identification numbers of key grid points and degrees of freedom across the SM.
  - **Process:** Based on which type of secondary mirror is desired, calls the necessary mirror module. Since the individual mirror modules input the mirror dimensions,

the same module could be used to build the SM bulk data as is used to build the PM bulk data; the only difference would be the dimensions of the mirror, optical shape and (perhaps) mesh density.

- **SST**
  - **Purpose:** Build the secondary support tower by calling the appropriate construction module.
  - **Inputs:** Type of SST desired, dimensions and mesh densities for the SST
  - **Outputs:** SST bulk data and identification numbers of key grid points and degrees of freedom across the SST.
  - **Process:** Based on which type of secondary support tower is desired, calls the necessary construction module.
- **Mono** or **Hex**
  - **Purpose:** Build a single mirror element. May be a primary or secondary mirror, depending on input dimensions.
  - **Inputs:** Starting GRID ID numbers to use for PM grid points. Coordinate system ID number. Materials and property ID numbers to use for PM or SM elements. Dimensions of the mirror including diameter and thickness. Optical shape of the mirror. Mesh density of the mirror plate element.
  - **Outputs:** Bulk data for a single mirror segment, including grid points and elements, and identification numbers of key grid points and degrees of freedom across the mirror segment.
  - **Process:** Place x- and y-coordinates across the mirror surface based on dimensions. The mesh density determines the number of grid points to use per unit area. The optical shape defines the z-coordinates of the grid points. The shape may be of an on-axis or off-axis mirror, depending on the optical inputs. Algorithms within the module determine how the grid points are connected by plate elements, and create the appropriate plate elements across the mirror surface. Grid points and elements are numbered sequentially, given an initial grid point and element ID number. Property ID card numbers are associated with

the relevant element cards. Critical grid points are identified across the mirror that may be used by other modules. These grid points could include attachment points or locations across the mirror surface that will be used to measure optical performance.

- **Tripod** or **Tower**
  - **Purpose:** Build the secondary support tower on which the secondary mirror is attached.
  - **Inputs:** Starting GRID ID numbers to use for SST grid points. Materials and property ID numbers to use for SST elements. Dimensions of the tower including height and width. Mesh density of the tower bar element.
  - **Outputs:** Bulk data for the SST including grid points and elements, and identification numbers of key grid points and degrees of freedom across the tower legs.
  - **Process:** Each module defines a unique SST architecture, but all must connect to the same OTA and support a secondary mirror. Unique designs include the tripod (as used to support the secondary mirrors on all of the TPF designs, for example), or a tower such as is used by the Hubble Space Telescope. In each case, the tower is comprised of bar elements. Grid points are laid out based on the width of the tower, and rise to the desired height of the SM. The mesh density determines the number of grid points to use per unit length. Algorithms within the module determine how the grid points are connected by bar or beam elements, and create the appropriate finite elements. Grid points and elements are numbered sequentially, given an initial grid point and element ID number. Property ID card numbers are associated with the relevant element cards. Critical grid points across the SST are identified that may be used by other modules. These include attachment points for the SM, and attachment points to the OTA.
- **Connect**
  - **Purpose:** Attach components together and assemble the structure.
  - **Inputs:** Attachment grid points on either side of an interface.

- **Outputs:** Bulk data for the connection elements.
- **Process:** Different connection modules are used to attach modules to each other. For example, a 'bipod' module receives information on which grid points on the lower surface of a mirror (or ring connecting mirror segments) should be attached to the optics bench using bipods. The connection module checks the alignment between components and creates elements between the attachment grid points. The actual bipods may be defined as bar or beam elements, or the connection may be simplified as a rigid element. Other connections are made between the secondary mirror and the SST, between the SST and the OTA, and between the OTA and the bus.

An example of the component construction process is shown with the Thirty Meter Telescope. A key dimension is the distance between the primary mirror and secondary mirror. For a Cassegrain telescopes [71], this distance is defined using a combination of optical parameters.

$$d = \frac{M \cdot f_1 - b}{M + 1} \tag{4.30}$$

where M is the ratio of final focal length to the primary mirror focal length f_1, and b is the eye relief, or the distance of the detector below the primary mirror. Once the distance d between the mirrors is defined, additional structures such as the tripod to support the secondary mirror are created. A change in any of the optical design variables affects the telescope height. For instance, increasing the primary mirror focal ratio increases the focal length f_1, thereby lengthening the distance between the mirrors. The effect on height is obvious in Figure 4-7(d), which shows a tall TMT realization with the largest focal ratio of the four examples.

Similarly, the size of the truss elements supporting the primary mirror of TMT can be defined in terms of the number of segments. For the design created, sub-assemblies of seven mirror segments are considered to be connected together as part of a raft assembly. These rafts are then placed on top of hexapod cells that made up the truss (also referred to as the 'backstructure'), as shown in Figure 4-8. Four rafts of seven segments (raft segments grouped by color) are shown on top of the upper triangular layer of the backstructure, where each triangle is the top of a hexapod. Using simple geometry one can calculate that the

sides of the triangle are each $\sqrt{21}$ times the segment radius. With this information, the vertices of the triangle can be defined in a global coordinate space and grid points placed at the appropriate x and y positions. The z-position for each raft is determined based on the curvature of the mirror.

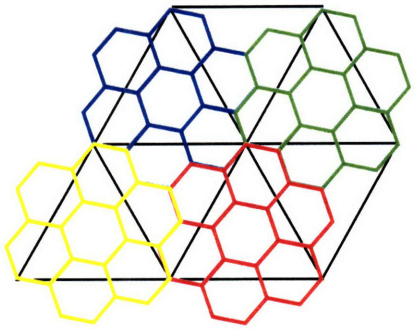

Figure 4-8: Illustration of seven-segment mirror rafts above triangular truss cells

As segment size changes, not only do the truss cells change dimensions, but fewer or more rafts may be needed to fill the entire primary mirror. The effect of varying the segment size is shown in Figure 4-9 with segment diameters of 0.5 meters and 1 meter. Each circle represents the concentrated mass for a single seven-segment mirror raft. The top layer of the truss backstructure supporting the primary mirror rafts is also illustrated as a series of triangular cells, each of which lie beneath the raft. Note that attachments between the backstructure and rafts are not yet included in the figure. The proper number of rafts and the complete truss structure are generated automatically based on the segment size. The number of grid points across the primary mirror and backstructure, as well as the number of bar elements in the truss structure are variable. As raft diameter decreases and more rafts are needed to fill the 30 meter aperture, a denser truss structure is generated beneath the mirror. This same approach to truss density is also used to increase element mesh fidelity for a structure. Mesh fidelity across mirror surfaces or along secondary support towers beams is variable, and the requisite number of grid points and elements are automatically created for a desired finite element mesh. Mesh density becomes then another parameter available to the designer and passed to each function.

Figure 4-10 shows the progression of the TMT model. Once the raft positions in x, y and z coordinates are laid out (Figure 4-10(a)) the top layer of the backstructure is generated (Figure 4-10(b)), followed by the bottom layer and bars connecting the two (Figure 4-10(c)).

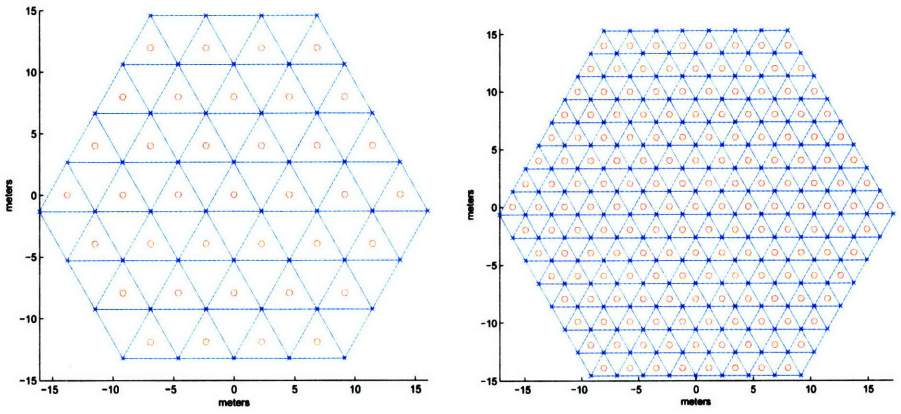

(a) 0.5 meter segment diameter (b) 1 meter segment diameter

Figure 4-9: Effect of changing segment size on number of rafts (represented by circles) and top layer of backstructure truss (triangles)

A separate lattice structure is built to further support the backstructure, and to connect it to the elevation axis (Figure 4-11). The number of gridpoints and elements is determined largely by the segment size, with the grid point locations dependent upon the diameter of the mirror, curvature of the surface and thickness of the backstructure truss. Additional components, such as the secondary support tower, secondary mirror and stabilizing wires are shown in Figure 4-7.

Important component connections include the primary mirror rafts to the backstructure, the secondary mirror to the SST, and the entire OTA to the ground support structure (or from the OTA to a spacecraft bus, in the case of a spaceborne telescope). The raft-backstructure interface for TMT consists of stiff 100Hz springs in the vertical direction, to represent the dynamics of that connection point. For space telescopes which have no need of a heavy backstructure for gravity support, the mirrors may be connected to the telescope assembly using bipods, represented either as bars or as rigid elements. The SM-SST interface is engineered to reduce torsion of the secondary mirror about the tripod, and bar elements are used to support the mirror.

Engineering parameters

Besides the grid points and element connections, a finite element model also must define engineering parameters such as element properties and material constants. Element properties include cross sectional areas and area moments of inertia for bars or plate thicknesses.

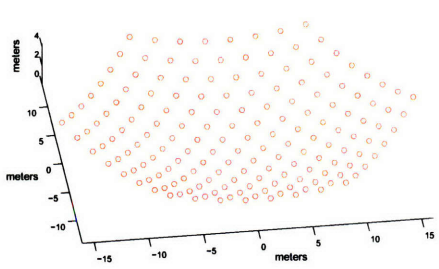

(a) Raft centers of gravity

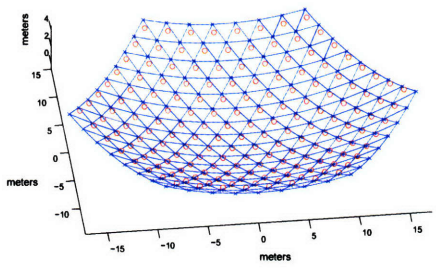

(b) Upper layer of backstructure added

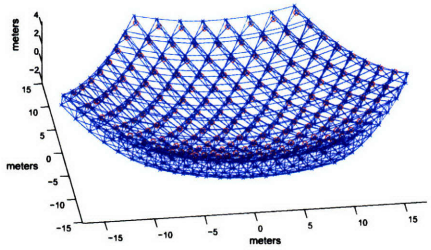

(c) Lower and middle layers of backstructure added

Figure 4-10: Stages of model generation: TMT rafts and backstructure

Material properties include Young's moduli, Poisson's ratio and material density. These constants are kept in the top-level Parameters module so any changes can be immediately reflected by re-running the model.

The material and element property cards are prepared in the high-level finite element module and are associated with elements using identification numbers. To avoid storing absolute numbers within the individual modules, even the property ID numbers are assigned in the Parameters module and passed to lower modules for inclusion in the element cards.

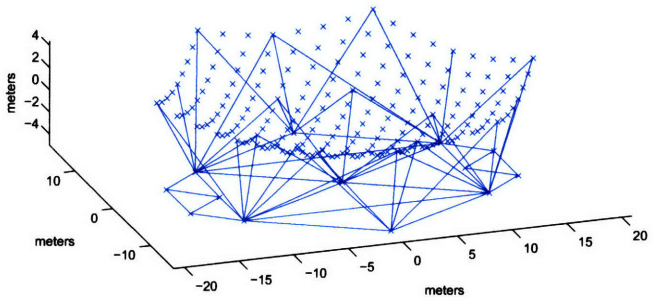

Figure 4-11: Lattice supporting the TMT backstructure

Mass estimation

In the conceptual design of spacecraft systems, mass is often an indicator of total cost due to the expense of launch systems, and is generally one of the key outputs at the start of the modeling process. Mass is included in finite element models both through the total volumes of elements times the material density, as well as by including concentrated masses for non-structural components. Masses associated with spacecraft subsystems such as power, propulsion or communications may be based on historical databases [91]. The mass of the reaction wheel assembly is determined based on the control authority required. In Section 4.4.1 a separate analysis is performed to determine the necessary slew torque profile, flywheel inertias and resulting RWA mass for a parameterized spacecraft. Given the mass values for these subsystems components, concentrated mass elements can be placed across the finite element model based on the locations of these subsystems in the bus. Mass associated with optical element such as beam combiners or fold mirrors may be placed on the optical bench at the location of those elements in the optical train.

For the ground-based system, counterweights are needed to balance the telescope about its elevation axis. In the case of TMT, the counterweight center of gravity is assumed to be 13 meters below the elevation axis if the axis is below the primary mirror. If the elevation axis is above the primary mirror, the counterweight is assumed to be at the center of gravity of the secondary support tower. Using either of these moment arms and knowing the mass of the telescope and the distance of its center of gravity from the elevation axis, the necessary counterweight mass can be computed by balancing the moments due to gravity on either side of the elevation axis. Since the TMT model lacks a counterweight structure, the counterweight mass is not included in the finite element model. The total TMT mass is the sum of the FEM and counterweight masses.

4.3.3 Structural model validation

Once the parametric finite element model is constructed, it is important that the model be optimized and validated against existing designs. While the goal of the conceptual modeling methodology is to investigate design points outside of those that currently exist, comparison to several existing point designs provides confidence in the modeling environment. This validation step indicates whether the environment is constructing realistic structures in terms

of mass, stiffness and dynamic behavior. It also is necessary to verify the computational process that assembles the model, and to ensure that no mathematical mistakes have been made. Since the goal of the conceptual design methodology is to indicate which designs are superior relative to others, optimization at this stage is not meant to achieve absolute performance results. Rather optimization of the design ensures that the basic structural realizations meet expected metrics. For example, lowest spacecraft fundamental frequencies should be near commonly accepted values that provide sufficient stiffness for launch loads.

Validation is possible if structural realizations of the parameterized model match either existing telescopes or higher fidelity point-design models. In this case, with the design variables set so that the parameterized model resembles the "truth" structure, structural behavior or dynamic outputs are compared. The parameterized model should capture correct behavior of at least one truth model for validation of the model output. If validation can be performed against several point designs, the ability of the parameterized model to track changes across architectures can also be checked.

In the case of TMT, a higher fidelity model had already been created for an earlier point design. This model, termed the GSMT Strawman, is shown in Figure 4-12. The Giant Segmented Mirror Telescope (GSMT) was a precursor design to the TMT. MIT's TMT model is compared to Strawman to validate basic metrics such as mass and displacement under gravity. The parameterized model design variables are set to the same values as for the Strawman point design, and the mass is computed. Table 4.5 shows the results for the cases of the elevation axis below the primary mirror (as with Strawman) and the elevation axis above the mirror. Mirror raft masses are similar between Strawman and MIT. The total telescope masses are all of similar orders of magnitude, with the Strawman mass between the two MIT examples. Note that the MIT model with elevation axis above the primary mirror has the least mass of the three designs. In this case less additional counterweight mass is required to balance the telescope, since the elevation axis is between the primary mirror and secondary mirror tower which act to balance each other. The MIT model with elevation axis below the primary mirror (the same as Strawman) is heavier than the Strawman. This is likely due to the lack of mass optimization for the MIT model.

The parameterized model is further validated by comparing the deflections of the primary mirror in the presence of gravity. Figure 4-13(a) shows the deflections of the grid points (normalized to the center grid point) across the Strawman aperture, and Figure 4-

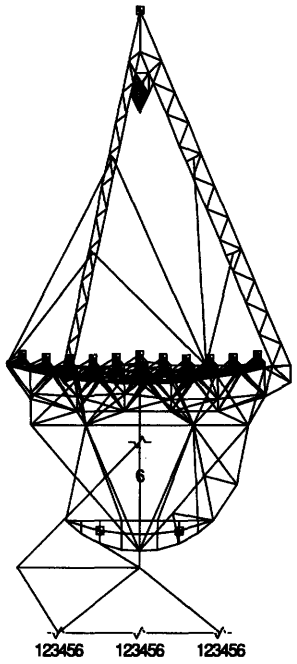

Figure 4-12: FE model of the Giant Segmented Mirror Telescope (GSMT) Strawman design, provided by the NOAO.

Table 4.5: Mass comparison between MIT and GSMT Strawman design

	Strawman	**MIT** Axis below PM	**MIT** Axis above PM
Raft mass	1581 kg	1,705 kg	1,705 kg
Mass on elevation axis	700,000 kg	877,880 kg	623,940 kg

13(b) shows a similar plot for MIT's TMT. The Strawman mirror displaces approximately ± 1300 μm, while this sample realization of MIT's model displaces approximately -1900 μm to +2650 μm. The poorer performance from the MIT model results from a lack of optimization, both of the truss bar properties but also of the truss layout. For similar stiffness across the mirror, the areal density of the truss is larger for MIT's model than it is in Strawman. In the plots of Figure 4-13 this is partially compensated for by changing the density of the bar material so that the truss areal densities are more in-line with each other.

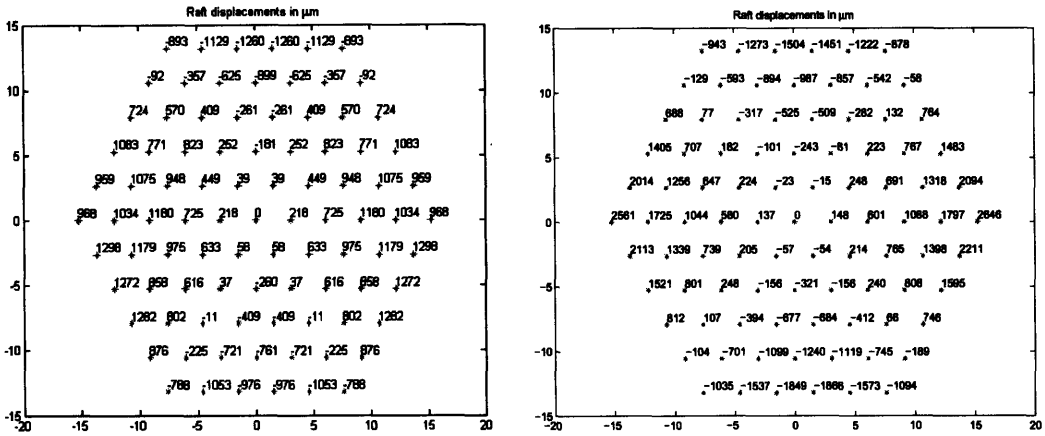

(a) GSMT Strawman (b) MIT's TMT

Figure 4-13: Deflections of the raft nodes in microns across the primary mirrors due to gravity

4.4 Parametrization of integrated model components

Other models of the dynamic system are also parameterized along with the finite element model. This section describes the parametrization of both the reaction wheel size and the resulting RWA disturbances, based on slew/settle requirements and spacecraft inertia.

4.4.1 Reaction wheel sizing

System metrics such as settle time after a slew maneuver are also used to evaluate the designs. Science observations cannot be made until the transient dynamics resulting from the slew damp out. A longer settle time reduces the time available to the telescope to take science images, and thus reduces the scientific return that can be collected over its lifetime. Since the slew requirements factor into the sizing of the reaction wheels, a separate module is used to size the reaction wheels' inertia and resulting disturbance amplitudes, and to determine the settle time after a slew maneuver.

The slew requirements are set in terms of the length of time it takes for the telescope to slew a number of degrees. The requirements can be changed in the Parameters module, so that different slew requirements can be compared based on the total time for both slew and settle. Figure 4-14(a) shows an example maneuver of a spacecraft slewing five degrees over 180 seconds. Angular rates and accelerations of the spacecraft rigid body are included. A bang-bang torque command is assumed, shown in Figure 4-14(b). Other torque input

profiles that avoid the sharp rise and fall of the bang-bang may be preferable in practice.

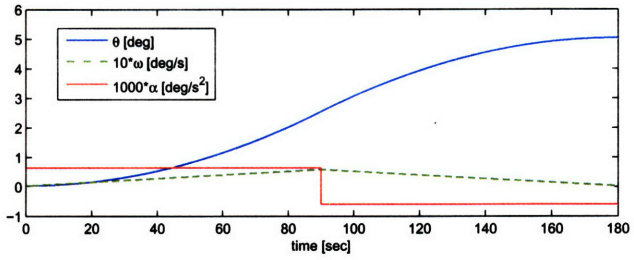

(a) Slew angle, angular rate and acceleration

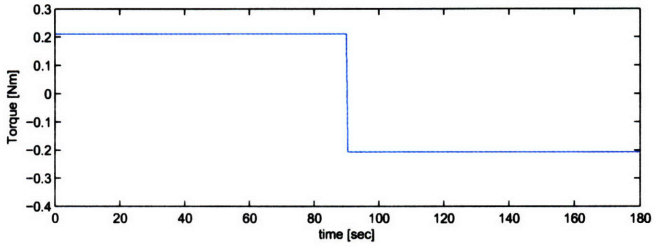

(b) Slew torque profile

Figure 4-14: Slew angle and torque profiles

Once the torque profile is decided upon, the actual magnitudes are set so that rotation about the axis with the largest principal moment of inertia meets the slew requirement. Since the moments of inertia change with every regeneration of the finite element model, the necessary torque requirement will change with every new structural realization. Settle time is computed by running a time simulation of the integrated model using the assumed torque profile. The simulation runs until the response envelope of the optical performance falls beneath a set threshold.

Once the torque requirements about the global spacecraft axes are determined, the reaction wheels must be sized so that the sum of the individual wheel torques matches the required spacecraft torque. A single wheel produces a moment ${}^{w}\tau_z$ about its rotational axis where ${}^{w}(\cdot)$ represents a vector in the frame of the reaction wheel. The moment can be divided into components T_x, T_y and T_z along the spacecraft axes using the Euler angles describing the orientation of the wheel in the spacecraft frame (denoted by ${}^{s/c}(\cdot)$).

$$
{}^{s/c}\begin{Bmatrix} T_x \\ T_y \\ T_z \end{Bmatrix} = \begin{Bmatrix} \cos\beta\sin\theta\cos\gamma + \sin\beta\sin\gamma \\ \sin\beta\sin\theta\cos\gamma - \cos\beta\sin\gamma \\ \cos\theta\cos\gamma \end{Bmatrix} {}^{w}\tau_z \tag{4.31}
$$

The angles of rotation are β about the original z-axis in the spacecraft frame, followed by θ about the new y-axis and γ about the new x-axis. The component transformation vectors for all n_{wheels} are collected into a matrix R to sum the torques from the entire assembly

$$\overset{s/c}{\begin{Bmatrix} T_x \\ T_y \\ T_z \end{Bmatrix}} = \begin{bmatrix} R_1 & R_2 & \cdots & R_n \end{bmatrix} \begin{Bmatrix} {}^{w}\tau_{z_1} \\ {}^{w}\tau_{z_2} \\ \vdots \\ {}^{w}\tau_{z_n} \end{Bmatrix} \tag{4.32}$$

where ${}^{w}\tau_{z_i}$ represents the torque produced by the i^{th} wheel. The spacecraft torques, T_x, T_y and T_z, are the totals resulting from the entire reaction wheel assembly. The actual allocation of wheel torques ${}^{w}\tau_{z_i}$ across the n_{wheels} depends on the slewing maneuver, and may be complicated further by the need to avoid identified "noisy" wheel speeds, or to ensure that any single wheel does not saturate. In this case, to determine required wheel size, the wheel torques are calculated for the simple torque maneuver about a single axis (T_x in this example). Torques about the other axes are set to zero.[3]

$$\overset{s/c}{\begin{Bmatrix} T_x \\ 0 \\ 0 \end{Bmatrix}} = \begin{bmatrix} \cdots & R_x & \cdots \\ \cdots & R_y & \cdots \\ \cdots & R_z & \cdots \end{bmatrix} \begin{Bmatrix} {}^{w}\tau_{z_1} \\ {}^{w}\tau_{z_2} \\ \vdots \\ {}^{w}\tau_{z_n} \end{Bmatrix} \tag{4.33}$$

The matrix R is re-written as row vectors. Solutions to Equation 4.33 are found by solving for the nullspace of the rows of $\tilde{R}$, defined by.

$$\tilde{R} = \begin{bmatrix} \cdots & R_y & \cdots \\ \cdots & R_z & \cdots \end{bmatrix}. \tag{4.34}$$

A minimum of three wheels are required for attitude control of the three spacecraft axes, and most often four or more wheels are used in practice to provide redundancy. The matrix R is then $3 \times n_{wheels}$, with more columns than rows, and $\tilde{R}$ is $2 \times n_{wheels}$. Assuming that no wheels are aligned exactly together, the rank of $\tilde{R}$ should be two (the number of rows), and there are exactly $(n_{wheels} - 2)$ orthogonal nullspace basis vectors [93] that represent separate distributions of torque to the individual wheels. Each of these vectors can be scaled so that

[3]Refer to [92] for a more rigorous method of distributing spacecraft torques amongst the wheels.

the final torque magnitude about the rotation axis matches the required spacecraft torque, T_x in Equation 4.33. For the total spacecraft torque requirement shown in Figure 4-14(b), example wheel torque distributions using five reaction wheels are shown in Figure 4-15. In this case, there are three possible options for distributing the total torque about the wheels, based on three nullspace vectors.

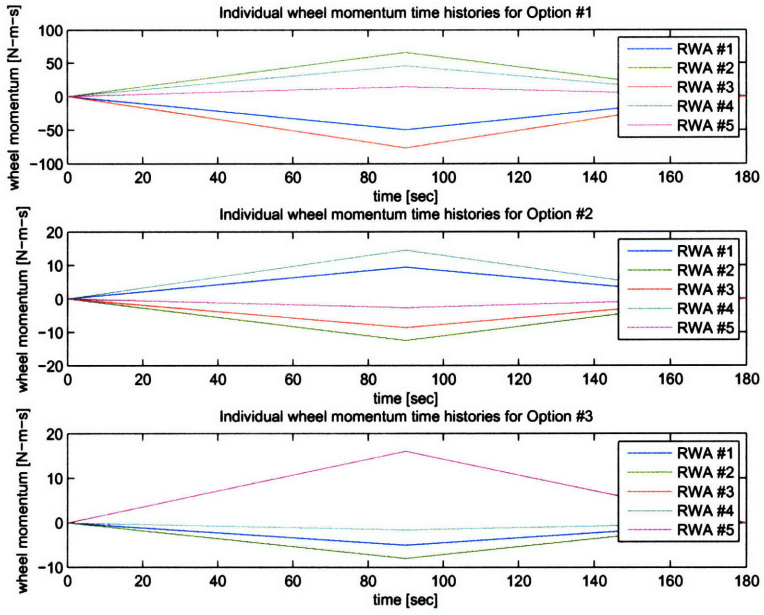

Figure 4-15: Options for distributing total torque amongst five reaction wheels

For a conservative estimate of wheel size, the maximum torque across the n_{wheels} is selected. The physical wheel size and the magnitude of the disturbances are related to the inertia J of the flywheel, related to torque through

$$\tau_z = J\dot{\omega} \tag{4.35}$$

given a wheel acceleration $\dot{\omega}$. In the case of the bang-bang torque profile, the inertia J is solved for directly given the slew time t_{slew} and a maximum permissable wheel speed ω_{max}.

$$J = \frac{\tau_{z_{max}}}{\omega_{max}} \cdot \frac{t_{slew}}{2} \tag{4.36}$$

Once the flywheel inertia J is found for a given design, the wheel mass is approximated using a database of flywheels [4] to compute curvefits of mass to flywheel inertia (Figure 4-16(a)).

[4] Collected by members of the ARGOS team in the MIT SSL

Finally, the wheel mass is fed back into the FEM as a concentrated mass representing the RWA.

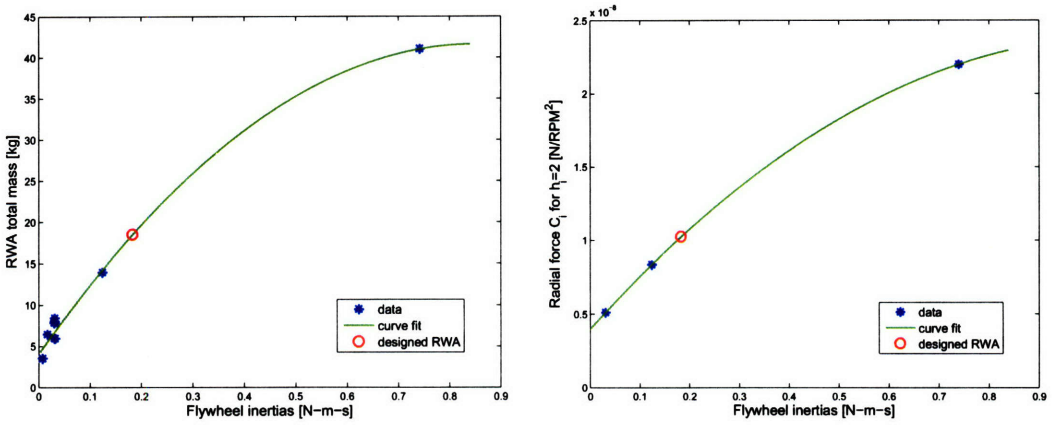

(a) Mass versus inertia

(b) Harmonic amplitude versus inertia

Figure 4-16: Curvefits of reaction wheel properties with flywheel inertia, with a sample design point circled

4.4.2 Disturbance inputs

The disturbance model is based on a harmonic representation of the reaction wheel disturbances described in [77]. An example of the amplitude coefficients and harmonic numbers for an unbalanced Ithaco E-wheel is shown in Figure 3-10. Given a structure of the harmonics (harmonic numbers and relative sizes of the amplitude coefficients), actual amplitudes can be scaled based on the size of the wheels. This scaling allows the disturbance inputs to vary with the design parameters. There is a tradeoff between large wheels allowing fast slews but with more disturbance energy, and smaller wheels with slower slews but with less disturbance energy.

The scaling of the force and torque amplitudes is determined from a curvefit shown in Figure 4-16(b). The curvefit is between the flywheel inertia and the radial force coefficient of the second harmonic, and is based off of three complete wheel models (including harmonics and amplitude coefficients) described in [78]. The second harmonic was chosen in place of the first, fundamental harmonic because of the three wheels one was balanced. Balancing reduces the amplitude of the fundamental harmonic but not of higher harmonics. This method of scaling, while approximate in nature, allows changes in the slewing requirements and mass of the telescope to be reflected in the vibrational disturbances. As the telescope

grows larger, or as slewing requirements increase, there is a corresponding increase in the inertia of the RWA flywheels. As the inertia increases, Figure 4-16(b) is used to scale the disturbance amplitudes, which results in larger disturbances exciting the system.

4.5 Trade study example: the Thirty Meter Telescope

The framework for parametrization of finite element and integrated models is applied to analyze alternate designs for the Thirty Meter Telescope. The model, several of whose structural realizations are shown in Figure 4-7, is created by a team in the MIT SSL [5] following the rules described in this chapter. This section provides a description of the model and analysis results.

4.5.1 TMT model

The basic architecture under investigation for the TMT is shown in Figure 4-7. The primary mirror (PM) diameter is thirty mirrors filled with hexagonal mirror segments. The diameter of each mirror segment is a design variable (1 meter for all analyses shown here), and every seven segments lie on a raft. The secondary mirror is at the apex of a tripod secondary support tower (SST). The entire telescope can rotate on an elevation axis which may be above or below the PM. Given this basic architecture, there are still design variables that must be chosen very early in the design process. These include:

- Telescope type
- Location of elevation axis
- Primary mirror focal ratio (f-number)
- Telescope final focal ratio (FFR)
- Optical controller bandwidth

The telescope type could be either Cassegrain or Gregorian. For Cassegrain telescopes a convex secondary mirror lies ahead of the focal point of the primary mirror, and for Gregorian telescopes a concave secondary mirror lies beyond the PM's focal point. For the

[5]Team members included Deborah Howell, Soon-Jo Chung, Julien Lamamy, with support from TMT engineers at the National Optical Astronomy Observatory (NOAO)

analysis the difference is determined through the sign of the final focal ratio (FFR), where Cassegrains are set by a positive FFR and Gregorians by a negative FFR [71]. The value for the PM focal ratio and absolute value of the final focal ratio are additional design variables, as is the location of the elevation axis, above or below the PM, shown in Figure 4-17. The final design variable is the control bandwidth for the closed loop control of the mirror surface.

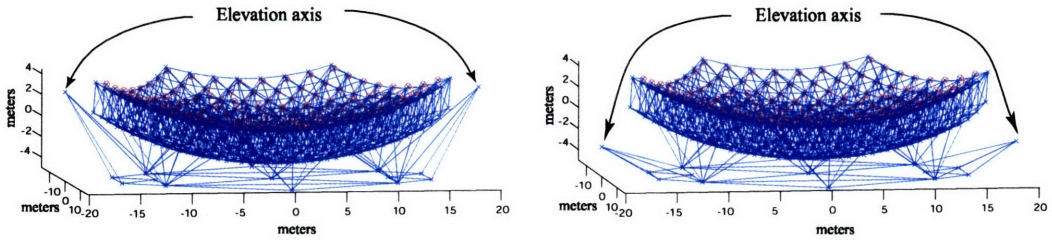

(a) +3.5m above PM

(b) -2.2m below PM

Figure 4-17: TMT elevation axis locations

All of the design variables are related to physical dimensions through equations such as 4.30 that determines the height of the secondary mirror tripod above the PM. The structural model for the system is prepared as described in Section 4.3.2, and a normal modes analysis is run for each design realization. The modal frequencies for the first 100 modes are shown in Figure 4-18 for a sample design realization [6]. The first mode for this system is at 1.04 Hz. The modeshape is a rocking of the telescope on its elevation axis, as shown in Figure 4-19(a). The first torsional mode of the SST occurs at 1.63 Hz, shown in Figure 4-19(b), and the first "saddle mode" where the primary mirror is distorted occurs at 6.13 Hz (Figure 4-19(c)). The modal frequencies climb slowly to 17 Hz, where they level off. Examination of the modeshapes shows that the modes up to 17 Hz are dominated by the SST and rocking of the telescope on its elevation axis, while all of the modes clustered around 17 Hz involve deflections of the primary mirror. Since many of the dynamic disturbance sources for ground-based telescopes are low-frequency in nature, there is a wish to increase the first frequency to 2 Hz or higher; this could be accomplished by stiffening the tripod legs and the connection to the elevation axis.

[6] The design variables are: Gregorian configuration with PM focal ratio of 1.0, final focal ratio of -15, and elevation axis 3.5 meters above the PM

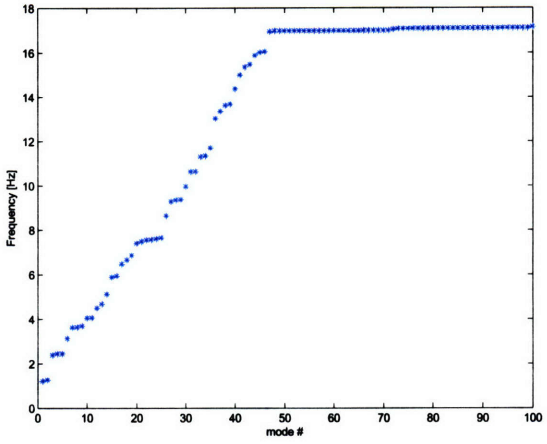

Figure 4-18: First 100 modes of a TMT sample design

TMT optics

The optics model is provided by the NOAO in the form of linear sensitivity matrices that transform z-displacements of the primary mirror nodes and all displacements and rotations of the secondary mirror node into weighted Zernike coefficients a_i for the first nine Zernike terms [74] (described in Section 3.2.1). The optics model is integrated with the structural outputs from the state-space system, described by Equation 3.29, given the sensitivity matrix C_1 for the primary mirror degrees of freedom and C_2 for the secondary mirror degrees of freedom.

$$\begin{Bmatrix} a_1 \\ \vdots \\ a_9 \end{Bmatrix} = \left[\left[\begin{array}{cc} C_1 C_{d_{PM}} & C_2 C_{d_{SM}} \end{array} \right] \Phi \quad 0 \right] \begin{Bmatrix} x \\ \dot{x} \end{Bmatrix} \tag{4.37}$$

The final output metrics are the root-sum-squared (RSS) value of the tip and tilt Zernikes (numbers 1 and 2, where number 0 refers to piston) termed the image motion, and the root-sum-squared value of all other Zernikes (numbers 3 through 8) termed the image quality.

$$z_{motion} = \sqrt{\sum_{i=1}^{2} a_i^2} \tag{4.38}$$

$$z_{quality} = \sqrt{\sum_{i=3}^{8} a_i^2} \tag{4.39}$$

Image motion is impacted most by the large tip and tilt rotations of the secondary mirror;

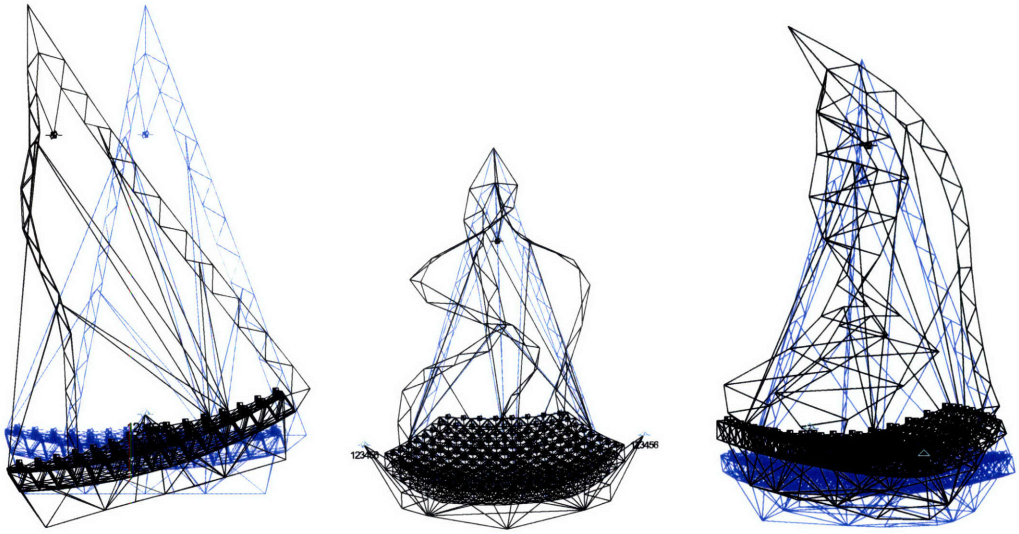

(a) 1.04 Hz, rocking on elevation-axis

(b) 1.63 Hz, SST torsion

(c) 6.13 Hz, PM saddle mode

Figure 4-19: TMT modeshapes

the low frequency flexibility of the parameterized TMT secondary tower adversely affects these performances outputs. Image quality is affected more by the movement and deflections of the primary mirror; since the primary mirror is largely rigid across the disturbance frequencies, these metrics are closer to the desired values.

Dynamic disturbances

Wind blowing into the telescope housing and around the mirrors is the anticipated source of dynamic disturbance. A parametric wind model is provided to MIT by the NOAO [10]. The model includes the effect on the primary and secondary mirrors from wind entering through the dome opening. It also models the effect on the primary mirror of wind entering through side vents and of shear layer modes that result from vortices as wind passes over the dome opening. An example PSD of the disturbance on the PM due to wind coming through the dome opening is shown in Figure 4-20. This PSD is applied to the system as described in Section 3.4. The final optical performance outputs are the summation of the outputs from all four wind disturbance sources.

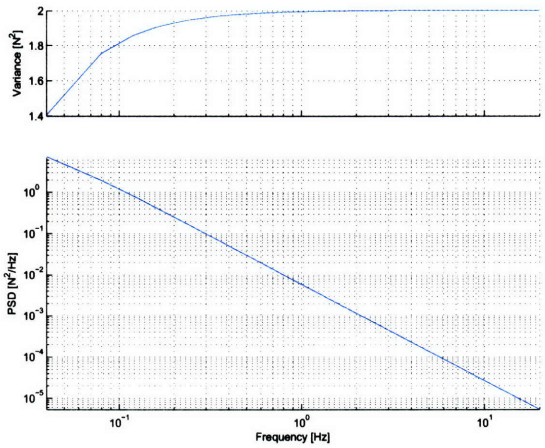

Figure 4-20: Example disturbance PSD from wind impacting the primary mirror

Optical control

The final component of the TMT integrated model is control for both primary mirror shape and secondary mirror tip and tilt. In the model, the mirror rafts are connected to the truss backstructure by 100 Hz springs in the vertical (line-of-sight) direction (Figure 4-21), and the secondary mirror is connected to the SST by a similar 100 Hz torsional spring. Relative force (or torque) actuators are placed across each spring. A proposed actuator and sensor suite for TMT is described in [94]; gap sensors between each segment determine the relative orientation of each segment. From this data the overall shape of the primary mirror can be computed. Since these gap sensors are not modeled, the Zernike outputs in the TMT integrated model resulting from only primary mirror displacements are used to represent this sensor information for mirror shape control. Similarly, the total Zernike tip and tilt outputs are used for the secondary mirror control, representing a wave front sensor further down the optical path.

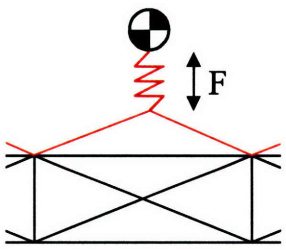

Figure 4-21: Illustration of raft-spring connection joint with relative force actuator

The control algorithms for both the primary and secondary mirrors are based on a paper by MacMartin and Chanan [11]. Given a relationship between the actuator forces u and the Zernike sensor input y, $y = Pu$, the actuator forces are minimized by $u = P^{\dagger}y$ where $(\cdot)^{\dagger}$ is the pseudo-inverse [7]. The force influence matrix P is found by computing the transfer function relating actuator force to Zernike output at zero frequency (undisturbed)

$$\left.\frac{y_{\text{zernikes}}}{u_{\text{actuators}}}\right|_{\omega=0} = C(-A)^{-1}B + D \equiv P \tag{4.40}$$

The zero frequency values are then used as the gains in an integral controller, with a control bandwidth of ω_{BW}.

$$u_{\text{actuators}} = \frac{P^{\dagger} \cdot 2\pi\omega_{BW}}{s} \cdot y_{\text{zernikes}} \tag{4.41}$$

A controller canonical state-space realization of this transfer function is created and integrated with the model.

Sample TMT results

The final TMT integrated model is shown in Figure 4-22. The "TMT Plant" represents the structural model, which is acted upon both by the wind disturbances and by the force and torque actuators on the primary and secondary mirrors. Structural outputs include the physical displacements of each raft node, and all six degrees of freedom for the secondary mirror node. These outputs are multiplied by the optical sensitivity matrices C_1 (for the primary mirror nodes) and C_2 (for the secondary mirror nodes) to give Zernike coefficients. The coefficients are both fed back to the controllers and are output as final system performances.

Figures 4-23(a) through 4-23(f) show the PSDs and cumulative RMS curves for some of the Zernike outputs in both open loop and closed loop. The tip/tilt Zernikes, numbers 1 and 2, are controlled by the secondary mirror actuators which attenuate the response up to the corner frequency (1 Hz in these examples). For higher Zernikes, the closed loop response is improved using the primary mirror actuators. Motion of the secondary mirror also affects higher Zernikes, including numbers 3 (Figure 4-23(c)) and 6 (Figure 4-23(f)),

[7] MacMartin and Chanan [11] use a relationship between *displacement* of the actuator x versus sensor input. Since the parameterized TMT actuators act over springs with spring constant k, forces are used in place of displacements, and are related to the raft displacements through $u = -kx$.

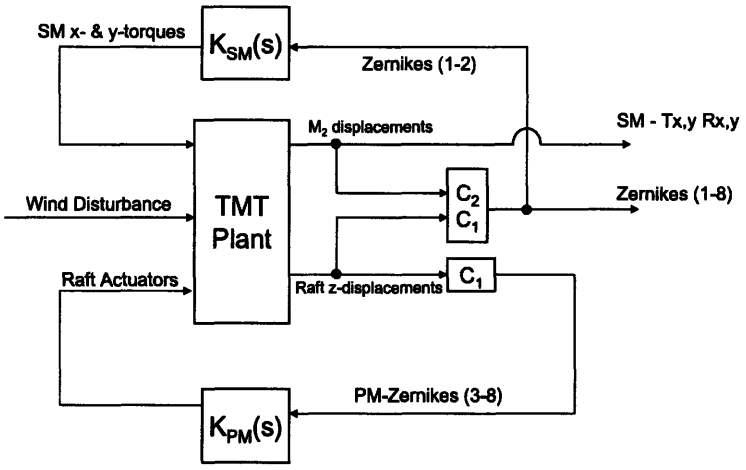

Figure 4-22: Block diagram of the TMT integrated model

but since the secondary mirror is not controlled for these outputs the attenuation is less than for Zernikes 1 and 2. In each example however, closed loop control improves the system performance up to the control bandwidth.

The wind disturbances contribute most at low frequencies, below 1Hz. In each of these plots there are no additional contributions to the final performance RMS values above 10Hz (note the flatline of each RMS curve by 10Hz). The final RMS values for each Zernike are root-sum-squared as in Equations 4.38 and 4.39 for the final design performance outputs. Table 4.6 gives the final open and closed loop RMS for the plots in Figure 4-23, as well as the final image motion and quality metrics.

Table 4.6: Final performance values for example TMT design

Zernike #	**Open Loop [μm]**	**Closed Loop [μm]**
1	1.80	0.687
2	45.32	29.45
3	0.021	0.013
4	0.314	0.169
5	0.029	0.018
6	0.034	0.021
Image motion [nm]	45.35	29.46
Image quality [nm]	0.888	0.698

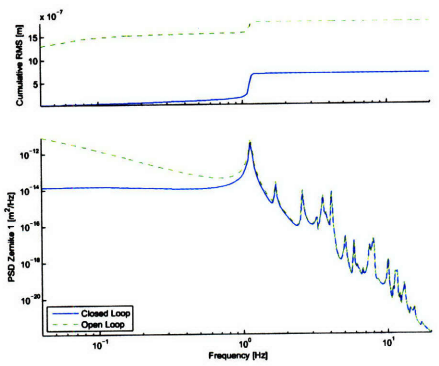

(a) Zernike 1 (tip)

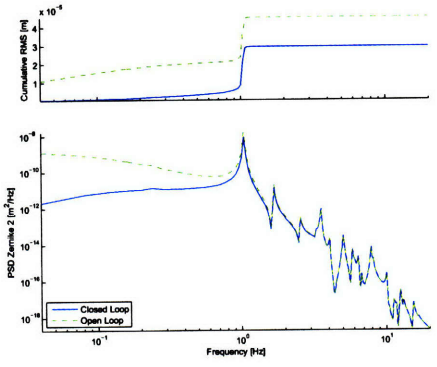

(b) Zernike 2 (tilt)

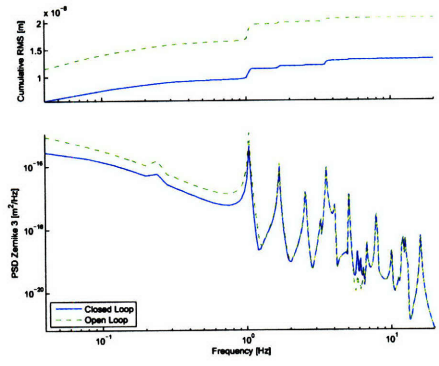

(c) Zernike 3 (focus)

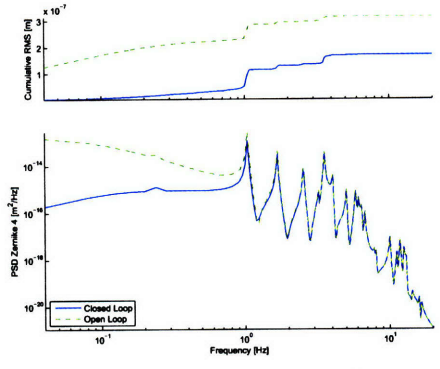

(d) Zernike 4 (astigmatism)

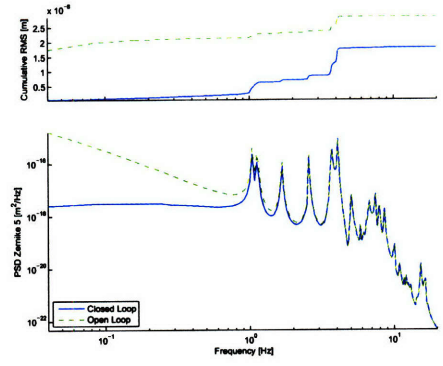

(e) Zernike 5 (astigmatism)

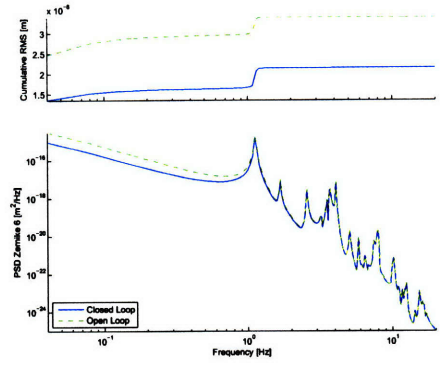

(f) Zernike 6 (coma)

Figure 4-23: Zernike PSDs and cumulative RMS curves

4.5.2 Design variable trades

The goal of the TMT parameterized model is to allow trade space analysis of critical design variables. These variables, chosen at the very start of the design, influence overall mission performance and cost, so it is desirable to determine how changes in the variables would affect the design metrics. Besides the optical performance outputs, total mass and cost of TMT are important design metrics. Mass is output from the finite element model. The cost model was provided to MIT by the NOAO. Values such as the diameter of the secondary mirror and height of the entire telescope (which drives size of the enclosing dome) are used to estimate a dollar cost of the structure.

Table 4.7 outlines the design variables and gives the range of values examined. Telescope type is either Cassegrain or Gregorian and is set by the sign of the final focal ratio. The elevation axis is either above or below the primary mirror, with only a single position for each choice. Continuous variables include the focal ratio of the primary mirror, and final focal ratio of the entire telescope. Appropriate ranges are given for both variables. The effect of control bandwidth is also examined.

Table 4.7: MIT TMT trade space parameters

Parameters	**values**	**units**
Telescope type	Cassegrain (FFR>0) vs. Gregorian (FFR<0)	-
Elevation axis	+3.5 -2.2	m
PM focal ratio	[0.8 0.9 1.0 1.1 1.2 1.3 1.4 1.5]	-
Final focal ratio (FFR)	± [12 14 16 18 20 22]	-
Control bandwidth	0.1 1.0 2.0	Hz

Single Parameter Trades

Initial analysis of the trade space involves examining the effect of varying individual parameters on output metrics, keeping all other values at nominal or, as in the figures shown, drawing isogrid lines along which all other parameters are the same. These single parameter trades can be used to quickly identify trends.

The two plots in Figure 4-24 show the effect of PM focal ratio (on the left) and final focal ratio (on the right) on the total mass. The dotted lines on each plot connect those designs where all other design variables are held constant. While only several example lines

are drawn on each plot, the lines indicate how families of designs are related as the design variable across the y-axis changes.

The effect that PM focal ratio has on mass is seen to be dependent on other variables: given an elevation axis below the PM, increasing the focal ratio increases the total structural mass for both Gregorian and Cassegrain telescopes. For elevation axes above the PM however, the shorter Cassegrain telescopes tend to decrease in mass as focal ratio increases. For the Gregorian telescopes with elevation axis above the PM there is a mass minima observed between a focal ratio of 1.0 and 1.1. This is due to the reduction in counterweight mass as the location of the structure center of gravity becomes coincident with the elevation axis. When the elevation axis is above the PM the center of gravity for short telescopes is often below the elevation axis. As focal ratio increases the telescope height increases and the center of gravity approaches and eventually passes the elevation axis. When the points are coincident, the necessary counterweight mass falls to zero as the telescope is perfectly balanced. This effect is also observed with the Cassegrain telescopes at higher focal ratio (between 1.4 and 1.5) but is not as pronounced as for the taller Gregorian telescopes.

All other design variables held constant, an increase in the magnitude of FFR in Figure 4-24(b) is seen to decrease the mass. The effect is very much dependent on the elevation axis; changing FFR when the elevation axis is above the PM and with larger PM focal ratios tends to have a much greater impact on mass than with other cases. There is relatively little change in mass across FFR values for the case of elevation axis above the PM.

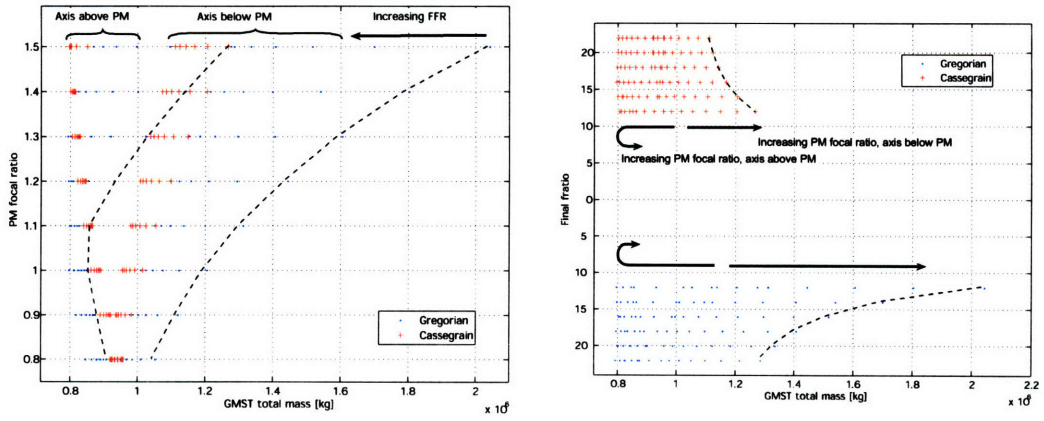

(a) Mass versus PM focal ratio

(b) Mass versus final focal ratio

Figure 4-24: Effect of parameter variation on mass

The plots in Figure 4-25 show the effect of designs variables (PM focal ratio on the left,

and final focal ratio on the right) on the total cost. The dotted lines represent constant values of the other design variables. Both plots show similar trends with cost increasing with PM focal ratio and decreasing with the absolute value of final focal ratio. The costs are more sensitive to PM focal ratio and final focal ratio for a Gregorian telescopes, however the overall costs are less with the Cassegrains.

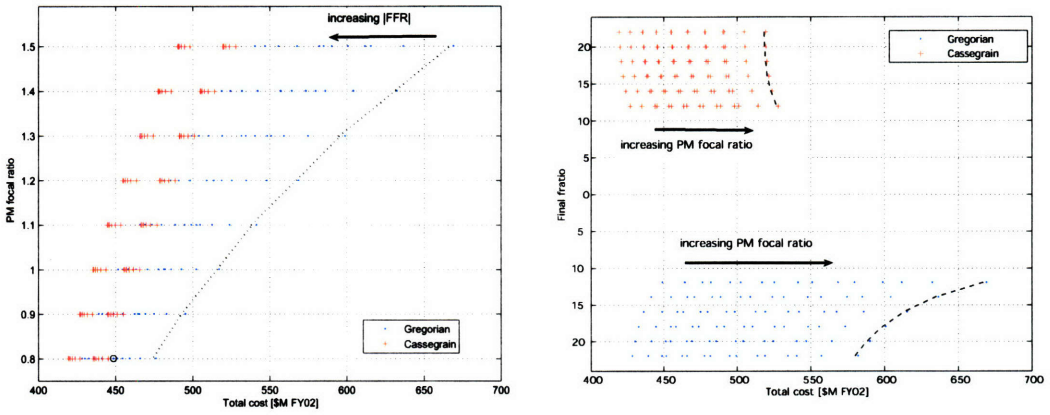

(a) Cost versus PM focal ratio

(b) Cost versus final focal ratio

Figure 4-25: Effect of parameter variation on cost

Figure 4-26 shows the effect of PM focal ratio on the image quality performance output by examining the Gregorian versus Cassegrain telescopes at high and low elevation axes separately. Lines connecting designs with equal final focal ratio are also drawn on each plot. All plots use a control bandwidth of 0.1 Hz. Each of the four plots shows similar behavior; increasing PM focal ratio worsens the image quality metric. This makes sense for these dynamic responses since a taller secondary tower would be expected to have greater dynamic deformation in the presence of wind. For the Gregorian telescopes increasing the final focal ratio magnitude shortens the telescope and improves image quality.

The four plots in Figure 4-27 show the relationship between mass and image quality. Lines of constant PM focal ratio are drawn, and for each line the direction of increasing final focal ratio (absolute value) is shown with arrows. As seen before, the case of the elevation axis above the PM has a mass minima. The minima is much more obvious for the Gregorian telescope, while the Cassegrain seem to be on that side of the curve where increasing mass generally improves performance. Also apparent is that performance improves with lower PM focal ratios and higher FFR. For the case of the elevation axis below the PM, lower mass most often gives better performance.

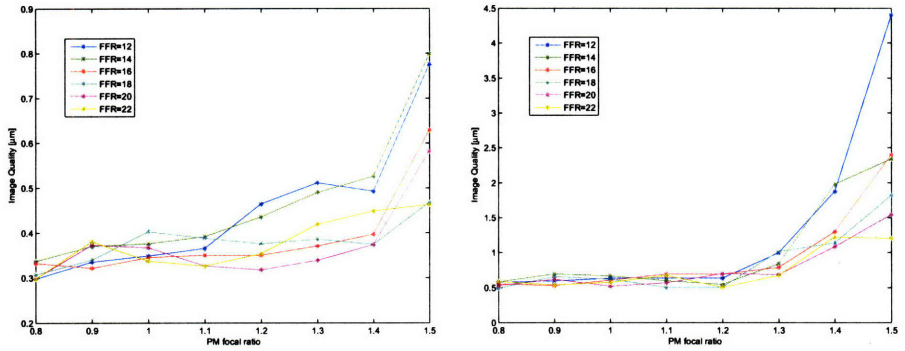

(a) Cassegrain telescope, axis above the PM (b) Cassegrain telescope, axis below the PM

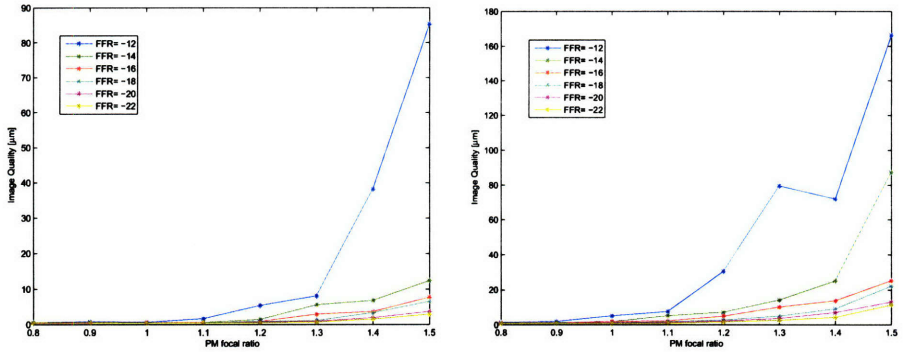

(c) Gregorian telescope, axis above the PM (d) Gregorian telescope, axis below the PM

Figure 4-26: Detailed PM focal length versus image quality plots

The PM focal ratio curves in the Cassegrain plots show a saw-toothed variability. For each PM focal ratio curve the only varying parameter is FFR. This variability can be seen even in Figures 4-26(a) and 4-26(b), where the FFR-curves intersect each other. The curves reinforce the result that FFR has less affect on the Cassegrain performance than other variables.

Due to the simplified actuator/sensor model, the effect of increasing bandwidth on the output metrics is always to improve the performance without consequence in terms of stability margins. This effect is not considered physical, and more detailed sensor/actuator models together with advanced controllers are needed to show instabilities at higher bandwidths.

Full trade studies

Examination of the full trade space is performed to identify the architecture families that best meet all of the system metrics. Each combination of design variable values, given

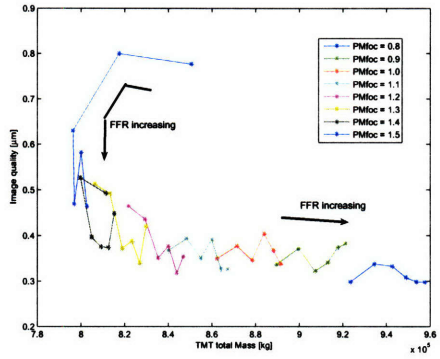

(a) Cassegrain telescope, axis above the PM

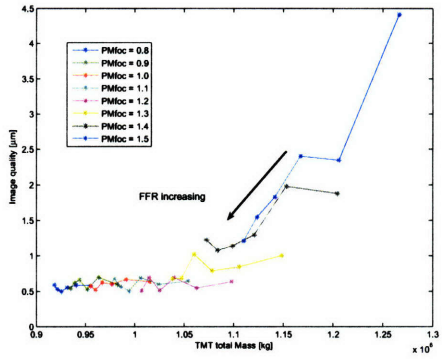

(b) Cassegrain telescope, axis below the PM

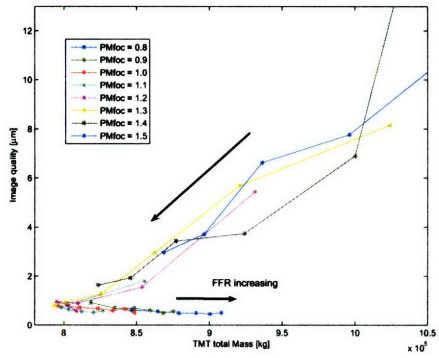

(c) Gregorian telescope, axis above the PM

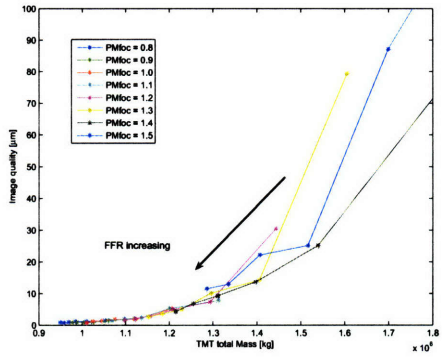

(d) Gregorian telescope, axis below the PM

Figure 4-27: Detailed mass versus image quality plots

in Table 4.7, is used to generate a unique integrated model. A total of 576 designs are evaluated and key metrics are plotted against each other.

Mass versus cost is plotted in Figure 4-28. There is a very obvious curve of optimal designs in the lower left of the plot, running between $420 and $500 million, and from 800,000 kg to 950,000 kg. By choosing different designs along this front, tradeoffs between cost and mass can be made. Individual designs across the entire plot are identified to determine which traits are superior in terms of these metrics. There are obvious differences both in elevation axis and telescope type.

The elevation axis difference is most pronounced; all of the points above the optimal front that rise to the upper left (high cost, high mass) quadrant of the plot have an elevation axis below the primary mirror. These exhibit the behavior that mass rises with cost. Those designs with elevation axis above the primary mirror lie on the arc on the lower half of the plot, with a mass minimum of approximately 800,000 kg at $500 million. This minimum was observed before, in Figure 4-27(a) and 4-27(c) for instance, and occurs as the SST

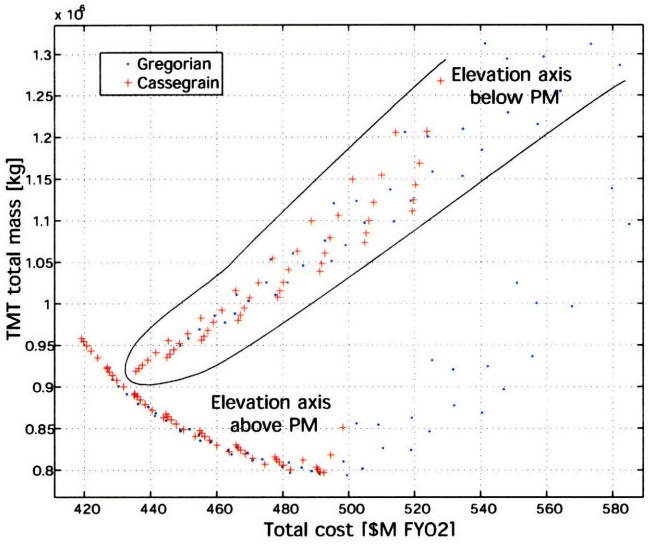

Figure 4-28: Mass versus cost trade space results

increases in height, raising the structure center of gravity past the elevation axis, reducing the counterweight mass to zero. The corresponding increase in total cost is likely due to the larger dome structure needed for a taller telescope.

The other obvious trait from this chart is the dominance of Cassegrain designs over Gregorian for both cost and mass across the entire trade space. While both are represented along the optimal front, the heaviest and most expensive designs are all Gregorian. On average the PM-SM separation distance is greater for Gregorian telescopes than the Cassegrains. This results in greater mass since the structure CG is usually further from the elevation axis and the counterweight mass increases. Costs also increase because a greater dome diameter is needed for taller telescopes.

Total cost is compared to both image motion and image quality in Figure 4-29. Image motion in particular shows large values on the order of 1 mm especially for the Gregorian telescopes. The Cassegrain telescopes have much smaller values, most below 50 microns. Image quality values are much smaller, but the overall trends are similar; the Gregorian values are on the order of 10 microns, while the Cassegrain values are mostly less than 1 micron. The differences between the telescopes are likely the result of the Gregorian telescopes being taller than the Cassegrains. Wind disturbances on the secondary mirror have a greater effect on the taller SSTs, resulting in worse performance.

Mass versus image motion and quality are shown in Figure 4-30. The Cassegrain designs

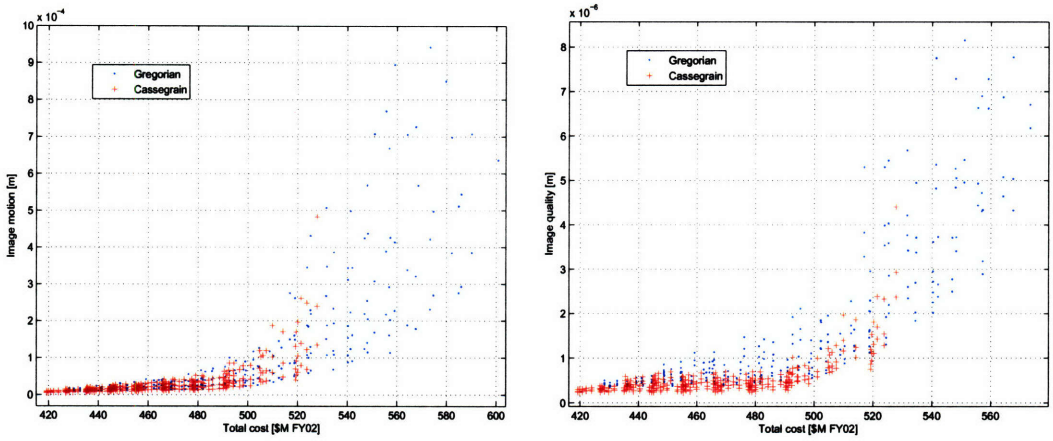

(a) Cost versus image motion

(b) Cost versus image quality

Figure 4-29: Cost versus performance trade space results

have better performance across all mass levels, often by an order of magnitude.

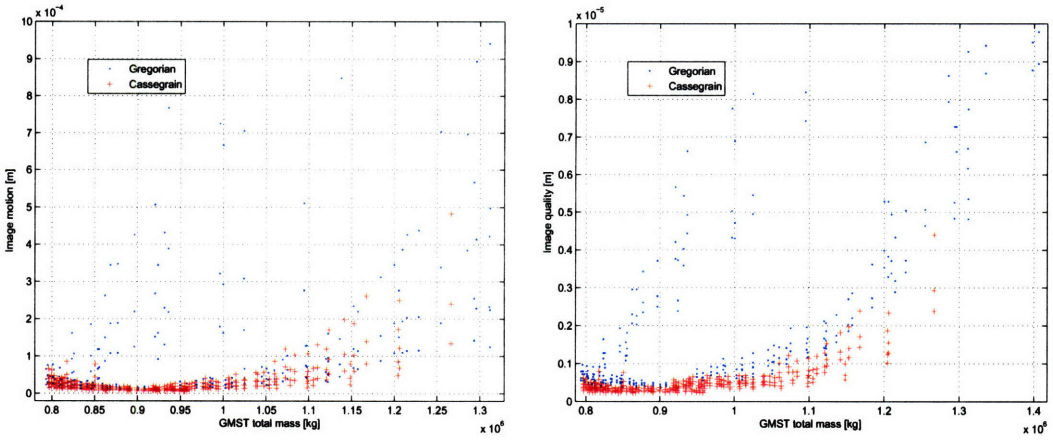

(a) Mass versus image quality

(b) Mass versus image motion

Figure 4-30: Mass versus performance trade space results

The dynamics analysis shows that increasing FFR and decreasing PM focal ratio reduces cost and improves performance. Cassegrains show better results across metrics; the shorter telescopes tend to be less massive, their dome costs are less and the dynamic wind disturbance has less of an effect on the performance. Finally having the elevation axis above the primary mirror usually led to a dramatic decrease in total mass.

4.6 Conclusions

In order to examine alternative designs in the conceptual design stage, or to evaluate the effect of off-nominal uncertainty parameters, methods of parameterizing structural finite element models and integrated models are described. Different methods may be used based on the parameters of interest. The linear fractional transformation (LFT) provides a fast method of evaluating variations in parameters that enter the physical equations of motion or integrated state-space model linearly. The example shown of the TPF-SCI model indicates how the LFT can be used to vary potentially uncertain parameters such as Young's modulus or modal damping, or design variables such as isolator corner frequencies or optical bandwidths.

In order to parameterize design variables that determine the very shape and dimensions of a structure, a parameterized modeling environment is created that automatically generates and evaluates finite element models and integrated models. An example automated finite element model of the ground-based Thirty Meter Telescope is shown. As high-level design variables such as location of the elevation axis or curvature of the primary mirror change, completely new FE models are produced. Similar parametrization is demonstrated on integrated model components such as the reaction wheel assemblies. The mass and disturbance energy of the RWA varies as the inertia of the spacecraft changes and as spacecraft slew requirement vary.

Lastly, an analysis of the parameterized TMT design is performed that indicates better optical performance in the Cassegrain designs, and lower mass for those designs with the elevation axis below the primary mirror.

Chapter 5

Critical Parameter Identification and Uncertainty Analysis

Along with trade space exploration, analyses in the conceptual design stage must include the first steps to quantify the inherent uncertainty of a design. Uncertainty analysis of the performance predictions is an important tools for the analytic validation of the designs. A comprehensive uncertainty analysis must indicate by launch whether the mission will meet its requirements even in the presence of remaining uncertainties. By initiating such analyses at the start of the design lifecycle across design trade studies, robustness to uncertainty can be used as a metric to compare competing designs. Even for point designs, an early evaluation of the uncertainties can motivate further research that will lead to a more robust design and, in time, provide the necessary data for a more complete uncertainty analysis at later stages of the lifecycle.

This chapter focuses on the methods used to evaluate the uncertainty during conceptual design trades of integrated models. At this design stage there are few details on the types of uncertain models that describe the input parameters, and there is no hardware with which to compare model predictions. Based on these conditions, the approach to uncertainty analysis is illustrated in Figure 5-1. The approach concentrates on bounded, parametric uncertainty analysis where a key concern is the identification of those parameters that most contribute to the model outputs. The first section of this chapter considers methods of identifying critical uncertainty parameters out of a large set of system parameters. These methods include a sensitivity analysis and a simulation-based approach from the field of

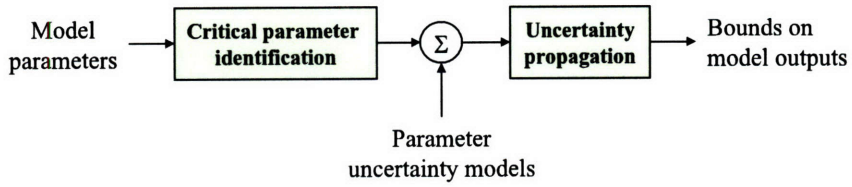

Figure 5-1: Approach to uncertainty analysis. Methods highlighted by blocks described in this chapter.

Design of Experiments. An overview of factorial experiments and analysis of variance is provided.

Following the identification of critical parameters, the uncertainty models of those parameters must be defined. These models are either bounded or probabilistic in form. Several uncertainty propagation techniques based on the type of input model are described. These propagation techniques either place bounds on the model outputs or define the probability that an output will meet its requirement. In choosing which technique is appropriate to use, the maturity of the design and the stage of the design lifecycle are considered. A parametric, bounded approach is ultimately used based on the available parameter information and needs of the conceptual design methodology at this stage.

The final section shows an example critical parameter identification analysis on the Terrestrial Planet Finder, Free-Flying Interferometer (TPF-FFI) model. Critical parameters are identified using Design of Experiment techniques, followed by a bounded parametric uncertainty analysis.

5.1 Identification of critical uncertainty parameters

5.1.1 Sensitivity analysis

The sensitivity of performance outputs to system parameters provides information that is used in several ways during design and re-design. For the present purpose of parametric uncertainty analysis, the parameters evaluated are limited to those that most influence the outputs. Even if a parameter is very uncertain, if it has no effect on the outputs those uncertainties will not contribute to the performance uncertainty. In terms of system re-design, the sensitivities indicate which parameters are the most useful "knobs" for changing the outputs toward a desired requirement. Sign information on the sensitivity values can indicate

whether increasing or decreasing a particular variable improves the performance [26]. Also, many design optimization techniques use sensitivities in the form of gradient information to determine a search direction.

Because of the usefulness of parameter sensitivities for identifying critical parameters, and since the DOCS toolbox already contains sensitivity tools, this approach is used first in identifying critical uncertainty parameters. Methods of computing performance sensitivities depend on the form of the model. Gutierrez [26] describes the governing sensitivity equation that can be used when the system is driven by white noise. The method used here is for a state-space model in which the final performance is computed using the frequency response function and the disturbances are described by PSDs. After the derivation of the analytic sensitivity method, an example will be presented using the TPF-FFI spacecraft with 13 physical parameters and 140 damping values.

Frequency response function sensitivity

The PSD approach for performance prediction, described in Section 3.4, relies on the frequency response function (FRF) of the system. The FRF for a system with disturbance inputs w and performance outputs z is computed in Equation 3.43, repeated here.

$$G_{zw} = C_z \left(sI - A\right)^{-1} B_w + D_{zw} \tag{5.1}$$

The PSD of the outputs is computed using Equation 3.44 with the FRF and the disturbance PSD S_{ww}.

$$S_{zz}(\omega) = G_{zw}(\omega)\, S_{ww}(\omega)\, G_{zw}^H(\omega) \tag{5.2}$$

The variance of the performance outputs, Σ_z, is found using the single-sided integral of the performance PSD given in Equation 3.46 where the frequency ω is in radians per second (rad/sec).

$$\begin{aligned} \Sigma_z(\omega) &= \frac{1}{\pi}\int_0^{+\infty} S_{zz}(\omega)\; d\omega \\ &= \frac{1}{\pi}\int_0^{+\infty} G_{zw}(\omega)\, S_{ww}(\omega)\, G_{zw}^H(\omega)\; d\omega \end{aligned} \tag{5.3}$$

The root mean square performance values σ_{z_i} for each output i are found by taking the square root of each value along the diagonal of Σ_z. Of interest in a sensitivity analysis

is how those RMS values vary with a given parameter, p. This is written as $\frac{\partial \sigma_{z_i}}{\partial p}$, and is found by computing the sensitivity of the variance $\sigma_{z_i}^2$ to p, and applying the following relationship.

$$\frac{\partial \sigma_{z_i}}{\partial p} = \frac{1}{2\sigma_{z_i}} \frac{\partial \sigma_{z_i}^2}{\partial p} \tag{5.4}$$

The sensitivity matrix of the variance matrix, $\frac{\partial \Sigma_z}{\partial p}$, is found by differentiating Equation 5.3 with respect to p.

$$\frac{\partial \Sigma_z}{\partial p} = \frac{\partial}{\partial p}\left(\frac{1}{\pi}\int_0^{+\infty} G_{zw}\, S_{ww}\, G_{zw}^H \, d\omega\right) \tag{5.5}$$

Since the differentiation with respect to p has no dependence on ω, the differential operator $\frac{\partial}{\partial p}$ is moved inside of the integral, and the integrand expanded based on the dependence of G_{zw} on p.

$$\begin{aligned} \frac{\partial \Sigma_z}{\partial p} &= \frac{1}{\pi}\int_0^{+\infty} \frac{\partial}{\partial p}\left(G_{zw}\, S_{ww}\, G_{zw}^H\right) \, d\omega \\ &= \frac{1}{\pi}\int_0^{+\infty} \left(\frac{\partial G_{zw}}{\partial p}\, S_{ww}\, G_{zw}^H + G_{zw}\, S_{ww}\, \frac{\partial G_{zw}^H}{\partial p}\right) \, d\omega \end{aligned} \tag{5.6}$$

Note that this assumes that the disturbance PSD S_{ww} is not a function of p; only parameters of the FRF are considered. Equation 5.6 is then solved by computing the partial differential of G_{zw}, using Equation 5.1.

$$\begin{aligned} \frac{\partial G_{zw}}{\partial p} = \frac{\partial C_z}{\partial p}(sI-A)^{-1}B_w \;+\; & C_z(sI-A)^{-1}\frac{\partial A}{\partial p}(sI-A)^{-1}B_w \\ & + C_z(sI-A)^{-1}\frac{\partial B_w}{\partial p} + \frac{\partial D_{zw}}{\partial p} \end{aligned} \tag{5.7}$$

Note that this expansion makes use of the matrix relation

$$\frac{\partial X^{-1}}{\partial p} = -X^{-1}\frac{\partial X}{\partial p}X^{-1}$$

to take the derivative of the inverse of $(sI - A)$.

In solving Equation 5.7 all that is needed are the sensitivities of the original state matrices to p, and these were computed back in Equation 4.13. The parameters p used here make up the Δ blocks used in the LFT transformation.

Application of this sensitivity approach to the TPF-FFI spacecraft is demonstrated next.

TPF-FFI sensitivities

A sensitivity analysis is performed on the TPF-FFI spacecraft integrated model, examined in Section 3.4.2. The spacecraft model includes the two line-of-sight performance outputs, as well as the wave front error determined by the root-sum-square of the weighted output Zernikes. The wave front error metric is a non-linear combination of the outputs, and can not be computed directly from the linear state-space model. This means that the general sensitivity equations described in the previous section, while useful to investigate individual Zernikes coefficients, cannot be used to determine the sensitivity of the wave front error. Only sensitivities for the line-of-sight outputs will be examined here. A method to identify critical parameters influencing non-linear effects such as wave front error will be described in the following section.

The first step in a sensitivity or critical parameter identification routine is to determine which parameters will be evaluated. Since the goal of the analysis is to identify the subset of all parameters in the model that most affect the outputs, deciding a-priori which subset of parameters to include in the sensitivity analysis necessarily requires engineering judgement on the part of the designer. The goal of the pre-selection is to identify which parameters may have an influence on the outputs or may have larger uncertainty bounds. While these selections are obviously based on the knowledge and experience of the designer, it is suggested that a large number of potential critical parameters be included in this first screening process. This leaves identification of the most critical parameters, those that influence the system most, to the analytical techniques described here.

In the case of the TPF spacecraft model, identified parameters include concentrated masses for the secondary mirror and at mounting points on the primary mirror. Material constants such as Young's modulus can be evaluated for different components of the structure, including along the sunshade booms and along the tower legs supporting the secondary mirror. Other parameters include stiffness values of springs connecting appendages to the structure, or corner frequencies of the low-pass filters representing vibration isolators. All of the finite element parameters used in this uncertainty analysis are listed in Table 5.1, along with the nominal values of the parameters. Parameters for other integrated model components, such as the isolator corner frequencies and control bandwidth, are listed in Table 5.2

Table 5.1: Identified parameters from the TPF-FFI FE model

Component	EID #	element	parameter	units	nominal value
SST legs	60003 → 60053	cbar	E	N/m2	1.15×10^{11}
PM plates	70001 → 70968	ctria3	E	N/m2	8.96×10^{10}
Sunshade booms	50000 → 50005 50007 → 50012 50014 → 50019 50021 → 50026	cbar	E	N/m2	1.15×10^{11}
Sunshade masses	50931 → 50934	conm2	M	kg	39.1036
Light trays springs (translation)	95901 96901	cbush	K_1, K_2, K_3	N/m	1.75×10^8
Light trays springs (rotation)	95904 96904	cbush	K_4, K_5, K_6	Nm	112985
Radiator springs: (translation)	11901 12901 13901 14901 15901 16901	cbush	K_1, K_2, K_3	N/m	1.75×10^8
Radiator springs: (rotation)	11904 12904 13904 14904 15904 16904	cbush	K_4, K_5, K_6	Nm	112985
SM	60054	conm2	M	kg	19.4819
PM mounts	72011 → 72019	conm2	M	kg	0.79921

Table 5.2: Parameters in the TPF integrated model

Parameter	units	nominal value
RWA isolator corner frequency	Hz	10
Bus isolator corner frequency	Hz	2
Controller bandwidth	Hz	10

Sensitivities are computed for all of the parameters listed. The results are plotted in Figure 5-2, with a selection of damping results given separately in Figure 5-3. The results are normalized based on the nominal parameter values. This allows sensitivities on parameters with different units to be compared to one another on the same plot. Starting with the sensitivities $\frac{\partial \sigma_{z_i}}{\partial p}$ computed from Equation 5.4, the percentage change in performance due to parameter variation is found using [26]

$$\frac{p_{\text{nom}}}{(\sigma_{z_i})_{\text{nom}}} \frac{\partial \sigma_{z_i}}{\partial p} = \frac{\frac{\partial \sigma_{z_i}}{(\sigma_{z_i})_{\text{nom}}}}{\frac{\partial p}{p_{\text{nom}}}} \approx \frac{\frac{\Delta \sigma_{z_i}}{(\sigma_{z_i})_{\text{nom}}}}{\frac{\Delta p}{p_{\text{nom}}}} \approx \frac{\%\text{ change in } \sigma_{z_i}}{\%\text{ change in } p}. \tag{5.8}$$

Negative sensitivity corresponds to an inverse relation between the parameter and the

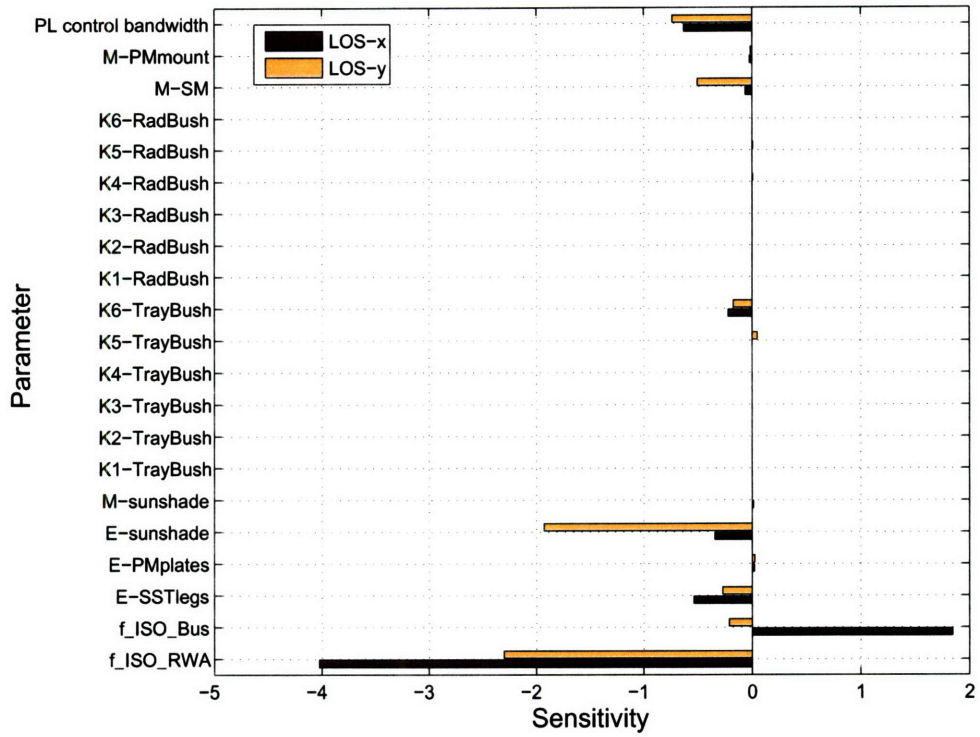

Figure 5-2: Output RMS sensitivity for 21 parameters

output. For example, as the parameter is raised 1%, the output decreases by the percentage sensitivity. So, in Figure 5-2, as the isolator corner frequency for the RWA is increased 1%, the filtered LOS-x should decrease 4%. Likewise, if the sensitivity is positive, a 1% change of the parameter value would increase the output by the amount of the sensitivity.

An examination of Figures 5-2 and 5-3 indicates that the results appear to be fairly insensitive to damping across all but a couple of modes, compared at least to the other parameters. Given the uncertainty of the modal damping model, especially at the cryogenic temperatures that TPF will experience, this result should not be interpreted to suggest that damping is not a factor. Rather, at small variations about the nominal results, other parameters dominate this particular model. Research in more appropriate damping models at cryogenic temperatures is still a critical part of understanding the parametric uncertainties of this TPF model. Given that damping is already identified as a source of uncertainty in the TPF program, the role of the other parameters will be focused on in greater detail for this analysis.

In Figure 5-2, several parameters stand out, including control bandwidth, mass of the

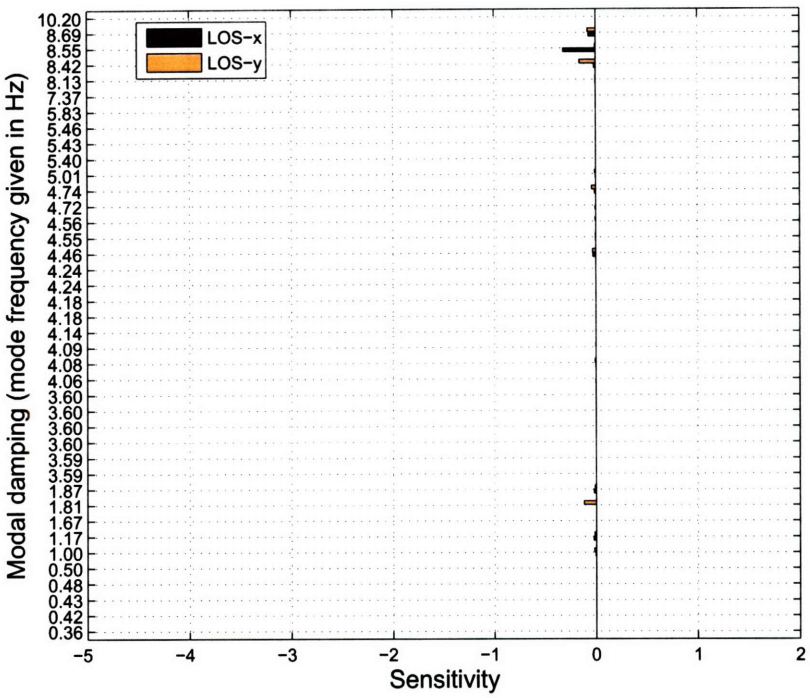

Figure 5-3: Output RMS sensitivity for damping on first 40 flexible modes

secondary mirror, moduli of both the sunshade booms and SST, and both isolator frequencies. The output also seems to be somewhat sensitive to the z-axis rotational stiffness of springs connecting the stray light trays to the OTA ('K6-TrayBush' on the plot legend). In nearly all of these cases, the sensitivities are negative. This indicates, not surprisingly, that improved performance can come through higher control bandwidths and stiffer bars for the sunshade and SST. Less expected, perhaps, is that increasing the mass of the secondary mirror is beneficial, particularly for LOS-y. Since the final masses for many of these components may not be known at this stage of the design, the dynamic response would actually improve should the final SM mass be larger than anticipated. Other parameters, such as the masses placed at the primary mirror mounting points, most of the stray light tray stiffnesses, and even the modulus of the primary mirror, do not affect the system outputs. Whether or not these parameters have large uncertainties associated with them, their small influence on the performances means that these parameters are not retained in further uncertainty analyses.

The isolator corner frequencies dominate the results in Figure 5-2. The 10 Hz reaction wheel isolator has the largest effect, with a 1% increase in frequency providing between 2

and 4% improvement in performance. A closer examination of the closed loop PSD curve for this system, shown in Figure 5-4, provides some physical interpretation of the results. A trio of critical modes is directly below the 10 Hz isolator. The largest mode at 8.55 Hz contributes over half of the total RMS output for LOS-x. The isolator model (shown in Figure 3-12) would provide amplification of the system for several hertz above and below its 10 Hz corner frequency, so lowering the frequency closer to 8.55 Hz would further excite these critical structural modes. The results from the sensitivity plot seem to agree with intuition, in suggesting to raise the isolator frequency for improved performance.

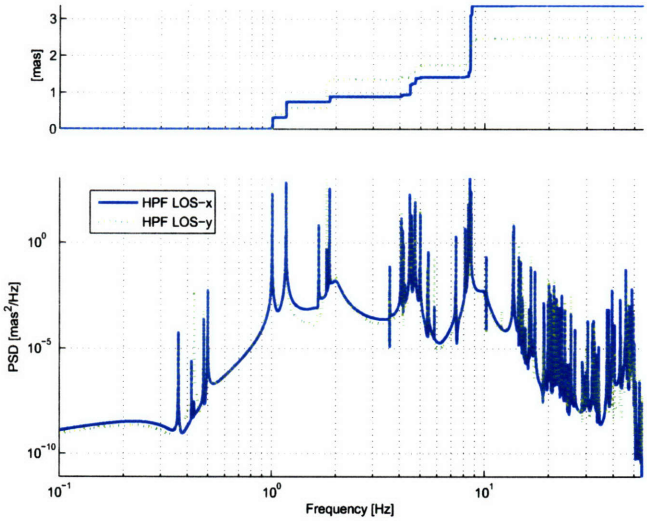

Figure 5-4: PSD and cumulative RMS curve for the closed loop TPF-FFI system

In terms of critical parameter identification, the results of the sensitivity analysis are that out of the original 22 identified parameters (18 finite element, 3 integrated modeling, and damping), only 7 are shown to appreciably affect the final performance outputs. The parameter space that must be explored for an uncertainty analysis has been reduced threefold. The remaining parameters, roughly in decreasing order of importance, are as follows.

- RWA isolator corner frequency
- Bus isolator corner frequency
- Modulus of the sunshade booms
- Controller bandwidth

- Modulus of the SST legs
- Secondary mirror mass
- Stray light tray, z-axis rotational stiffness

The analytic sensitivity analysis method in DOCS is straightforward, but it still is limited to the outputs of state-space systems. The non-linear wave front error performance could not be included. This technique would not work on models requiring time-domain simulations, or on thermal analyses not framed in terms of a state-space model. Since designers for optical systems such as TPF are greatly interested in non-linear behavior and thermal effects, an alternative approach is required to identify critical uncertainty parameters for models that cannot be represented in state-space form. The next section introduces methods of critical parameter identification, based on computer simulations, that are applicable to both linear and non-linear models.

5.1.2 Computer simulations and analysis of variance

This section provides background on Design of Experiments methods, factorial designs and the analysis of variance. The use of these techniques for critical parameter identification is described.

Introduction to Design of Experiments

Design of Experiments (DOE) refers to the field of techniques used to gain maximum information out of a limited set of experiments. Since its inception in agricultural research in the 1930s, experimental design has been used in fields from industrial process improvement to scientific research. The field covers statistical experimentation such as Monte Carlo sampling and its various derivatives [51], Taguchi methods of quality control [95], analysis of variance (ANOVA) techniques to identify key contributors to an output metric [59], and response surface modeling to create approximation models using the results from only a few actual experiments [96].

While many aspects of experimental design have to do with actual physical tests in which random errors between otherwise identical experiments can produce different results, the area of computational simulation is unique since the experiments are deterministic.

Repeating any simulation will give the exact same result. The elimination of random error has led to a branch of DOE sometimes referred to as Design and Analysis of Computer Experiments, or DACE [47, 51, 50]. These experiments use many of the same approaches as traditional DOE, but the emphasis is on how to reduce the number of lengthly computer simulations required in a study. Given a unique input vector p and output metrics σ related by some costly simulation $\sigma = f(p)$, computer experiments guide selection of the inputs to produce either output statistics, response surface models, or to show which inputs contribute most to the output. This final application, determining which inputs have the greatest influence on the outputs, is used in place of the sensitivity analysis technique of the previous sections for critical parameter identification.

The advantage of DOE for integrated modeling simulations is apparent as the models grow larger and more complex. Linear models can be studied in the frequency domain where advanced disturbance and sensitivity algorithms can be employed. In the cases of non-linear or thermal models, frequency domain algorithms are either not valid or require simplifications and assumptions of the underlying system. If computationally intensive time-domain solutions are required or if the desired model output include non-linear metrics such as WFE, DOE methods can provide the means to identify critical parameters. Two experimental techniques for determining the relative influence of input parameters are described next.

Factorial Experiments

Given a system with one or multiple input parameters, or *factors* in DOE terminology, one goal is to determine the effect of factors on an output metric. The 2^k or full factorial design is one approach to this problem. Given k factors, labeled A, B, C, etc., an experiment is run in which each factor is set at low and high values. For a 2-factor design, this involves 4 runs as shown in Figure 5-5(a). A 3-factor experiment would require $2^3 = 8$ runs, as shown in Figure 5-5(b). The outputs from individual runs can be labelled based on which factors are at the high values. The outputs from a run with A and B factors high and C low, for example, would be labelled ab. The outputs when all factors are at their low value are labelled (1). Table 5.3 shows the individual runs and the labels for a 2^3 design, with a -1 representing low values and $+1$ representing high values

The factor *effect* can be computed as the difference between the averaged values of the

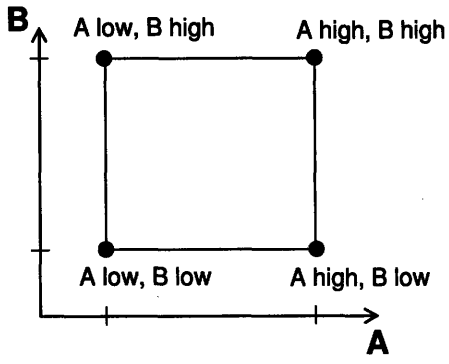

(a) 2^2 factorial design with 4 runs

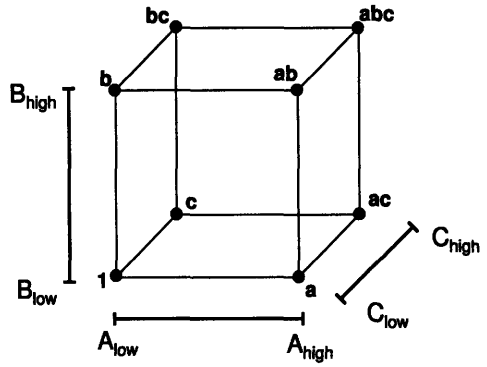

(b) 2^3 factorial design with 8 runs. Each point is labelled by which factors are at the high level.

Figure 5-5: 2^k factorial designs

Table 5.3: 2^3 factorial design

Run #	A	B	C	output labels
1	-1	-1	-1	(1)
2	+1	-1	-1	a
3	-1	+1	-1	b
4	+1	+1	-1	ab
5	-1	-1	+1	c
6	+1	-1	+1	ac
7	-1	+1	+1	bc
8	+1	+1	+1	abc

factor at high and low levels. For example in the case of the 2^3 design, the effect of factor A would be

$$\begin{aligned} A &= \frac{a+ab+ac+abc}{4} - \frac{(1)+b+c+bc}{4} \\ &= \frac{1}{4}[a+ab+ac+abc-(1)-b-c-bc] \\ &= \frac{1}{4}[-(1)+a-b+ab-c+ac-bc+abc] \end{aligned} \tag{5.9}$$

Similarly, the effects of factors B and C would be

$$B = \frac{1}{4}[-(1)-a+b+ab-c-ac+bc+abc] \tag{5.10}$$

$$C = \frac{1}{4}[-(1)-a-b-ab+c+ac+bc+abc] \tag{5.11}$$

Note that the terms in brackets, known as the *contrasts*, are merely the dot products of the experimental outputs with the appropriate column of coefficients (+1, -1) in Table 5.3. Once the factorial table has been generated for a design, matrix notation is used to compute the factor effects.

The effects for individual factors like A or B are the *main effects*. Along with these main effects are *interaction effects* which indicate the strength of the interaction between two or more factors. A large interaction effect indicates strong coupling between factors. The contrasts for interactions can be computed easily by multiplying appropriate columns of the factorial table. The coefficients that would describe the AB interaction in the 2^3 design, for example, result from the multiplication of columns A and B of Table 5.3.

$$A: \begin{bmatrix} -1 \\ +1 \\ -1 \\ +1 \\ -1 \\ +1 \\ -1 \\ +1 \end{bmatrix} * B: \begin{bmatrix} -1 \\ -1 \\ +1 \\ +1 \\ -1 \\ -1 \\ +1 \\ +1 \end{bmatrix} \rightarrow AB: \begin{bmatrix} +1 \\ -1 \\ -1 \\ +1 \\ +1 \\ -1 \\ -1 \\ +1 \end{bmatrix}$$

The resulting interaction effect then would be

$$AB = \frac{1}{4}[+(1) - a - b + ab + c - ac - bc + abc] \tag{5.12}$$

with the contrast in brackets. A full table of coefficients can be generated in this way, with each column acting as a vector whose dot-product with the experimental outputs leads to the appropriate effect. The entire coefficient table for the 2^3 design is given in Table 5.4.

Two-level full factorial designs such as in Table 5.3 can be created easily in MATLAB using the statistics toolbox command `ff2n.m`. The full interaction coefficient table can be generated using element multiplication of the appropriate columns.

Table 5.4: Coefficient table for computing main and interaction effects

A	B	C	AB	AC	BC	ABC
-1	-1	-1	+1	+1	+1	-1
+1	-1	-1	-1	-1	+1	+1
-1	+1	-1	-1	+1	-1	+1
+1	+1	-1	+1	-1	-1	-1
-1	-1	+1	+1	-1	-1	+1
+1	-1	+1	-1	+1	-1	-1
-1	+1	+1	-1	-1	+1	-1
+1	+1	+1	+1	+1	+1	+1

Fractional Factorial Experiments

Although the full factorial design provides a great amount of information regarding the main and interaction effects, it requires a large number of runs as the number of factors increases. To evaluate four factors requires 16 runs, five factors require 32 runs, ten factors require 1024 runs, and so on. An alternative is a fractional factorial experiment. Using the assumption that the higher interaction effects such as ABC are negligible, a fraction of the experiments necessary for a full factorial design are run and the main effects computed.

A fractional factorial design is created based on a full factorial design for a lesser number of inputs. For example, a one-half fraction or a 2^{k-1} design uses half the number of runs needed in a full 2^k design. If there are four parameters, $k = 4$, the full-factorial design of a $2^{4-1} = 2^3$ system (such as Table 5.3) is first created. The additional column for the fourth factor is then built by equating it with a higher interaction term, such as ABC. The factorial design in this case is given in Table 5.5.

Table 5.5: 2^{4-1} fractional factorial design

Run #	A	B	C	D=ABC	output labels
1	-1	-1	-1	-1	(1)
2	+1	-1	-1	+1	*ad*
3	-1	+1	-1	+1	*bd*
4	+1	+1	-1	-1	*ab*
5	-1	-1	+1	+1	*cd*
6	+1	-1	+1	-1	*ac*
7	-1	+1	+1	-1	*bc*
8	+1	+1	+1	+1	*abcd*

The equations describing factor effects can be written similar to those in Equations 5.9 through 5.11, but note that now not all of the interactions can be independently computed. The effect computed using the D-column of Table 5.5 is the effect of the sum of D and ABC. The interactions are *aliased* together, and the individual effects cannot be identified without additional experiments. Likewise, in this example, each of the main effects is aliased with other three-way interactions (A+BCD, for example), and each two-way interaction is aliased with another two-way interaction (AB+CD, for example).

The alias structure determines the *resolution* of the design. Resolution III-V designs are defined as follows [59].

1. **Resolution III designs:** Main effects are not aliased together, but are aliased with two-way interactions. Two-way interactions may be aliased with other two-way interactions.

2. **Resolution IV designs:** Main effects are not aliased with other main effects nor with two-way interactions. Two-way interactions may be aliased with other two-way interactions.

3. **Resolution V designs:** Main effects or two-way interactions are not alised with any other main effect or two-way interaction.

Depending on the situation, lower resolution designs may be perfectly acceptable. If higher order interactions can be assumed to be negligible, then the effects computed are approximately the same as the true main order effects. If the goal of an analysis is to identify several critical input parameters for further study, then a resolution III design on a large number of parameters may be acceptable as a first shot. Additional studies using higher resolutions design matrices can then be performed for the identified critical parameters.

If more factors are desired with still fewer runs, smaller fractions of the full factorial design can be used. For example, given nine factors the 2^{9-5} design yields $2^4 = 16$ runs. A sample is given in Table 5.6. This particular design is of resolution III, so main effects are aliased with two-way interactions.

The generating sequence of letters that determine the aliasing structure (e.g. D=ABC) for each design can vary based on the desired resolution, alias structure, and number of runs desired. The MATLAB command `fracfact.m` in the statistics toolbox can create a design

Table 5.6: 2^{9-5}_{III} fractional factorial design yielding 16 runs

Run #	A	B	C	D	E=ABC	F=BCD	G=ACD	H=ABD	J=ABCD
1	-1	-1	-1	-1	-1	-1	-1	-1	+1
2	-1	-1	-1	+1	-1	+1	+1	+1	-1
3	-1	-1	+1	-1	+1	+1	+1	-1	-1
4	-1	-1	+1	+1	+1	-1	-1	+1	+1
5	-1	+1	-1	-1	+1	+1	-1	+1	-1
6	-1	+1	-1	+1	+1	-1	+1	-1	+1
7	-1	+1	+1	-1	-1	-1	+1	+1	+1
8	-1	+1	+1	+1	-1	+1	-1	-1	-1
9	+1	-1	-1	-1	+1	-1	+1	+1	-1
10	+1	-1	-1	+1	+1	+1	-1	-1	+1
11	+1	-1	+1	-1	-1	+1	-1	+1	+1
12	+1	-1	+1	+1	-1	-1	+1	-1	-1
13	+1	+1	-1	-1	-1	+1	+1	-1	+1
14	+1	+1	-1	+1	-1	-1	-1	+1	-1
15	+1	+1	+1	-1	+1	-1	-1	-1	-1
16	+1	+1	+1	+1	+1	+1	+1	+1	+1

matrix based on such a generator. Select design generators given in Montgomery [59] have been used in the TPF-FFI analysis at the end of the chapter.

Analysis of Variance

Once the simulations have been run and the results collected, analysis of variance (ANOVA) methods can be used in order to determine the relative influence of the factors (parameters) to the model outputs. ANOVA methods are used with empirical testing in order to decompose the observed variations in the output into contributions from the individual inputs as well as a contribution due to random errors in the system. Statistical methods are used to determine whether the variations due to factors are statistically significant, or whether the variation is caused mostly from errors. In the case of deterministic computer simulations there is no experimental error and no random variation between identical simulations. All of the variability in the outputs can be assigned directly to individual factors.

The contributions of factors to variations of the output are determined by computing the sum of squares of the outputs. The total sum of squares of a set of data, y, coming from N simulations is found using

$$SS_{Total} = \sum_{i=1}^{N} y_i^2 - \frac{(\sum_{i=1}^{N} y_i)^2}{N} \tag{5.13}$$

The individual factor sum of squares can be found using the factor contrasts (the bracketed values in Equations 5.9 through 5.12). The sum of squares are related to the contrasts through

$$SS_i = \frac{[\text{Contrast}_i]^2}{8}. \tag{5.14}$$

The summation of all the sum of squares of the factors and their interactions (along with the sum of squares due to error, if the experiment had any) is the total sum of squares, found in Equation 5.13. In the two factor case this resolves to:

$$SS_{Total} = SS_A + SS_B + SS_{AB} + SS_{Error} \tag{5.15}$$

where for deterministic computer experiments $SS_{Error} = 0$. The relative influence value [22] for each factor can be computed as simply the ratio of each factor or interaction sum of squares to the total sum of squares.

$$RI_i = \frac{SS_i}{SS_{Total}} \tag{5.16}$$

Those main factors with the largest percentage RI contribute the most to the final simulation outputs. These methods can be used with any model, state-space or otherwise. The steps involved are:

1. Select a range of parametric inputs (factors) in the integrated model simulation routine.

2. Create a fractional factorial experiment in which each of the inputs are varied between low and high levels.

3. Run the computer simulations.

4. Use ANOVA techniques on the simulation results to identify which parameters most affect the performance output.

If this method is used to identify parameters for an uncertainty analysis, those factors (parameters) with the largest RI values are identified as the critical uncertainty parameters to be retained for the uncertainty analysis. Method of evaluating the uncertainty for integrated models are described next.

5.2 Uncertainty analysis methods

All model-based predictions of system performance must be evaluated with the appreciation that there will be a discrepancy between the actual and predicted performances due to uncertainties that exist in the model. Uncertainty is never entirely eliminated from any model. Parameters such as material properties may vary from published values, and even empirically identified parameter values may change over time or with environmental conditions. Phenomena such as friction or damping are notoriously challenging to model properly. Moreover all modeling techniques ultimately rely on assumptions that differ, however minutely, from the actual physics of a real structure. Even the existence of the finished hardware will not eliminate the uncertainty in a system; the system can change over time or through disassembly/reassembly, and measurements of the final outputs can always be influenced by further uncertainties (noise) in the sensors.

The methods used in an uncertainty analysis are closely connected to the stage of the design lifecycle. In later stages, when hardware and data are available, many uncertainty tools exist to update models based on data. Just prior to launch, the final uncertainty predictions must come from probabilistic methods that compute the probability of mission success based on rigorous evaluation of all the possible uncertainty sources. In earlier stages of design, such as during the conceptual and preliminary stages, other techniques must be employed that rely less on hardware data and more on the propagation of uncertainties through the model and on historical uncertainty bounds.

The aim of this section is to first consider sources of uncertainty, typically divided between parametric and non-parametric sources. This is followed by an overview of commonly used uncertainty analysis methods, with particular emphasis on parametric propagation techniques. Finally, the needs of the conceptual design methodology are considered to determine which methods are most appropriate for comparing the robustness of conceptual design models.

5.2.1 Source of model uncertainty

Table 5.7 lists many typical sources of uncertainty for flexible optical structures, based on SSL modeling and manufacturing experience. While some of the sources are not applicable to a satellite in orbit (gravity effects, effect of moisture, etc.) they will be a factor for testbeds or pre-launch tests. At the early stages of the lifecycle, only a subset of the items listed in Table 5.7 can be evaluated.

A common approach to examining the effect of uncertainties in a model is to first partition the uncertainty as resulting from parametric versus non-parametric sources. Parametric uncertainties stem from variations in the values of model parameters. Uncertainties in parameters, such as material properties, can be propagated through the model given an uncertainty description of the parameters. Non-parametric uncertainties refer to a much larger group of possible uncertainty sources, since they include any source other than the variation of parameters. Most of the sources listed in Table 5.7 are non-parametric in nature. These include model error, which may involve simplifications in the model structure (e.g. springs in place of complex joints) or incorrect choice of elements, or uncertainties due to non-linear effects such as joint stick/slip. Model fidelity issues such as mesh density may be a factor, especially for early, low-fidelity finite element "stick" models.

Starting from a list of uncertainty sources as given in Table 5.7, the first step in an uncertainty analysis is to determine which sources may be a factor in the system, and which of the model's uncertainties can be evaluated at a given point in the design process. In practice, there are many more methods for evaluating parametric uncertainties than there are for non-parametric, especially when only a model and no hardware is available. The next step is an overview of methods to analyze non-parametric and parametric uncertainties in the early stages of design, particularly when no hardware or data exist.

5.2.2 Non-parametric uncertainty analysis

Many methods in the literature quantify non-parametric uncertainties by relying on the comparison of model predictions to hardware data. Paez, Hunter and Cafeo [97] describe how variations among multiple data sets can be used to generate stochastic processes that describe the output behavior. Campbell [16] compares the uncertainty between nominal hardware and a nominal model (of a system in gravity, for example), and maps the results

Table 5.7: Uncertainty sources

Material	**Gravity**	**Environmental**
Modulus	Joint pre-loading (locking)	Temperature varying E
Density	Body forces	Temperature varying ν
Point mass	Pre-stiffening	Temperature varying d_{31}
Damping coefficient	Sag (coupling)	Preload (thermal strain)
Composite ply orientation	Gravity-sensor coupling	Moisture
Composite matrix chemsity	Suspension dynamics	(mass, shape change)
	Pendulum modes	Outgassing
Model Error	B/C compliance	Air dissipation
Mismodeled loading	B/C damping	Density variation of air
Modeling simplification	B/C energy leakage	Speed variation of light in air
Rigid links	B/C noise sources	Acoustic noise
Rigid substructures		
Beam approx. for truss	**Degradation**	**Non-Linear**
Element formulation	Fastener hole wear	Modulus non-linearity
Model reduction	Change in modulus	Bearing stiction
Boundary conditions	Cracks/crack density	Bearing rattle
Cross-inertias	Bearing wear	Bearing imbalance
(bending, rotary)		Bearing shape irregularity
Sensor misalignment	**Manufacturing/Testing**	Joint stick/slip
Rotation, translation	Geometric tolerance	Loose fastener
Interface compliance	Material residual stress	
Preload	Fastener torque	**Policy**
(De)stiffening	Preload	Cost
Static deformation		Mission goal
Fastener preload		
Eccentric loading		**Miscellaneous**
Joint rigidity		Optical effect of air
Gross incompetence		

to a modified model of the structure (of the system on-orbit) to predict the uncertainty bounds of the modified (on-orbit) hardware. While these methods are powerful tools for evaluating the non-parametric uncertainties of structural models, they all require hardware to exist. If only a model is available there are a limited number of tools available to place bounds on the system due to these uncertainties.

Some of the non-parametric uncertainties listed in Table 5.7 can be evaluated using more detailed models. For example, the effect of mesh fidelity can be evaluated by increasing the mesh density and observing the resulting changes in model outputs. When the changes are appropriately small, no further increases in mesh fidelity is required. Non-linear effects can

be addressed by building a non-linear model of a system. Other non-parametric uncertainties are more challenging to identify and reduce. Model errors due to the incorrect use of elements may not be apparent without comparison to data.

A tool to describe the total uncertainty in dynamic models is Hasselman's database of aerospace structures [25]. This is a compilation of data gained from prior flexible structures for estimating the uncertainty of new models. The differences between model and data from the historical structures are collected in covariance matrices. These covariances can then be used in a linear covariance propagation routine to estimate the uncertainty in a new model of a similar structure. Bounds on the transfer functions of the new models are produced. This approach is used by Bourgault [40] to examine model uncertainty for the Space Interferometry Mission. The method is limited by the number of historical structures in the database, and by the degree of similarity of those structures with planned future missions. Given the efforts to make future space imagers increasingly lightweight, this method may not be appropriate if their dynamic behavior is significantly different from the structures in the database.

Another approach that also relies on historical trends in uncertainty is the use of model uncertainty factors (MUFs). While there are few sources describing MUFs in the literature (one is [41], which describes how to compute MUFs using data) they are suggested by industry to be used in a similar manner to structural factors of safety typically employed to multiply expected static loads. A frequency-based MUF, as shown in Figure 5-6(a), multiplies performance PSDs, as shown in Figure 5-6(b), to produce an upper bound on the system outputs. The MUF is frequency weighted to reflect the decreased confidence in the model at higher frequencies or at higher modal densities. When applied by experts in the field, the MUF may be an appropriate method of accounting for all sources of uncertainty in the model. Its limitation is that it lacks any insight into the actual behavior of the model, and provides limited guidance on ways of reducing the overall system uncertainty.

5.2.3 Methods of parametric uncertainty analysis

In a parametric uncertainty analysis, uncertain inputs are propagated through the model to produce a bound or distribution of uncertain outputs. The type of propagation method used depends on how the input uncertainties are modelled. Two classes of models are bounded or probabilistic. Bounded models, also referred to as convex uncertainty models, are absolute

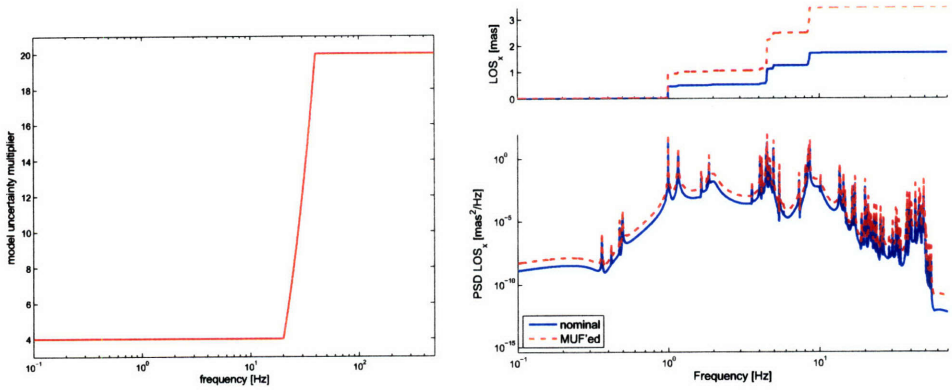

(a) MUF

(b) Nominal and MUF'ed closed loop LOS-x response

Figure 5-6: Frequency-based model uncertainty factors

limits above and below the nominal values that a parameter value would stay within. These models provide no information on the likelihood of a parameter being at any given value between those bounds, but only that the parameter value would remain within the bounds. Probabilistic models provide more information on the likelihood that a value is a certain distance from the nominal and are based on probability density functions (PDFs). What follows is a brief overview of popular methods used for each of these uncertainty models.

Bounded models

Bounded uncertainty models place upper and lower bounds on each of the parameters (Figure 5-7) and propagate these bounds to produce upper and lower bounds on the final system outputs (Figure 5-8). Bounded models may be considered to be more conservative than probabilistic models; unlike PDFs, which describe the likelihood of a system output meeting a requirement, bounded approaches can only describe whether or not the upper bound exceeds the output requirement. If probability descriptions of the parameters are not available however, bounded approaches provide a means of using the best available information to describe system uncertainties. Many methods used for propagating bounds involve running the simulation at multiple points across the bounded parameter space. Alternative methods include exhaustive searches, Monte Carlo sampling, and examining the corners (or vertices) of the bounded parameter space.

The exhaustive search method (described in [15]) divides each parameter space into a range of values. A full factorial experimental design can be created so that every combina-

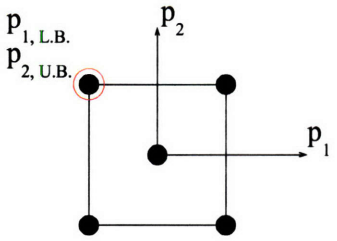

Figure 5-7: Example of worst-case bounds about two parameters

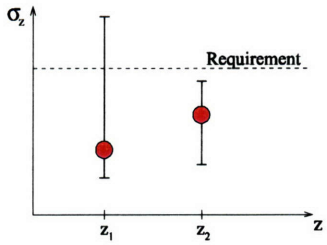

Figure 5-8: Uncertainty bounds for two outputs about their nominal values

tion of values across all parameters are used in the simulation. This allows the parameter space to be covered uniformly, but requires a large number of simulations. Given k parameters each divided into a range of n possible values, n^k runs are necessary. For 10 parameters each divided into only 10 values, this number is 10^{10} runs, which would be prohibitively large for the dynamic simulations being run.

An alternative approach is Monte Carlo sampling, which treats the parameter bounds as the limits of a uniform PDF. Instead of stepping through every parameter value like the exhaustive search method, Monte Carlo takes random samples from the parameter space. The simulation outputs are collected and the extreme values are the performance bounds of the system. If the actual parameter PDFs were described by uniform functions, the results could be interpreted as a discrete probability mass function (PMF), to which a continuous output PDF could be fitted. In the bounded case however, it is still assumed that the actual input PDFs are not known, and so the output points do not have a probabilistic interpretation. If the nature of the system is such that the upper bound could result from any combination of parameter values that are between the bounds, Monte Carlo allows the parameter space to be investigated with fewer runs than the exhaustive search method. Nevertheless, a large number of Monte Carlo runs may be necessary to adequately sample the space and identify the upper performance bounds.

If it can be reasonably assumed that the upper bound performance of the system will occur at the parameter limits, only combinations of parameters at their limits need to be run in a simulation. This requires many fewer simulations runs than the exhaustive search or Monte Carlo methods. This approach to uncertainty has been termed the vertex approach, since it predicts bounds on the performance by checking each of the vertices of the uncertainty space. Elishakoff and Ben-Haim refer to these methods as uncertainty

using convex models [62, 61] since the method assumes that there are no combinations of values from between the limits that cause a greater output response. If each vertex for k parameters is checked, the number of simulations is now only 2^k. For the case of 10 parameters, this reduces the simulations needed to 1024 - still a large number but a significant improvement over the alternative methods. This number still grows quickly with k, so for computationally intensive models it helps to limit the parameters to those which influence the system most.

A related bounded approach described by Gutierrez [26] uses the first-order sensitivity information between the output performances σ and input parameters p to compute the performance bounds based on small changes in p.

$$\Delta\sigma \approx \frac{\partial\sigma}{\partial p}\Delta p \tag{5.17}$$

Once the sensitivities are computed, the performance uncertainty $\Delta\sigma$ at different levels of Δp can be determined. Since this approach relies on first order gradient information, its validity is only as good as that of the gradient. Often this limits the approach to small perturbations in p. If the sensitivities are not available, such as for the non-linear WFE, this approach may not be practical.

Probabilistic models

Most often in engineering applications, the requirements must ultimately be met with a given probability of success. Bounded approaches provide only an absolute answer to whether or not an output meets its requirement, but provide no insight into whether an output is *likely* to meet that worst-case bound. Probabilistic approaches give the likelihood that an output will meet or exceed requirements. This reduces the conservatism of the bounded uncertainty analysis.

A probabilistic uncertainty approach computes the probability density function (PDF) for model outputs, given the input PDFs. The normal or Gaussian PDF is used in many applications. Its basic form for a random variable x is [98]

$$f_X(x) = \frac{1}{\sqrt{2\pi}\sigma}\exp\left[-\frac{1}{2\sigma^2}(x-m_x)^2\right] \tag{5.18}$$

with a mean value of m_x and variance σ^2. Many uncertainty techniques are based on the

Gaussian distribution. The mean value is just the nominal response of the model given the nominal values of the input parameters. All that remains of the uncertainty analysis is to propagate the variance of the input parameters through the model, to determine the variance of the outputs.

Reliability methods based on propagating variance are described in Melchers [99], including the First- and Second-Order Reliability Methods (FORM and SORM), which determine the probability of failure of a system with normal random variable inputs. The limit state function, which defines the failure regions of the response, are approximated by either first or second order functions. Examples are shown in References [100] and [101].

Linear Covariance Propagation (LCP) is an alternative approach that uses a Taylor series expansion of the outputs and then assumes that Higher Order Terms (H.O.T.) in the design objective function are negligible:

$$J(\alpha) = J_o + \frac{\partial J}{\partial \alpha} + H.O.T. \approx J_o + \frac{\partial J}{\partial \alpha} \tag{5.19}$$

where α is a vector of uncertain parameters and the sensitivities of the output to the parameters α can be computed by the sensitivity method desribed in Section 5.1.1. Under the assumption that α is a normally distributed vector random variable, $\alpha \sim N(\mu_\alpha, \Sigma_{\alpha\alpha})$, the variance of the objective can be computed from the sensitivity,

$$E[J] \approx J(\mu_\alpha) \tag{5.20}$$

$$E[J^2] \approx \frac{\partial J}{\partial \alpha} \Sigma_{\alpha\alpha} \frac{\partial J^T}{\partial \alpha} \tag{5.21}$$

When the parameters are independent, the contribution of each parameter to the variance of the output can be computed:

$$E[J^2] \approx \sum_{i=1}^{n_p} \frac{\partial J}{\partial \alpha_i} \sigma_{\alpha_i}^2 \frac{\partial J^T}{\partial \alpha_i} \tag{5.22}$$

where n_p is the number of parameters. Given the sensitivities of the system to the input parameters, this method quickly evaluates the uncertainty due to many input parameters, but it assumes that all of the parameter uncertainties are described using Gaussian PDFs.

If parameter uncertainty models are described by any probability density function other than Gaussian, propagation techniques can quickly become more computationally inten-

sive. Instead of solving for just two numbers: the mean and variance of the normal curve, it may be necessary to compute every point on the output PDF. There are some references that recommend transforming non-Gassian PDFs to Gaussian, and then using the techniques just described to propagate the Gaussian distribution. References such as Rackwitz and Fiessler [102] and Thoft-Christensen and Murotsu [103] present a basic transformation approach that is presented in Appendix A.

Transformation of PDFs into Gaussian is only an approximation. Especially when a high probability of success is required and the tail of the cumulative distribution function (CDF, integral of the PDF) curves must be accurately modeled, or when the Gaussian transformation no longer captures important higher order behavior of the actual PDF, it is necessary to turn to direct methods of propagating PDFs. Monte Carlo sampling is perhaps the best-known propagation technique, in which random samples based on the input PDF are run through the model. Once enough output data points have been collected, their mean and moments can be taken to form the output PDF. Reference [51] provides a good overview of Monte Carlo sampling, along with other sampling techniques that try to reduce the large computational time. These include Stratified Monte Carlo sampling, Quasi-Monte Carlo sampling, and Latin Hypercube sampling.

An alternative propagation technique relies on the analytic PDF transformation equation [82].

$$f_\Sigma(\sigma) = \left|\frac{\partial p}{\partial \sigma}\right| f_P(p) \tag{5.23}$$

The Change of Variables method based on this equation is described in Appendex B. Although this approach does provide greater detail of the distributions tails, it can also be computationally expensive, especially if the function is non-monotonic, leading to a singularity in the sensitivity $\frac{\partial p}{\partial \sigma}$.

Disadvantages of probabilistic uncertainty techniques include the computational time required for these approaches, especially for very large models. The other key problem is the accuracy of input distributions. While the Gaussian distribution is often chosen because of its simplicity, it may not be the appropriate distribution for a given input. More accurate distributions for the many parameters that make up a dynamic integrated model are not readily available in open literature. They can be difficult to determine empirically because

of the large number of tests required for confidence in the distribution. These problems in terms of using probabilistic approaches for early-stage integrated modeling analysis will be discussed next.

5.2.4 Integrated modeling uncertainty analysis

The choice of uncertainty analysis method for spacecraft integrated models depends both on how the results would be used at the current design stage, and on the availability and quality of uncertainty models that describe the input parameters. In the conceptual or early preliminary stages of the design lifecycle, the goals of the analysis are not necessarily to confirm that the requirements will be met to a particular percentage probability. The conceptual models themselves are low-fidelity (stick model FEM, simplified or approximated integrated model components, lack of testbed data for component validation) that they are not expected to be able to very accurately predict the final flight performance of the mission. The benefit of these early stage integrated models are more to provide insights into the design, and when multiple models are available to indicate which design will give better performance relative to the other. Uncertainty analysis at this stage can indicate whether a design is robust to parametric uncertainty, but for this purpose a bounded analysis may be as valid as a probabilistic one. In any case, methods such as Monte Carlo which give very accurate output distributions but at a high computational cost may be too computationally limiting at these early stages, when quick design studies of potential architectures are being evaluated for feasibility.

The other issue is that of availability of parameter uncertainty models. Probabilistic descriptions of all of the inputs to a model may be difficult to come by. Unless this data is stored in databases for future use, it may be costly to procure samples and run tests to characterize all of the inputs. A data set for modulus of a lexan strut was acquired by the author [104], but only a limited number of samples were available, so the statistical significance of the data may be questioned. Simonian [105] has tried to produce distributions of modal damping based on data sets from a number of surveyed satellites. Generally however, probabilistic descriptions of material properties or other tolerances are not available. An option is to assume a Gaussian distribution, since a standard deviation may be available from either data sheets or corporate knowledge, but then validity of the assumption is at issue. Ben-Haim and Elishakoff in [61], and Elishakoff in [62], suggest that in the absence

of a valid probability distribution, non-probabilistic methods may be just as applicable.

> "Models of uncertainty of both sorts - probabilistic and non-probabilistic - are relevant in appropriate circumstances."

> "... where the necessary information to formulate a stochastic model is at hand, it is fully justifiable to apply probabilistic methods. ... The situation is different if we do not possess sufficient probabilistic information. Often only very limited knowledge is available and appropriate mathematical tools are needed."

The point is made that incorrect probability inputs can in some cases skew the results. This can fool the analyst into believing incorrectly that the given probability of success was met. Especially given the lack of probabilistic parameter models at early stages of design, bounded methods may provide just as valid information as to the robustness of the system.

For these reasons: the general immaturity of the integrated models and the lack of empirically-based parameter distributions, a bounded approach is recommended for the dynamic analysis using conceptual integrated models. At the very least, it is presupposed that lower- and upper-bounds on each parameter are available. The vertex method will be used to examine each corner of the parameter space. This method was used by Masterson [15], who shows on a simplified version of the Terrestrial Planet Finder, Structurally Connected Interferometer that the vertex search provides an upper bound on the response compared to 500 Monte Carlo runs. A similar validation exercise is shown in the next section, which suggests that although the response space is not entirely convex (i.e. there are isolated cases in which parameters inside the bounds exceed the vertex responses), convexity is an appropriate assumption for this stage in the analysis.

5.3 Example: TPF-FFI

An example of the critical parameter identification method and bounded uncertainty analysis is shown with the TPF-FFI integrated model assembled in Chapter 3. The nominal results of the model were given in Section 3.4.2, which showed that the closed loop line-of-sight jitter performance met the requirement of 10.48 mas, while the wave front error failed to meet its requirement of 12.08 nm by several orders of magnitude. While additional analysis of the wave front error is certainly recommended for the nominal model, a critical

parameter analysis is still appropriate at this stage. By identifying parameters that most influence the outputs, additional studies can begin to better characterize those parameters and determine how to reduce their influence. An uncertainty analysis at this stage also provides the first indication of how wide the uncertainty space is about the nominal values.

5.3.1 Critical parameter identification

The critical parameter identification technique using design of experiments to guide the simulations is demonstrated. This technique is first compared to the sensitivity analysis from Section 5.1.1. While the relative influence results from Equation 5.16 are not themselves sensitivities, both methods should be able to identify the parameters that most influence the outputs. Note that since wave front error is not directly output from the state-space model, sensitivities to it can not be computed using the analytic method described. The relative influence values of parameters to WFE can be evaluated however, and are shown in the following results.

All of the parameters given in Tables 5.1 and 5.2, except for optical control bandwidth, were included in the critical parameter identification. Damping was also included, for a total of 13 parameters. Instead of the full factorial design with $2^{13} = 8192$ runs, a fractional factorial design of resolution IV was generated requiring only 32 runs. The resulting relative influence (RI) values are illustrated using bar charts in Figure 5-9. Since the total sum of squares of the responses include interaction effects along with the parameter main effects (Equation 5.15), the bars will not necessarily sum to 1.0. The RI values in percentages are also given in Table 5.8. For each parameter, the RI values are given for the outputs LOS-x, LOS-y and WFE, with boxes drawn around RI values greater than 10% to highlight the parameters that most effect the outputs.

The two plots in Figure 5-9 (and results in Table 5.8) represent two levels of parameter variation about the nominal values. Different levels were examined to judge their effect on the critical parameters identified. In the first, 5-9(a), each parameter is varied 0.01% about its nominal value, and in 5-9(b) each parameter is varied by 0.5%. Obvious differences in the final RI values can be seen between these two plots. In 5-9(a), the modulus of the sunshade booms strongly influence the LOS and WFE outputs, and the modulus of the SST bars influence LOS-x. Other than these parameters however, nearly all of the variation in outputs is caused by the isolator corner frequencies. Their effect is even greater in Figure 5-

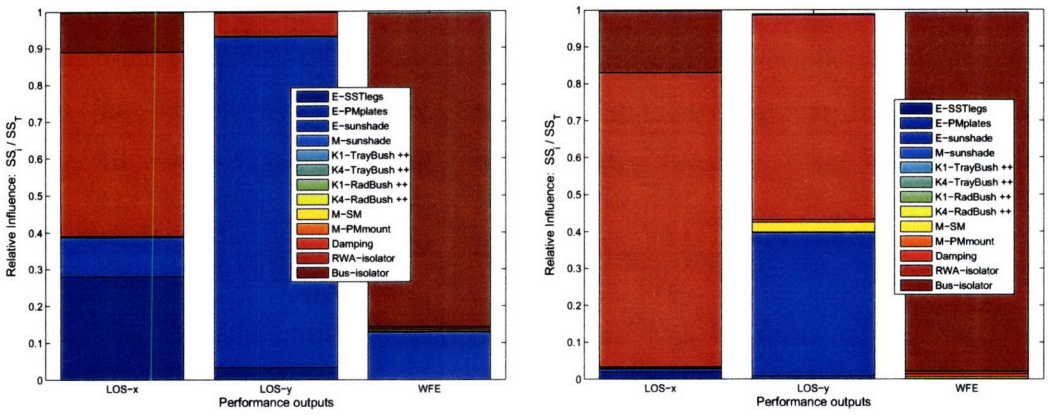

(a) $\Delta = 0.01\%$ (b) $\Delta = 0.5\%$

Figure 5-9: Initial ANOVA results for two levels of variation

9(b), where they dominate the response of LOS-x and WFE with an RI value of over 96%. That the RI value is nearly 100% also indicates that there is very little interaction between parameters; all of the variations are main effects of the isolators. In Figure 5-2 isolator frequency was already shown to influence the performance more than parameters such as modulus; these ANOVA results support that trend, especially at greater variations from the nominal parameter values.

These results also suggest that such dominant parameters as the isolator corner fre-

Table 5.8: TPF-FFI ANOVA results: percentage relative influence values including isolators

	$\Delta = 0.01\%$			$\Delta = 0.5\%$		
Parameter	LOS_x	LOS_y	WFE	LOS_x	LOS_y	WFE
SST bar modulus	27.9	3.2	-	1.9	0.8	-
PM plate modulus	-	-	-	-	-	-
Sunshade boom modulus	10.7	89.8	12.8	0.7	38.7	-
Sunshade mass	-	-	0.2	-	-	-
Tray trans. stiffness	-	-	-	-	-	-
Tray rot. stiffness	0.2	-	-	0.3	0.2	-
Radiator trans. stiffness	-	-	-	-	-	-
Radiator rot. stiffness	-	-	-	-	-	-
SM mass	-	0.1	0.5	-	2.6	0.5
PM mount masses	-	-	-	-	-	-
Damping	0.2	0.1	0.5	0.3	0.7	0.8
RWA isolator freq.	49.9	6.3	0.4	79.5	55.4	0.7
Bus isolator freq.	10.9	0.3	85.1	16.8	0.3	97.1

quencies are not appropriate to include in this critical parameter identification routine. To begin with, the values can be changed by the designer, so the corner frequency is more a design variable than an uncertainty parameter. Further, because the frequency is a variable specifically chosen to influence the performance, it should be expected to have a high RI value. By dominating the ANOVA results, the effect of any other parameter that is not known by the designer (the exact value of modulus, for example) is reduced or eliminated, potentially hiding an important uncertain parameter. A second round of critical parameter identification is recommended, using only those parameters that are not also design variables.

The results from this analysis are still useful in that they can be qualitatively compared to the sensitivity analysis of Section 5.1.1. Both techniques identify the greatest contributors as from the RWA and bus isolators, followed by the sunshade and SST moduli. (Note that the ANOVA analysis did not include optical control bandwidth, which was an important parameter identified in the sensitivity analysis.) Each technique also identified the lesser influence of SM mass, as well as the still lesser influence of damping and the stray light tray rotational stiffness. All of the other parameters have negligible influence on the outputs.

This initial run verifies that the same information can be obtained using an analytical sensitivity analysis as with an ANOVA analysis of computer simulation results. The simulations did require many more computer runs: 32 runs at each of the two levels, compared to a single analysis in which the partial differentials of the state matrices were computed with respect to the parameters. The advantage of using computer simulations is that the results do not depend on having a state-space representation of the system, and the outputs need not be the outputs of that system. Wave front error is not directly calculated from the state matrices, so a sensitivity to it cannot be found; it is trivial to include such outputs in the ANOVA analysis when the simulation itself is being re-run. DOE-driven computer simulations followed by ANOVA provides a means of identifying critical uncertainty parameters when sensitivity analysis techniques are not appropriate.

Given the results from the first analysis, it is obvious that the isolator corner frequencies are swamping the influences of the other parameters. A second analysis is run without varying the isolators, but including additional parameters such as material density of the PM plates, modulus of the truss elements connecting the bus to the payload, and modulus and density of the optical bench supporting the PM and associated optical instruments.

These additional parameters were chosen based upon engineering judgement of which system parameters are likely to have a large influence on the outputs. Fifteen parameters were selected for this case:

- SST bar modulus
- Modulus of primary mirror plates
- Density of primary mirror plates
- Sunshade modulus
- Payload-Truss bar modulus
- Optical bench modulus
- Optical bench density
- Stiffness of stray light tray springs in translation
- Stiffness of stray light tray springs in rotation
- Stiffness of radiator springs in translation
- Stiffness of radiator springs in rotation
- Sunshade mass
- Secondary mirror mass
- Primary mirror mount masses
- Modal damping

Since a vertex-search uncertainty analysis on so many parameters would take prohibitively long ($2^{15} = 32,768$ runs) the critical uncertainty parameter identification technique is run again. A fractional factorial experiment of resolution IV with 32 runs is generated. The system is run at multiple parameter levels about the nominal. Figure 5-10 shows the relative influence results with variations Δ of 0.01%, 0.1%, 0.5%, 1%, 5% and 10%. The results are also given in Table 5.9. There is not nearly the difference between these plots as is seen in Figure 5-9. In that case, the isolators dominate the results at higher levels of variation and swamp out the effect of all other parameters. The plots in Figure 5-10 show a greater degree of uniformity, and, while there are differences across the plots, the same parameters tend to contribute to the variations for each Δ.

In Table 5.9 relative influence values above 10% are boxed in order to highlight the largest contributors. It is clear that three of the parameters: density of the PM plates, modulus of the sunshade booms and modulus of the optical bench plates are important

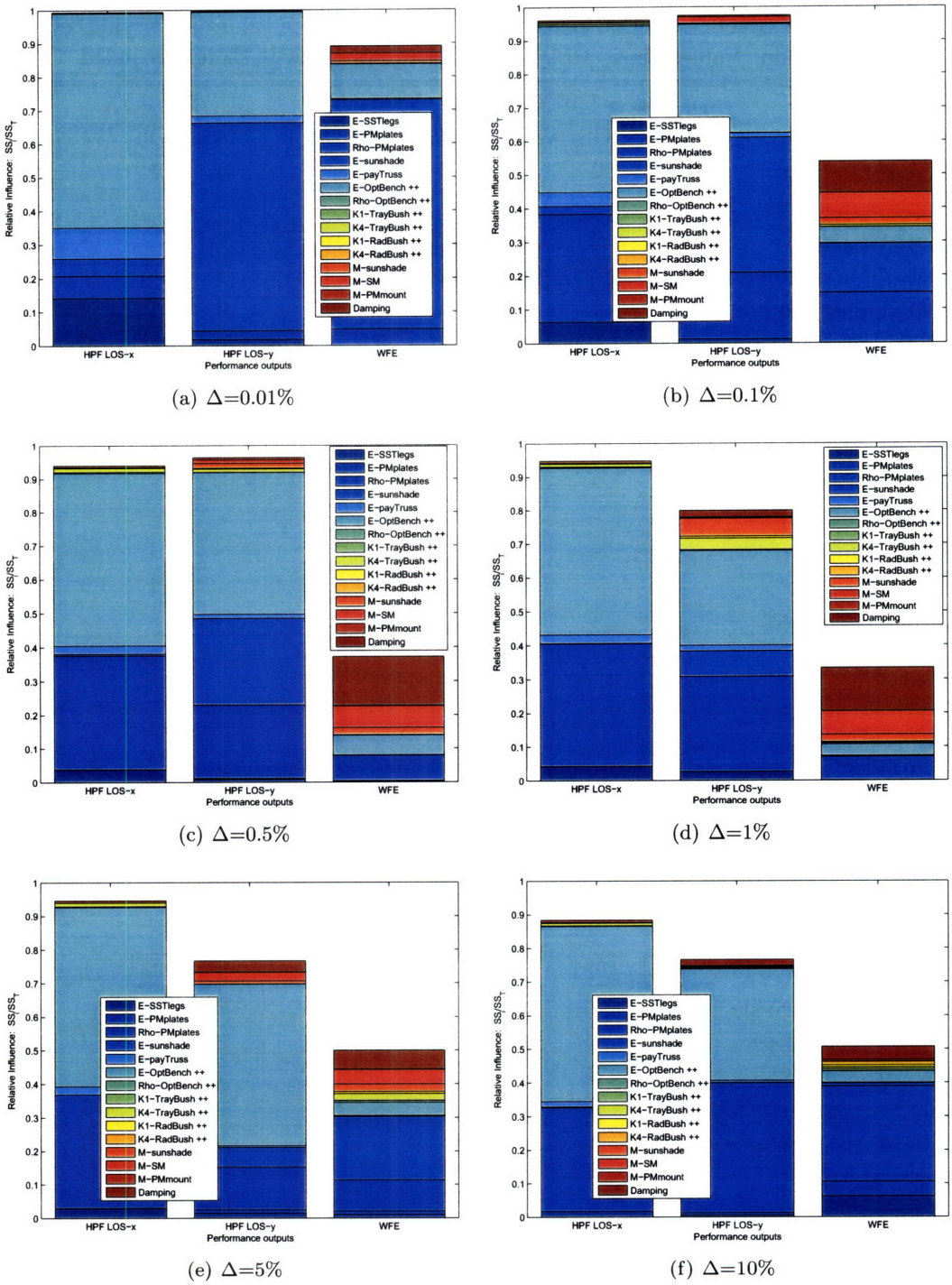

(a) Δ=0.01%

(b) Δ=0.1%

(c) Δ=0.5%

(d) Δ=1%

(e) Δ=5%

(f) Δ=10%

Figure 5-10: TPF-FFI relative influence values across varying levels of parameter variation

Table 5.9: TPF-FFI ANOVA results: percentage relative influence values at varying levels of parameter variation. Values above 10% boxed and values below 0.5% not included.

	$\Delta = 0.01\%$			$\Delta = 0.1\%$			$\Delta = 0.5\%$		
Parameter	LOS_x	LOS_y	WFE	LOS_x	LOS_y	WFE	LOS_x	LOS_y	WFE
SST bar modulus	14	2	-	6	1	-	4	1	-
PM plate modulus	-	-	-	-	-	-	-	-	-
PM plates density	7	3	5	32	20	15	34	22	8
Sunshade boom modulus	5	62	68	2	40	14	1	25	-
Payload-truss modulus	9	2	-	4	1	-	2	1	-
Optical bench modulus	64	31	10	50	32	5	51	42	6
Optical bench density	-	-	-	1	-	-	-	-	-
Tray trans. stiffness	-	-	-	-	-	-	-	-	-
Tray rot. stiffness	-	-	-	1	-	1	1	1	-
Radiator trans. stiffness	-	-	-	-	-	-	-	-	-
Radiator rot. stiffness	-	-	-	-	-	-	-	-	-
Sunshade mass	-	-	1	-	-	2	-	1	2
SM mass	-	-	2	-	2	8	-	1	6
PM mount masses	-	-	-	-	-	-	-	-	-
Damping	-	-	2	1	-	9	1	1	14

	$\Delta = 1\%$			$\Delta = 5\%$			$\Delta = 10\%$		
Parameter	LOS_x	LOS_y	WFE	LOS_x	LOS_y	WFE	LOS_x	LOS_y	WFE
SST bar modulus	4	3	-	3	1	1	2	-	6
PM plate modulus	-	-	-	-	1	1	-	1	4
PM plates density	36	28	7	34	13	9	31	39	28
Sunshade boom modulus	-	7	-	-	6	19	-	-	1
Payload-truss modulus	3	2	-	2	1	-	2	1	-
Optical bench modulus	50	28	3	53	48	4	52	33	3
Optical bench density	-	-	-	-	-	1	-	-	-
Tray trans. stiffness	-	-	-	-	-	-	-	-	1
Tray rot. stiffness	1	3	-	1	-	2	1	-	1
Radiator trans. stiffness	-	-	-	-	-	-	-	-	1
Radiator rot. stiffness	-	1	-	-	-	1	-	-	1
Sunshade mass	-	5	2	-	1	2	-	-	-
SM mass	-	-	7	-	3	4	-	-	-
PM mount masses	-	-	-	-	-	-	-	-	1
Damping	1	2	13	1	3	6	1	2	4

contributors across all of the experiments. The wave front error output is sensitive to more parameters than are the line-of-sight jitter outputs. In particular, variations in damping and mass of the secondary mirror contribute more to WFE than to either LOS metric. The effect of the secondary mirror mass is surprising, since WFE is computed based only on displacements of the primary mirror (through the PM zernikes). This suggests an interaction between the secondary mirror mass and the PM displacements. Since most of the WFE contribution comes from a rocking mode of the entire spacecraft, it is possible that changes in the secondary mirror mass influence that rocking mode and thereby the wave front error output. The relative influence plots in Figure 5-10 also suggest that the effect of parameter interactions is larger for WFE than they are for LOS, since the sum total of main effect contributions is much less for WFE. From Equation 5.15 this indicates that, with the absence of error in these deterministic computer experiments, the remaining relative influence contributors that would cause the bar plots to sum to 1.0 must be interaction effects.

Based on the relative influence results the number of uncertainty parameters that contribute significantly to the system outputs can be reduced. Parameters such as the stiffness of the radiator springs, mass of the primary mirror bipod mount, and density of the optical bench are shown to have only negligible contributions to the outputs and can be excluded from further analysis. Ultimately of the original 15 parameters, only eight are retained for an uncertainty analysis:

- SST bar modulus
- Density of primary mirror plates
- Sunshade modulus
- Payload-Truss bar modulus
- Optical Bench modulus
- Sunshade mass
- Secondary mirror mass
- Modal damping

A vertex-search uncertainty analysis with eight parameters will require 256 evaluations of the model. This number, while still large, is significantly less than the 32,768 runs that would have otherwise been necessary, and is well within the computational ability of a fast

desktop computer. The uncertainty analysis and its results are described next.

5.3.2 Uncertainty analysis

This TPF-FFI analysis is performed on a lower-fidelity model of the structure in the very early stages of mechanical design. No measurements have been performed (or are available) to describe the probabilistic distributions of the identified critical uncertainty parameters. Even if a complete probabilistic description of the parameters were available, the nature of many of the model sub-components (filters for isolators, geometric description of the optical outputs, etc.) will result in non-parametric uncertainties due to differences between the approximations and actual hardware. Until these uncertainties are also assessed (through higher fidelity models or testbed data) it is not possible to provide a probability that the mission will meet its requirements. At this stage of this analysis, it is possible to identify the trends due to parametric uncertainty and to begin research on creating better uncertainty models of the identified critical parameters.

Bounds on the outputs are found using the vertex-method search across the bounds of the parameter inputs. Table 5.10 gives the bounds for each of the eight uncertain parameters. Note that even these bounds are based on engineering judgement, and not on empirical data. The bounding values were found by assuming a 5% variation for the modulus of the SST legs, sunshade booms and payload truss bars. A 1% variation was assumed for the density of the PM plates and modulus of the optical bench. The bounds for the sunshade and secondary mirror masses are guesstimates, and the damping bounds are based on common values used for modal damping in flexible systems.

Table 5.10: Uncertainty bounds on critical parameters

Parameter	**units**	**Lower Bound**	**Nominal**	**Upper bound**
SST legs modulus	N/m^2	1.09×10^{11}	1.15×10^{11}	1.35×10^{11}
PM plate density	kg/m^3	2507	2532.08	2557
Sunshade modulus	N/m^2	1.09×10^{11}	1.15×10^{11}	1.35×10^{11}
Payload-truss bars modulus	N/m^2	1.09×10^{11}	1.15×10^{11}	1.35×10^{11}
Optical bench modulus	N/m^2	1.98×10^{11}	2.00×10^{11}	2.02×10^{11}
Sunshade mass	kg	35	39.1036	45
Secondary mirror mass	kg	19	19.4819	23
Modal damping	-	0.01%	0.01%	0.1%

Simulations of the model were run at each corner of the uncertainty space for a total of

$2^8 = 256$ runs. All of the results are plotted in Figure 5-11. The nominal results are marked with a circle, and the limits of the performance bounds are marked with horizontal bars at the top and bottom of each column of points. Note that even though this plot resembles a probabilistic distribution centered around a mean value, it should not be interpreted probabilistically. The inputs to the analysis are not probabilistic, so neither are the outputs. The relevant information is that, based on simulations at each of the 256 input bound vertices, the worst-case performances are no greater than the upper limits of the simulation results.

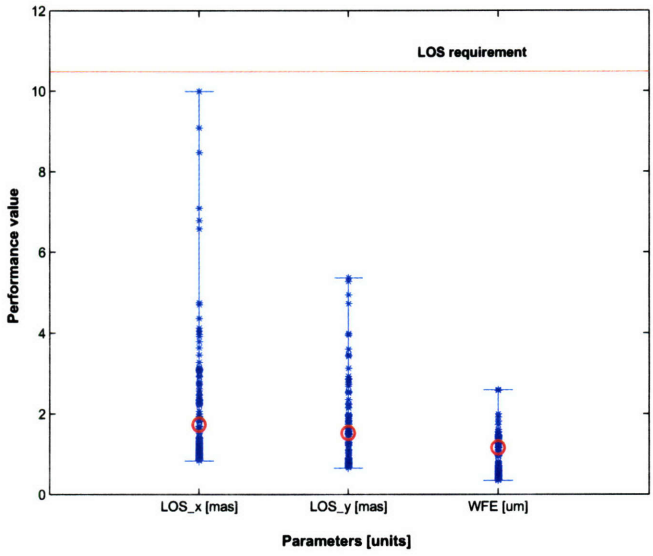

Figure 5-11: Simulation results from the uncertainty bounds vertex-search. The nominal output is denoted with a circle.

A line is draw on Figure 5-11 to represent the LOS jitter requirement of 10.48 mas. Even with uncertainty, LOS jitter about both the x- and y-axes remains below the requirement. This good news is tempered by the fact that non-parametric uncertainty is not accounted for in this analysis. Especially in the case of LOS-x, there is not much margin left between the performance upper bound and the requirement line. Compared to a 8.8 mas margin for the nominal response, the upper bound of the uncertain response only leaves 0.50 mas of margin. LOS-y is better, in that parametric uncertainty accounts for less than half the margin between the nominal performance and the requirement. Compared to the 8.96 mas margin in the nominal system, 5.12 mas remains between the LOS-y upper bound and the requirement. These results are good, in that even the presence of uncertainty the mission

meets its LOS requirement. However, the results also suggest that more analysis of the actual parametric bounds and of the non-parametric sources of uncertainty is necessary to ensure that the requirements are met in the final hardware. The wave front error output is on the order of microns, where the requirement is on the order of nanometers. The requirement line is not drawn on Figure 5-11 because it is never met across the uncertainty space.

For each of the three performances, it is of interest to note that besides indicating the worst-case results, many of the simulations are actually *better* than the nominal outputs. This suggests that the design could still be optimized for performance.

Although a probabilistic analysis is not attempted for this system due to the lack of probabilistic parameter distributions, a Monte Carlo analysis is performed to verify that the vertex search bounds are capturing the true worst-case performance of the system. The concern is whether there exist combinations of uncertainty parameter values between the limiting bounds that lead to worse performance outputs than at the bounds. If the worst-case results occur at the extremes of the bounded uncertainty space, the model is described as convex. Masterson [15] examines this problem for a simplified model of the TPF-Structurally Connected Interferometer concept. Using a Monte Carlo analysis with 500 samples, she shows that all of the Monte Carlo results are below the worst-case outputs from a vertex search, supporting the argument that the model is convex.

The convexity of the TPF-FFI model is testing by running a Monte Carlo analysis with 700 samples through the simulation. A different set of parameters is used in this example. The parameters and their bounds are given in Table 5.11. Note that the isolator is allowed to vary and wave front error is not included.

Table 5.11: Uncertainty bounds on critical parameters for comparison of vertex search to Monte Carlo results

Parameter	**units**	**Lower Bound**	**Nominal**	**Upper bound**
SST legs modulus	N/m^2	1.0925×10^{11}	1.15×10^{11}	1.2075×10^{11}
Sunshade modulus	N/m^2	1.0925×10^{11}	1.15×10^{11}	1.2075×10^{11}
Sunshade mass	kg	35	39.1036	45
Secondary mirror mass	kg	19	19.4819	23
Stray light tray rotational stiffness	Nm	101690	112985	124280
RWA isolator corner frequency	Hz	9	10	11

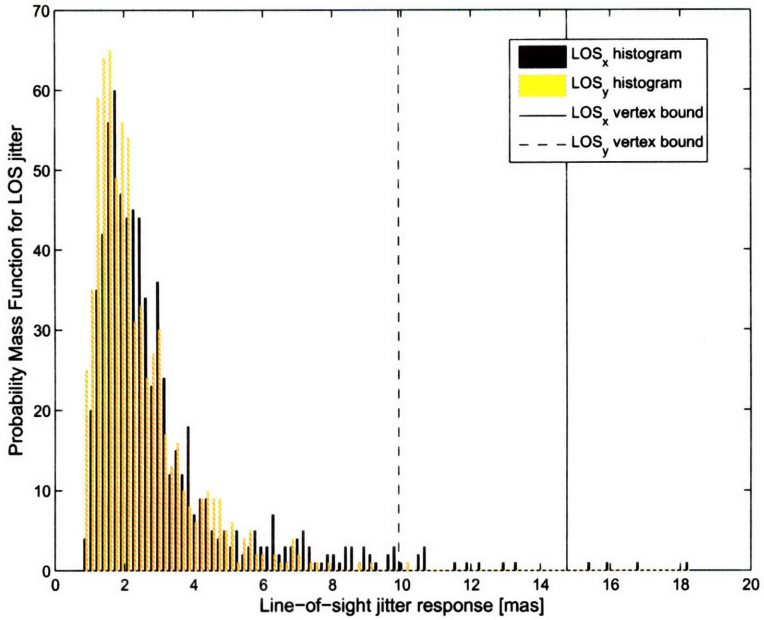

Figure 5-12: Probability mass function from Monte Carlo results, compared to worst-case vertex bound (vertical lines)

The parameters are sampled by assuming a uniform distribution between the lower and upper bounds. The resulting probability mass functions (PMF)[1] for LOS-x and LOS-y are given in Figure 5-12. The PMF is obviously slewed toward the lower end of the output values, and in fact falls off very sharply below the nominal results (1.7 mas and 1.5 mas for LOS-x and LOS-y, respectively).

Figure 5-13 compares the worst-case bounds from the vertex search to the results from the Monte Carlo simulations. Note that this figure shows that for these parameters the baseline results from the vertex search actually are worse than the results given in Figure 5-11; LOS-y has less than 1 mas of margin, and the upper bound for LOS-x is above the requirement. Comparing the vertex search method to Monte Carlo, for both performance outputs, there are clearly a small number of points that exceed the vertex search bounds limits. It is thought likely that in a modally dense system such as TPF, there are combinations of parameter values, not necessarily at the bounds, in which several modes lie on top of each other with the combined effect of adding significantly to the final RMS result. Luckily however, this seems to be a very rare occurrence. For LOS-x, there are

[1]The probability mass function (PMF) is the discrete counterpart to the continuous probability density function (PDF) [98]

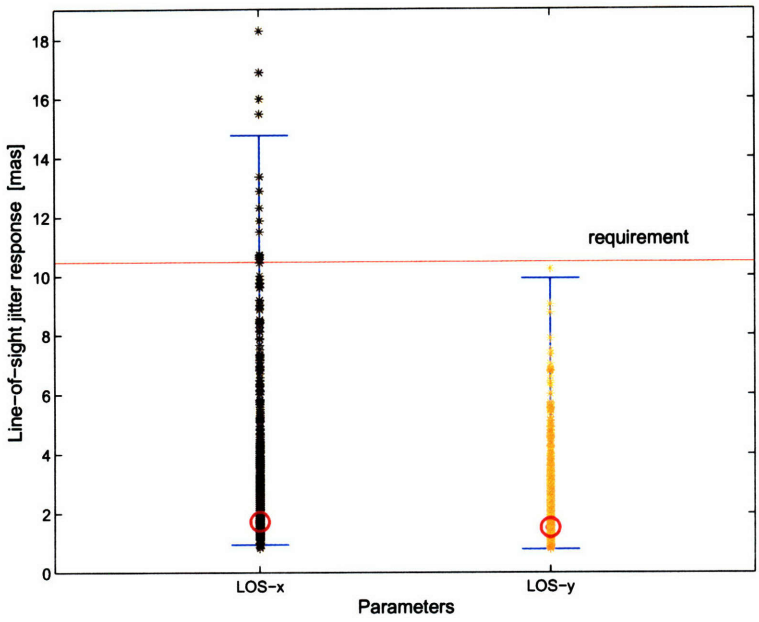

Figure 5-13: Comparison of results from worst-case vertex search (bars) to Monte Carlo samples (*). Nominal results indicated by (o).

only four instances out of 700 trials of the Monte Carlo results exceeding the vertex search bounds; 99.4% of the trials were below the vertex search bound. Only one point exceeded the LOS-y bound, so that 99.9% of the trials were below the vertex search bound. These results tend to validate the assumption that the vertex search method captures nearly all of the parametric uncertainty in the system. Especially given the time savings between the methods, the vertex search method is considered an appropriate tool for early-stage uncertainty analysis. Any remaining uncertainties due to the method could be grouped in with non-parametric sources of uncertainty, and accounted for at this stage using model uncertainty factors.

5.4 Conclusions

Methods of critical uncertainty parameter identification and uncertainty analysis for integrated models in the early stages of design are described. The results from a sensitivity analysis are compared to a method based on Design of Experiments techniques. The DOE approach is shown to identify the same critical parameters as the sensitivity analysis for a state-space system. The advantage of the DOE approach is that by using only simulation

outputs, the technique is not limited to states-space systems. Any simulation: linear or non-linear, frequency or time domain, can be used in the DOE approach.

Application of the mature field of DOE, with tools such as factorial experiments and analysis of variance, has benefits for analysis of opto-mechanical structures. Especially given the increasing importance of non-linear and thermal studies for spacecraft such as TPF, DOE provides established techniques for getting the most information out of a limited number of expensive (in time and computer resources) simulations. The need for these techniques is only increasing as computer become faster; now that design and analysis using simulations is practical for large models, techniques are still needed to direct the computer experimentation for the most efficient use of resources.

An example is shown using Design of Experiments and a bounded uncertainty analysis on the TPF-FFI integrated model. A large field of uncertain parameters was reduced to the eight parameters that most influence the outputs. The simulation-based approach to critical parameter identification is able to analyze not only LOS, but also the non-linear WFE which can not be included in an analytic sensitivity analysis. The resulting uncertainty analysis indicates that while LOS requirements are still met even with parametric uncertainty, there is not much margin remaining for non-parametric uncertainty. WFE was not met even in the nominal case. The vertex search method for propagating input uncertainty bounds is compared to the results of Monte Carlo sampling and is shown to be an appropriate tool for determining preliminary parametric uncertainty bounds of a model.

The uncertainty framework is summarized in Figure 5-14. For each design point, the design can be optimized to ensure that the nominal results meet the performance requirements. Once this is complete, engineering judgement can be used to survey the system parameters and choose all that may contribute to the parametric uncertainty of the system. From this larger group, the subset of parameters that quantifiably influence the outputs are identified through either a sensitivity analysis, or by running simulations based on a fractional factorial design matrix and analyzing the results using ANOVA. Once the critical uncertainty parameters are identified, bounded uncertainty models of the parameters are set, and output performance bounds can be computed using either the vertex search method, or by Monte Carlo sampling if time permits.

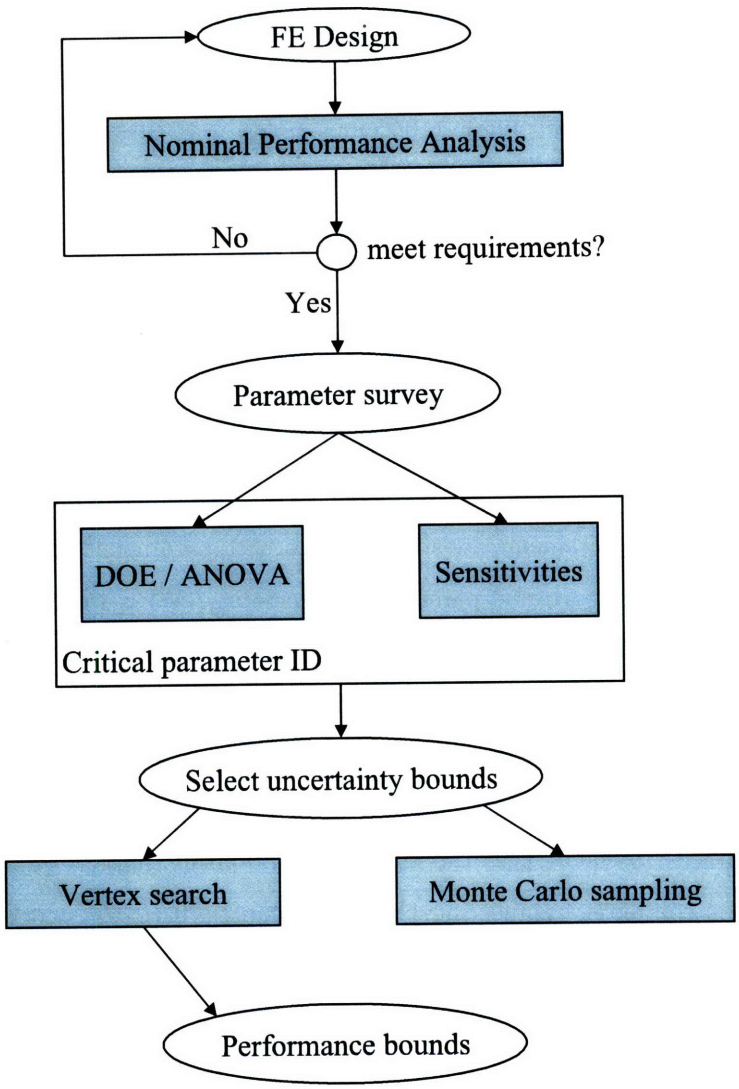

Figure 5-14: Uncertainty characterization framework

Chapter 6

Modular Optical Space Telescope Example

All of the tools and methods described in the previous chapters are applied to a new telescope design. The Modular Optical Space Telescope (MOST) is meant to represent the next generation of large optical space systems, in which lightweight mirrors, sparse or segmented apertures and the increased use of control are brought together to achieve high performance using larger mirrors (3+ meters in diameter) for greater optical resolution.[1] The challenge of these missions is that they must not only meet the optical science requirements, but also meet a range of other system metrics such as cost, mass, time to market, and availability on-orbit. The designs must be robust against uncertainties in the outputs and uncertainty analysis should begin at the start of the design cycle to support analytical validation of the design. Given that there is no heritage of flight-tested architectures, the designer is free to explore across the design variable trade space for architectures that best make use of new technologies while meeting the often conflicting requirements. The methods outlined in this thesis will be used together to support this multi-disciplinary conceptual design study.

The chapter will first describe the MOST modeling process, which is validated at a single design point with a comparison to the TPF-FFI structure. Figures of merit for both optical performance and system metrics will be defined. Using the free design variables, single- and double-parameter trades are first run to identify initial trends in the outputs. A larger trade space is then run and the results plotted to highlight the effect of individual

[1] In comparison, Hubble's primary mirror is 2.4 meters in diameter, and segmented mirror for JWST is planned to be 6.5 meters.

variables. Finally, for the identified optimal designs, the critical parameter identification technique is employed and a bounded uncertainty analysis run to judge the robustness of the designs. The final outputs are the identified superior architectures as well as feedback to the designer on which design variables are appropriate "knobs" for moving along the optimal front.

6.1 MOST model

The MOST parameterized finite element model and integrated dynamics model are constructed following the approaches used for TMT and the TPF spacecraft. An overview of the model is followed by results for a sample design realization.

6.1.1 Overview

Figure 6-1 shows three sample realizations of the MOST finite element model.[2] The basic spacecraft architecture includes a primary mirror and secondary mirror on the payload side of the spacecraft, and a separate bus containing subsystems such as reaction wheels. This basic architecture is similar to the TPF-FFI collector design described earlier. Whereas TPF was a single point design however, the MOST model is fully parameterized. Similar to the TMT design described in Section 4.5, optical parameters such as curvature of the mirror can be varied, leading to a shortening or lengthening of the PM-SM distance and appropriate changes in the secondary support tower (SST) height. Beyond these dimensional changes however, the TMT design was static in terms of design. MOST expands upon the TMT modeling process using modular functions in which individual components are built independently, and can be swapped to create new architectures. Figure 6-1 illustrates this modular concept by swapping out the type of aperture. Figure 6-1(a) shows a monolithic mirror. By changing a single top-level parameter a new mirror module is called, and in the place of the monolithic mirror a segmented mirror such as in Figures 6-1(b) and 6-1(c) is used instead. The use of modularity in the modeling effort allows a much wider range of spacecraft forms to be created and evaluated against each other than was possible with TMT.

The MOST model follows the parametrization rules formulated in Section 4.3. Every pa-

[2]The MOST finite element model was build by a collaboration of graduate students in the MIT SSL.

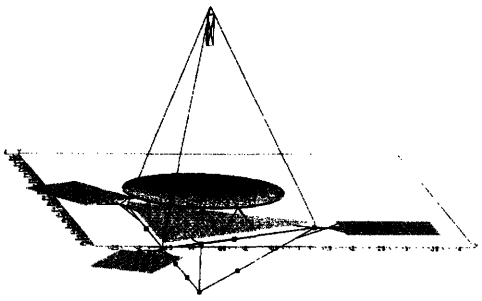

(a) 3 meter $f/1.0$ monolithic mirror

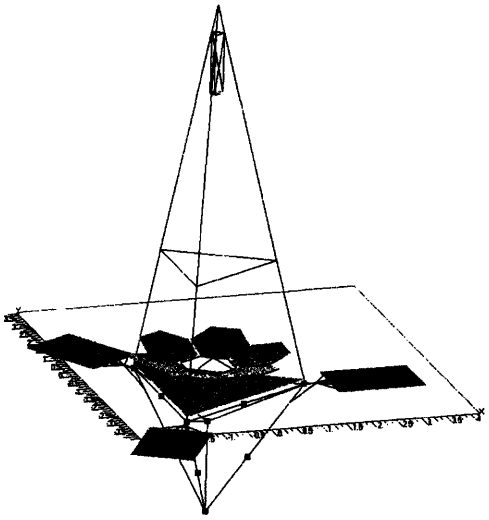

(b) 3 meter $f/2.0$ segmented mirror with crossbars on the SST

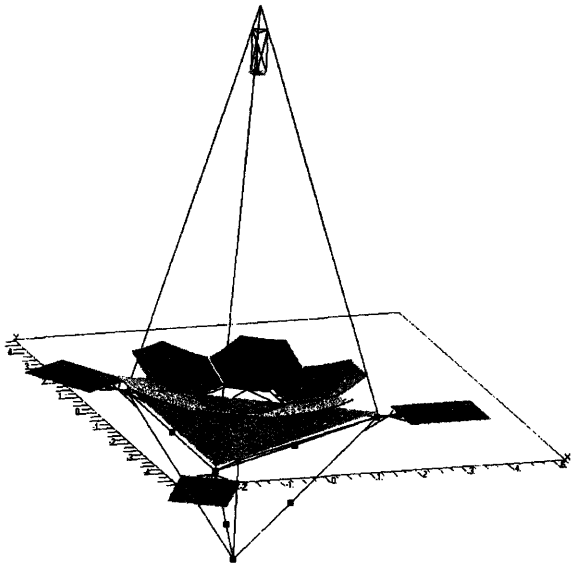

(c) 5 meter $f/1.5$ segmented mirror

Figure 6-1: Sample MOST architectures

rameter in the system is collected into a high-level *Parameters* function. These include high level discrete variables, such as which aperture or secondary support tower to use[3]. Continuous variables include diameter of the mirror and optical parameters such as f-number and final focal ratio that define the overall height and dimensions of the spacecraft. Individual components such as a ribbed primary mirror (Figure 6-2) require inputs such as the number of rings of ribs, and aspect ratio of the ribs. All material properties (modulus, material density, Poisson's ratio, etc.) and element geometry (plate thicknesses, bar cross-sectional areas and area moments of inertia) are stored and can be updated as materials change, or as new values are obtained from either vendors or material testing. Identification numbers for Nastran grid points, elements, properties and materials are even defined at the highest level so that as new Nastran cards are added, or if any identification numbers overlap, the numbers can be changed without the need to edit the lower-level functions. Beyond the finite element parameters, additional parameters for the integrated dynamics model or analysis routines are used, including modal damping, isolator filter corner frequencies, and slew rates.

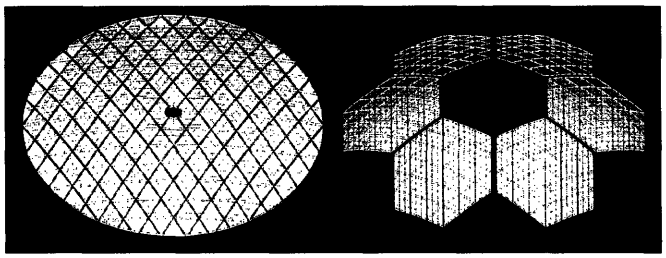

Figure 6-2: Sample finite element models of the rib-stiffened mirrors used on MOST [106] The view shows the backs of the mirrors with ribs standing up from the facesheet. Several finite element plate elements are visible in each cell.

The individual components of the structure and of the integrated model are created in separate modules that communicate with one another to assemble the components into a complete spacecraft. A block diagram of the modules that build the finite element model is shown in Figure 6-3. Each line drawn between blocks (which are individual MATLAB functions) represents data being passed into and out of the function. Choices of architecture, dimensions and relevant Nastran material and property identification numbers are passed

[3]Although not shown in this work, additional designs of the SST have been implemented besides the tripod tower shown here. Changes in the aperture are also possible, including using multiple mirrors in a Golay-type of arrangement, or creating an off-axis system with non-symmetric curvature of the primary mirror.

down to lower level functions. Data passed upward to higher level functions include grid points used to connect components together (for example to connect the primary mirror to the optical bench) or element identification numbers needed to define the inputs and outputs of the state-space model. As long as these data structures are maintained, the components modules themselves can be updated or even replaced entirely, with new functions seamlessly integrated into the structural system. In this manner, additional mirror, bus or secondary support tower designs can be quickly generated, connected to the spacecraft and evaluated with the full suite of analytical tools.

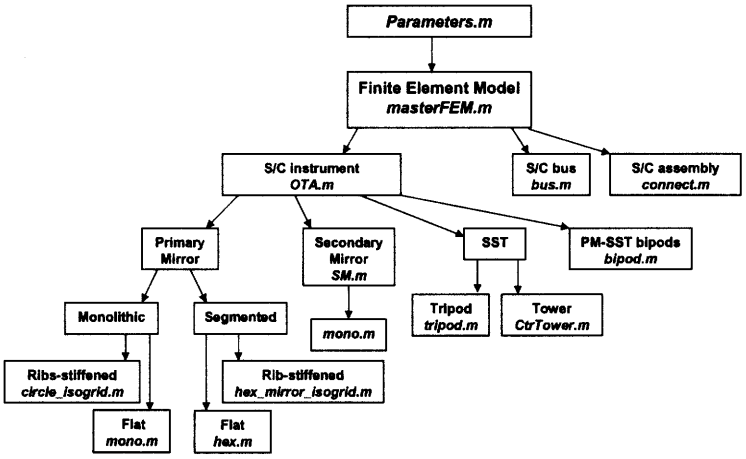

Figure 6-3: Block diagram showing MOST finite element modules. MATLAB function names given in italics.

For the MOST spacecraft as it is currently modeled, key design variables and typical values are given in Table 6.1. Some of these will be varied in the next sections.

6.1.2 Output metrics

Figures of merit for the MOST project include both optical performance outputs as well as mission metrics. For the optical performances, line-of-sight (LOS) jitter and wave front error are both computed under steady-state dynamic excitation from reaction wheel disturbances. The harmonic structure of the disturbance models (harmonic numbers and relative amplitudes of the coefficients) are based on the Hubble reaction wheels. The absolute amplitudes of the coefficients are scaled by the slewing needs of the model, as was described in Section 4.4.1. The broadband reaction wheel model is used.

Line-of-sight is computed based on a variation of Equation 3.9 for a focal telescope, and

Table 6.1: MOST design variables with nominal values or ranges

Parameter	Nominal values
Mirror type	Monolithic vs. Segmented, Flat vs. Ribbed mirrors
SST type	Tripod, with and without horizontal crossbars
PM diameter	3 or 5 meters
f-number	1.0 - 2.0
Final focal ratio	20
Conic constant	-1
Mirror areal density	10 - 20 kg/m^2
Mirror rib aspect ratio	4
Radius of SST struts	7.4 cm
Solar panel fundamental frequency	0.5 Hz
Modal damping	1%
RWA isolator corner frequency	10 Hz
Bus isolator corner frequency	2 Hz
Slew profile	5 degrees in 10 seconds

includes tip and tilt of a fast-steering mirror (FSM) that can be used for closed-loop optical control:

$$\begin{aligned} LOS_x &= -\frac{1}{f_1}\delta_{P_y} + \frac{(M-1)}{Mf_1}\delta_{S_y} + \frac{1}{Mf_1}\delta_{F_y} + 2\alpha_{P_x} - \frac{2}{M+1}\alpha_{S_x} - \frac{2}{M+1}\alpha_{F_x} \quad (6.1) \\ LOS_y &= \frac{1}{f_1}\delta_{P_x} - \frac{(M-1)}{Mf_1}\delta_{S_x} - \frac{1}{Mf_1}\delta_{F_x} + 2\alpha_{P_y} - \frac{2}{M+1}\alpha_{S_y} - \frac{2}{M+1}\alpha_{F_y} \end{aligned}$$

where f_1 is the focal length of the primary mirror, f_2 the focal length of the secondary mirror and M is the secondary mirror magnification. The translations δ and rotations α are of single grid points on the primary mirror (P), secondary mirror (S), and fast steering mirror (F).

Along with line-of-sight, an approximation for wave front error (WFE) is found by computing the root sum square of the z-displacements (out of the plane of the mirror) of 20 sample points across the face of the primary mirror.

$$WFE = \sqrt{((\delta z_i)^2} \quad (6.2)$$

This method is only a substitute for a Zernike-based computation of wave front error, but will still provide a response that varies in a manner similar to the outputs of an optically modeled wave-front error.

Requirements are set for both of the performance outputs. For diffraction limited performance, LOS jitter is constrained to be less than

$$\Theta_{LOS} \leq 1.22\frac{\lambda}{D} \tag{6.3}$$

where λ is the wavelength of light, and D is the mirror diameter [70]. To ensure that the science requirements are met, this is treated as a 3σ bound, so the 1σ requirement is one third of this [24]. For a 3-meter mirror observing visible light at a wavelength of 600 nm, the resulting LOS requirement is 16.8 mas. Since performance degradation is due to more factors than just the dynamic disturbances investigated here, it is assumed that dynamics is only budgeted 10% of this requirement. This means that the final LOS requirement for dynamic jitter of a 3-meter mirror is 1.7 mas.

The requirement on wave front error based on surface displacements of the primary mirror is given as

$$WFE \leq \frac{\lambda}{20} \tag{6.4}$$

Again treating this as a 3σ requirement and allocating only 10% to dynamics results in a requirement of 1 nm for a visible telescope.

Besides these performance metrics, MOST is also evaluated based upon mission metrics that involve costs and mission effectiveness. The outputs include mass and settle time after a slew. Mass is always of critical concern in any aerospace application because of the high launch costs per unit mass. One of the goals of MOST is to examine how larger telescopes can be built without prohibitively massive structures. To evaluate the effect of design variables on mass (and, implicitly, launch costs) the final mass as computed by Nastran is saved for each design.[4]

Settle time is computed to represent one aspect of the availability of the telescope to take science images. The availability should be maximized, to make the most use of the telescope, but is limited by several factors. These could include the selected orbit, and how much time an earth-observing imager has over any one location, or downtime required for communication with a ground station. In terms of dynamics, flexible modes excited by a slew to a new target must damp out before the telescope can resume taking images. These

[4]While mass is being used as a surrogate for cost in this chapter, it is understood that other factors such as technology development, complexity of integration and test, operations, etc. are also significant contributors to cost.

transient dynamics cannot be evaluated using the steady state analysis routines that give optical performances. Rather, the model is excited with a representative slew maneuver and a time history of the response is produced. The time between the termination of the slew and the time at which the envelope on the optical jitter finally decays below the requirement is recorded as the mission settle time. The total of slew time plus settle time is output as the amount of time the telescope is not available. For this MOST analysis, the slew and torque profiles used are shown in Figure 6-4. The torque profile starts and ends at zero torque and with zero slope; this excites fewer modes than the bang-bang profile shown back in Figure 4-14. The slew maneuver shown here is 5 degrees over 10 seconds, and the settle time is recorded once the line-of-sight jitter envelope is below the requirement of 1.7 mas.

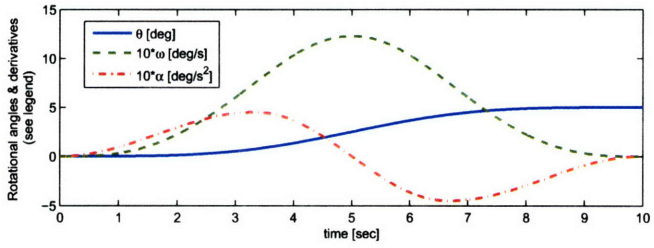

(a) Slew angle, angular rate and acceleration

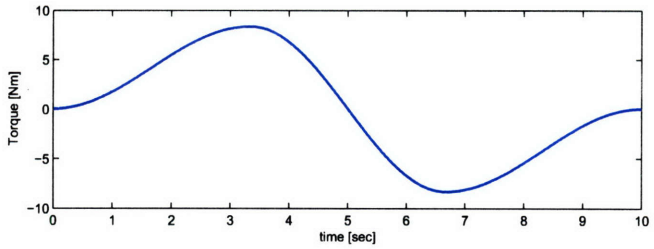

(b) Zero initial condition, zero slope slew torque profile

Figure 6-4: MOST slew angle and torque profiles

6.1.3 Dynamic response

The MOST finite element model is run through Nastran for a normal modes analysis[5], and the results used to construct a state-space integrated model as was described in Section 3.3. The block diagram of the model is shown in Figure 6-5. It includes two layers of vibration isolation, modeled as low-pass filters. The first, between the reactions wheels and the bus has a nominal 10 Hz corner frequency, and the second between the bus and the optical

[5]Nastran solution 103

telescope assembly has a nominal 2 Hz corner frequency. Rotational rigid body modes are stabilized using an attitude control system, and translational rigid body modes are removed, as they are not observable by the outputs. The outputs include the LOS and the relative z-displacements of sampled nodes (which are root-sum-squared for the WFE).

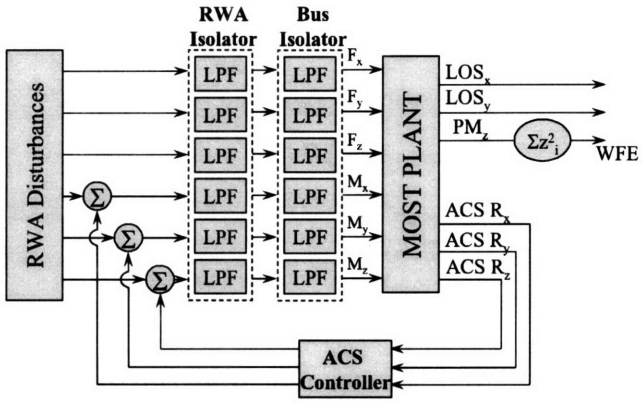

Figure 6-5: Block diagram of MOST integrated model

A sample realization of the design is prepared for a 3-meter segmented mirror with an f-number of 1.5 and mirror areal density of 10 kg/m^3. Nastran solves for the first 200 modes, which include modal frequencies up to 100 Hz. Since the frequencies which contribute to the output RMS values are well below 100 Hz, the number of modes is more than adequate to describe this system (Figure 6-6). The modeshapes are visualized using FE pre- and post-processing software; some critical modes are shown in Figure 6-7. The first flexible mode (mode #7 after the six rigid body modes) is the anticipated flapping of the solar panels at 0.49 Hz, very close to the desired 0.5 Hz that was set as a design variable of the system. Over 60% of the 200 modes turn out to be only solar panel modes with no discernable motion of the payload or bus. The first structural modes are of the mirror petals bending on their attachment points at 9.31 Hz. This frequency is lower than expected, and suggests that further stiffening of the connections is necessary. The aluminum mirror petals are themselves deformed in torsion about their attachment points at 19.67 Hz. This is much lower than the 100 Hz fundamental frequency that is desired for the hexagonal segments; other mirror models using different materials have a 100 Hz fundamental frequency.[6] A 20 Hz minimum fundamental frequency was levied on the SST to account for launch loads,

[6]While aluminum mirrors may be used as a mass surrogate in a MOST testbed, material properties representing silicon carbide are used for the mirrors in the larger trade space plots later in this chapter.

while the actual first bending mode of the SST is at 38.75 Hz. This result suggests that the tower is actually overdesigned, and that mass could be saved by reducing its stiffness. In any case however, these frequencies are believable for flexible structures, and the modeshapes show no anomalies.

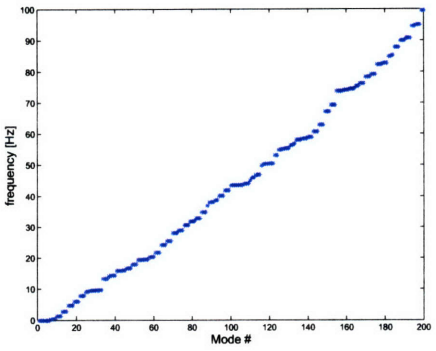

Figure 6-6: Modal frequencies for a sample MOST realization

The response to reaction wheel disturbances is computed with power spectral densities (PSD). PSD curves for the LOS outputs are given in Figure 6-8. At low-frequencies the ACS system drives the outputs to zero. Within the flexible regime, three significant modes contribute to most of the RMS LOS, as are observed in the cumulative RMS curves of Figure 6-8. The first is a solar panel mode at 0.497 Hz that includes rocking of the spacecraft about the line-of-sight. The second, smoother contribution is the RWA-bus isolator mode at 2 Hz. The third is the mirror petal bending mode at 9.31 Hz, visualized in Figure 6-7(b). In later designs, these mirror modes are stiffened. In particular, replacing the material properties of the mirrors, from aluminum to silicon carbide, dramatically increases the frequency of the mirror modes from tens of hertz to nearly 100 Hz.

The final RMS outputs for this design are 0.0506 mas for LOS about the x-axis and 0.0517 mas for LOS about the y-axis; these values are much lower than the 1.7 mas LOS requirement. There are several likely reasons for this apparent good fortune. The first is that the reaction wheels were sized for the torque profile, but with no margin for momentum storage; taking this into account the actual reaction wheels and their ensuing disturbances would likely be larger, degrading performance. The other likely reason is the stiffness of the SST. Bending of the tower and motion of the secondary mirror was identified as a prominent cause of line-of-sight jitter for TMT, whereas the first mode for MOST's SST (at 38.75 Hz) does not contribute at all to the final performance. This adds to the argument that the SST

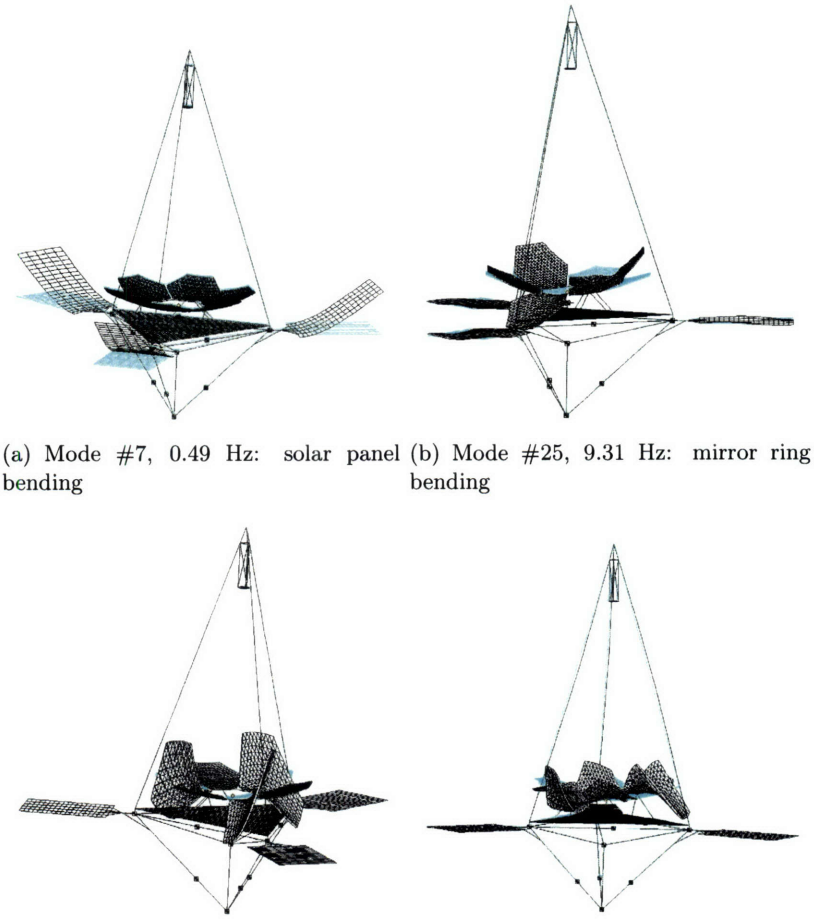

(a) Mode #7, 0.49 Hz: solar panel bending

(b) Mode #25, 9.31 Hz: mirror ring bending

(c) Mode #55, 19.67 Hz: deformation of mirror petals

(d) Mode #92, 38.75 Hz: SST bending

Figure 6-7: Modeshapes for a sample MOST realization

is likely too stiff, and that mass could be saved by allowing the tower to be more flexible.

The approximated wave front error for this design is 6.17 nm, which is above the 1 nm requirement but at least on the same order of magnitude. Different design realizations will show an improvement in this value. The settle time for this system is 548 seconds, or over 9 minutes. Lastly, the total spacecraft mass is predicted to be 522 kg. This is a definite improvement over Hubble, which has a smaller monolithic mirror (2.4 meters) but weighs 11,000 kg. The mass value is closer to a TPF collector spacecraft which weights 1622 kg with a 4.2 meter mirror.

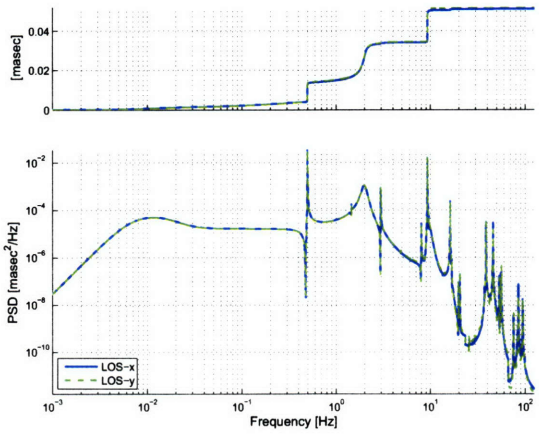

Figure 6-8: Line-of-sight performance PSDs for a sample MOST realization

6.1.4 Validation against TPF-FFI

As a means of validating the MOST parameterized model, a single design realization is compared to the TPF-FFI collector spacecraft, created by Ball Aerospace and provided by JPL. This validation is meant to increase confidence that the designs produced by the MOST parameterized modeling environment produce a realistic model, and that when the MOST structure is set to the same dimensions as a similar structure, similar results in terms of fundamental frequencies and mass values are obtained.

A MOST spacecraft realization is created with a 4.2 meter monolithic mirror, having an f-number of 1.19, the same as TPF-FFI. The mirror areal density is set at TPF's 37 kg/m^2 (although the final areal density is slightly off of this value).

The first 140 modal frequencies are plotted against each other in Figure 6-9. Because TPF has many more appendages than MOST (such as long sunshade booms, stray light trays, radiators and solar panels), it has more low-frequency modes where the appendages are rocking about the joint that connects them to the spacecraft. After the first 40 modes however, both sets of frequencies rise uniformly. The first flexible mode for both systems are the appendages: for MOST it is the solar panel mode at 0.487 Hz and for TPF it is the sunshade boom at 0.363 Hz. The first MOST mirror mode is the 31^{st} mode at 10.8 Hz (Figure 6-10(a)), and involves bending of the primary mirror on its mounts. A similar mode for TPF is the 25^{th} at 4.06 Hz (Figure 6-10(b), with only the telescope assembly illustrated), which involves the mirror rocking on its mounts. These values are in the same frequency region if not identical. TPF's mirror seems to be stiffer than MOST's, and the frequency

that the mirrors rock on their mounts is off by 6 Hz.

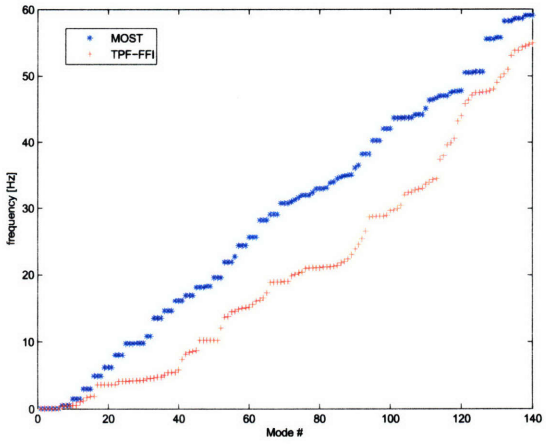

Figure 6-9: Comparison of first 140 modal frequencies of MOST and TPF-FFI

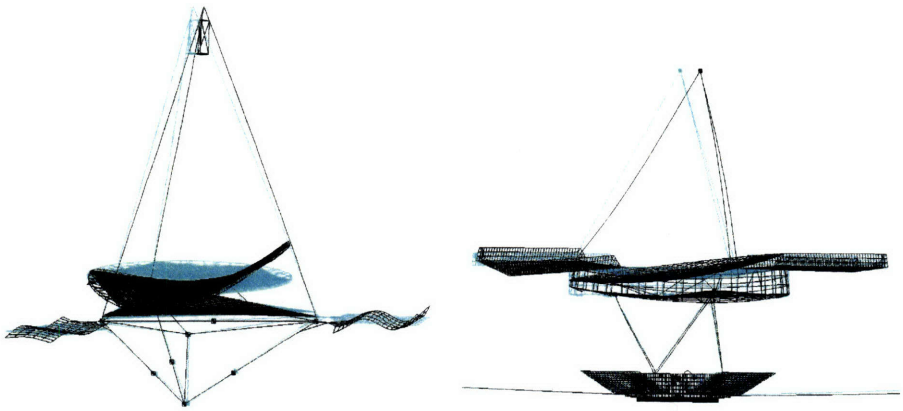

(a) MOST 31^{st} mode: 10.8 Hz

(b) TPF 23^{rd} mode: 4.06 Hz (radiators removed for clarity)

Figure 6-10: Comparison of mirror modes for MOST and TPF-FFI

Table 6.2 compares mass properties of the two spacecraft. The total masses are only 125 kg apart (<9% difference), and the mirror masses only 32 kg apart (<7% difference, resulting from the larger areal density for the final MOST mirror). The mass fraction of primary mirror to total spacecraft is larger for MOST, but this may be a result of MOST lacking additional components such as TPF's appendages. Difference are found between the location of the center of gravity (CG) and the moments of inertia about the CGs. For MOST, the CG is immediately below the primary mirror and the moment of inertias are smaller and close in value, suggesting a more compact spacecraft. TPF's center of gravity, on the other hand, is a meter below the mirror, suggesting that the mass is more distributed

between the mirrors and the bus. The moments of inertia are an order of magnitude larger than MOST, with a pronounced difference in the z-axis (along the line-of-sight) versus the x- and y-axes. Since the total spacecraft mass is approximately the same as MOST, the difference in inertias must be due to the location of mass. TPF has many more appendages than MOST, including solar panels, radiators, two 3 meter long stray light trays and four 10 meter long sunshade booms.

To consider the effect of these appendages on the TPF model, the mass and inertias of TPF were computed for the structure with the sunshade booms and stray light trays removed. In this case, the mass dropped to 1055 kg, and moments of inertia dropped to 2673 kg/m^2 about the x-axis, 2686 kg/m^2 about the y-axis and 1760 kg/m^2 about the z-axis. These values are even smaller than for MOST, but all on the same order of magnitude. This suggests that if anything, MOST may be overly bulky for its size. Generally however, these results suggest that the basic MOST structure has similar mass properties as TPF.

Table 6.2: Mass properties of MOST versus TPF-FFI

	MOST	**TPF-FFI**
S/C mass (kg)	1497	1622
PM mass (kg)	540	508
PM areal density (kg/m^2)	39.1	37.2
Mirror mass fraction	36.0 %	31.3 %
PM–CG distance (m)	0.305	1.025
Moment of Inertia (x) (kg·m^2)	4104	22431
Moment of Inertia (y) (kg·m^2)	4091	22755
Moment of Inertia (z) (kg·m^2)	4469	56030

These two spacecraft, while exhibiting some differences, still match each other well in terms of component and spacecraft masses, and modal frequencies. These results suggest that the MOST modeling effort has been successful at creating a realistic spacecraft structure. Although validation to additional design points is always desirable, this single comparison nevertheless increases confidence in the process.

6.2 Uni- and bi-variate parameter trades

An initial examination of the design space should be first run across key design variables individually. These single (or at most double) axis trades can provide insights into the

system, and suggest useful ranges of the design variables, before a much larger and more computationally intensive full trade space is run. The nominal design is of a 3-meter mirror with an f-number of 1.5, mirror areal density of 15 kg/m^2, mirror rib aspect ratio of 4, no crossbars on the SST, and a SST strut radius of 7.4 cm.

6.2.1 Single axis trades

A single axis trade study is run first to identify system response characteristics while varying individual design variables. If a single design variable is of particular interest (perhaps if all other design variables have been set), the resulting plots may be useful by themselves. But even assuming that the larger multi-variate trade space will eventually be run, these plots can begin to suggest trends in the data, and can be used to identify regions of behavior that warrant greater study. Since running a single axis study often involves fewer computer simulations, these insights can be obtained quicker than with the full trade space. Three single-axis trades are shown here, for f-number (Figure 6-11), mirror areal density (Figure 6-14) and mirror rib aspect ratio (Figure 6-15). In each, the variable of interest is discretized into 51 values between the limits of the design space. Both monolithic and segmented systems are examined, and plotted against each other.

The first plot, Figure 6-11, shows the effect of varying f-number on the four outputs: mass, settle time, wave front error and line-of-sight jitter (about the x- and y-axes). As f-number increases, the primary mirror becomes less curved and the distance between the primary and secondary mirrors increases (leading to a taller telescope). As anticipated, mass increases monotonically (6-11(a)). The few small blips on the curve likely result from errors in the fit that is performed on the mirror (with the rib height and face sheet thickness) to get the desired mirror areal density. Similarly, wave front error also increases monotonically (6-11(c)). At low f-numbers the effect of increased curvature is to stiffen the mirrors. As the mirrors become less curved, they become more flexible and WFE increases.

The settle time (6-11(b)) and line-of-sight jitter (6-11(d)) plots are more interesting. In particular, the settle time response goes off the chart between an f-number of 1.56 and 1.72. The system fails to settle by 2000 seconds, at which point the transient response analysis is ended. Since the settle time is based on the line-of-sight response, a comparison with the LOS plot shows that it too jumps at those parameter values, particularly LOS$_y$. This warrants a closer examination of those systems. The simulation results for a monolithic

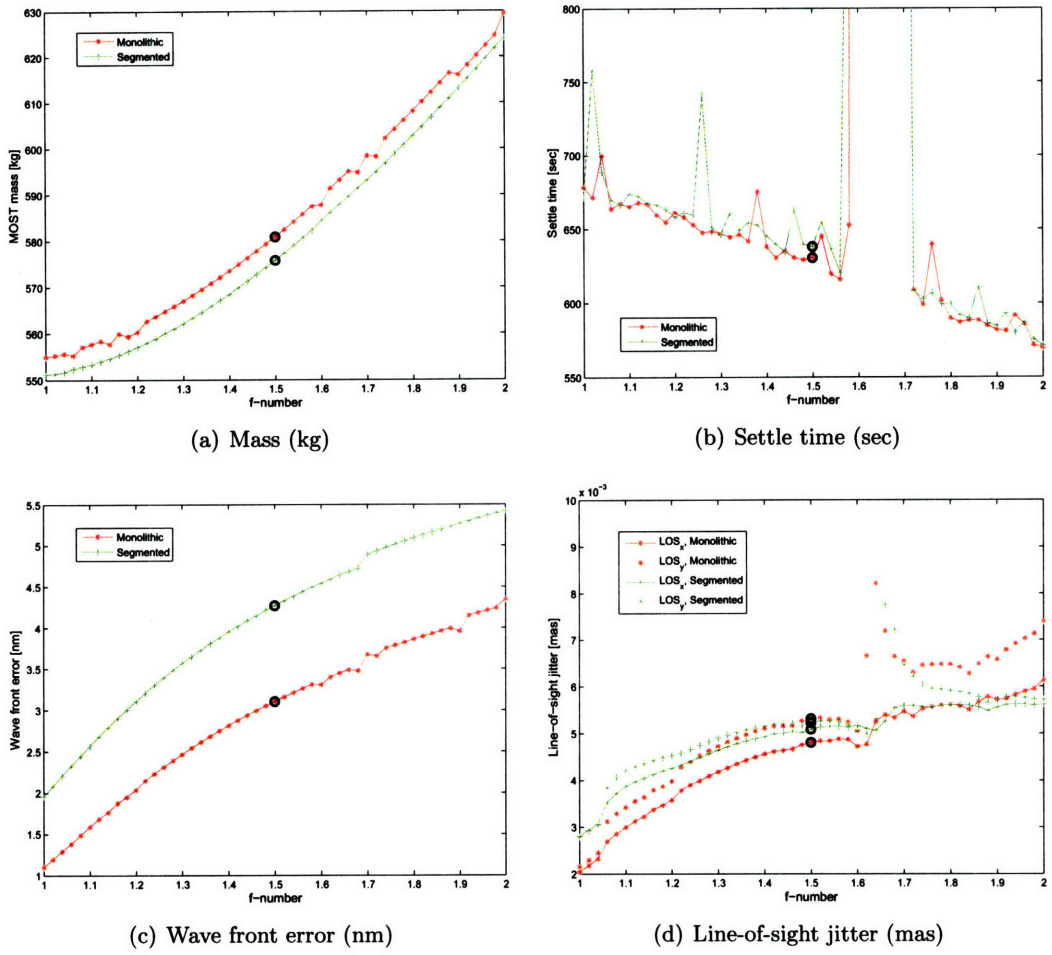

(a) Mass (kg)

(b) Settle time (sec)

(c) Wave front error (nm)

(d) Line-of-sight jitter (mas)

Figure 6-11: Variation of outputs with f-number. "Nominal" points with f-number of 1.5 circled

telescope at f-numbers of 1.56 and 1.64 were examined. These points represent the response immediately before the LOS jump, and at the top of peak. Comparing the cumulative RMS curves for both designs (shown in Figure 6-12 for the relevant frequency regions) one sees that the main difference is the jump in RMS output that occurs between 40 and 41 Hz. In the $f/1.56$ design, there are two modes in the neighborhood of those frequencies; in the $f/1.64$ design those two modes seem to have fallen on top of each other.

Physical understanding of the behavior comes from visualizing these two modeshapes, which are identified as fast steering mirror displacement modes and SST bending modes. For both systems, the fast steering mirror is translating and rotating just above 40 Hz (40.48 Hz for the $f/1.56$ system, 40.92 Hz for the $f/1.64$ system). In the $f/1.56$ system two SST bending modes are at higher frequencies, at 43.11 and 43.17 Hz. In the $f/1.64$

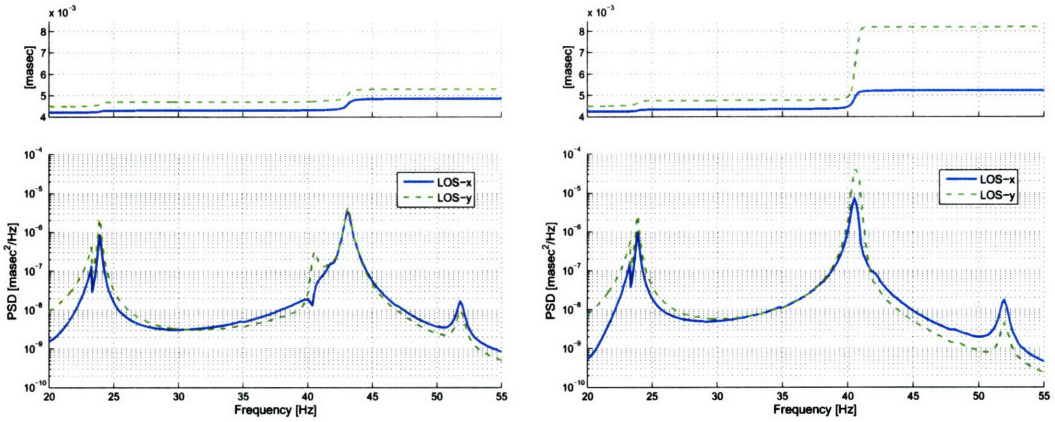

(a) $f/1.56$ (b) $f/1.64$

Figure 6-12: PSD response curves showing FSM and SST modes falling on top of each other at an f-number of 1.64

system however, SST modes at 40.52 and 40.55 Hz lie nearly right on top of the FSM mode. Since LOS is defined using displacements and rotations of the both the FSM and SST (from Equation 6.1), the effect of these modes on top of each other excites the output and causes the large peaks observed in the single axis trade plots. Because both monolithic and segmented apertures use the same FSM and SST grid points, this effect is seen in both systems.

Besides this effect, the settle time plots seem to have more variability with f-number than the LOS, which rise smoothly except for the region around $f/1.6$. Looking across all four plots an obvious tradeoff makes itself evident: mass, WFE and LOS have superior values at low f-numbers, while settle time is shortest at larger f-numbers. This conflict will have to be resolved based upon which metrics are most important to the ultimate needs of the mission.

The next variable examined is areal density of the primary mirror. In the model, areal density changes based on the number of ribs, rib height and width, and face sheet thickness. Since setting the areal density requires balancing all of these parameters, the actual density of the actual mirror model may vary from the desired value. This effect is shown in Figure 6-13, which shows that the actual model for both the monolithic and segmented mirrors have higher densities than are desired. In the segmented case, the areal density is set for the individual segments, but the final reported value also includes the mass of the connecting ring; as a result the reported areal densities are on average 8 kg/m^2 higher than the set

parameter value. In any case, both curves increase nearly parallel with the line of symmetry. The single axis trade plots are drawn with the actual areal densities for each mirror type.

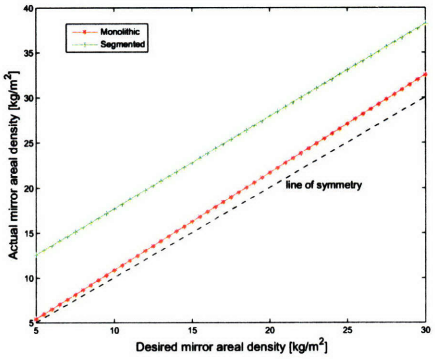

Figure 6-13: Comparison of desired to actual mirror areal density

Figure 6-14 shows the outputs as they change with areal density. Mass (plot 6-14(a)) increases at higher density values, as it should. The mass curve is less steep for segmented systems, suggesting that for these systems mirrors can be made heavier without paying as large a mass penalty as with the monolithic designs. Settle time (plot 6-14(b)) again shows the greatest variation of all the outputs. The sawtooth patten between 25 and 34 kg/m^2 implies that settle time is very sensitive to small changes in the system. This suggests that it may be difficult to make settle time robust to uncertainties.

The optical performances (plots 6-14(c) and 6-14(d)) both show the characteristic that monolithic systems are superior to segmented systems at nearly every value for areal density. The two systems exhibit different trends across areal density, with the best segmented results at lower areal densities and the best monolithic results at larger areal densities. This result likely is a factor of the dominant modeshapes of each system. For the monolithic aperture, bending of the primary mirror (as is seen in Figure 6-10(a)) causes optical degradation. This can be improved by stiffening the mirror through increases in the rib cross-sectional areas and the face sheet thickness, as occurs at higher areal densities. The segmented systems are affected more by the flapping of the hexagonal petals on the connecting rings (shown in Figures 6-7(b) through 6-7(d)). This motion becomes more pronounced as the mirrors become heavier, so lighter mirrors with lower areal densities are preferred.

It is also obvious based on these results that the monolithic systems on the whole give better performance than the segmented systems. In order to reap the mass and launch storage benefits of the segmented systems, control of the mirror petals and optical surfaces

may be necessary to match the performance levels of the monolithic system.

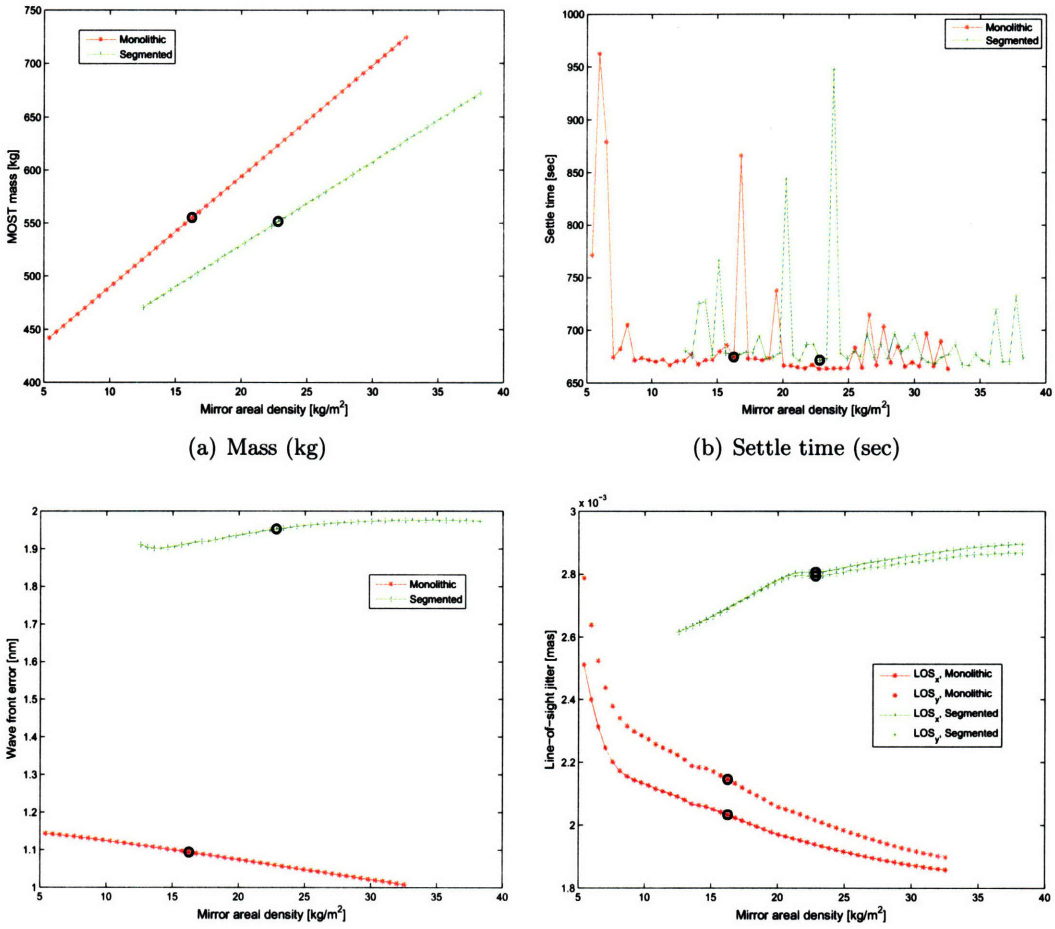

(a) Mass (kg)

(b) Settle time (sec)

(c) Wave front error (nm)

(d) Line-of-sight jitter (mas)

Figure 6-14: Variation of outputs with mirror areal density (kg/m^2). "Nominal" points with desired areal density of 15 kg/m^2 circled (actual areal density values differ).

Figure 6-15 shows the effect of changing the aspect ratio of the mirror rib cross sections. The ribs have a square cross-section when the aspect ratio is 1.0, and are tall and slender at higher values. The nominal design point is 4.0. The mass curves (plot 6-15(a)) show a relationship between aspect ratio and mass. As aspect ratio increases, rib thickness is kept constant and the rib height increases. This results is a heavier mirror, so that along with increasing aspect ratio, areal density of the mirrors is also effectively increasing. Areal density is not held constant as was desired for this trade. For a single-axis trade where areal density remains constant with changing rib aspect ratio, the rib thickness would need to be reduced as rib height increases. These results suggests that further modifications to the

rib-stiffened mirror model may be in order, to allow truly independent trades of the input parameters.

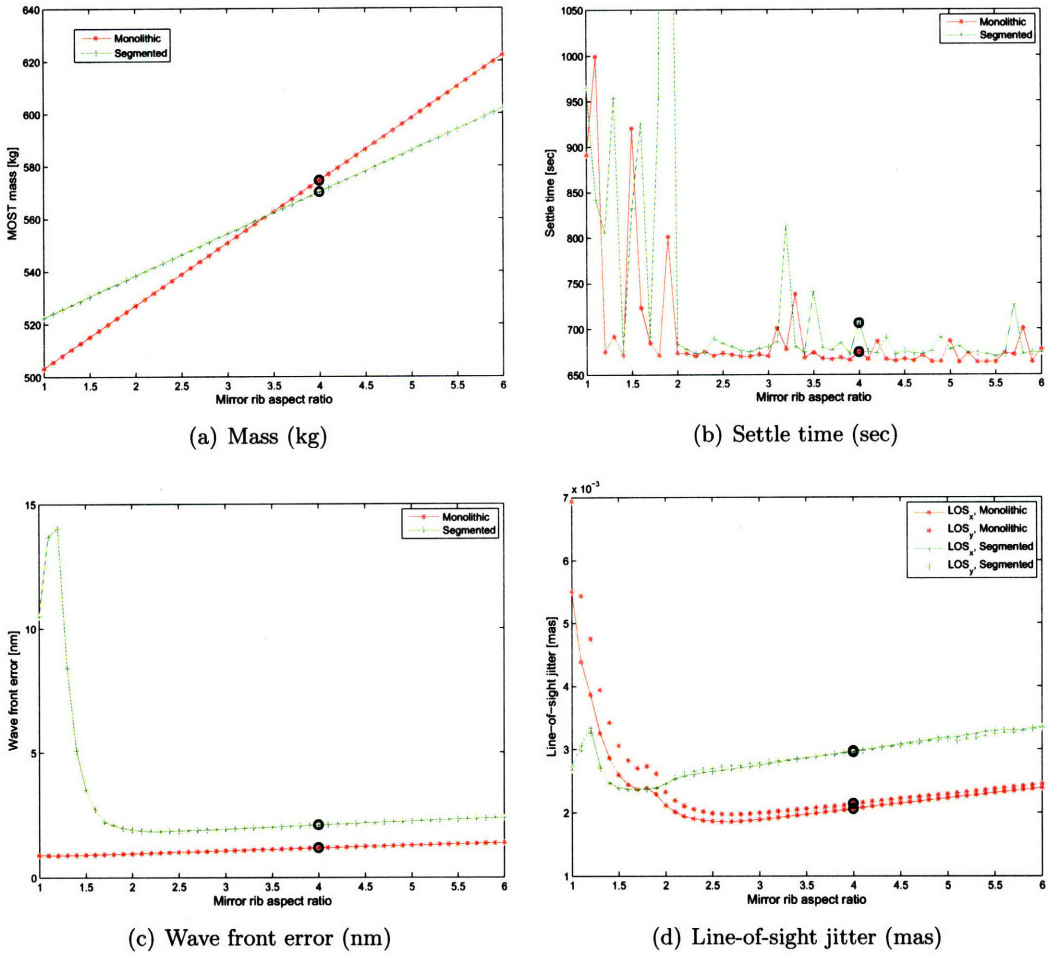

(a) Mass (kg)

(b) Settle time (sec)

(c) Wave front error (nm)

(d) Line-of-sight jitter (mas)

Figure 6-15: Variation of outputs with mirror rib aspect ratio. "Nominal" points with aspect ratio of 4 circled

The mass curves are also interesting in that at lower aspect ratios, the segmented mirrors are actually more massive than the monolithic. Just as with the areal density versus mass curves (plot 6-14(a)), the slope of the monolithic mass curve is higher than the slope of the segmented. In this case, the difference in slopes actually results in the lines crossing each other, specifically at an aspect ratio of 3.45.

The three other plots each indicate that as the aspect ratio falls below 2, the performances of the system degrade quickly. The settle time, still erratic as in the previous figures, increases by minutes, the line-of-sight outputs reach their maxima, and the wave front error

sharply increases for the segmented system. Since stiffness provided by the ribs decreases as the ribs become squatter, at smaller values of aspect ratio the mirrors are closer to thin, un-stiffened plates.

Interestingly, most of the line-of-sight and wave front error curves exhibit a minima between 1.5 and 2.5. Above these values the performances grows steadily worse, even with taller (and stiffer) ribs. This implies that there are higher order interactions between the aspect ratio, rib height and mirror facesheet thickness. For example, in the areal density single-axis trades, facesheet thickness increases with areal density and the performances improve for monolithic systems. In these aspect ratio trades, face sheet thickness remains constant, even as areal density is increasing (due to the taller ribs), and performance grows worse for all systems. Another higher order interaction may involve the larger spacecraft system. As rib aspect ratio increases, plot 6-15(a) shows that spacecraft mass increases. This results in larger spacecraft moments of inertia, which drive the reaction wheels to larger sizes. As the reaction wheels grow larger, their disturbances increase, resulting in worse performance outputs. Further examination of the interaction of mirror parameters with spacecraft performance is recommended.

Besides using these single axis trade plots to identify trends across individual design variables, the plots can also be used to guide a larger multi-variate trade space examination. The smoothness of the curves indicate what discretization level is necessary for variables in the trade space analysis. The smaller step size used in the preceding plots allows fine characteristics of the single axis curves to be seen, but this level of discretization across many variables in a full factorial search would lead to an excessive number of simulations. The plots shown here indicate that larger step sizes would be appropriate to explore the limits of the MOST design space. Most of the curves are fairly smooth and either rise or fall monotonically (except for the settle time, which seems to be particularly sensitive to inputs). Exceptions, such as the f-number versus LOS plot of Figure 6-11(d), are identified that may require a finer step size. In that plot, there are three distinctive regions in the curves: the curves rise monotonically until an f-number of 1.6; between 1.6 and approximately 1.8 there is an obvious jump in the response, and the curves gradually rise again above 1.8. This recommends a step size for f-number of at most 0.2. This is implemented in the next section.

A final point should be made that the single axis trades do not give a complete picture of

how the system will behave when multiple variables are still being changed. As an example, the f-number versus wave front error plot in Figure 6-11(c) shows smooth, monotonically increasing curves for both monolithic and segmented systems. Figure 6-16(a) shows the same plot, but the mirror material has been changed from silicon carbide (with a Young's Modulus of 375×10^9 Pa) to aluminum (with a Young's Modulus of 70×10^9 Pa)[7]. The change to aluminum, which may be used in a planned testbed of MOST as a mass substitute for optical mirrors, has a large effect on the response; the basic trends observed with the silicon carbide mirror (in Figure 6-11) no longer hold true. There is much greater variability across both curves. Successive points are nearly a nanometer apart, where before the average change was less than 0.07 nm. More striking is that whereas with silicon carbide both curves were monotonic upward, there are definite non-monotonic trends in the new data. For monolithic aluminum mirrors the WFE has noticeable dips and local minima at higher f-numbers. The overall trend of the segmented system is not to trend upward; rather, for the first half of the curve, performance actually improves with increasing f-number, and it worsens for the second half. An optimum can be discerned at an f-number of approximately 1.5. Similar trends can be seen by comparing the line-of-sight plots with silicon carbide (Figure 6-11(d)) versus aluminum (Figure 6-16(b)) mirrors. The peak response due to the FSM/SST modes is seen in both plots, showing that this particular characteristic is common across design variables.

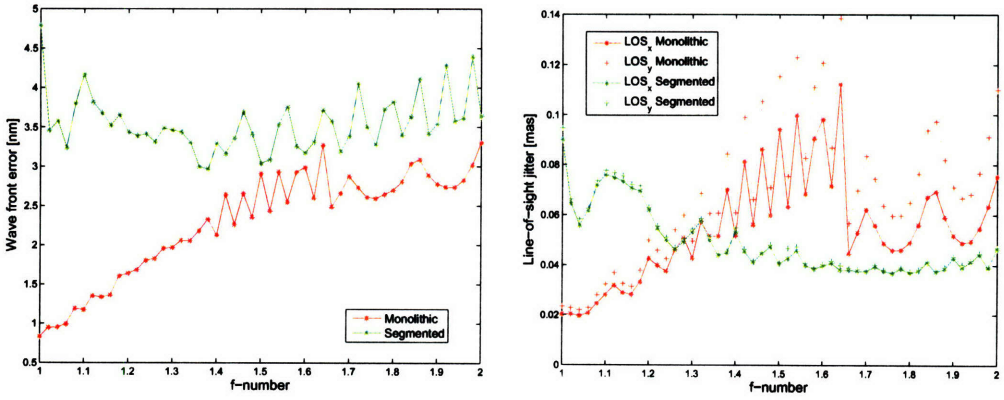

(a) Wave front error (nm)

(b) Line-of-sight jitter (mas)

Figure 6-16: Alternate single axis trade results with an aluminum mirror

[7]Areal density has also changed from 15 kg/m^2 to 10 kg/m^2, but by itself that does not cause as large a change in response as does changing the material properties.

6.2.2 Isolator frequency trades

A bi-variate trade study is also performed that shows the effect of trading isolator frequencies on the MOST performance outputs. The integrated models developed for MOST use two stages of isolation to attenuate disturbance vibrations. The main source of vibration, the reaction wheel assembly, would sit on one isolator. A second stage of isolation would then lie between the bus and the optical telescope assembly. The isolators themselves are modeled using low-pass filters (from Section 3.2.3) with variable corner frequency. Double axis trades of corner frequency can be run to investigate the interaction between the isolators.

Initially, a trade is run comparing the effect on performance of using only a single stage of isolation versus two stages. The results are shown in Figure 6-17. The example system is of a 3-meter diameter segmented mirror. A thick line represents the response of LOS_x versus the corner frequency of only a single stage of isolation ("RWA"). Plotted against this are curves of the response using two stages of isolation. It is interesting to note that not all two-stage isolator combinations show improvement over a single stage. If the second ("bus") stage is above 7 Hz, then part or even most of the response is worse than if only a single stage had been used. Below 7 Hz however, all remaining combinations of corner frequencies do provide greater attenuation at most frequencies (the only exceptions are where the frequencies lie on top of each other, or on a system mode). In fact, using a second stage can provide up to two orders of magnitude performance improvement, with the correct selection of frequencies. If the bus isolator can be built with a 1.2 Hz frequency there is a wide range of frequencies for the RWA isolator that give the best response.

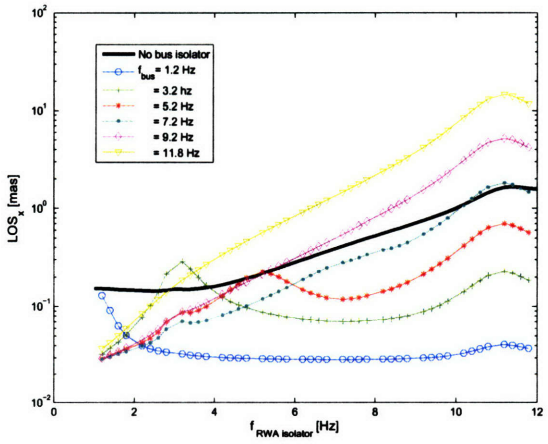

Figure 6-17: A comparison of single-stage versus two-stage isolation, for a 3m segmented mirror

The full bi-variate trade space response is shown in Figure 6-18, in which the line-of-sight and wave front error responses are plotted against both bus and RWA corner frequencies. These plots map the response surfaces of a structural dynamic system to variable inputs. The ridge that can be seen running up the diagonal of each plot represents designs in which the isolator frequencies lie on top of one another. The peaks build upon one another and contribute more to the response. Another obvious effect is when an isolator frequency lies close to or on top of a structural frequency. The isolator will in this case excite the structural mode. These situations are observed in both plots as ridges parallel to the axes. In Figure 6-18(a), excitation of a mode at 11.3 Hz creates ridges running up the sides of the response space. For Figure 6-18(b), a 5 Hz mode creates a strong peak right in the middle of the response space. The worst performance in both plots occurs when both isolators lie together on top of a mode.

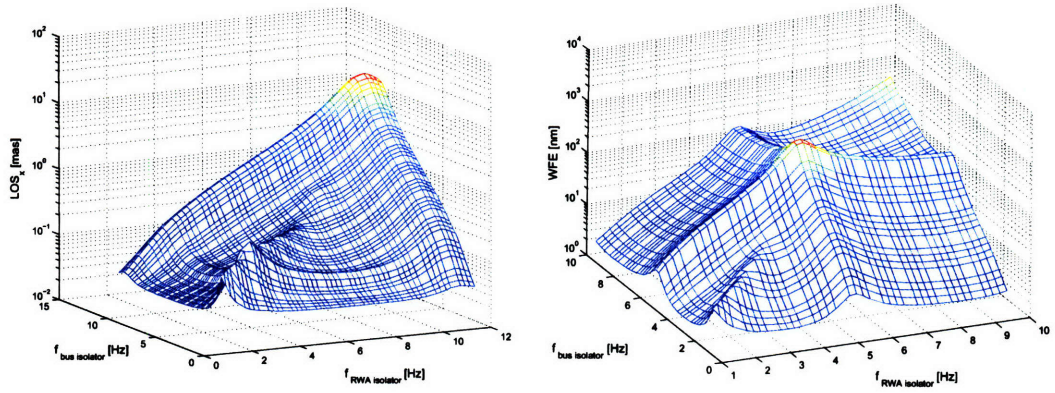

(a) LOS_x response for a 3m segmented mirror

(b) WFE response for a 5m monolithic mirror

Figure 6-18: Examples of trading isolator corner frequencies for two design realizations

These plots indicate which combinations of frequencies should be avoided, but also which combinations provide robust attenuation to the disturbances. In Figure 6-18(a), valleys between the ridge lines indicate frequencies that provide superior performance. The steepness of valley floor indicates the sensitivity of the response. The flatter regions are more robust to variations in the isolator, but perhaps more importantly allow flexibility in the isolator design. Within these regions the two isolator stages can be traded against each other based on additional figures of merit, such as cost or complexity. In Figure 6-18(b), for a 5-meter monolithic system, a bowl-shaped region in the rear of the plot seems to provide a local minima robust to variations, however the response is nearly two orders of

magnitude higher than other regions of the trade space. The regions of greatest attenuation are where one isolator is as low as possible and the other only must avoid the 5 Hz mode, but these locations are on steep slopes. If the performance response has very little margin for uncertainty, the sensitivity to the isolators could become an issue.

Similar to the single axis trade plots, these response surfaces provide a great deal of information about how a particular design variable influences the system. In the next section, the larger trade space evaluation will investigation how changing many variables leads to the identification of superior families of architectures.

6.3 Multi-parameter trades

The real power of the parameterized spacecraft modeling approach is demonstrated with a multi-variate trade space evaluation. All architectures across a range of design variables can be created, analyzed, and evaluated against the other architectures. This type of design space exploration has been performed before; Jilla evaluated spacecraft architectures across a large trade space, comparing competing system-level metrics such as cost and mission reliability obtained by algebraic relationships from input variables such as orbital altitude, number of apertures, and failure rates [22]. The advance in this work is to show a similar type of trade analysis, but with fully integrated structural, optics and controls models. These results can drive the mechanical design of the structure by identifying how key variables interact with each other.

These trades, each of which require complete finite element models to be run, are certainly more computationally intensive than the algebraic models created in [22]. Increases in computing speed allow this type of simulation-based design, that was not possible even five years ago, with standard desktop computers. The models, which average around 4000 nodes (24,000 degrees of freedom), take approximately 5 minutes per design realization for model creation and analysis. The analyses were run on Dell Optiplex GX620 desktop computers, using 3.6 GHz Pentium processors with 3.5GB of RAM. Even given the increases in computer speed, it is important to consider which parameters to choose and how the design space should be explored in an efficient manner. For exploration of the design space, a full factorial evaluation of every combination of design values is run. Alternative techniques not explored here include optimization approaches as described in [22]. Heuristic optimization

approaches such as generic algorithms or simulated annealing could easily be incorporated into the MOST analysis codes to explore the space. The full factorial approach does not necessarily drive the design to the optimal architecture, but does allow the complete design space to be sampled so that general trends can be identified.

In choosing which parameters to vary, especially when using a full factorial design matrix, the number of parameters should be limited to high-level variables that define the architecture. Table 6.3 lists the variables chosen for the MOST analysis. Many of these were investigated in the single-axis trades. The variables define the type of telescope and dimensions of the entire structure, through the f-number. Parameters used to define technologically advanced components like the rib-stiffened mirrors are included, such as areal density and rib aspect ratio. Methods of stiffening the secondary support tower are examined, including changing the radius of the tower struts, and adding horizontal crossbars between each leg (as illustrated in Figure 6-1(b)).

Table 6.3: Design variable ranges for MOST multi-parameter trades

Variable	**range**
Mirror type	Monolithic vs. Segmented
f-number	1.0, 1.2, 1.4, 1.6, 1.8, 2.0
PM areal density (kg/m^2)	5, 10, 15, 20, 25, 30
PM rib aspect ratio	2, 4, 6
Use of SST crossbars	yes, no
Radius of SST struts (cm)	5, 7.4, 10

The design ranges for the continuous variables are based on the single axis trade studies. In the previous section, an f-number step size of 0.2 was decided upon to capture effects that varied on that scale. Since the effect of mirror areal density on a telescope is of special interest for many telescope designers, a finer grid is selected using a step size of 5 kg/m^2. In the case of the other variables such as rib aspect ratio and SST strut radius, the single axis results showed smooth variation across the range boundaries. In order to gage trends across these parameters, a minimum number of values are acceptable for a preliminary study. Given the number of design variables and values given in Table 6.3, a full factorial design matrix of 1296 designs is created and the simulations are run. All of the simulations were run over a weekend on two of the Dell Optiplex computers.

6.3.1 Design trends

Methods of visualization and means of interpreting the results are further contributions to the MOST project. The 1296 design realizations are evaluated based on the four model figures of merit, so a series of two-axis scatter plots are produced to compare the designs against often competing metrics. Figure 6-19 compares the two system metrics: mass versus settle time. Figure 6-20 compares the two optical performance metrics: wave front error versus line-of-sight, and Figure 6-21 compares a systems metric, mass, to the line-of-sight performance. The useful information for design is how the design variables change across these plots. In order to visualize these changes, each figure includes six copies of the *exact same scatter plot* color-coded based on the different design variable inputs. In Figure 6-19, for example, every plot 6-19(a) through 6-19(f) shows the same data points against the same axes. The circled point on each plot in Figure 6-19 represents a single design realization; looking across the plots it can be seen that the design is a monolithic aperture of $f/1.4$, with a mirror areal density of 15 kg/m^2, rib aspect ratio of 6, strut radius of 10 cm, that uses crossbars on the SST. The colors and markers change to represent the range of values of the different variables. Plot 6-19(a), for example, compares monolithic versus segmented systems, while 6-19(b) compares values of f-number.

Several plots in Figure 6-19 immediately jump out with clearly distinguished differences between parameter values. Plot 6-19(b) shows a clear stratification of f-number, where higher values provide progressively better settle times. (Note also the absence of values for $f/1.6$; as was indicated on the single axis trade plots, these did not settle before the slew/settle time simulation ended.) Even though larger f-numbers result in taller telescopes, the effect on mass with increasing f-number is less pronounced. There are obvious effects on mass in plots 6-19(e) for strut radius and 6-19(c) for areal density, in which both show a strong relationship between mass and parameter value. The other three plots: mirror type, aspect ratio and the presence of a SST crossbar are not nearly as clear, and there are no obvious trends that dominate. The overall shape of the scatter plot indicates that a pareto-optimal front exists. The pareto-front, defined as the set of designs where improving one metric requires degrading another [107], is the line of points closest to the optimal point of lowest mass and shortest settle time. Mass can be reduced only by allowing settle time to lengthen, and settle time can only be reduced by accepting a heavier spacecraft.

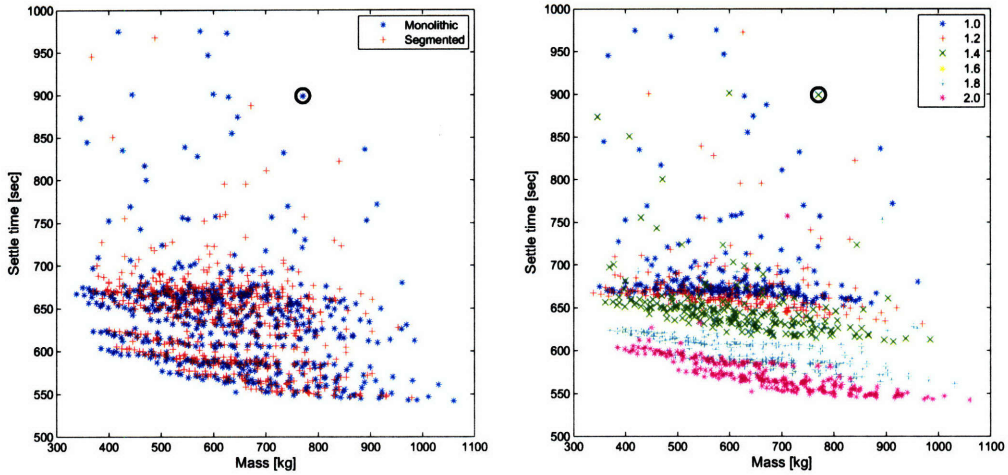

(a) Mirror type

(b) f-number

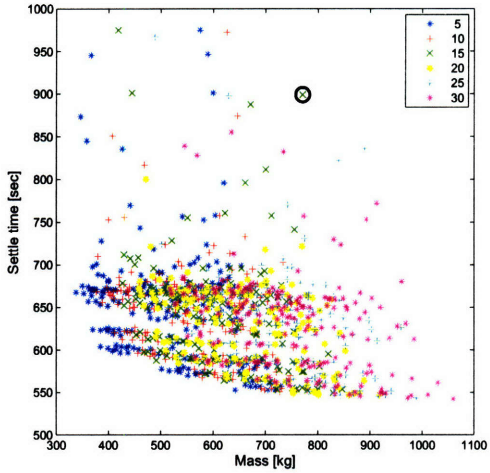

(c) PM areal density (kg/m^2)

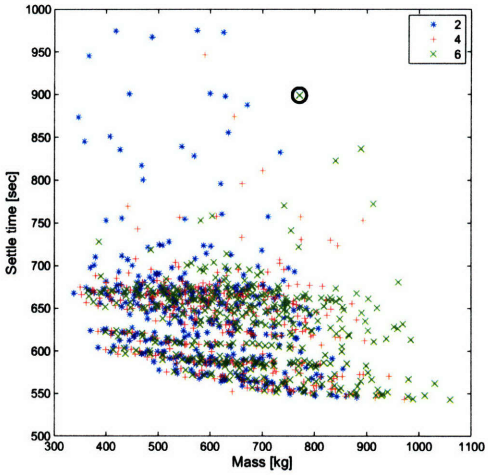

(d) Aspect ratio of mirror ribs

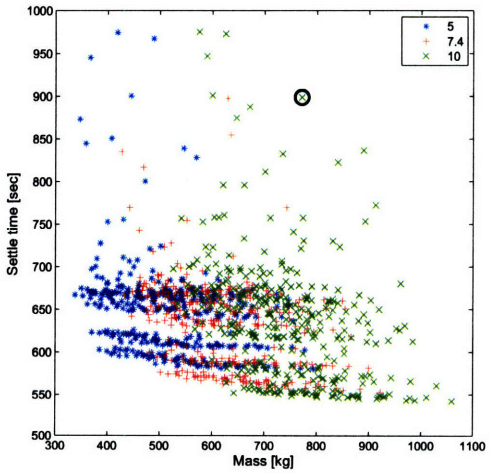

(e) Radius of SST struts (cm)

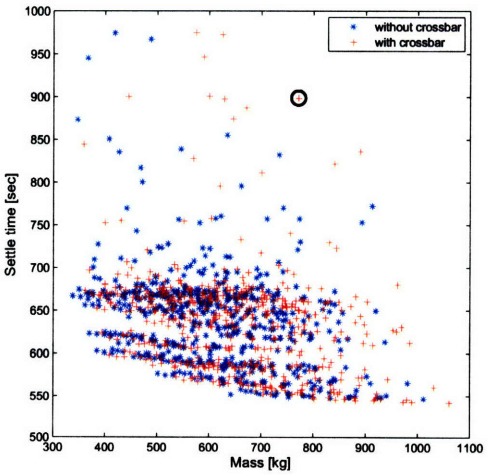

(f) SST crossbars

Figure 6-19: Trade space results for MOST mass versus settle time. The circled point on each plot represents the same design realization.

Requirements on these outputs (which are not set) would be needed to determine what designs along that front are allowable. If multiple allowable design points exist, then trades can be made between these metrics based on other system costs.

The stratification of f-number in plot 6-19(b) is also seen in Figure 6-20, plot 6-20(b), which compares the two performances. In this case however, lower f-number is obviously superior. This conflict, between performance and settle time, was identified from the single axis trades. The very shape of the performance scatter plot is unusual, in that there is a strong bifurcation of the designs. Plot 6-20(a) shows that this bifurcation obviously results from choice of mirror type. Monolithic apertures tend to have a smaller variation in WFE, but much larger (by several orders of magnitude) in LOS. The opposite is true for segmented apertures, which vary more in WFE. Since the segmented mirror petals are cantilevered out from their holding ring, they are more prone to out-of-plane bending on their struts, leading to degraded wave front error (modeled in this system as overall z-displacement of sampled points). A monolithic mirror does not have this issue, since it is supported from below by bipods. Rather, the large, stiff mirror may be more likely to tip and tilt on those bipods, causing both the mirror and the optical bench below it to bend. Since LOS is determined partly from rotations of both the PM and fast mirror mirror, which is mounted on the optical bench, these rotations cause a worsening of the line-of-sight jitter that is not seen in the segmented system.

In plot 6-20(c), larger mirror areal density seems to be preferred, and in fact the smallest areal density (5 kg/m^2) leads to the worst performance extremes for both mirror types. Similarly, the very worst designs also have a mirror rib aspect ratio of 2 (plot 6-20(d)). However, focusing in on the optimal corner of plot 6-20(d) suggests that an aspect ratio of 2 also leads to the very best designs. This is a prime example of how viewing these plots side-by-side facilitates an understanding of the higher level interactions between variables. For both types of aperture, monolithic and segmented, the effect of rib aspect ratio on performance depends on the areal density setting. Increase the areal density, and for the same value of rib aspect ratio, the designs go from some of the worst performers to some of the best.

The other plots in Figure 6-20 do not show such obvious differences between parameter values. The overall shape of this scatter plot indicates that there is no pareto-front. There are only a small set of designs in the lower-left corner of the plot that have the best

performance. Moving away from these designs will degrade both performance metrics.

Figure 6-21 compares mass versus line-of-sight performance. Just as was seen in the previous f-number plots, 6-19(b) and 6-20(b), the variation of f-number in plot 6-21(b) shows clearly defined strata at low LOS. The strata are very flat, meaning that for any value of f-number improving the line-of-sight will very quickly produce a heavier spacecraft. Other results, such as the effect on mass of changing the strut radius or areal density have already been noted. It is perhaps more useful for this series of plots to examine the shape of the pareto-front, and to determine which design variables are efficient "knobs" to move along the front. A pareto-front does exist and the scatter plot suggests that improving performance will be costly in terms of mass. To move along a curve, f-number is obviously not a useful variable; all of the optimal designs have an f-number of 1.0 and changing that will only degrade both metrics. Rather, the plots recommend both strut radius and areal density as appropriate knobs. Changing either of these will have an appreciable effect on mass, and a more limited but still discernable effect on LOS.

These results are some of the most useful that come out of these plots. They not only provide an indication of the level of performance that can be achieved across the design space, but also recommend to the designer which variables will be the most efficient levers for moving through the design space.

6.3.2 Identified optimal designs

The general trends that were identified using the design plots included improved performance with low f-number and low rib aspect ratio, the effect of strut radius and areal density on mass, and an indication of appropriate variables to move the designs along the optimal front. Exploring the trade space in greater detail involves identifying the specific designs that are along the optimal fronts, and comparing the results to requirements to determine which families of architectures meet the requirements.

Given the collection of results from a trade space simulation, MATLAB tools were developed to query individual points on a scatter plot. Two examples are shown in Figure 6-22, which zoom into the optimal corners from plots 6-19(b) and 6-20(a) and pick out promising design points. The number next to each selected point represents the index number of the design in the design matrix.

Plot 6-22(a) highlights five points along the mass-settle time pareto front. These points

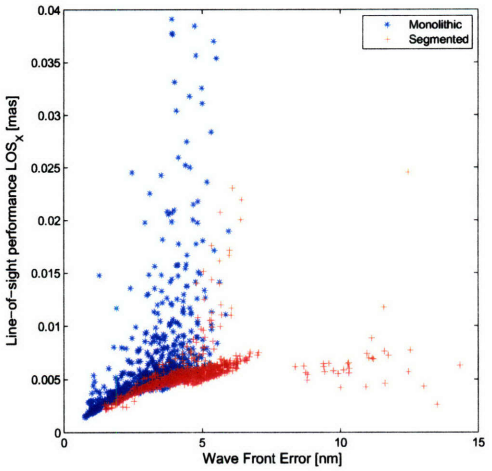

(a) Mirror type

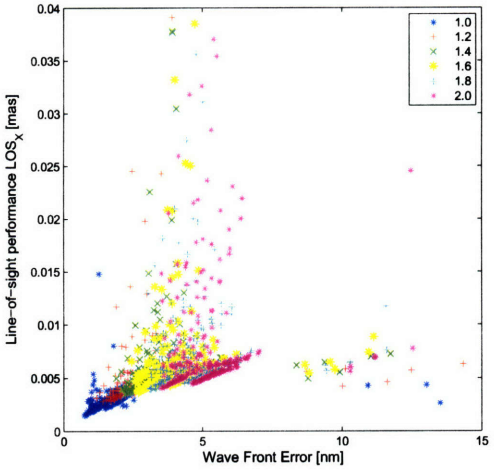

(b) f-number

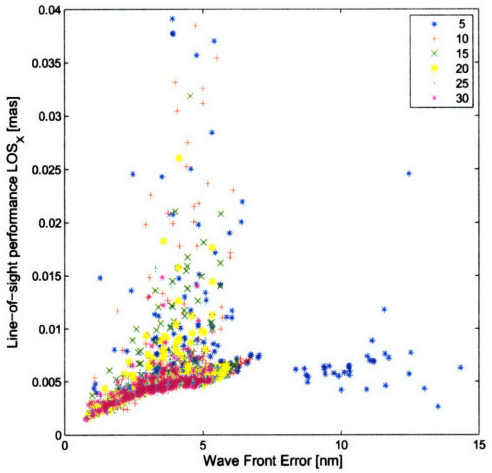

(c) PM areal density (kg/m^2)

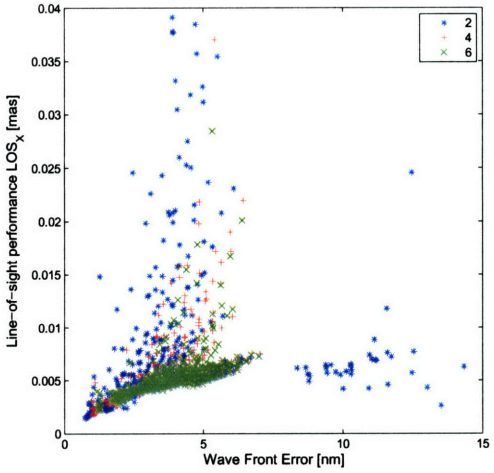

(d) Aspect ratio of mirror ribs

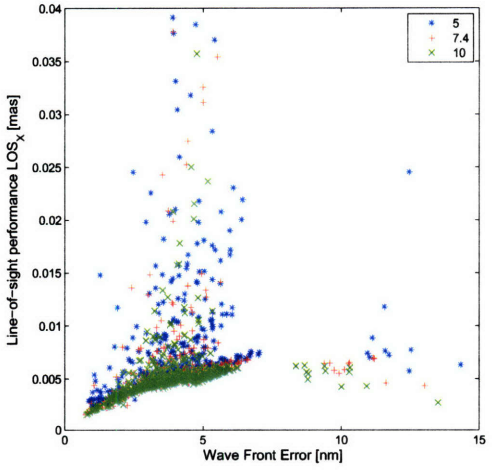

(e) Radius of SST struts (cm)

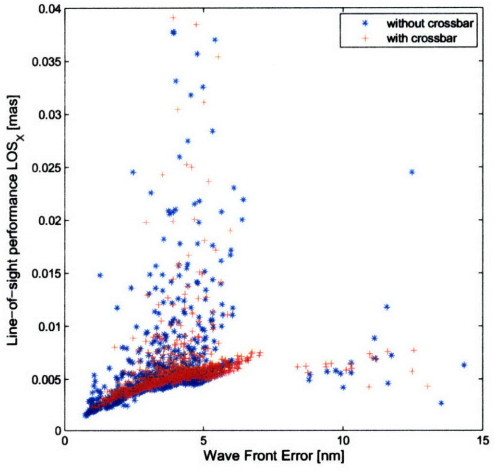

(f) SST crossbars

Figure 6-20: Trade space results for MOST wave front error versus line-of-sight jitter

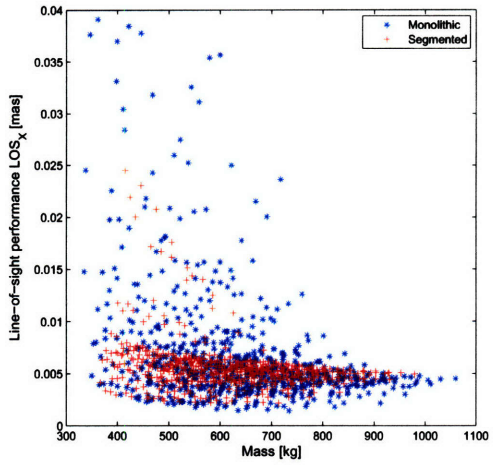

(a) Mirror type

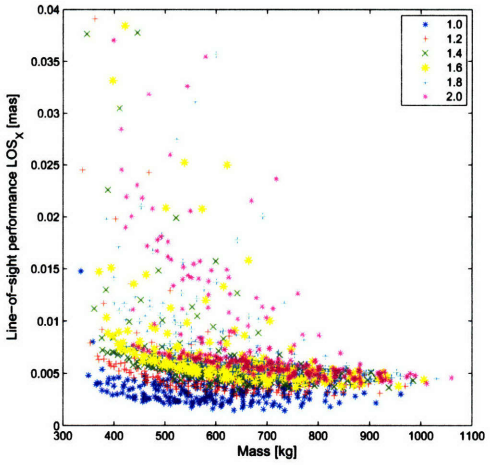

(b) f-number

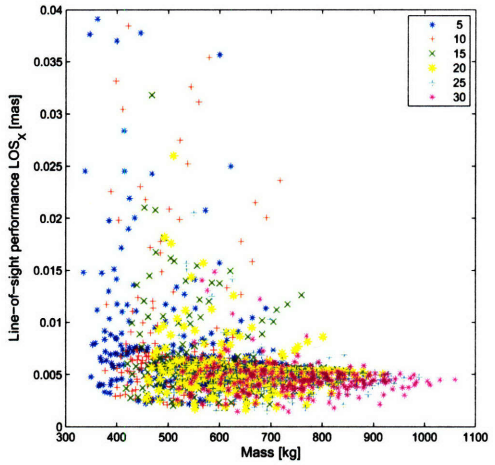

(c) PM areal density (kg/m^2)

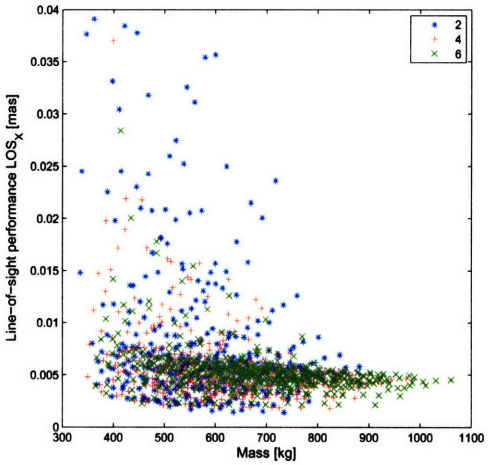

(d) Aspect ratio of mirror ribs

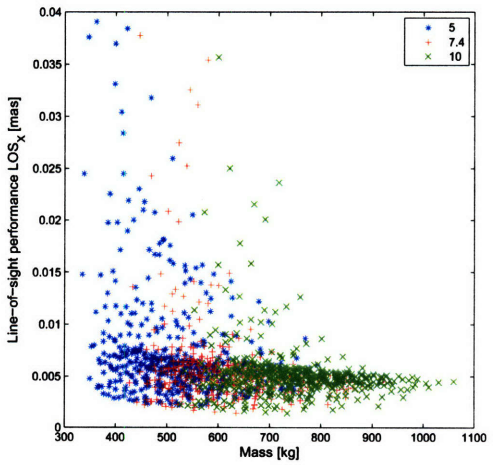

(e) Radius of SST struts (cm)

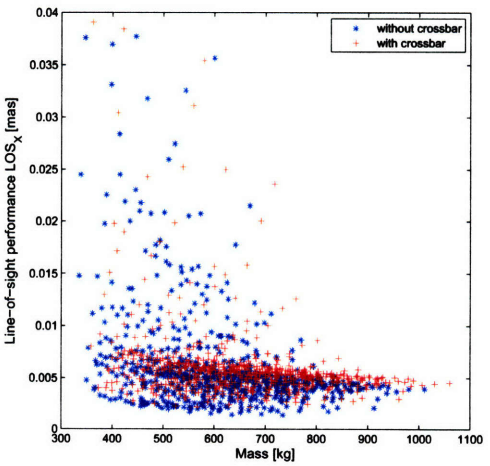

(f) SST crossbars

Figure 6-21: Trade space results for MOST mass versus line-of-sight jitter

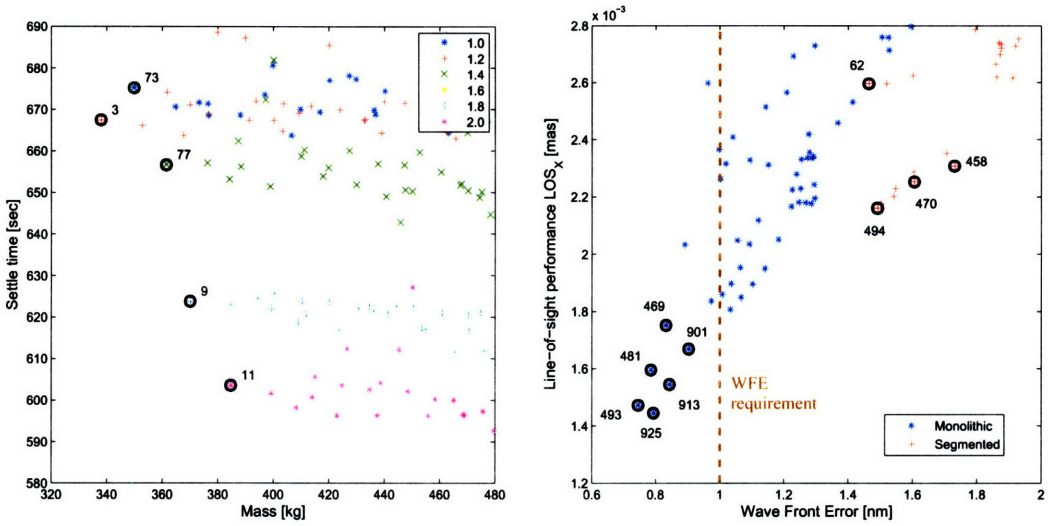

(a) Mass versus settle time

(b) WFE versus LOS

Figure 6-22: Sampled points at optimal corners of two scatter plots

were chosen to span across the f-number values in this plot. The actual design values and figures of merit outputs are given in Table 6.4. All of the designs are of monolithic mirrors with areal densities of 5 kg/m^2 and smaller rib aspect ratios. The smallest strut radius is used and there are no SST crossbars. These variable choices all lead to low-mass systems, and the mass values are certainly some of the lightest across the design space. Problems with these designs arise when one examines their optical performances. The LOS values are all still many orders of magnitude below their requirements (the LOS values shown are given in micro-arcseconds, where the requirement is in milli-arcseconds), but the wave front error outputs, especially for points 9 and 11, are large compared to many other points in the design space. It is useful to consider the requirements of the system in order to identify which designs are allowable. There are no requirements yet set for mass or settle time, and the LOS requirement is met in all cases shown here. Only the WFE requirement of 1 nm need be considered, but as shown in plot 6-22(b) it causes the majority of the design points - including the five identified in Table 6.4 - to be thrown out.

Ultimately only 14 designs meet the wave front error requirement of 1 nm. Those 14 designs are identified in Table 6.5. Several observations can be made about these designs. They are all monolithic apertures with an f-number of 1.0 and do not use SST crossbars. The low f-number suggests that the settle time may be poor for all designs, although the actual settle time values are not much worse than those identified in Table 6.4. The

Table 6.4: Details from design points identified in plot 6-22(a)

	Design numbers				
Parameters	73	3	77	9	11
Mirror type	Mono	Mono	Mono	Mono	Mono
f-number	1.0	1.2	1.4	1.8	2.0
Areal density (kg/m^2)	5	5	5	5	5
Rib aspect ratio	4	2	4	2	2
SST crossbar	No	No	No	No	No
SST strut radius (cm)	5.0	5.0	5.0	5.0	5.0
Outputs					
Mass (kg)	350	338	362	370	385
Settle time (sec)	675	667	657	624	604
LOS$_x$ (μas)	4.8	24.5	11.2	60.3	70.6
LOS$_y$ (μas)	5.7	32.8	14.8	91.5	118.0
WFE (nm)	1.1	2.5	3.4	6.0	6.5

mirror rib aspect ratios are 2 for 12 of the 14 designs, and the areal densities are mostly above 15 kg/m^2. Despite interest in much lower areal densities to decrease spacecraft mass, 5 kg/m^2 is not represented at all, and there is only a single design (#445) that utilizes 10 kg/m^2. The SST strut radius varies across its entire range.

What is surprising is how quickly the field of designs was reduced. All segmented systems, any architecture with an f-number greater than 1.0, and alternate SST architectures were eliminated. Based on the current models and requirements, mirror areal density and strut radius are left as the only free variables to trade. The dominance of monolithic versus segmented systems was expected, especially given that there was no control of the segmented mirror petals to account for their increased flexibility. Since the MOST program is interested in investigating segmented architectures, both for mass purposes as well as their ability to be folded into a launch fairing, the best 14 segmented designs are also identified and listed in Table 6.6. These show the same results as with the best monolithic designs: an f-number of 1.0, no SST crossbars, low rib aspect ratios and higher mirror areal densities. Areal density and strut radius are again the only free parameters within this design set.

The final results from this particular analysis identify the best MOST designs as shorter telescopes (low f-number) with no crossbars on the tripod secondary support towers. The rib-stiffened mirrors have squat ribs and are preferably heavier for a given area, although the results do show that lower areal density mirrors (less than 15 kg/m^2) are acceptable for

Table 6.5: Designs satisfying WFE requirement (all monolithic apertures)

	Parameters					Outputs				
Design #	$f/\#$	Areal density (kg/m^2)	Rib aspect ratio	Cross-bars	Strut radius (cm)	Mass (kg)	Settle time (sec)	LOS_x (μas)	LOS_y (μas)	WFE (nm)
493	1.0	30	2	No	7.4	635	855	1.5	1.6	0.75
925	1.0	30	2	No	10.0	735	832	1.4	1.5	0.79
481	1.0	25	2	No	7.4	594	671	1.6	1.7	0.79
913	1.0	25	2	No	10.0	693	663	1.5	1.6	0.84
469	1.0	20	2	No	7.4	552	670	1.8	1.9	0.83
901	1.0	20	2	No	10.0	651	670	1.7	1.8	0.90
457	1.0	15	2	No	7.4	510	671	2.0	2.3	0.89
61	1.0	30	2	No	5.0	543	666	2.8	2.8	0.87
49	1.0	25	2	No	5.0	502	724	2.8	3.1	0.91
37	1.0	20	2	No	5.0	460	671	2.9	3.4	0.95
445	1.0	10	2	No	7.4	469	817	2.6	3.0	0.96
889	1.0	15	2	No	10.0	610	667	1.8	1.9	0.97
133	1.0	30	4	No	5.0	633	671	3.0	2.4	0.98
121	1.0	25	4	No	5.0	576	669	2.4	2.3	1.00

some designs.

These results should motivate several additional lines of research into these systems, particularly concerning the rib-stiffened mirrors. Although low aspect ratio (and shorter ribs) have been shown here to be better for performance, taller ribs would generally be preferred if actuators were used on the ribs to change the shape of the mirror. This is of particular interest since introducing active wave front error control may increase the number of valid designs. Also, the segmented mirrors were not able to compete as well against the monolithic circular mirror, but applying tip-tilt control of the hexagonal petals may improve the results significantly. Finally, the mass savings expected for segmented mirrors were never fully realized. This may result from the design requirement that the baseline hexagonal petals have a 100 Hz fundamental frequency, compared to only 20 Hz for the large, circular mirror. If this 100 Hz requirement could be relaxed, there is likely to be a mass savings that would benefit the segmented architectures.

All of these results assume that the individual point designs are distinguishable from each other. If the uncertainty of each design is so large that two or more design points are within the bounds of an uncertainty bounding box, any statements made about the uniqueness of

Table 6.6: Best designs with a segmented aperture

	Parameters					Outputs				
Design #	$f/\#$	Areal density (kg/m^2)	Rib aspect ratio	Cross-bars	Strut radius (cm)	Mass (kg)	Settle time (sec)	LOS_x (μas)	LOS_y (μas)	WFE (nm)
62	1.0	30	2	No	5.0	519	671	2.6	2.8	1.46
494	1.0	30	2	No	7.4	612	673	2.2	2.1	1.49
926	1.0	30	2	No	10.0	714	673	2.2	2.2	1.50
50	1.0	25	2	No	5.0	488	967	2.6	2.9	1.52
482	1.0	25	2	No	7.4	582	673	2.2	2.2	1.54
914	1.0	25	2	No	10.0	684	664	2.2	2.2	1.55
38	1.0	20	2	No	5.0	458	673	2.6	2.9	1.60
902	1.0	20	2	No	10.0	653	677	2.3	2.3	1.60
470	1.0	20	2	No	7.4	552	691	2.3	2.2	1.61
890	1.0	15	2	No	10.0	623	760	2.4	2.3	1.70
458	1.0	15	2	No	7.4	521	728	2.3	2.3	1.73
26	1.0	15	2	No	5.0	427	678	2.8	3.1	1.79
950	1.0	10	4	No	10.0	612	758	2.7	2.7	1.86
938	1.0	5	4	No	10.0	572	674	2.6	2.6	1.86

a particular design or family of designs may be questionable. The next sections will apply the uncertainty parameter identification and bounded analysis routines on the trade space results. This will be done to determine the size of the design point uncertainty space, and to compare the robustness of different designs to parametric uncertainty.

6.4 Uncertainty analysis across the trade space

The MOST design approach is aimed particularly at high-performance, high-risk missions which need to employ novel new technologies and spacecraft architectures to achieve their goals in terms of both performance and system costs. The large, flexible structures that are being proposed for MOST face the same situation as missions such as the Terrestrial Planet Finder, in that full systems tests before launch may not be possible for design validation. Given this situation, it is necessary to consider how to validate the designs through analytical means. An aspect of that validation is running uncertainty analyses throughout the design lifecycle. This starts with the identification of critical sources of uncertainty that require additional analysis, and ends prior to launch with the probability that the mission will meet

its requirements.

The same approach to uncertainty that was described in Chapter 5 is now incorporated into the MOST analysis framework. This intersection of uncertainty analysis with parameterized modeling provides a powerful design tool that examines the conceptual design space for both nominal performance results and robustness to uncertainty. Along with identifying superior designs on the basis of their nominally meeting requirements, designs can also be identified and categorized based on their susceptibility to parametric uncertainty.

This analysis provides useful information first on the robustness of the designs, but it also guides how design variables can be used. If, for example, the uncertainty bounding box for a particular design is so large that many alternative designs with different design variable values are within its limits, it is questionable whether changing the design variables being considered (f-number, areal density, etc.) would actually influence the system in the way the nominal results suggest. On the other hand, if the bounding boxes are tight about each design point, there is increased confidence that varying the design variables is a valid means of improving the design.

An example of the uncertainty technique proposed in Chapter 5 is shown applied across the MOST design space. Critical uncertainty parameters are first identified from a larger set of parameters. After that, uncertainty bounds about many design points are generated based upon a bounded description of the parameter uncertainty.

6.4.1 Critical parameter identification

A list of parameters likely to contribute to the performance uncertainty was selected from the "Parameters" module. These parameters are separate from the design variables used to compare different architectures. The values for the design variables (f-number, areal density, etc.) are all chosen by the designer and, for the purposes of the uncertainty analysis, may be considered fixed for each design point. Ten parameters are selected based on engineering judgement that they may contribute to the system uncertainty. They are:

- Mirror plate density
- Mirror plate modulus
- Bus mass

- Solar panel density
- Solar panel modulus
- Optical bench density
- Optical bench modulus
- Mirror bipods modulus
- SST strut modulus
- Modal damping

Of the four mission figures of merit, only line-of-sight is directly output from the state-space system and could be evaluated using an analytic sensitivity analysis. In order to also gage the effect of these uncertainty parameters on outputs such as wave front error, settle time and mass, the analysis of variance approach using computer simulations from Section 5.1.2 is needed.

The ANOVA results from the TPF-FFI analysis (from Table 5.9) show that even when different levels of parameter variation were used (0.1%, 1%, 10%) many of the same parameters are identified in each run. As a result, the computer simulations for MOST are run at only a single level of variation: 10% of the parameter nominal values. For each design point investigated, the 10 parameters are varied using a resolution IV design matrix (main effects are not aliased with other main effects nor with 2-way interactions) of 32 runs.

This critical parameter analysis technique is applied to a set of the design points across the MOST trade space. It is run on four of the designs identified on the pareto-front from Figure 6-22(a) (designs 3, 9, 11, and 77) and on four of the performance-optimal designs from both monolithic and segmented systems in Figure 6-22(b) (458, 493, 494 and 925). Two representative ANOVA plots from this group are given in Figure 6-23, and all of the results are presented in Tables 6.7 and 6.8. The relative influence values greater than 10% are highlighted using boxes. It is obvious looking across the tables that of these 10 parameters, there are only six that have a strong influence on the model outputs. These six are density and modulus of the primary mirror material, mass of the bus components, density of the solar panels, modulus of the SST struts and modal damping.

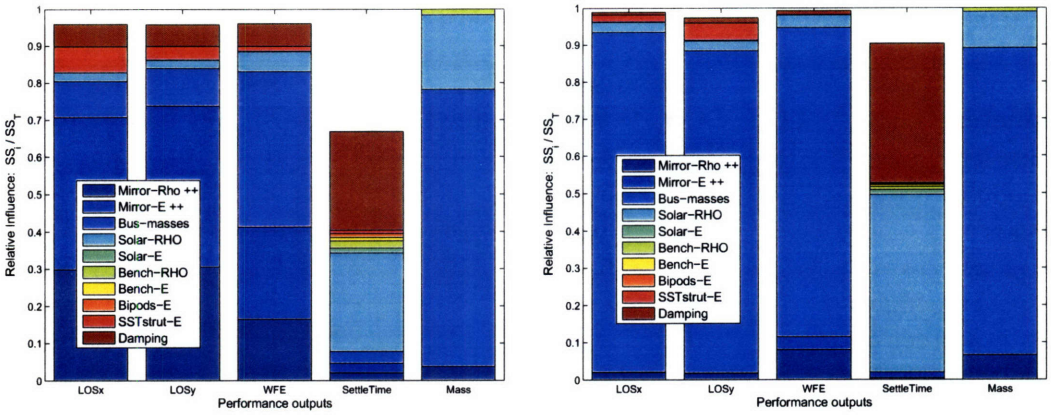

(a) Design #9

(b) Design #458

Figure 6-23: Relative influence plots for two MOST design realizations

These results may have a direct influence on future modeling efforts for the MOST spacecraft. The influence of the mirror and SST strut material properties could be anticipated, given the importance of these structural components in the optical outputs. If the current values for density and modulus were general values obtained from look-up tables, it would be advisable to decide upon specific materials and to find their material properties directly from industrial sources. Similarly, modal damping is an often-targeted source of uncertainty given the great many questions about the nature of damping and appropriate ways to model its effect. Since values of modal damping have been suggested to change dramatically based on the anticipated thermal environment[8], an understanding of the orbit and spacecraft environment for MOST could guide selection of a damping value.

The solar panel density, which is related directly to the mass of the solar panel, could have been expected given the contribution of solar panel modes in the cumulative RMS output curves (the 0.497 Hz mode from Figure 6-8). Their apparent importance in the system warrant either more detailed modeling, or a re-designed isolation system to attenuate their effect.

Perhaps the most surprising result is the large influence of bus mass on the system. Currently, bus mass is estimated just from a curve-fit of mirror mass to bus mass across several legacy space systems. Since this parameter is identified as such a large influence in the system, it would be advisable to commit research resources to better modeling the

[8]Very low modal damping of 0.01% or less has been recommended by engineers at JPL for infrared telescopes with optical instruments kept at cryogenic temperatures.

Table 6.7: Relative influence percentages for MOST: designs 3, 9, 11 and 77

	Design point 3					Design point 9				
Parameters	**LOS_x**	**LOS_y**	**WFE**	**time**	**mass**	**LOS_x**	**LOS_y**	**WFE**	**time**	**mass**
PM density	38	38	4	3	4	30	31	16	2	4
PM modulus	29	31	5	4	-	41	43	25	3	-
Bus mass	9	9	79	2	76	10	10	42	3	74
Solar panel density	5	4	6	5	19	2	2	5	26	20
Solar panel modulus	-	-	-	7	-	-	-	-	1	-
Optics bench density	-	-	-	5	2	-	-	-	2	2
Optics bench modulus	-	-	-	-	-	-	-	-	1	-
Mirror bipods modulus	-	-	-	8	-	-	-	-	1	-
SST strut modulus	-	-	-	5	-	7	4	1	1	-
Modal damping	3	3	2	11	-	6	6	6	26	-

	Design point 11					Design point 77				
Parameters	**LOS_x**	**LOS_y**	**WFE**	**time**	**mass**	**LOS_x**	**LOS_y**	**WFE**	**time**	**mass**
PM density	28	29	13	-	4	34	41	1	-	12
PM modulus	45	48	26	38	-	25	27	-	1	-
Bus mass	7	8	46	-	74	14	12	93	-	68
Solar panel density	2	2	6	5	21	2	2	5	52	18
Solar panel modulus	-	-	-	-	-	-	-	-	-	-
Optics bench density	-	-	-	2	1	-	-	-	-	1
Optics bench modulus	-	-	-	-	-	-	-	-	-	-
Mirror bipods modulus	-	-	-	-	-	-	-	-	-	-
SST strut modulus	9	4	2	1	-	15	9	-	-	-
Modal damping	5	5	4	14	-	6	6	-	44	-

spacecraft bus components. Individual components should be identified and effort taken to determine the total anticipated mass for each design realization.

Since the critical parameters are similar for all of the eight investigated design points, no further simulations are performed for critical parameter identification. The next step is to perform an uncertainty analysis across the design space using these six uncertainty parameters.

6.4.2 Design point uncertainty analysis

A bounded uncertainty analysis is performed by searching the parameter range vertices for the worst-case values. Example uncertainty bounds for the six parameters are given

Table 6.8: Relative influence percentages for MOST, designs 458, 493, 494 and 925

	Design point 458					Design point 493				
Parameters	**LOS_x**	**LOS_y**	**WFE**	**time**	**mass**	**LOS_x**	**LOS_y**	**WFE**	**time**	**mass**
PM density	2	2	8	-	7	2	3	4	-	23
PM modulus	-	-	3	2	-	3	9	-	1	-
Bus masses	91	87	83	-	83	76	59	92	-	74
Solar panel density	3	3	3	48	10	2	2	1	26	3
Solar panel modulus	-	-	-	1	-	-	-	-	1	-
Optics bench density	-	-	-	1	1	-	-	-	-	-
Optics bench modulus	-	-	-	1	-	-	-	-	1	-
Mirror bipods modulus	-	-	-	-	-	-	-	-	1	-
SST strut modulus	2	5	-	-	-	3	6	-	-	-
Modal damping	1	2	1	38	-	1	2	-	56	-

	Design point 494					Design point 925				
Parameters	**LOS_x**	**LOS_y**	**WFE**	**time**	**mass**	**LOS_x**	**LOS_y**	**WFE**	**time**	**mass**
PM density	5	3	5	2	14	6	7	4	1	21
PM modulus	-	-	-	6	-	-	1	-	1	-
Bus masses	92	86	93	2	80	92	90	95	8	76
Solar panel density	1	1	1	-	5	1	1	1	10	3
Solar panel modulus	-	-	-	4	-	-	-	-	-	-
Optics bench density	-	-	-	1	1	-	-	-	-	-
Optics bench modulus	-	-	-	3	-	-	-	-	8	-
Mirror bipods modulus	-	-	-	4	-	-	-	-	3	-
SST strut modulus	1	7	-	2	-	-	-	-	10	-
Modal damping	-	-	-	15	-	-	-	-	2	-

in Table 6.9.[9] These values were not obtained from any empirical testing, but rather are estimated values from engineering judgement.

A full factorial design matrix is prepared for the six parameters. Although $2^6 = 64$ performance simulations are required, evaluating modal damping does not necessitate a finite element analysis, so only 32 FE models must be generated and evaluated. The worst values for each model output are retained. Boxes can be drawn about each design point on the scatter plots to represent the uncertainty bounds of each design point.

All of the designs from the critical parameter identification analysis along with a selection of designs along the mass-LOS pareto-front and at the optimal corner of the WFE versus LOS scatter plot were investigated. Twenty-two design points were evaluated in all. The

[9]Note that the nominal bus mass is calculated separately for each design.

Table 6.9: Uncertainty bounds on MOST critical parameters

Parameter (FE element)	units	Lower Bound	Nominal	Upper bound
PM density (ctria3, cquad4)	kg/m^3	3100	3200	3400
PM modulus (ctria3, cquad4)	N/m^2	350×10^9	375×10^9	400×10^9
Bus masses (conm2)	kg	$0.95 \times m_{nom}$	m_{nom}	$1.05 \times m_{nom}$
Solar Panel density (cquad4)	kg/m^3	2816	2916	3000
SST strut modulus (cbar)	N/m^2	170×10^9	189×10^9	208×10^9
Modal damping	-	0.4%	0.5%	1.0%

collection of results can be used to evaluate the robustness of the design, but also illustrate the power of parameterized modeling combined with non-deterministic analyses to guide conceptual design. This will be discussed in the next section.

6.5 Discussion of uncertainty results and design approach

The traditional approach to structural modeling in early phases of the design lifecycle was to build and analyze a point design. Consider the example of Figure 6-24, which focuses on a "nominal" design for MOST: a monolithic aperture with f-number=1.0, rib-stiffened primary mirror with areal density of 5 kg/m^2 and rib aspect ratio of 4, no crossbars on the SST and SST struts with a radius of 7.4 cm.[10] A static structural and integrated model can be analyzed in terms of nominal performance (indicated by stars), uncertainty (the bounding box), and sensitivity to material or geometry parameters. Model-based analysis of alternative architectures and telescope forms would not traditionally occur however. Running finite element analyses for many modes, evaluating slew/settle time histories, performing PSD-based disturbance analysis and re-running the simulation multiple times for this type of bounded uncertainty analysis has historically been too computationally intensive for rapid design studies. Even a small finite element such as MOST still has tens of thousands of degrees of freedom, and a model with higher finite element mesh densities may easily have hundreds of thousands of degrees of freedom. Obtaining modal frequencies and modeshapes from this system would take significant time, as would running dynamic analyses with state-space systems of hundreds or thousands of states (MOST typically outputs 200 modes, for a 400-state system). More than anything else, the methods of analysis used

[10]Note that there is no such point design for MOST; the design point (#505) was selected for illustrative purposes only.

on MOST have benefitted from increases in computational power; the finite element and dynamic analysis routines run fast enough to make multiple analysis runs practical for these design studies. The conceptual design space has opened up from that one, single design point (Figure 6-24), to a multitude of unique structural realizations (Figure 6-25), each comprised of an independent finite element model, and each subject to a suite of analysis tools.

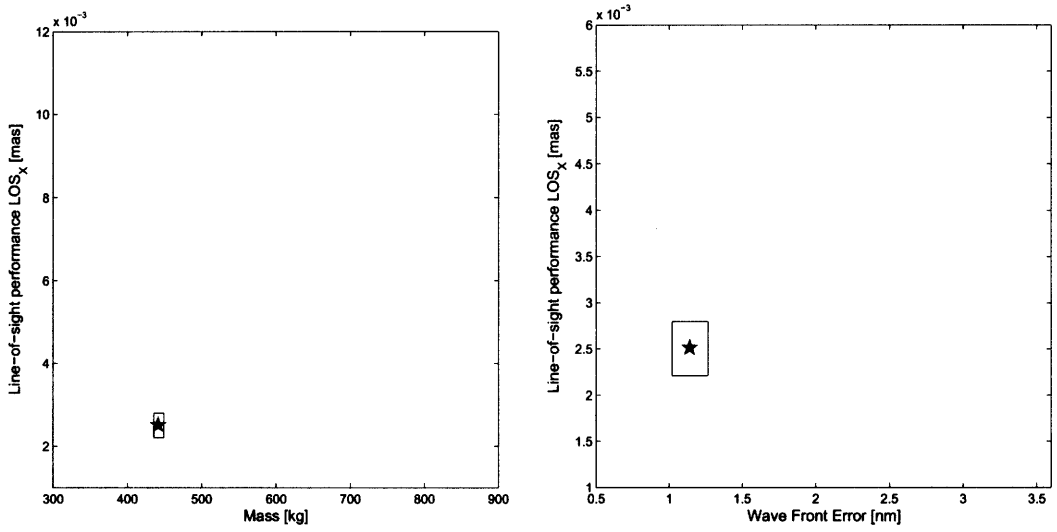

(a) Mass versus LOS_x (b) WFE versus LOS_x

Figure 6-24: A single point design with uncertainty bounds

Compared to the single point design, other designs are identified which either make up a pareto-optimal front along with the point design (Figure 6-25(a)), or whose nominal values are superior to the point design (Figure 6-25(b)). New regions of the design space can be explored, and alternative architectures identified using model-based, quantitative analysis techniques.

Once a selection of superior *nominal* designs are identified, the question arises as to whether these designs are unique. If the uncertainty bounds of an optimal design encompass many other points, it is not possible to say with confidence that the chosen design is actually superior to any of the others. There is always a chance that the optimal design, once realized in hardware, would fall into a corner of the uncertainty space with worse performance than other designs, as illustrated in Figure 6-26(a). Also, if the uncertainty bounds encompass designs across a variable's range, it calls into question whether changing

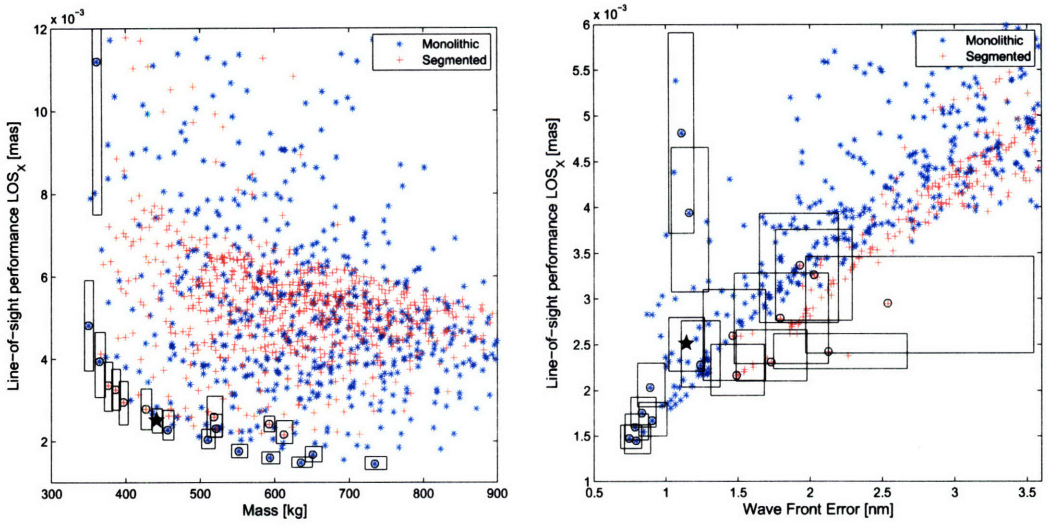

(a) Mass versus LOS_x (b) WFE versus LOS_x

Figure 6-25: Opening up the design space using parameterized structural modeling techniques combined with non-deterministic analysis. The "nominal" design is indicated with a star.

that particular variable actually will have the anticipated effect. If, however, the uncertainty bounds are tight about each point, as drawn in Figure 6-26(b), confidence increases in both the uniqueness of the design and in the ability to reach a particular level of performance using particular design variables.

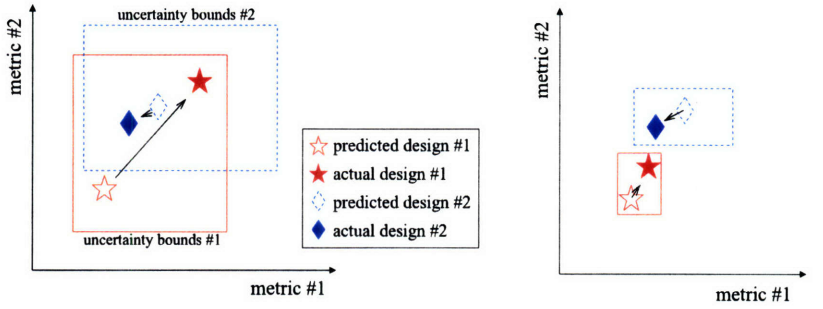

(a) Large uncertainty bounds (b) Small uncertainty bounds

Figure 6-26: Illustration of the role of uncertainty bounds in choosing between conceptual designs

The uncertainty bounds of the MOST results in Figure 6-25 show examples of both situations, but generally are tight about the design points. Especially along the mass versus LOS optimal front in 6-25(a), the bounds are small enough to enclose only the single

design point. These points exhibit greater robustness to parametric uncertainty, and are unique compared to the other designs across the trade space. It can be observed that the variability of the LOS output (height of the bounding box) increases to the left side of the optimal front, at lower mass designs. This shows that besides an optimal front in terms of mass versus LOS, there is also an optimal front in terms of mass versus design robustness. If the robustness of these points will drive the design, there is a trade-off between how heavy the spacecraft is allowed to become versus how much expense and effort will be expended to reduce those uncertainty bounds.

The bounds about the optimal points in the WFE versus LOS scatter plot of Figure 6-25(b) tend to be larger and more varied in shape. There is a noticeable difference in the bounds between the monolithic and segmented systems; the aspect ratio of the bounds for monolithic apertures tend to be tall and narrow, while for the segmented apertures they tend to be shorter and wide. This follows the trends of these systems first identified in the full scatter plot from Figure 6-20(a); segmented systems showing greater variability across WFE and less in LOS, and vice versa for the monolithic systems. The size of the uncertainty space also varies amongst the optimal designs for each type of system; the optimal monolithic design points actually have the smallest bounds in the plot. This is positive news for the designer, in that it suggests that the designs with best performance also are the most robust. The collection of the six best designs at the lower left corner of Figure 6-25(b) (designs 493, 925, 481, 913, 469 and 901, in which only the areal density and strut radius change) are distinguishable from all of the other design points in terms of performance (although there is some overlap of bounding boxes within this cluster). The same cannot be said of the best performing segmented systems. The uncertainty bounds for these systems tend to be larger than the bounds about the optimal monolithic designs, and the bounding boxes enclose many monolithic systems. The segmented systems are not distinguishable from the monolithic, meaning that even if the segmented *nominal* performance was superior (which it is not) to the monolithic mirrors, the actual hardware could have worse performance. Or, to put it another way, it is not possible to choose between the selected segmented designs versus any of the enclosed monolithic designs for a unique outcome. The design choice may lead to multiple outcomes, where one possibility is that the chosen design will have worse performance than the abandoned designs.

Figure 6-27 compares the same plots, but color coded as a function of f-number.

The exact same bounding boxes are shown. This plot illustrates the uniqueness of f-number amongst the optimal designs. Especially in 6-27(a), but also amongst the best designs in 6-27(b), the uncertainty bounds only enclose $f/1.0$ designs. While f-number is not a promising design variable that can be used to move the design along the optimal front, these plots increase confidence that an $f/1.0$ system (or at most an $f/1.2$ system) is appropriate to obtain the desired mass and optical performance results.

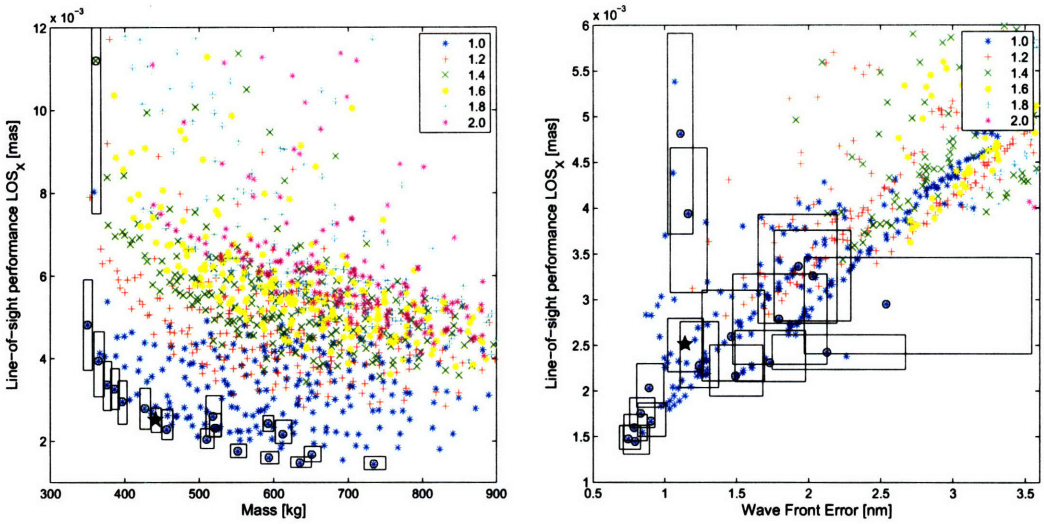

(a) Mass versus LOS_x

(b) WFE versus LOS_x

Figure 6-27: Uncertainty bounds across varying f-number

Variation of mirror areal density is shown with the uncertainty bounds in Figure 6-28. It was suggested before that areal density would be an appropriate design variable to change, in order to move along the optimal front. Plot 6-28(a) confirms this by indicating that even with uncertainties, a change of areal density in 5 kg/m^2 increments will cause a unique movement along the LOS versus mass pareto-front. The uncertainty boxes of the WFE versus LOS plot (6-28(b)) enclose many more areal density values, and of the evaluated points every value in the range is represented. This suggests that an attempt to improve the performance outputs by changing areal density may *not* always result in a better design, based on the actual hardware values of the uncertain parameters. At the least however, this plot does suggest that those six optimal points at the very bottom left of the scatter plot are still the best performers at any areal density greater than 20 kg/m^2.

The last uncertainty plot examined is Figure 6-29, which plots mass versus settle time. Even in the single-axis trade plots, settle time seemed to exhibit great variation across

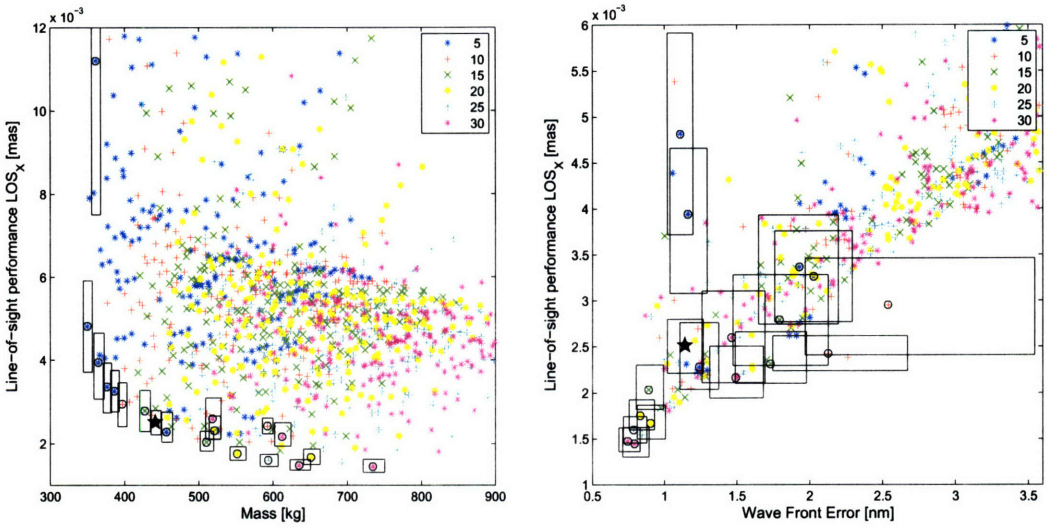

(a) Mass versus LOS_x

(b) WFE versus LOS_x

Figure 6-28: Uncertainty bounds across varying mirror areal density (kg/m^2)

ranges of design variables. Across the uncertainty space, the bounds on settle time are even greater than the variation of design points. This result indicates that predicting settle time in the presence of uncertainty will be challenging. Since the source of this great variation is likely the system damping, more effort should be made in determining an appropriate level of modal damping and in reducing the uncertainty bounds on the modal damping value.

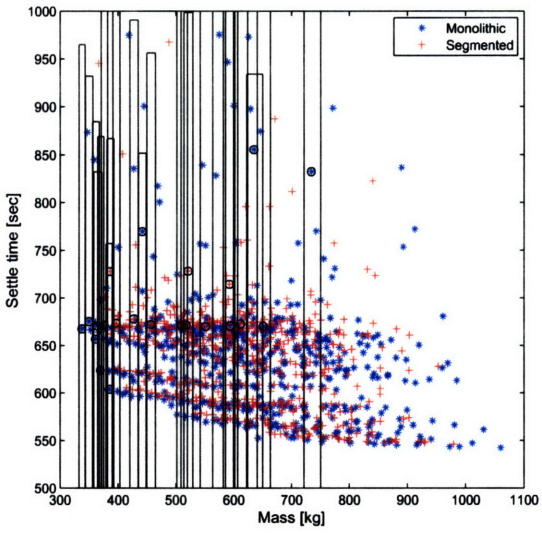

Figure 6-29: Uncertainty bounds for the mass versus settle time scatter plot

6.6 Conclusion

The design of the Modular Optical Space Telescopes is used as an example of how parameterized modeling and uncertainty analysis of integrated opto-mechanical systems allow a much broader examination of the conceptual design trade space and can drive the design to particular architecture families that exhibit superior performance and robustness to uncertainty. This model-based approach to design provides the same information that a single low-fidelity finite element "stick" model does, but whereas traditional approaches in early stages of design would build only a single model, the approach used for MOST shows how any number of separate, unique structural realizations can be generated. Instead of using analysis tools such as dynamic performance prediction or uncertainty propagation to merely determine whether a single point design meets its requirements or not, these analysis techniques are used at the beginning of the design lifecycle to drive some of the key design decisions that define the spacecraft.

The approach outlined in this chapter emphasizes the multi-faceted nature of the design evaluation. Once the parameterized model is developed, with access to the design variables of interest, single axis trades should be run first to understand the basic behavior of the system across variable ranges. Any interesting or unusual characteristics identified at this stage can be investigated by examining the individual designs. The single parameter trade curves can also motivate design variable step sizes to be used in a larger trade space analysis. This larger analysis is undertaken next. A full factorial evaluation of every variable combination is used on MOST, although it is recommended that optimization schemes be applied in the MOST environment. The results from the full factorial trades can be visualized to highlight particular design variables, and the optimal designs can be identified. Once a selection of promising nominal design points are found, critical parameter identification techniques reduce a large collection of uncertain parameters to those parameters which most influence the system. Non-deterministic analysis techniques such as a bounded uncertainty analysis are run to gage the robustness of the selected designs. All of this information is used first to identify superior, robust architecture families. The plots can be used to identify the pareto-optimal fronts, along which figures of merit can be traded against each other. And finally the simulations point out those design variables that even in the presence of uncertainty can be used to trade between competing figures of merit.

These results do not come without a price. To begin with, construction of the parameterized model requires more effort than would a single point design FE model. Instead of building a single model using finite element pre-processing software, MOST is created by writing MATLAB m-files that construct all of the appropriate Nastran input cards. Care must be taken that each component is built appropriately, given the unique dimensions, shapes, and mesh fidelity parameters that may be input into the file. Similarly, the assembly of the individual components into a single spacecraft must occur in a completely generic fashion, where attachment points must be designed to accept different mirrors, secondary towers, or spacecraft buses.

Once the parameterized model is complete, there is an acknowledged computational expense to running the simulation. The 1296 initial design realizations took a weekend running on two computers. After that there were nearly as many simulation runs for the critical parameter identification across eight design points (each requiring 32 runs) and the uncertainty analysis across 22 points (each requiring 64 simulations, although half as many FE solutions).

This being said, the simulation took half the time on computers newly bought in 2006 as they did on the second fastest available computer. Since the simulations do not depend on each other, the entire batch job could be given to a cluster of computers and run overnight. The computational power available to today's engineers makes this method of simulation-based analysis practical where even five years ago it might have been considered too computationally and time intensive to use in actual design studies such as MOST

Ultimately, superior architectures were identified for the MOST spacecraft. All designs met the line-of-sight requirement, but only 14 out of 1296 designs met the wave front error requirement of 1 nm. These 14 designs all used monolithic circular mirrors with an f-number of 1.0. The areal densities of the mirror tended to be heavier, mostly above 20 kg/m^2. The rib aspect ratios were small, and crossbars were never used on the SST. No alternative SST designs were examined in this study, although others have been created for a larger analysis of MOST. Similar results were shown when the 14 best architectures using a segmented primary mirror were examined. In both cases, monolithic and segmented, the only free variables remaining for the designer were the areal density and the rib aspect ratio.

Next steps for the MOST spacecraft should include the application of controllers on the segmented mirror petals, to improve the performance of the segmented designs relative to

the monolithic. Also, optimization routines can be used to explore the design space. It may be that superior designs exist between the design points examined in this full factorial evaluation, and optimization routines may do a better job at identifying these points. Finally, further study of how long it takes the performance to settle after a slew is needed to first reduce the nominal settle times (currently around 10 minutes), and to determine why the settle time is so sensitive to uncertainty in the system.

Chapter 7

Conclusions and Contributions

7.1 Thesis summary

This thesis proposes a methodology using parameterized structural and integrated dynamics models, coupled with non-deterministic analysis tools, to identify robust designs for opto-mechanical systems in conceptual design. This is motivated by the need for the next generation of space telescopes to meet ever more stringent optical performance requirements, while at the same time satisfying systems metrics such as low mass and cost, availability of the spacecraft to take science images and robustness of the design to uncertainty. Being robust to uncertainty is ever more important, since these mission will not be validated using a full systems test prior to launch. Instead, design validation is dependent upon model analysis supported by data from testbeds or prototypes. Example lightweight, high-performance space telescopes include upcoming NASA missions such as the Terrestrial Planet Finder spacecraft, which will use combinations of advanced optical designs and active control to push the boundaries of science and technology. Optical requirements for these missions are on the orders of milli-arcseconds for pointing, and nanometers for optical pathlength control. Meeting these requirements on flexible structures that must remain lightweight for launch will require new methods of design.

Given these challenges, this thesis proposes moving the initial structural modeling and dynamic analysis from the preliminary design stage, at which point a single point design has been already selected, to the conceptual design stage. During the conceptual stage, many competing designs are still being considered and compared to one another. These designs may use completely different approaches to meeting science requirements; for example,

either a coronagraph telescope or an optical interferometer (or perhaps both) may be used for the Terrestrial Planet Finder mission. The designs will also vary based on the type of aperture, dimensions of the spacecraft, and combinations of passive or active disturbance attenuation techniques. Since design decisions made at the start of a program have a strong effect on the ultimate costs of a mission, greater insight into the relative performance and robustness characteristics of competing designs would be a powerful tool in driving the design decisions toward an optimal design. This greater insight is provided in the conceptual stage through quantitative, model-based analysis across a large design space. Models of the spacecraft are automatically created and analyzed based on a vector of design inputs.

Chapter 1 introduces the methods used in this thesis, including design analysis using parameterized finite element and integrated models, followed a parametric uncertainty evaluation. This approach follows closely on work such as Jilla [22], in which a large trade space is sampled using optimization routines to choose high-level design variables. The models in that work were based around design variables such as orbital altitude and reliability of components. Those design variables focus on system metrics such as performance, cost and survivability for distributed satellite systems, and were related to the model outputs by algebraic relations. The design variables considered in this thesis are focused on the physical spacecraft. The designer can vary parameters such as the type of primary mirror or secondary support tower, the dimension and shape of the optics, or values that define vibration attenuation approaches such as isolation and active control of the optical pathlength. This allows a unique structural and dynamics model to be built for every set of design variables. Although optimization routines are not used in this work, the design space for the parameterized opto-mechanical model can be explored to identify trends in performance and robustness across the design choices.

Chapter 2 motivates this approach to conceptual design by comparing it to the traditional method of using experience or evolution of existing architectures to choose a single point-design, before any models are built. While that approach has worked well on past missions, the challenge of the newest generation of space telescopes is that the architectures and technologies being considered (e.g. lightweight, rib-stiffened mirrors and adaptive control of optical surfaces) have not been flown in space before, and there is no heritage of experience to draw upon. In [31], Baker and Hoffman make the point that when "unconventional configurations are being designed," relying on traditional approaches in the conceptual stage

may lead to designs with "show stopping structural issues." To counter this, and to support validation of designs through analytic means, the parameterized modeling approach allows evaluations of many architectures, each with unique combinations of design variables. This allows superior designs to be identified that meet the performance requirements, but also that make best use of technologies to satisfy the system-level metrics such as mass and cost. Since evaluation of many unique structural designs is computationally challenging, an example is shown of the dramatic increases in computer speed just within the last six years. Where formerly it took over two hours to run a mathematical operation common in dynamic analysis, on computers purchased in 2006 the same operation takes just over a minute. This speed increase allows for simulation-based trade space analyses, where before such an approach would not have been practical.

An overview of the integrated models used in this work is given in Chapter 3. These include structural finite element models, from which modal frequencies and modeshapes are obtained using Nastran. Optical performances are derived, based either on approximations using the displacement of optical elements or on a Zernike decomposition of primary mirror deformations. The effect of isolation and optical control is approximated using filters. A frequency-based disturbance analysis is run by propagating power spectral density curves of reaction wheel disturbances through the state-space model, to obtain PSDs of the performance outputs. An example using the TPF-FFI spacecraft shows that using a broadband disturbance model, the line-of-sight (LOS) jitter outputs meet their requirement while wave front error (WFE) exceeds its requirement by several orders of magnitude. A 1 Hz mode of the TPF-FFI spacecraft is identified as causing the WFE degradation; since reaction wheel speeds can be tuned to avoid that particular frequency, additional analysis is recommended to determine WFE when that particular mode is not excited.

A necessary component of the conceptual stage trade space analysis is the parameterized model, allowing the designer to evaluate the effect of changing design variables. Chapter 4 presents two methods of model parametrization. The linear fractional transformation (LFT) is used in the DOCS toolset to create parameter dependent state-space models. Examples of its use on the TPF-structurally connected interferometer are shown. In order to evaluate the effect of changing design variables such as dimensions, that require moving grid points and changing element connectivities, an environment is developed for the automatic generation of new finite element models given a set of high-level parameters. The rules for this

parametrization approach are described. They include keeping all parameters for the entire model in a top-level module, so that any parameter can be varied without the need to edit lower-level functions. A module hierarchy is recommended, in which parameter values are passed down to lower-level functions that create separate components of the larger finite element model. Information such as connection grid points is passed up to high-level modules which then assemble the FEM, interface with Nastran, create the integrated model, and run the analyses. Additional aspects of the parameterized modeling approach include a reaction wheel sizing algorithm that bases the size of the flywheels on the spacecraft inertias and slew requirements, and scales the reaction wheel disturbances with flywheel inertia.

An example of this parameterized modeling approach is shown with the Thirty Meter Telescope, a ground-based telescope whose actively controlled primary mirror aperture is created using many smaller mirror segments. A trade space analysis is performed varying parameters such as telescope type, location of the elevation axis and focal ratio (f-number) of the mirror. The results suggest that a Cassegrain telescope with smaller f-number and larger final focal ratio and with an elevation axis above the primary mirror will provide the best combination of performance, mass and cost.

Once superior designs are identified based on their nominal performance, it is just as important in conceptual design to evaluate their performance under uncertainty. As long as performance requirements are met, the designs' robustness to uncertainty should be a key distinguishing characteristic that drives which architectures are selected for further study. Chapter 5 describes techniques for identifying sources of uncertainty and for propagating uncertainties through the model. In the case of parametric uncertainty, several methods of identifying the critical uncertainty parameters are described. The first is to compute the analytic sensitivities of the outputs of a state-space system to the parameter inputs. This approach, built into DOCS, is shown to identify critical parameters for the TPF-FFI spacecraft. The issue with this method, as with the LFT parametrization technique, is that it is only valid for state-space systems. The influence that parametric uncertainties have on outputs such as mass, settle time or wave front error (which is computed as a root-sum-square of displacement outputs) cannot be computed in this manner.

An alternative approach is proposed, in which the mature field of Design of Experiments is applied to the spacecraft design problem. The values of a large selection of spacecraft parameters are varied based on fractional factorial design matrices. The simulations are run

and the results are evaluated using the analysis of variance to indicate which parameters most influence the simulation outputs. Using DOE techniques, it is possible to get information on the effect of the parameters in fewer runs than would be necessary if a full factorial experiment were attempted. This approach is also shown using the TPF-FFI model, where 15 initial parameters are reduced to eight parameters that strongly influence the system. The identified parameters were the same as with the sensitivity analysis for line-of-sight jitter (the only output the sensitivity analysis can evaluate), verifying the results of the technique. The DOE/ANOVA approach was run several times, changing the level of parameter variation from 0.01% to 10% of nominal. For the designs that were not dominated by any one single parameter, the results were similar across levels of variation.

Once the parameters that actually influence the outputs are identified, a parametric uncertainty analysis is run. Several approaches to uncertainty are described, including the change-of-variables approach that analytically propagates a probability density function through a model to determine the PDF of the output. For integrated modeling in the conceptual design stage however, the lack of empirically-based parameter uncertainty models recommends a bounded approach to uncertainty. For the TPF-FFI model, bounds are placed about the eight remaining critical parameters and a vertex search is employed to determine the worst-case performances based on simulations run at the vertices of the uncertainty space. The results for TPF-FFI show that both LOS outputs still meet their requirements with uncertainty, however the margin between the worst-case bound and the requirement is greatly reduced. Uncertainty results from 700 Monte Carlo samples show that although there are isolated cases in which parameter values between the bounds cause an exceedence of the worst-case vertex search bounds, these cases are rare. The vertex search method is an appropriate tool for parametric uncertainty propagation at this stage in the design lifecycle.

Finally, the entire approach to conceptual design is implemented in Chapter 6, with an analysis of the Modular Optical Space Telescope. The MOST example brings together all of the concepts developed in this thesis, and shows how their combined use can guide the design to specific architecture families that exhibit both superior and robust performance. Once the parameterized model is generated, single-axis trades are first run to identify trends in the response. For the MOST model, this identified a range of f-numbers (between 1.6 and 1.7) in which overlapping fast steering mirror and secondary support tower modes

cause a jump in the response. The single axis trades were also instrumental in highlighting an issue with the rib-stiffened mirror model, in that rib aspect ratio could not be varied separately from mirror areal density, as desired. Bi-variate trades allow an examination of the response across changing isolator corner frequencies, and illustrate the benefits of two layers of dynamic isolation.

Multi-parameter trades are run next, with variable step sizes based on the shape of the single-parameter trade curves. Nearly 1300 simulations were run over a weekend. The DOE/ANOVA critical parameter identification technique was used on designs that either showed the best performance or were along pareto-optimal fronts of interest. Of ten parameters identified in the model, only six significantly influence the outputs and are retained. An uncertainty analysis using the vertex search method is performed to bound all of the model outputs including line-of-sight jitter, wave front error, mass, and settle time after a slew.

The methods outlined in this thesis provide valuable information that can be used to guide architecture selection during conceptual design. Visualization functions that were developed along with the MOST model provide a powerful means of comparing designs. The effect of the design variables can clearly be seen in scatter plots that compare competing outputs. Results such as the dominant role of f-number in all of the outputs stand out in these plots. The shapes of the scatter plots provide information on whether different metrics can be traded against each other; there are obvious pareto-optimal fronts for mass versus settle time and mass versus line-of-sight jitter. Examining the plots shows which variables are useful knobs for moving along these pareto-fronts. The uncertainty analysis bounding boxes indicate whether varying these knobs should have the desired effect, or whether changing a variable could likely worsen the performance compared to alternative designs.

All of these results are useful insights into the system, and they all are based on the same level of analysis that is given to a point design model such as TPF-FFI. The size of the MOST finite element models is comparable to the first TPF, SIM or JWST models that were produced. The simulations were run on commercially available computers, over a period of days rather than weeks or months. While development of the parameterized models does require more time and resources than for a single point design finite element model, it allows designs to be compared in a way that was not possible before. The methodology

proposed in this thesis should reduce mission risk and increase the probability of design validation and success by allowing more informed design choices to be made earlier in the design lifecycle.

7.2 Contributions

This thesis makes contributions to the field of design and analysis of opto-mechanical space structures by proposing the combination of trade space analysis using parameterized models and non-deterministic analysis techniques in the early stages of design. Specific contributions to the field follow.

- Developed method to identify superior architectures of high-performance structural concepts using parameterized structural and dynamic models subject to uncertainty. Used uncertainty bounding methods to show which high-level design variables can be used to move along the trade space pareto-front.

- Incorporated Design of Experiments (DOE) techniques with dynamic analysis of space telescope opto-mechanical integrated models to guide critical parameter identification of such models.

- Characterized the modular software environment needed to automatically generate finite element models and dynamic integrated models from an input design vector, allowing models to be generated by multiple people in a team-based environment.

- Identified appropriate uncertainty tools for the conceptual design stage, when no hardware or input parameter models are available

- Developed software tools in MATLAB for running a large trade space analysis given a design matrix. Formulated basic user inputs so that generic systems could be evaluated. Created MATLAB tools to visualize the effect of varying each of the input parameters.

- Applied uncertainty identification techniques to a real program being developed by NASA (TPF-FFI). Compared DOE-based critical parameter identification to direct computation of parameter sensitivities; showed agreement between techniques for LTI

models. Compared vertex-search uncertainty analysis bounds to Monte Carlo propagation, and demonstrated usefulness of worse-case bounds approach in terms of computation savings and accuracy. Created and provided software tools as requested by the Jet Propulsion Laboratory for uncertainty analysis of non-LTI systems.

- Implemented the integrated modeling and trade space tools for two high-performance optical systems: TMT sponsored by the NOAO, and MOST.

- Implemented the uncertainty characterization tools across the MOST trade space. Illustrated how the resulting uncertainty bounds guide the design to use certain design variables for balancing requirements.

7.3 Future work

Recommendations for future work are made for the areas of trade space analysis, parameterized model creation, and uncertainty evaluation.

- Trade space analysis

  - Apply optimization routines to explore the design space. The multivariable trade space exploration method used here was a full factorial search across the design space, where only six design variables were varied, and continuous variables such as f-number were discretized into a limited set of values. The number of simulations increase rapidly as more design variables are added, and it may be that superior designs exist between the design points examined in evaluation. Many optimization routines are described in the field of multi-disciplinary optimization and design, and these may do a better job at identifying optimum points across more variables. Methods used by Jilla [22] are a starting point for using optimization with the parameterized structural models developed in this thesis.

  - Apply ANOVA tools across the simulation results to determine the relative influence of the design variables (where in the thesis ANOVA was used on only uncertainty parameters). Interactions between design variables can be identified by running a full factorial experimental design, or appropriate fractional factorial designs.

- Validate the parameterized model results through hardware data. A reconfigurable testbed should be developed in order to validate the trends identified using the parameterized models. While absolute performance predictions may not be accurate, the models should be able to identify trends as design variables such as the curvature of a mirror (or mirror blank for a testbed), height of the secondary support tower, or even type of aperture are changed. These changes can be implemented by allowing components of the testbed, such as the mirror blank, to be swapped out.
- Consider methods of developing subsystem requirements from the trade space results. Since all parameters may be accessed by the designer, once the high-level design variables are chosen the model would still be useful in terms of exploring lower-level parameter trades. Values that are held constant in this work, such as first mode of the mirror, could be traded against competing subsystem parameters in order to identify requirements for those parameters.

- Parameterized spacecraft dynamic models
  - Include optical control both for wavefront sensing and control as well as tip/tilt pointing stability.
  - Stiffen or implement tip-tilt control for the mirror petals of a segmented aperture, to eliminate the low-frequency "flapping" of the petals on their mounts.
  - Since the mass savings expected for the segmented mirrors were never fully realized, consider reducing the fundamental frequency of the individual segmented mirror petals from 100 Hz, in order to reduce mass.
  - Update the rib-stiffened mirror model so that rib aspect ratio can be traded under fixed constant areal density, so that the effect of rib aspect ratio alone can be analyzed.
  - Low aspect ratio mirror ribs were identified as superior for performance, but taller ribs would generally be preferred if actuators were used on the ribs to change the shape of the mirror, improving wave front error. Examine the tradeoff in greater detail, and determine if there is an optimum rib height.
  - Additional study of how long it takes the performance to settle after a slew is

needed to first reduce the nominal settle times (currently on the order of minutes), and to determine why the settle time is so sensitive to uncertainty in the system.

- Uncertainty evaluation
  - Investigate identified sources of parametric uncertainty in order to place realistic bounds on the parameter values.
  - Consider methods of evaluating non-parametric uncertainty on conceptual design models. Specifically consider whether applying model uncertainty factors (MUFs) across the trade space provides useful information.
  - Validate trends identified by vertex-search bounded uncertainty method using a reconfigurable testbed. Determine whether uncertainty bounds are accurately predicted with vertex search, and whether the relative sizes of the uncertainties across multiple testbed configurations tracks with the model predictions.

Appendix A

Transformation of PDFs into Gaussian

Methods of transforming generic probability density functions (PDFs) to Gaussian are described in Rackwitz and Fiessler [102] and Thoft-Christensen and Murotsu [103]. The basic idea is to match both the probability density functions and the cumulative distribution functions (CDF) of both the original, non-normal random variable and a new, normal variable at a given design point.

$$F_x(x^*) = \Phi\left(\frac{x^* - \mu'_X}{\sigma'_X}\right) \tag{A.1}$$

$$f_X(x^*) = \frac{1}{\sigma'_X}\varphi\left(\frac{x^* - \mu'_X}{\sigma'_X}\right) \tag{A.2}$$

where μ'_X and σ'_X are the mean and standard deviation of the new, normal random variable. The PDF (f_X) and CDF (F_X) of the original, non-random variable are matched at the design point x^* to the standard normal distribution and density functions, given by Φ and φ, respectively.

While the choice of the design point is up to the user, a useful starting point is

$$x^* = \mu_X + \alpha\sigma_X \tag{A.3}$$

where μ_X and σ_X are the mean and standard deviation of the original, non-normal variable.

The multiplicative factor α can be selected as desired, although Reference [103] suggests that $\alpha = 3.0$ is often appropriate.

Once the design point is selected, the mean and standard deviations of the normal random variable are computed via:

$$\sigma'_X = \frac{\varphi\left(\Phi^{-1}\left(F_X(x^*)\right)\right)}{f_X(x^*)} \tag{A.4}$$

$$\mu'_X = x^* - \sigma'_X \cdot \Phi^{-1}\left(F_X(x^*)\right) \tag{A.5}$$

As an example of the technique, consider the transformation from a log-normal random variable to normal. A random variable X is log-normal if the natural logarithm of X is Gaussian [108].

$$\ln X \sim \aleph(\lambda, \zeta) \tag{A.6}$$

where λ is the mean of $\ln X$ and ζ is the standard deviation of $\ln X$. The PDF of the random variable X itself is

$$f_X(x) = \frac{1}{\sqrt{2\pi}\lambda x} \exp\left[-\frac{1}{2}\left(\frac{\ln x - \lambda}{\zeta}\right)^2\right] \tag{A.7}$$

Figure A-1 shows a sample of log-normal distributions for various values of ζ and with a median value of $x_m = 1.0$, related to λ by

$$\lambda = \ln x_m$$

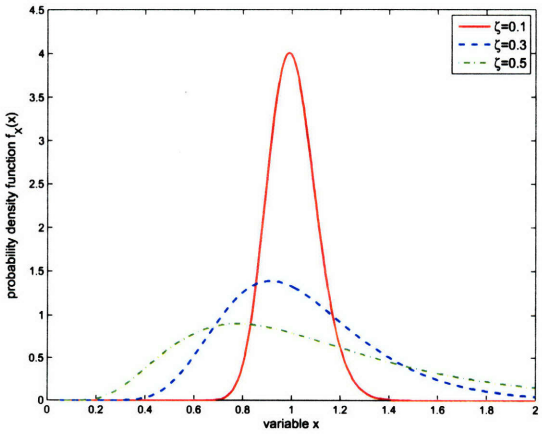

Figure A-1: Log-normal probability density curves

The transformation to normal variables is performed by first selecting the design point x^*. Following the steps above, this is done using the mean and standard deviation of the log-normal distribution. These quantities are related to λ and ζ through:

$$\mu_X = \exp\left(\lambda + \frac{1}{2}\zeta^2\right) \tag{A.8}$$

$$\sigma_X = \mu_X\sqrt{\exp\left(\zeta^2\right) - 1} \approx \zeta\mu \tag{A.9}$$

Examples of the function for different values of α and ζ are shown in Figure A-2.

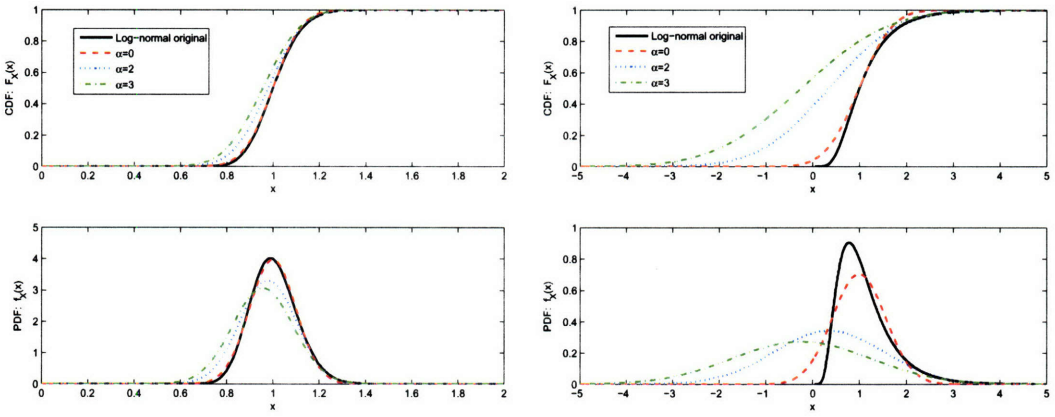

(a) $\zeta = 0.1$ (b) $\zeta = 0.5$

Figure A-2: Log-normal PDF transformed into a Gaussian approximation

From the figures, it is obvious that there are differences between the log-normal and its transformed Gaussian normal approximation. For instance, negative values are not admissible for the original log-normal function, but are present in the Gaussian approximation. Also, the CDFs exhibit large discrepancies at values far from the design point. The usefulness of this approximation will obviously depend on the degree of difference between the Gaussian and original PDFs, and on the level of accuracy needed in the application.

The functions are equal at the design points, and α can be chosen to shape the rest of the function as desired. If the tail of the CDF distribution, where it approaches 1.0, must be accurately modeled, then the larger values of α should be used. Likewise, if it is more important to match the entire log-normal CDF, then $\alpha = 0$ is more appropriate.

Appendix B

Change of variables probabilistic propagation method

The Change of Variables method computes the probability density function (PDF) of the output σ given an input p related by some function $\sigma = g(p)$. The method uses the PDF transformation [82]

$$f_\Sigma(\sigma) = \left|\frac{\partial p}{\partial \sigma}\right| f_P(p) \tag{B.1}$$

to obtain the joint output PDF $f_\Sigma(\sigma)$ given the joint PDF of the inputs $f_P(p)$, along with the sensitivity of the input to the output, $\frac{\partial p}{\partial \sigma}$. Solving Equation B.1 generally requires the functional relationship be inverted, $p = h(\sigma)$, so that

$$f_\Sigma(\sigma) = \left|\frac{\partial h(\sigma)}{\partial \sigma}\right| f_P[h(\sigma)] \tag{B.2}$$

For systems analysis, σ is often a performance found using frequency domain methods, with the inputs p buried in the process. In such situations is can be difficult to explicitly form the inverted relationship $p = h(\sigma)$ and the sensitivity $\partial p/\partial \sigma$. Most often only the sensitivity of the output to the input $\frac{\partial \sigma}{\partial p}$ is known. However, when the function is known implicitly, the PDF transformation can be applied numerically to sample the PDF of σ . The approach rewrites the differential relationship as

$$\left|\frac{\partial \sigma}{\partial p}\right| \cdot f_\Sigma(\sigma) = f_P(p) \tag{B.3}$$

This is an algebraic relationship that can be solved for f_Σ.

$$f_\Sigma(\sigma) = \frac{f_P(p)}{\left|\frac{\partial \sigma}{\partial p}\right|} \tag{B.4}$$

Solving for $f_\Sigma(\sigma)$ now only requires the computation of the more common gradient of σ with respect to p. In the case of multiple input-multiple output systems, this is the determinant of the Jacobian J.

$$J = \det \begin{bmatrix} \frac{\partial \sigma_1}{\partial p_1} & \cdots & \frac{\partial \sigma_1}{\partial p_n} \\ \vdots & & \\ \frac{\partial \sigma_n}{\partial p_1} & & \frac{\partial \sigma_n}{\partial p_n} \end{bmatrix} \tag{B.5}$$

Note that an equal number of inputs and outputs are required so that the Jacobian remains square. If there is a smaller number of outputs, "dummy" outputs must be included at this stage, to be removed from the results later.

This approach to solving for the distribution of an output is often described in textbooks on the subject of random variables, but is not found in research literature. Textbook examples most often include simple single input-single output functions that can be solved analytically, with pencil and paper. In order to apply this procedure to much larger problems such as model parameters inputs to state-space outputs, it is necessary to sample the functions, instead of attempting to perform the inversion. Given a range of values across the inputs p, it is possible to compute the output σ, the input PDF $f_P(p)$ and the determinant of the Jacobian J. Equation B.4 is then used to compute the output PDF at each point. Finally, the output PDF values are mapped from the input p-space to the output σ-space. Since the points mapped across the input range are not necessary equally spaced across the desired output range, the output PDF values must be binned across the appropriate output grid points. This procedure is described next, using inputs x and outputs y for a relationship $y = g(x)$.

1. Grid the input space x
2. Choose a point in the input space x_o
3. Compute the value of the input PDF at x_o, $f_X(x_o)$
4. Compute $y_o = g(x_o)$

5. Compute the Jacobian $\left|\frac{dy_o}{dx_o}\right|$ at x_o
6. Compute the value of the output PDF $f_Y(y_o) = f_X(x_o) \cdot \frac{1}{\left|\frac{dy_o}{dx_o}\right|}$
7. Repeat steps 2-6 through the x-grid range
8. Grid the output space y
9. Find all y_i in each Δy bin
10. Sum together all $f_Y(y_i)$ that correspond to those y_i in the bin for the final output distribution

Monotonic Example

This procedure will be demonstrated with two simple examples. First consider a system of equations described below, in which the inputs and outputs are related monotonically, meaning that through the sample space the gradients are never zero.

$$\begin{aligned} y_1 &= x_1 - x_2 \\ y_2 &= 4x_1 + x_1x_2 \end{aligned} \tag{B.6}$$

This procedure makes no assumption on the distributions of the input parameters. For these examples, the Gaussian distribution is used to model the input PDFs.

$$f_{X_i}(x_i) = \frac{1}{\sqrt{2\pi\sigma_{x_i}^2}} \cdot \exp\left(\frac{-(x_i - \mu_{x_i})^2}{2\sigma_{x_i}^2}\right) \tag{B.7}$$

If the inputs are independent, their joint PDF can be formed by multiplication. The resulting distribution is plotted in Figure B-1.

$$f_{X_1,X_2}(x_1, x_2) = f_{X_1}(x_1) \cdot f_{X_2}(x_2) \tag{B.8}$$

The gradients for a state-space system can be found using the sensitivity tools described in Section 5.1.1. For this simple example, the determinant of the gradient is quickly calculated analytically.

$$J_{ana} = x_1 + x_2 + 4 \tag{B.9}$$

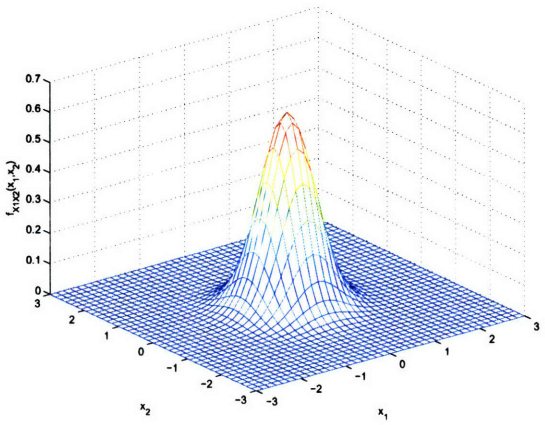

Figure B-1: Joint PDF for two independent Gaussian inputs

And finally the output distributions in the x-space are computed via

$$f_{Y_1^x,Y_2^x}(y_1, y_2) = \frac{f_{X_1,X_2}(x_1, x_2)}{|J|} \tag{B.10}$$

This output PDF is shown in Figure B-2(a). Once the PDF values are mapped from the input x-space to the output y-space, the PDF looks like Figure B-2(b).

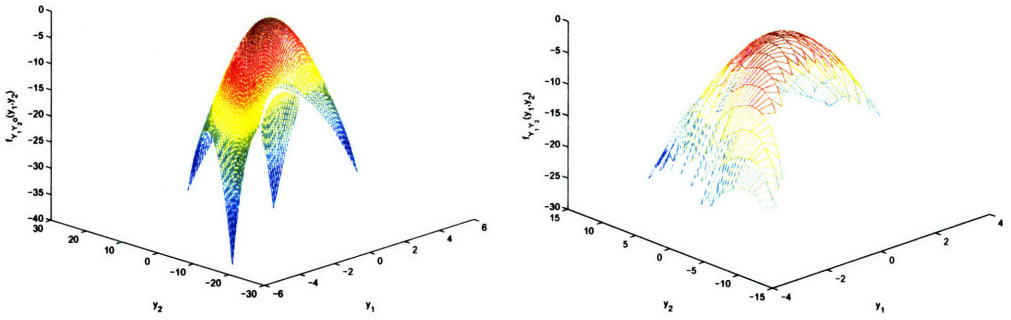

(a) Points mapped to the input grid, (x_1, x_2) (b) Points mapped to the output grid, (y_1, y_2)

Figure B-2: Output PDF mapping onto the input and output grid spaces

The resulting PDF surface is the joint PDF for both outputs. If one of the outputs is a "dummy" output, the undesired output can be removed by integration. For instance, if y_2 is the "dummy" output, the PDF of y_1 is

$$f_{Y_1}(y_1) = \int_{-\infty}^{\infty} f_{Y_1,Y_2}(y_1, y_2)\, dy_2. \tag{B.11}$$

The integration is performed numerically. The resulting individual PDFs and associated cumulative distribution functions (CDF) are shown in Figure B-3. Both CDFs asymptote to 1.0, guaranteeing that the output distributions are legitimate PDFs.

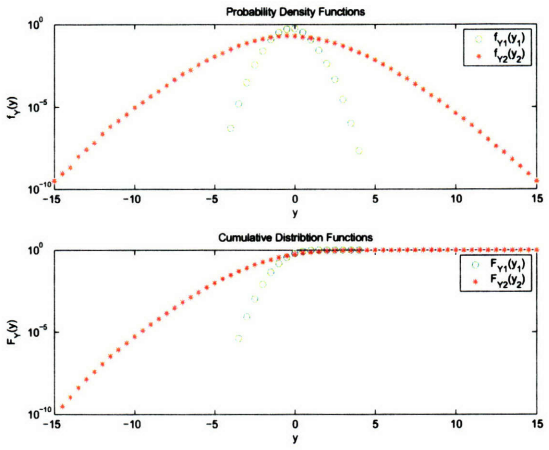

Figure B-3: Output PDF and CDF curves for the change-of-variables monotonic example

Non-Monotonic Example

The second example is of a similarly simple set of equations, but in this case the equations are non-monotonic. This results in gradients that go to zero. This will cause difficulties in Equation B.4, with J in the denominator.

The example system of equations is

$$\begin{aligned} y_1 &= x_1^2 + x_2^2 \\ y_2 &= 2x_1 + x_1 x_2 \end{aligned} \tag{B.12}$$

plotted in Figure B-4. The Jacobian J of this system is

$$J = 2x_1^2 - 4x_2 - 2x_2^2 \tag{B.13}$$

plotted in Figure B-5.

The difficulty is that a singularity appears in the output PDF in Equation B.4 as the Jacobian J goes through zero. In Figure B-5, this singularity is a line across the (x_1, x_2) input space as the surface of J passes through zero. The result of this singularity is seen as the PDF is plotted against the input x points in Figure B-6(a), and again as the PDF is

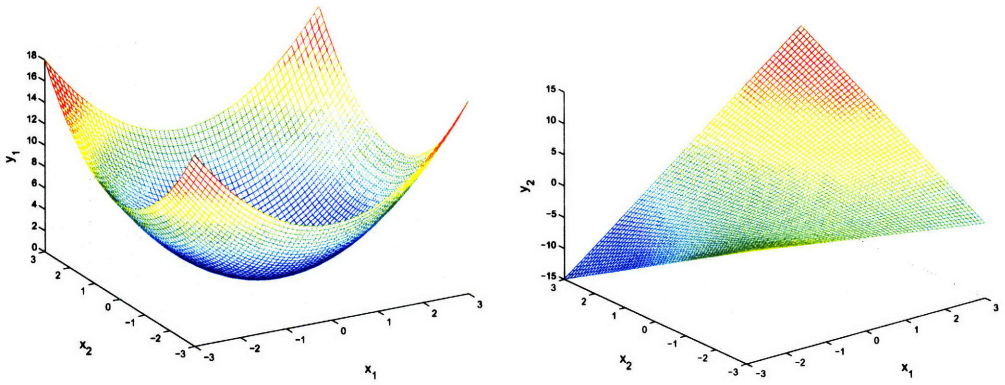

(a) Function $y_1(x_1, x_2)$ (b) Function $y_2(x_1, x_2)$

Figure B-4: Example non-monotonic system of equations.

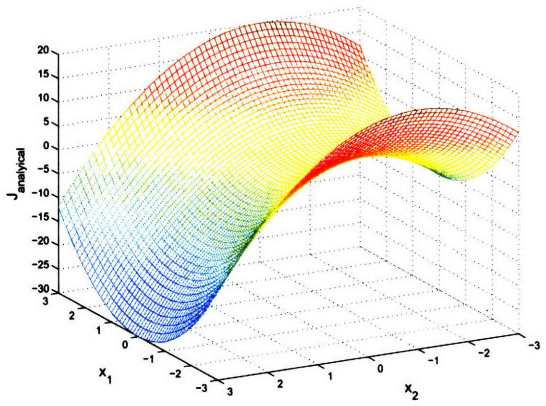

Figure B-5: Determinant of the Jacobian. Note that in the non-monotonic example, a line of the surface passes through zero.

plotted against the output y points in Figure B-6(b). About this singularity line the output PDF "wraps" around itself, creating two surfaces which must be summed together for the final output. It is also necessary to create a much finer mesh around the singularities, in order to capture the complete PDF; a coarse mesh will produce much higher values than actually exist. A Change-of-Variables function in DOCS allows for variable meshing, and provides the binning capability for non-monotonic systems such as this. The final resulting PDF for this example is shown in Figure B-7.

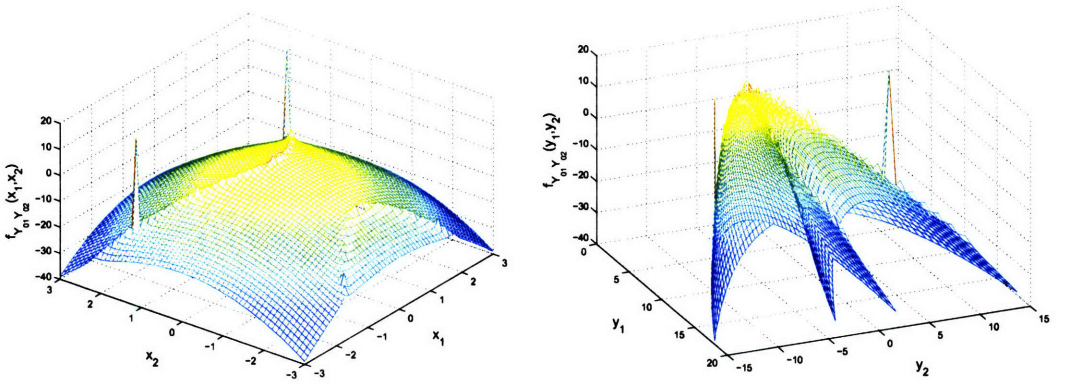

(a) Output PDF gridded in x-space

(b) Output PDF gridded in y-space, before binning. Note that the surface from plot (a) is wrapped about itself in this grid system.

Figure B-6: Output PDF samples of the non-monotonic system of equations

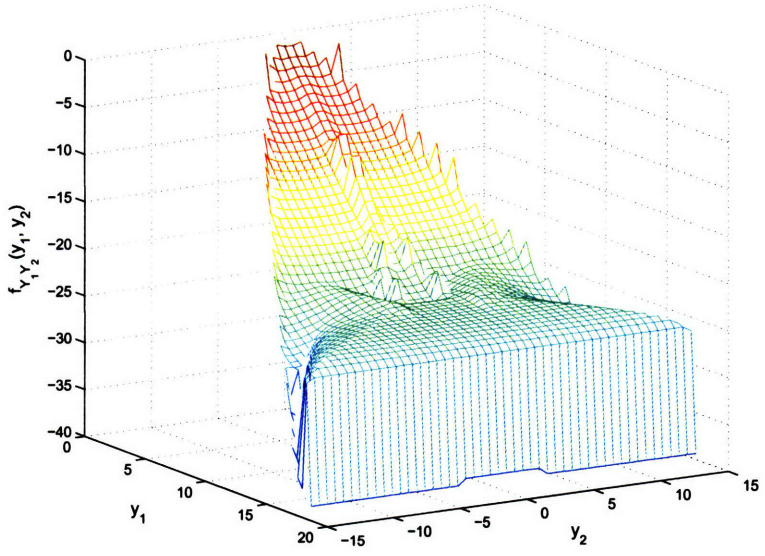

Figure B-7: Binned output PDF for the non-monotonic system of equations

Bibliography

[1] John Nella, Charles Atikinson, Allen Bronowicki, et al. James webb space telescope (JWST) observatory architecture and performance. In *Space 2004 Conference and Exhibit*, San Diego, CA, Sept. 28-30, 2004. AIAA-2004-5986.

[2] SIM Planetquest webpage, April 2006.
URL: <http://planetquest.jpl.nasa.gov/SIM/sim_index.cfm>.

[3] Terrestrial Planet Finder webpage, April 2006.
URL: <http://planetquest.jpl.nasa.gov/TPF/tpf_index.cfm>.

[4] Robert A. Brown, Christopher J. Burrows, Stefano Casertano, et al. The 4-meter space telescope for investigating extrasolar earth-like planets in starlight: TPF is HST2. In J. Chris Blades and Oswald H. Siegmund, editors, *Future EUV/UV and Visible Space Astrophysics Missions and Instrumentation*, volume 4854 of *Proc. SPIE*, pages 95–107, Feb. 2003.

[5] Gary H. Blackwood, Eugene Serabyn, Serge Dubovitsky, MiMi Aung, Steven M. Gunter, and Curt Henry. System design and technology development for the Terrestrial Planet Finder infrared interferometer. In Daniel R. Coulter, editor, *Techniques and Instrumentation for Detection of Exoplanets*, volume 5170 of *Proc. SPIE*, pages 129–143, Nov. 2003.

[6] Peter R. Lawson and Jennifer A. Dooley. *Technology Plan for the Terrestrial Planet Finder Interferometer.* Jet Propulsion Laboratory, California Institute of Technology, Pasadena, California, June 2005. JPL Publication 05-5.

[7] C. Noecker, O. Lay, B. Ware, and S. Dubovitsky. TPF interferometer performance requirements. In *Proceedings of SPIE Vol. 5170: Techniques and Instrumentation for Detection of Exoplanets*, Bellingham, WA, 2003. SPIE.

[8] Thirty Meter Telescope webpage, April 2006. URL: <http://www.tmt.org/>.

[9] Gary H Sanders. The Thirty Meter Telescope (TMT) project. In *AAS 205th Meeting*, January 11, 2005. URL: <http://www.tmt.org/media/G-Sanders-Jan05-AAS.pdf>.

[10] Douglas G. MacMynowski, George Z. Angeli, Konstantinos Vogiatzis, Joeleff Fitzsimmons, and Stephen Padin. Parametric modeling and control of telescope wind-induced vibration. In Simon C. Craig and Martin J. Cullum, editors, *Proc. SPIE*, volume 5497 of *Modeling and Systems Engineering for Astronomy*, pages 266–277, Sept 2004.

[11] Douglas G. MacMartin and Gary A. Chanan. Control of the California Extremely Large Telescope primary mirror. In J. Roger P. Angel and Roberto Gilmozzi, editors, *Proc. SPIE*, volume 4840 of *Future Giant Telescopes*, pages 69–80, Jan 2003.

[12] AIAA. Guide for the verification and validation of computational fluid dynamics simulations. American Institute of Aeronautics and Astronautics Guide, January 14, 1998. G-077-1998.

[13] IEEE. IEEE standard for software verification and validation, July 20, 1998. IEEE Std 1012-1998.

[14] A.M. Kabe and E.K. Hall II. On-orbit vibration technology assessment. Aerospace Report ATR-2001(8001)-1, The Aerospace Corporation, El Segundo, CA, August 22, 2001.

[15] Rebecca A. Masterson and David W. Miller. *Dynamic Tailoring and Tuning for Space-Based Precision Optical Structures.* PhD thesis, Massachusetts Institute of Technology, Cambridge, MA, February 2005.

[16] Mark E. Campbell and Edward F. Crawley. Development of structural uncertainty models. *Journal of Guidance, Control, and Dynamics*, 20(5):841–849, Sept.-Oct. 1997.

[17] Timothy Reed, Stephen E. Kendrick, Robert J. Brown, James B. Hadaway, and Don Byrd. Final results of the subscale beryllium mirror demonstrator (SBMD) program.

In H. Philip Stahl, editor, *Optical Manufacturing and Testing IV*, volume 4451 of *Proceedings of SPIE*, pages 5–14, 2001.

[18] Stephen E. Kendrick, Timothy Reed, and Scott Streetman. In-process status of the 1.4-m beryllium semi-rigid advanced mirror system demonstrator (AMSD). In H. Philip Stahl, editor, *Optical Manufacturing and Testing IV*, volume 4451 of *Proceedings of SPIE*, pages 58–66, 2001.

[19] Christopher Chrzanowski, Charles Frohlich, Badri Shirgur, and Ronald Mink. Design and structural/optical analysis of a kinematic mount for the testing of silicon carbide mirrors at cryogenic temperatures. In Lee D. Peterson and Robert C. Guyer, editors, *Space Systems Engineering and Optical Alignment Mechanisms*, volume 5528 of *Proceedings of SPIE*, pages 204–214, 2004.

[20] David W. Miller and Simon C.O. Grocott. Robust control of the multiple mirror telescope adaptive secondary mirror. *Opt. Eng.*, 38(8):1276–1287, August 1999.

[21] Soon-Jo Chung, David W. Miller, and Olivier L. deWeck. ARGOS testbed: study of multidisciplinary challenges of future spaceborne interferometric arrays. *Opt. Eng.*, 43(9):2156–2167, September 2004.

[22] Cyrus D. Jilla and David W. Miller. *A Multiobjective, Multidisciplinary Design Optimization Methodology for the Conceptual Design of Distributed Satellite Systems.* PhD thesis, Massachusetts Institute of Technology, Cambridge, MA, May 2002.

[23] Scott A. Uebelhart and David W. Miller. Conditioning, reduction, and disturbance analysis of large order integrated models for space-based telescopes. Master's thesis, Massachusetts Institute of Technology, Cambridge, MA, February 2001.

[24] Olivier L. de Weck and David W. Miller. Integrated modeling and dynamics simulation for the next generation space telescope. Master's thesis, Massachusetts Institute of Technology, Cambridge, MA, June 1999. SSL #5-99.

[25] Timothy Hasselman. Quantification of uncertainty in structural dynamic models. *Journal of Aerospace Engineering*, 14(4):158–165, October 2001.

[26] Homero L. Gutierrez and David W. Miller. *Performance Assessment and Enhancement of Precision Controlled Structures During Conceptual Design.* PhD thesis, Massachusetts Institute of Technology, Cambridge, MA, February 1999.

[27] Carl Blaurock. Disturbance-optics-controls-structures (DOCS). URL: <http://www.nightsky-systems.com/pdf/docs_intro.pdf>, Nightsky Systems, Inc., 2006.

[28] Gregory J. Moore. *MSC/NASTRAN Design Sensitivity and Optimization. User's Guide, version* 68. The MacNeal-Schwender Corp., Los Angeles, CA, 1994.

[29] Mark E. Botkin. Structural optimization of automotive body components based upon parametric solid modeling. In 8^{th} *AIAA/USAF/NASA/ISSMO Symposium on Multidisciplinary Analysis and Optimization*, Long Beach, CA, Sept. 6-8, 2000. AIAA-2000-4707.

[30] Peter A. Fenyes. Multidisciplinary design and optimization of automotive structures - a parametric approach. In 8^{th} *AIAA/USAF/NASA/ISSMO Symposium on Multidisciplinary Analysis and Optimization*, Long Beach, CA, Sept. 6-8, 2000. AIAA-2000-4706.

[31] M. L. Baker and K. Hoffmann. The impact of rapid structural analysis in configuration development. In *AIAA Space 2000 Conference and Exposition*, Long Beach, CA, Sept. 19-21, 2000. AIAA-2000-5308.

[32] N. M. Alexandrov, R. M. Lewis, C. R. Gumbert, L. L. Green, and P. A. Newman. Optimization with variable-fidelity models applied to wing design. In 38^{th} *Aerospace Sciences Meeting & Exhibit*, Reno, NV, January 10-13, 2000. AIAA-2000-0841.

[33] Robert E. Smith, Malcolm I.G. Bloor, Michael J. Wilson, and Almuttil M. Thomas. Rapid airplane parametric input design (RAPID). In 12^{th} *AIAA Computational Fluid Dynamics Conference*, San Diego, CA, June 19-22, 1995. AIAA-95-1687.

[34] Mark D. Sensmeier and Jamshid A. Samareh. Automatic aircraft structural topology generation for multidisciplinary optimization and weight estimation. In 46^{th} *AIAA/ASME/ASCE/AHS/ASC Structures, Structural Dynamics & Materials Conference*, Austin, TX, April 18-21, 2005. AIAA-2005-1893.

[35] Mark D. Sensmeier, Bret T. Stewart, and Jamshid A. Samareh. Rapid generation and assessment of aircraft structural topologies for multidisciplinary optimization and weight estimation. In 47^{th} *AIAA/ASME/ASCE/AHS/ASC Structures, Structural Dynamics & Materials Conference*, Newport, Rhode Island, May 1-4, 2006. AIAA-2006-1981.

[36] C. Cerulli, P. B. Meijer, M. J. L. van Tooren, and J. W. Hofstee. Parametric modeling of aircraft families for load calculation support. In 45^{th} *AIAA/ASME/ASCE/AHS/ASC Structures, Structural Dynamics & Materials Conference*, Palm Springs, CA, April 19-22, 2004. AIAA 2004-2019.

[37] Z. Peter Szewczyk and Harry Schaeffert. Object-oriented approach to structural modeling and analysis. In 37^{th} *AIAA Aerospace Sciences Meeting and Exhibit*, Reno, NV, January 11-14, 1999. AIAA-99-0108.

[38] David M. LoBosco and David W. Miller. Integrated modeling of optical performance for the Terrestrial Planet Finder structurally connected interferometer. Master's thesis, Massachusetts Institute of Technology, Cambridge, MA, May 2004. SSL #6-04.

[39] Myles Walton and Daniel Hastings. Quantifying embedded uncertainty of space systems architectures in conceptual design. In *AIAA Space 2001 - Conference and Exposition*, Albuquerque, NM, Aug. 28–30 2001. AIAA-2001-4573.

[40] Frédéric Bourgault and David W. Miller. Model uncertainty and performance analysis for precision controlled space structures. Master's thesis, Massachusetts Institute of Technology, Cambridge, Massachusetts, December 2000.

[41] M.A. Blair, J.W. Sills, Jr., and A. Semple. Determination of the model uncertainty factor using cross-orthogonality and overall load factor decomposition. In *Proceedings of SPIE: 12^{th} International Modal Analysis Conference*, volume 2251, pages 613–618, 1994.

[42] Xiaoping Du and Wei Chen. Methodology for managing the effect of uncertainty in simulation-based design. *AIAA Journal*, 38(8):1471–1478, August 2000.

[43] Vít Babuška, Delano Carter, and Steven Lane. Uncertainty propagation and substructure synthesis using LFTs. In *47^{th} AIAA/ASME/ASCE/AHS/ASC Structures,*

Structural Dynamics and Materials Conference, Newport, Rhode Island, May 1-4, 2006. AIAA-2006-2278.

[44] Roy R. Jr. Craig. *Structural Dynamics: An Introduction to Computer Methods.* John Wiley & Sons, New York, 1981.

[45] Eric Sandgren and T.M. Cameron. Robust design optimization of structures through consideration of variation. *Computer & Structures*, 80:1605–1613, 2002.

[46] Lusine Baghdasaryan, Wei Chen, Thaweepat Buranathiti, and Jian Cao. Model validation via uncertainty propagation using response surface models. In *Proceedings of DETC'02: ASME 2002 Design Engineering Technical Conferences and Computer and Information in Engineering Conference*, Montreal, Canada, September 29-October 2, 2002. ASME.

[47] Jerome Sacks, William J. Welch, Toby J. Mitchell, and Henry P. Wynn. Design and analysis of computer experiments. *Statistical Science*, 4(4):409–435, 1989.

[48] Leslie D. Liaw, Richard I. DeVries, and Donald L. Cronin. An MDO-compatible method for robust design of vehicles, systems, and components. In 7^{th} *AIAA/USAF/NASA/ISSMO Symposium on Multidisciplinary Analysis and Optimization*, St. Louis, MO, Sept. 2-4, 1998. AIAA-1998-4786.

[49] A. Jebb and H.P. Wynn. Robust engineering design post-Taguchi. *Philosophical Transactions of the Royal Society of London. Series A, Mathematical and Physical Sciences*, 327(1596):605–616, 1989.

[50] Timothy W. Simpson, Jesse Peplinski, Patrick N. Koch, and Janet K. Allen. On the use of statistics in design and the implications for deterministic computer experiments. In *Proceedings of DETC'97, 1997 ASME Design Engineering Technical Conferences*, Sacrameto, California, September 14-17, 1997. ASME.

[51] Anthony A. Giunta, Steven F. Wojtkiewicz Jr., and Michael S. Eldred. Overview of modern design of experiments methods for computational simulations. In *41st Aerospace Sciences Meeting and Exhibit*, Reno, Nevada, January 6-9, 2003. American Institute of Aeronautics and Astronautics. AIAA-2003-649.

[52] M.D. McKay, R.J. Beckman, and W.J. Conover. A comparison of three methods for selecting values of input variables in the analysis of output from a computer code. *Technometrics*, 42(1):55–61, February 2000.

[53] Jayant R. Kalagnanam and Urmila M. Diwekar. An efficient sampling technique for off-line quality control. *Technometrics*, 39(3):308–319, August 1997.

[54] Daniel D. Frey, Geoff Reber, and Yiben Lin. A quadrature-based sampling technique for robust design with computer models. In *Proceedings of IDETC/CIE 2005, ASME 2005 International Design Engineering Technical Conferences & Computers and Information in Engineering Conference*, Long Beach, CA, September 24–28, 2005. DETC2005-85490.

[55] Daniel D. Frey, Fredrik Engelhardt, and Edward M. Greitzer. A role for "one-factor-at-a-time" experimentation in parameter design. *Research in Engineering Design*, 14:65–74, 2003.

[56] Daniel D. Frey and Rajesh Jugulum. How one-factor-at-a-time experimentation can lead to greater improvements than orthogonal arrays. In *Proceedings of DETC'03, ASME 2003 Design Engineering Technical Conferences & Computers and Information in Engineering Conference*, Chicago, Illinois, September 2–6, 2003. DETC2003/DTM-48646.

[57] Genichi Taguchi, Subir Chowdhury, and Yuin Wu. *Taguchi's quality engineering handbook.* John Wiley, Hoboken, NJ and ASI Consulting, Livonia, MI, 2005.

[58] Thomas J. Lorenzen and Virgil L. Anderson. *Design of Experiments: A No-Name Approach.* Marcel Dekker, Inc., New York, 1993.

[59] Douglas C. Montgomery. *Design and Analysis of Experiments.* John Wiley & Sons, New York, 5^{th} edition, 2001.

[60] Thomas J. Santer, Brian J. Williams, and William I. Notz. *The Design and Analysis of Computer Experiments.* Springer Series in Statistics. Springer, New York, 2003.

[61] Yakov Ben-Haim and Isaac Elishakoff. *Convex Models of Uncertainty in Applied Mechanics.* Elsevier, New York, 1990.

[62] Isaac Elishakoff. Convex versus probabilistic models of uncertainty in structural dynamics. In M. Petyt, H.F. Wolfe, and C. Mei, editors, *Structural Dynamics: Recent Advances. Proceedings of the 4^{th} International Conference*, pages 3–21, Southampton, UK, July 15-18 1991. Elsevier Applied Science.

[63] Todd Mosher. Applicability of selected multidisciplinary design optimization methods to conceptual spacecraft design. In 6^{th} *NASA and ISSMO Symposium on Multidisciplinary Analysis and Optimization*, pages 664–671, Bellevue, WA, Sept. 4-6, 1996. AIAA-1996-4052.

[64] Todd Mosher. Spacecraft design using a genetic algorithm optimization approach. In *Proceedings of the IEEE Aerospace Conference*, volume 3, pages 123–134, Aspen, CO, March 21-28, 1998.

[65] Ellen Riddle. Use of optimization methods in small satellite systems analysis. In 12^{th} *AIAA/USU Conference on Small Satellites*, Utah State University, Logan, UT, Aug. 31–Sept. 3, 1998. SSC98-X-1.

[66] Chia-Yen Peng, Marie B. Levine, Lillian Shido, and Robert S. Leland. Experimental observations on material damping at cryogenic temperatures. In Lee D. Peterson and Robert C. Guyer, editors, *Proceedings of SPIE*, volume 5528, pages 44–62, Bellingham, WA, September 2004. SPIE.

[67] Chia-Yen Peng, Marie Levine, Lillian Shido, Marc Jacoby, and William Goodman. Measurement of vibrational damping at cryogenic temperatures for silicon carbide foam and silicon foam materials. In William A. Goodman, editor, *Proceedings of SPIE*, volume 5868, Bellingham, WA, August 2005. SPIE.

[68] Michael G. Béda. Structural analysis summary: Collector spacecraft. Powerpoint presentation, Jet Propulsion Laboratory, June 11 2004.

[69] C. Perrygo and R. Burg. Hand calculation of line-of-sight senstivity to optics displacements. NGST Systems Engineering memorandum, January 22, 1999.

[70] Eugene Hecht. *Optics*. Addison-Wesley Longman, Inc., Reading, MA, 3^{rd} edition, 1998.

[71] H. Rutten and M. van Venrooij. *Telescope Optics: A Comprehensive Manual for Amateur Astronomers.* Willmann-Bell, Inc., Richmond, VA, 1988.

[72] James C. Wyant and Katherine Creath. *Applied Optics and Optical Engineering*, volume XI, chapter "Basic Wavefront Aberration Theory for Optical Metrology", pages 1–53. Academic Press, Inc., Boston, 1992.

[73] James C. Wyant. Zernike polynominals. Website, April 2006. URL: <http://www.optics.arizona.edu/jcwyant/Zernikes/ZernikePolynomials.htm>.

[74] George Z. Angeli and Brooke Gregory. Linear optical model for a large ground-based telescope. In Mark A. Kahan, editor, *Proc. SPIE*, volume 5178 of *Optical Modeling and Performance Predictions*, pages 64–73, Jan 2004.

[75] Bill Bialke. High fidelity mathematical model of reaction wheel performance. In *Guidance and Control 1998*, volume 98 of *Advances in the Astronautical Sciences*, pages 483–496, Breckenridge, CO, February 4-8, 1998. American Astronautical Society. AAS 98-063.

[76] G.W. Neat, J.W. Melody, and B.J. Lurie. Vibration attenuation approach for spaceborne optical interferometers. *IEEE Transactions on Control Systems Technology*, 6(6):689–700, Nov. 1998.

[77] R.A. Masterson, D.W. Miller, and R.L. Grogan. Development and validation of reaction wheel disturbance models - empirical model. *Journal of Sound and Vibration*, 249(3):575–598, Jan. 2002.

[78] Rebecca A. Masterson. Development and validation of empirical and analytical reaction wheel disturbance models. Master's thesis, Massachusetts Institute of Technology, Cambridge, MA, June 1999.

[79] Kemin Zhou, John C. Doyle, and Keith Glover. *Robust and Optimal Control.* Prentice Hall, Upper Saddle River, New Jersey, 1996.

[80] Robert N. Jacques. *On-line System Identification and Control Design for Flexible Structures.* PhD thesis, Massachusetts Institute of Technology, Cambrige, MA, May 1994.

[81] Gregory J.W. Mallory and David W. Miller. *Development and Experimental Validation of Direct Controller Tuning for Spaceborne Telescopes.* PhD thesis, Massachusetts Institute of Technology, Cambridge, MA, April 2000.

[82] R.G. Brown and P.Y.C. Hwang. *Introduction to Random Signals and Applied Kalman Filtering.* John Wiley & Sons, New York, 3^{rd} edition, 1997.

[83] William M. Siebert. *Circuits, Signals, and Systems.* The MIT Press, Cambridge, Massachusetts, 1986.

[84] Kyle Yi-Ling Yang and Steven Hall. *Efficient Design of Robust Controllers for H_2 Performance.* PhD thesis, Massachusetts Institute of Technology, Cambridge, MA, February 1997. SERC #8-96.

[85] Christine M. Belcastro. Parametric uncertainty modeling: An overview. In *Proceedings of the American Control Conference*, pages 992–996, Philadelphia, PA, June 1998.

[86] Jean-François Magni, Samir Bennani, and Jean-Paul Dijkgraaf. An overview of system modelling in LFT form. In C. Fielding et al., editors, *Advanced Techniques for Clearance of Flight Control Laws*, number 283 in LNCIS, pages 169–195. Springer-Verlag, Berlin, 2002.

[87] Thomas Mannchen and Klaus H. Well. Uncertainty bands approach to LFT modelling. In C. Fielding et al., editors, *Advanced Techniques for Clearance of Flight Control Laws*, number 283 in LNCIS, pages 211–220. Springer-Verlag, Berlin, 2002.

[88] Juan C. Cockburn and Blaise G. Morton. Linear fractional representations of uncertain systems. *Automatica*, 33(7):1263–1271, 1997.

[89] Carl Blaurock. *Disturbance-Optics-Controls-Structures (DOCS) Overview.* Nightsky Systems, Inc., Raleigh, North Carolina, 2004.

[90] Carl Blaurock. *Disturbance-Optics-Controls-Structures (DOCS): NASTRAN Reference Manual.* Nightsky Systems, Inc., Raleigh, North Carolina, Nov. 19, 2004.

[91] Wiley J. Larson and James R. Wertz. *Space Mission Analysis and Design.* Microcosm, Inc. and Kluwer Academic Publishers, Torrance, CA, 2^{nd} edition, 1992.

[92] Ruth Azor. Momentum management and torque distribution. In *The 33rd Israel Annual Conference on Aviation and Astronautics*, pages 339–347, Israel, 1993. Israel Society of Aeronautics and Astronautics.

[93] Gilbert Strang. *Introduction to Linear Algebra.* Wellesley-Cambridge Press, Wellesley, MA, 1993.

[94] Terry S. Mast and Jerry E. Nelson. Segmented mirror control system hardware for CELT. In Philippe Dierickx, editor, *Proc. SPIE*, volume 4003 of *Optical Design, Materials, Fabrication, and Maintenance*, pages 226–240, July 2000.

[95] N. Logothetis and H.P. Wynn. *Quality Through Design: Experimental Design, Off-line Quality Control, and Taguchi's Contributions.* Oxford Series on Advanced Manufacturing. Clarendon Press, Oxford, 1989.

[96] Raymond H. Myers and Douglas C. Montgomery. *Response Surface Methodology: Process and Product Optimization using Designed Experiments.* John Wiley & Sons, New York, 2nd edition, 2002.

[97] Thomas L. Paez, Norman F. Hunter, and John A. Cafeo. A Karhunen-Loeve framework for modeling structural randomness. In *Proceedings of IMAC-XX*, Los Angeles, CA, Feb. 4-7 2002.

[98] Alvin W. Drake. *Fundamentals of Applied Probability Theory.* McGraw-Hill, Inc., New York, 1967.

[99] R. E. Melchers. *Structural Reliability Analysis and Prediction.* John Wiley & Sons, New York, 1999.

[100] B. H. Thacker, D. S. Riha, H. R. Millwater, and M. P. Enright. Errors and uncertainties in probabilistic engineering analysis. In *42nd AIAA/ASME/ASCE/AHS/ASC Structures, Structural Dynamics, and Materials Conference and Exhibit*, Seattle, WA, April 16-19, 2001. AIAA-2001-1239.

[101] Edward A. Rodriguez, Jason E. Pepin, Ben H. Thacker, and David S. Riha. Probabilistic structural response of a valve assembly to high impact loading. In *IMAC-XIX: A Conference on Structural Dynamics*, pages 1325–1331, Kissimmee, FL, Feb 5-8, 2001.

[102] Rüdiger Rackwitz and Bernd Fiessler. Structural reliability under combined random load sequences. *Computers and Structures*, 9:489–494, 1978.

[103] Palle Thoft-Christensen and Yoshisada Murotsu. *Application of Structural Systems Reliability Theory.* Springer-Verlag, New York, 1986.

[104] Carl Blaurock, Scott A. Uebelhart, and David W. Miller. Identification and propagation of probabilistic uncertainties for flexible space structures. In *Proceedings of SPIE: Space Systems Engineering and Optical Alignment Mechanisms*, volume 5528. SPIE, September 2004.

[105] S.S. Simonian. Survey of spacecraft damping measurements - applications to electro-optic jitter problems. In *The role of damping in vibration and noise control; Proceedings of the 11th Biennial Conference on Mechanical Vibration and Noise*, pages 287–292, Boston, MA, Sept. 27-30 1987. American Society of Mechanical Engineers.

[106] Elizabeth Jordan, Andrzej Stewart, Scott A. Uebelhart, Deborah Howell, and David W. Miller. Parametric modeling of space telescope architectures. In *SPIE Astronomical Telescopes and Instrumentation*, Orlando, Florida, May 24-31 2006.

[107] Olivier L. de Weck. *Multivariable Isoperformance Methodology for Precision Opto-Mechanical Systems.* PhD thesis, Massachusetts Institute of Technology, Cambridge, MA, September 2001.

[108] Alfredo Hua-Sing Ang and Wilson H. Tang. *Probability Concepts in Engineering Planning and Design, Volume 1: Basic Principles.* Wiley, New York, 1975.